ISSN en trámite

Geofísica Internacional

Revista Trimestral Publicada por el Instituto de Geofísica de la
Universidad Nacional Autónoma de México

México
Volume 53 Number 4
October - December
2014

— Geofísica Internacional —

Dr. Arturo Iglesias Mendoza
Director of Instituto de Geofísica

Dra. Tereza Cavazos
President of Unión Geofísica Mexicana

Editor Chief
Dr. Servando De la Cruz-Reyna
Instituto de Geofísica, UNAM
sdelacrr@geofisica.unam.mx

Technical Editor
Mtra. Andrea Rostan Robledo
Instituto de Geofísica, UNAM
arostan@igeofisica.unam.mx

Editorial Board
Donald Bruce Dingwell
Earth and Environment
Ludwig Maximilian University of Munich, Germany

Eric Desmond Barton
Departamento de Oceanografía
Instituto de Investigaciones Marinas, Spain

Jorge Clavero
Amawta Consultores, Chile

Gerhardt Jentzsch
Institut für Geowissenschaften
Friedrich-Schiller-Universität Jena, Germany

Peter Malischewsky
Institut für Geowissenschaften
Friedrich-Schiller-Universität Jena, Germany

François Michaud
Géosciences Azur
Université Pierre et Marie Curie, France

Olga Borisovna Popovicheva
Scobeltzine Institute of Nuclear Physics
Moscow State University, Rusia

Jaime Pous
Facultad de Geología
Universidad de Barcelona, Spain

Joaquín Rui
UA Science
University of Arizona, United States

Angelos Vourlidas
Solar Physics Branch
NASA Goddard Space Flight Center, United States

Théophile Ndougsa Mbarga
Department of Physics
University of Yaounde I, Cameroon

Associate Editors
José Agustín García Reynoso
Atmospheric Science Centro de Ciencias de la Atmósfera UNAM, Mexico

Tereza Cavazos
Atmospheric Science
Departamento de Oceanografía Física CICESE, Mexico

Dante Jaime Morán-Zenteno
Geochemistry
Instituto de Geología, UNAM, Mexico

Margarita López
Geochemistry
Instituto de Geología UNAM, Mexico

Avto Gogichaisvilii
Geomagnetism And Paleomagnetism
Instituto de Geofísica UNAM, Mexico

Jaime Urrutia-Fucugauchi
Geomagnetism And Paleomagnetism
Instituto de Geofísica, UNAM, Mexico

Felipe I. Arreguín Cortés
Hydrology
Instituto Mexicano de Tecnología del Agua IMTA, Mexico

William Lee Bandy
Marine Geology And Geophysics
Instituto de Geofísica UNAM, Mexico

Fabian García-Nocetti
Mathematical And Computational Modeling
Instituto de Investigaciones en Matemáticas Aplicadas y en Sistemas UNAM, Mexico

Graciela Herrera-Zamarrón
Mathematical Modeling
Instituto de Geofísica, UNAM, Mexico

Ismael Herrera Revilla
Mathematical And Computational Modeling
Instituto de Geofísica UNAM, Mexico

Rene Chávez Segura
Near-Surface Geophysics
Instituto de Geofísica UNAM, Mexico

Juan García-Abdeslem
Near-Surface Geophysics
División de Ciencias de la Tierra CICESE, Mexico

Alec Torres-Freyermuth
Oceanography
Instituto de Ingeniería, UNAM, Mexico

Jorge Zavala Hidalgo
Oceanography
Centro de Ciencias de la Atmósfera UNAM, Mexico

Shri Krishna Singh
Seismology
Instituto de Geofísica, UNAM, Mexico

Xyoli Pérez-Campos
Seismology
Servicio Sismológico Nacional, UNAM, Mexico

Blanca Mendoza Ortega
Space Physics
Centro de Ciencias de la Atmósfera, UNAM, Mexico

Inez Staciarini Batista
Space Physics
Pesquisador Senior Instituto Nacional de Pesquisas Espaciais, Brazil

Roberto Carniel
Volcanology
Laboratorio di misure e trattamento dei segnali DPIA - Università di Udine, Italy

Miguel Moctezuma-Flores
Satellite Geophysics
Facultad de Ingeniería, UNAM, Mexico

Assistance
Elizabeth Morales Hernández,
Management
eliedit@igeofisica.unam.mx

GEOFÍSICA INTERNACIONAL, Año 53, Vol. 53, Núm. 4, octubre - diciembre de 2014 es una publicación trimestral, editada por la Universidad Nacional Autónoma de México, Ciudad Universitaria, Alcaldía Coyoacán, C.P. 04150, Ciudad de México, a través del Instituto de Geofísica, Circuito de la Investigación Científica s/n, Ciudad Universitaria, Alcaldía Coyoacán, C.P. 04150, Ciudad de México, Tel. (55)56 22 41 15. URL: http://revistagi.geofisica.unam.mx, correo electrónico: revistagi@igeofisica.unam.mx. Editora responsable: Andrea Rostan Robledo. Certificado de Reserva de Derechos al uso Exclusivo del Título: 04-2022-081610251200-102, ISSN: en trámite, otorgados por el Instituto Nacional del Derecho de Autor (INDAUTOR). Responsable de la última actualización Saúl Armendáriz Sánchez, Editor Técnico. Fecha de la última modificación: 30 de septiembre 2014, Circuito de la Investigación Científica s/n, Ciudad Universitaria, Alcaldía Coyoacán, C.P. 04150, Ciudad de México.

Geofísica
Internacional

Vol. 53, Núm. 4, octubre-diciembre de 2014

Contents

Geofísica Internacional (2014) 53-4: 365-383

Original paper

A high-resolution palaeoclimate record for the last 4800 years from lake la Brava, SE pampas plains, Argentina

María A. Irurzun*, Claudia S. G. Gogorza, Ana M. Sinito, Marcos A. E. Chaparro, Aldo R. Prieto, Cecilia Laprida, Juan M. Lirio, Ana M. Navas and Héctor Nuñez

Received: June 25, 2012; accepted: November 26, 2013; published on line: October 01, 2014

Resumen

Los cambios climáticos son reflejados en las variaciones de diferentes parámetros. Las secuencias sedimentarias de lagos son buena fuente de esta información debido a que proveen grabaciones continuas y detalladas de cambios paleoclimáticos.

Para determinar los cambios en el clima al SE de la llanura Pampeana, se presentan estudios de magnetismo de rocas realizados en un testigo colectado del fondo de la Laguna La Brava (Argentina). También se midieron contenidos totales de sulfuro, carbón orgánico e inorgánico (TS, TOC y TIC), elementos alcalinos, metales pesados y livianos, y cambios en las comunidades de vegetación. Se realizaron cinco determinaciones de edades radiocarbónicas y se calcularon las edades calibradas. La tasa promedio de acumulación de sedimento es 1.3 mm/año y la secuencia representa los últimos 4800 años en edades calibradas (cal. BP).

El objetivo principal fue reconstruir el balance hidrológico de la laguna, cambios erosionales y de contribución de sedimento dentro del área de aporte, y explorar la medida en que pueden estar relacionados con cambios climáticos y/o actividades humanas. Los resultados de este trabajo y estudios previos sugieren cambios periódicos de condiciones frías a cálidas y húmedas. La relación entre plantas sumergidas y emergentes es consistente con el comportamiento de susceptibilidad magnética κ. Los cambios en TOC sugieren un ambiente húmedo durante períodos de mejoramiento magnético. Se identificaron eventos de desbordes y bajos niveles de la laguna. Para los últimos 50 cal. BP, cambios en la contribución de sedimento y procesos deposicionales fueron causados por impacto humano, en particular por el uso de recursos naturales.

Palabras clave: cambios paleoclimáticos, magnetismo de roca, testigos sedimentarios, América de Sur, nivel de la laguna, eventos secos.

M. A. Irurzun*
C. S. G. Gogorza
A. M. Sinito
M. A. E. Chaparro
Instituto de Física Arroyo Seco
Universidad Nacional del Centro de la Provincia de Buenos Aires
Pinto 399, 7000 Tandil, Argentina
**Corresponding author: airurzun@exa.unicen.edu.ar*

M. A. Irurzun
C. S. G. Gogorza
A. M. Sinito
M. A. E. Chaparro
A. R. Prieto
C. Laprida
Consejo Nacional de Investigaciones Científicas y Técnicas
Rivadavia 1917, C1033AAJ
Buenos Aires, Argentina.

A. M. Navas
Estación Experimental de Aula Dei
CSIC. Av. Montañana 1.005. 50059
Zaragoza, España

Aldo R. Prieto
Instituto de Investigaciones Marinas y Costeras
Laboratorio de Paleoecología y Palinología
Universidad Nacional de Mar del Plata
Funes 3250, B7600GYI Mar del Plata, Argentina

Juan M. Lirio
Héctor Nuñez
Instituto Antártico Argentino (IAA)
Cerrito 1248, Buenos Aires, Argentina

Cecilia Laprida
Departamento de Ciencias Geológicas
Facultad de Ciencias Exactas y Naturales
Universidad de Buenos Aires, CABA

Abstract

Climatic changes are reflected in variations of different parameters. Sequences of lake sediments are good sources of this information because they provide continuous and detailed records of palaeoclimatic changes. In order to determine the changes in climate in SE Pampas plain,in this paper we present a series of rock magnetic studies performed on a bottom core collected from Lake La Brava (Argentina).

In order to establish lake level variations, we also measure total sulphur, organic and inorganic carbon (TS, TOC and TIC) content,alkaline elements, light and heavy metals and changes in vegetation communities. Five radiocarbon age determinations were made from samples of organic-rich clay and calibrated ages were calculated. The averaged sediment accumulation rate is 1.3 mm/yr and the sequence represents a temporal extent of about 4800 calibrated years before the present (cal. BP).

The main aim was to reconstruct the hydrological balance of the lake, the changes in erosional strength and sediment supply within the catchment area since the Middle Holocene, and to explore the extent to which these may be linked to changes in climate and/or human activities. The results of this work and previous studies suggest periodic changes from cooler to warmer and humid conditions. Relationships between submerged and emergent plants are consistent with the behaviour of magnetic susceptibility. TOC changes suggest wet environment during magnetic enhancement. Floods and lower lake level events were identified in detail. Changes in sediment contribution and depositional processes for the last 50 cal. BP are caused by human impact, particularly by the use of natural resources.

Keywords: palaeoclimatic changes, rock magnetism, sediment cores, South America, lake level, dry events.

Introduction

Lakes are very useful deposits of material that came from different sources, sometimes arriving from great distances via the atmosphere. More immediate and important sources are the catchment area and materials produced within the lake itself. Lake sediments are very sensitive archives of changes in rainfall, wind, trophic state, anthropogenic use of the catchment area, etc. Numerous studies have been published using magnetic parameters to investigate lake sediments (e.g.Sandgren and Risberg, 1990; Forester *et al*., 1994; Dearing *et al*., 2001; Abbott *et al.*, 2003; Chaparro *et al.*, 2008; Irurzun *et al*., 2009, Gogorza *et al.*, 2004; 2006; 2012). Magnetic properties of sediments may act as sensitive recorders of palaeoclimatic changes, but they need to be interpreted in terms of climate by establishing models and correlations based on multi-proxy analyses that include both magnetic and non-magnetic techniques (Maher and Thompson, 1999; Geiss *et al.*, 2003).

The reconstruction of Holocene environmental variability across the subtropical Pampean plains of South America has been limited by the paucity of complete and well-dated palaeoclimatic archives (Piovano *et al.*, 2009). Results suggest that climate archives show a complex pattern of timing and climate interactions throughout the Holocene. The precise chronology and magnitude of some of these climatic shifts is still a matter of debate. According to Tonni *et al.* (1999) the climate was mostly arid until 1500 cal. BP and wet until the present. On the other hand, according to Piovano *et al.* (2009) and Zárate *et al.* (2000) the climate was dry; especially at around 4200 cal. BP. Mancini *et al*. (2005) suggest that from ~ 5000 cal. BP the climate became drier with episodic flooding events as a consequence of humid Atlantic air masses that spread into the continent (Schäbitz and Liebricht, 1998). Prieto *et al.* (2004) suggest a subhumid-dry climate from mid to late Holocene in the NE Pampas and that the aeolian input increased (Prieto, 1996). The data are also consistent with trends of precipitation decrease quantitatively estimated for the late Holocene southwestern Pampa region (Tonello and Prieto, 2010) and drying suggested by episodes of aeolian reactivation across the Pampa region during the mid- and late Holocene (Zárate and Tripaldi, 2012).In the last two millennia climate has been rather unstable, with wetter phases interrupted by dry phases, such as the Little Ice Age (Cioccale, 1999; Piovano *et al*., 2002; Laprida *et al*., 2009a;Stutz *et al*., 2012).

The Pampas Plain is one of the most important zones for agricultural production in Argentina and one of the most likely to be affected by climate changes (Laprida *et al.*, 2009a). To know the natural trends and the anthropogenic effect on the system is extremely necessary. The study of magnetic parameters in shallow lake sediments in the Pampean plain is extremely scarce. Most of the works have been carried out on soils and paleosols (Nabel *et al*., 1999; Orgeira *et al*., 2003; 2004; 2009; Bidegain *et al*., 2009; Zárate *et al.*, 2009) or short shallow lake sediment cores for the last 500 years (Lirio *et al.*, 2007; Laprida *et al.*, 2009a-b; 2011; Stutz *et al.*, 2002; 2012).

It is evident the need to obtain longer sequences to better understand long-term variations in environmental changes.In this work we are going to focus on palaeoenvironmental changes to achieve lake level variations for the last 4800 yrs using rock magnetic studies. Additionally, grain size, palynological, geochemical and preliminary micropalaeontological analyses were conducted.

Study site description

Lake La Brava (37º52’S 57º59’W) is one of the few permanent freshwater shallow lakes. The lake is located in the northern area of the Tandilia range, a low-altitude mountain system of the Pampas plains (Figure 1). Lake La Brava is an elongated shallow lake (surface area: 4.5 km^2, *ca*. 4.8 m maximum depth; 69 m a.s.l.).The modern regional vegetation is grasslands with a shrubby edaphic-dominant community in the low-altitude ranges. The present-day local climate is humid-temperate, with a mean annual precipitation of 800 mm; the area has a mean annual temperature of 13.3ºC (INTA, 2008). S and SE winds predominate with an average speed of 20 km/h,reaching gusts of 40 – 50 km/h (Balcarce Municipality; www.balcarce.gob.ar).

The origin of the lake, like most lakes of the region, is a wind deflation basin (Dangvas, 2005) formed during the times when the creek El Peligro was dry or had a temporary regime. The basin was formed as consequence of deposition of deflationed sediment at the northern edges which formed the paleodunes closing the original depression. The basin of the lake has the higher slope to the west, near La Brava Hill, and an elongated depocentre (Figure 1) with two sub-basins with maximum depths of 4.8 and 3.5 m (Lirio *et al*., 2007). The mean depth is 3.4 m and Secchi disk transparency of 1.4 m (Quirós, 1988), these conditions are insufficient for a stable thermal profile, sufficiently deep to avoid light penetration to the bottom sediments and adequate to support photosynthesis of higher aquatic plants (Quirós, 2004).

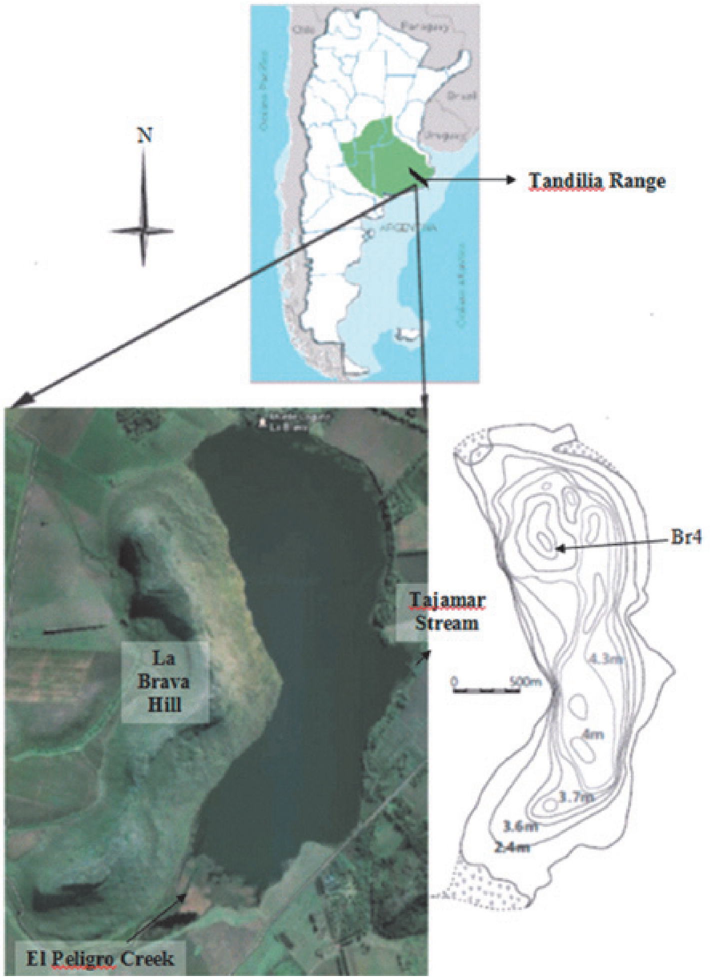

Figure 1 Geographical location of Lake La Brava and coring site.

Lake La Brava is in an advanced state of eutrophication with nitrogen/phosphorus ratios of 0.42 (Quirós *et al.*, 2002) and is classified as bicarbonate-sodium oligohaline (INIDEP, 2001). This shallow lake has shown changes in the average water level during the last three decades, mainly through groundwater which is controlled by the variability of the precipitation (Kruse, 1987). For instance, between 2006 and 2008 the mean annual precipitation (MAP) oscillated between 685 and 785 mm/yr; during 2009 the MAP dropped to 606 mm/yr and in 2010 the MAP rose again up to 833 mm/yr (http://www.siia.gov.ar/). The lake level, from a mark made in the dock (Sup. Data 1) dropped 50 cm from 2006 to 2009 and rose 40 cm from 2009 to 2010 (Sanzano, P. personal communication).

Sporadically it overflows into the Tajamar stream (Kruse, 1987), and has a tributary creek, El Peligro, which develops a delta where abundant vegetation grows (Lirio et al., 2007). The lake plant community is characterised by aquatic plants (emergent, submerged and floating). In the deepest zones with medium to high lighting Myriophyllum elatinoides,Ludwigiarepens and Ceratophyllum demersum develop. At the lake margins and in sheltered habitats Azolla fliculoides,Potamogeton pectinatus, Ricciocarpus natans and Lemnasp. are present (Cordini, 1942; Romanelli, 2006). The dominant shore species is Schoenoplectus californicus (bulrush), accompanied by Typha latifolia (cattail) to the southward margin. The bulrush occupies an almost continuous belt along 63% of the lake shore. The belt width is variable between years and in different sectors, varying between 9 and 30 m in 2006 (Romanelli, 2006) and between 20 and 130 m in1942 (Cordini, 1942). This fringe is more extended at the end of the summer and occupies ca. 20% of the surface.

Materials and methods

Field work and sampling

A long core (Br4, Figure 1 and Table I) was collected with a push corer installed on a raft with a central hole in water depths of about 3.4 m. The core sections were 2 m long with a diameter of 6 cm, and were collected in PVC tubes. Once the core was brought to the surface, they were cut into 1 m segments and split into halves by means of a nylon thread. The core was described, and subsampled with cubic plastic boxes of 8 cm^3 at intervals of 2.5 to 3 cm, and weighed in an electronic balance, Acculab GS-200 (precision of 0.1 g). A total of 204 subsamples were collected.

Methods

The following studies were carried out:

* For all the samples: volumetric magnetic susceptibility κ using a Bartington MS2 Susceptibility meter. Isothermal remanent magnetisation (IRM) in 24 increasing steps: 5, 10, 15, 20, 25, 30, 35, 40, 45, 50, 60, 70, 80, 90, 100, 150, 200, 300, 400, 500, 600, 800 mT, 1 and 1.2 T, reaching saturation (SIRM); back-field, in growing steps until cancelling the magnetic remanence were measured. Associated parameters were calculated: S-ratio (IRM_{-300mT}/SIRM) and coercivity of the remanence (B_{CR}). Anhysteretic remanent magnetisation (ARM), with a direct field of 0.05 mT and a peak alternating field of 100 mT were determined. The inter-parametric ratios: ARM/SIRM and SIRM/k were calculated. Remanent magnetisations were measured using a Minispin spinner fluxgate magnetometer Molspin Ltd.; a pulse magnetiser IM-10-30 AC Scientific was used for IRM experiments and an alternating field demagnetiser Molspin Ltd. with an ARM device was used for ARM acquisition.,TS, TOCand TIC were measured by using a Leco elemental analyser.Analysis of the clay, silt and sand fractions were performed using Beckman Coulter LS 13 320 laser diffraction particle size analyzer. Prior to the analysis the organic matter was eliminated with H_2O_2 (10%) heated to 80 ºC and samples were disaggregated with sodium hexametaphosphate (40%), stirred for 2 hours and dispersed with ultrasound for a few minutes.

* For a group of selected samples: A set of 62 samples was selected to perform thermal demagnetisation of SIRM to obtain Curie temperatures (T_C) of the different magnetic minerals present in the sediments. The selected samples correspond to highs or lows in the curves of concentration, mineralogy or magnetic grain size parameters. The samples were dried out in pyrex holders and consolidated with sodium silicate before the heating process in a Thermal SpecimenDemagnetiser, model TD-48 ASC Scientific. A good description of all magnetic measurements is shown in Chaparro, 2006 and Turner, 1997. The analysis of the total elemental composition was carried out after total acid digestion with HF (48%) in a microwave oven. A set of 42 samples was analysed for 17 elements: Li, K, Na (alkaline), Mg, Ca, Sr, Ba (light metals) and Cr, Cu, Mn, Fe, Al, Zn, Ni, Co, Cd and Pb (heavy metals). Analyses were performed by optic emission spectrometry using inductively coupled plasma (solid state detector). Concentrations were obtained after three measurements per element. Macroscopic sedimentological description was performed with

Table 1. General information from core sampling and information derived from dating processes and age model from core Br4. The calibration ages were obtained with Oxcal 4.1 (Bronk Ramsey, 2008). * This age correspond to historical documents, see text for details.

Length [cm]	Nº of samples obtained	Laboratory number	Depth from the top	Age ^{14}C ± s [yrs]	d^{13}C	Calibrated years BP. ± s [yrs]
551	204	Br4/10	27.5 cm	--	--	50 ± 20*
		LTL595A – BRAVA20	54 cm	684 ± 40	-24.2 ± 0.2	597 ± 30
		AA81420 – LB 4-67	184 cm	1899 ± 37	-24.2	1753 ± 49
		LTL594A – BRAVA114	305.5 cm	2579 ± 50	-28.8 ± 0.2	2690 ± 53
		AA81422 –LB 4-154	407.5 cm	3589 ± 40	-24.4	3757 ± 54
		LTL596A – BRAVA200	539 cm	4124 ± 65	-30.4 ± 0.4	4693 ± 103

a binocular magnifying glass.For pollen analyses, 66 subsamples were prepared with standard techniques (Faegri and Iversen, 1989). Pollen samples were mounted in jelly and counted using a Nikon H550S microscope at 1000x and 400x magnification. Pollen assemblages from lakeshore plants, aquatic macrophytes and introduced European taxa were selected from the total pollen. The two first were clustered on the assumption that distinctive zones of aquatic vegetation are associated with particular waterdepths. They were arranged from shore to inner of the lake as emergent (Cyperaceae, *Typha*, *Eryngium* and *Ranunculus*), submerged (*Myriophyllum* and *Ceratophyllum* leaf spines) and floating (*Azollafiliculoides*, Lemnaceae, Iridaceae and *Elodea*-type). Introduced pollen included exotic trees (*Eucalyptus* and *Pinus*) and ruderal weeds (Brassicaceae, *Erodium*, *Carduus*-type and *Rumex*). Pollen percentages were calculated on the sum of all pollen.

Results

Sedimentology

The grain size results of core Br4 are shown in figure 2. The presence of a few tephra levels situated between 83 and 86 cm indicate volcanic ash falls from the Andean volcanoes situated 700 km westward to the Lake La Brava. Plant remains such as leaves and blades and charcoal lenses were also found (Lirio *et al.*, 2007).

The grain-size composition is clearly dominated by silt, but subtle changes in clay and silt proportions allow the recognition of four intervals. The basal interval (548 – 370.5 cm) is composed by clayed silt, with sporadic minor proportion of sand (< 10%). From 370.5 and 186 cm, clayed silt, and sporadic sandy silt levels has been observed. The third interval (171 -43 cm) is composed mainly by sandy silt with sporadic clayed silt, indicating an increase in the mean of grain size. The topmost 43 cm of the core is composed by clayed silt and subordinated silty clay. Geochemical parameters do not show drastic changes or discontinuities between intervals. Subtle changes in lithology cannot be interpreted only as changes in the source area or in the input, because the lake basin is rather small and its morphology is relatively simple, covered by Late Pleistocene loess deposits reworked during the Late Holocene by eolian activity (Muhs and Zarate, 2001). Additionally, lake level is nowadays highly dependent on in situ rainfall and hydrological balance, and thus subtle changes in lithology can be mainly interpreted as changes in the lake level. High lake level is indicated by low mean grain size, whereas higher content of sand indicates fluvial facies migration to the lake center during predominantly relative dry phases.

Chronology

Five bulk sediment samples were dated by the ^{14}C-AMS dating technique (see Table I for details) and calibrated with SHCal04 (MacCormac *et al*., 2004). An age-depth model (Figure 2) was calculated with the Oxcal 4.1 calibration software (Bronk Ramsey, 2001; 2008). From pollen analysis the introduced taxa (Figure 3k) appear on the top ten samples. It is historically documented (BalcarceMunicipality, http://www.balcarce.gov.ar) that the onset of this impact began at the end of the nineteenth century with the arrival of the first colonists. For this reason the age assigned to sample 10 is 50 cal. BP.

The basal age of this core is *ca*. 4800 cal. BP.An average sedimentation rate of 1.3 mm/yr for core Br4 was obtained, with variations between 0.4 to 3.6 mm/yr.

Rock magnetic analysis

The magnetic concentration parameters, κ (Figure 3a), ARM (Figure 3b) and SIRM (Figure 3c) show similar features, suggesting they are mainly controlled by the concentration of the magnetic minerals (Irurzun *et al*., 2009). Logs of κ, SIRM and ARM show an oscillatory behaviour around their mean values and have three maxima at 4100, 1000 cal. BP and in the first 50cal. BP. There is another local maximum between 2600 and 2100 cal. BP in the κ curve, less suggested in ARM and SIRM.

To investigate the magnetic mineralogy, parameters derived from IRM curves were analysed to identify soft/hard magnetic minerals. Stepwise acquisition of the isothermal remanence (Figure 4a) shows that 90% of the SIRM is acquired with applied fields of about 250mT. After progressive removal of SIRM by back-field demagnetisation, B_{CR} mean values of 66±12mT were obtained. Values higher than 80mT (Figure 3g) suggest the presence of oxidised (titano) magnetite (Kruiver *et al.,* 2001; Roberts and Turner, 1993; Reynolds *et al.,* 1994) and/or antiferromagnetic minerals in low concentrations. A group of samples acquired 84% of the SIRM at 300 mT (Figure 4a), also indicating the presence of a small proportion of antiferromagnetic minerals.

S-ratio (Figure 3f) exhibits an oscillatory behaviour around 0.82 from the bottom of the core to 100 cal. BP, then abruptly changes to 0.9 and remains almost constant until the present. Soft minerals like magnetite have low B_{CR} and high S-ratio. Minima/maxima of B_{CR} correspond to maxima/minima of S-ratio, indicating that both parameters recorded the same trend

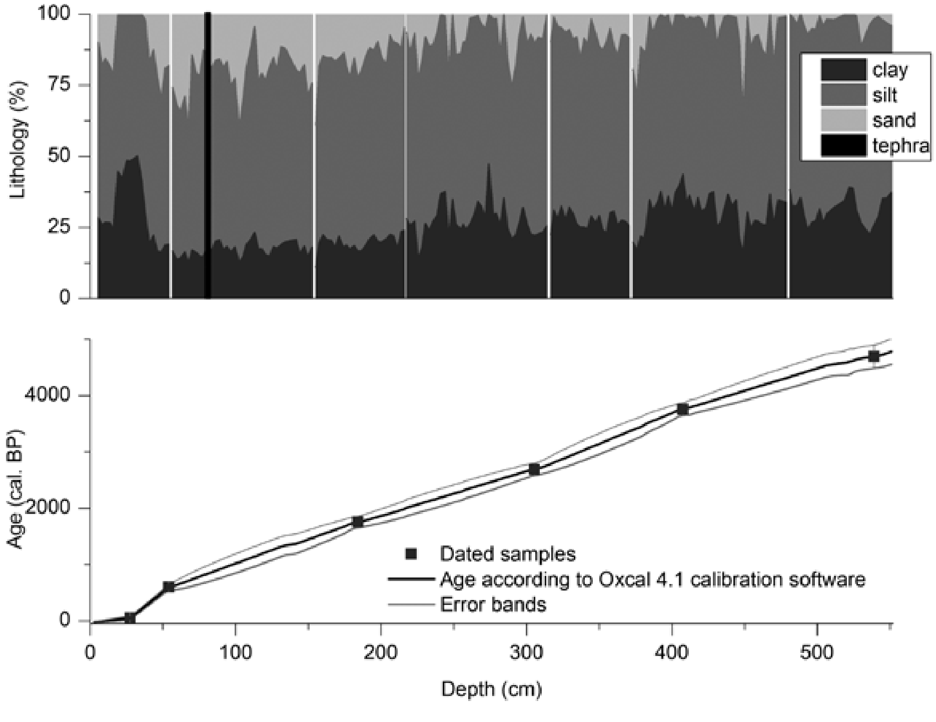

Figure 2. Logs of lithology, dated samples (cal. BP ±σ, see Table I for details) and calibration curve according to Oxcal 4.1 (Bronk Ramsey C.; 2008) *vs*. depth. Gaps in the upper figure only indicate core breaks.

in magnetic mineralogy. But the variations are more noticeable in B_{CR}, suggesting that differences in mineralogy are better captured by coercivity. B_{CR} shows its maxima at 4000, 2700 and 750 cal. BP. SIRM/k vs. B_{CR} (Peters and Dekkers, 2003) is plotted to discriminate magnetic mineralogy. Most samples have values in a region with characteristic magnetite and (titano) magnetite as dominant magnetic carrier. Around 15% of the samples are out from that region which could be explained by the presence of a low content of hematite and/or greigite.

Assuming a magnetic mineralogy with predominance of soft minerals like magnetite is possible to use the figure (Figure 4c) of Thompson and Oldfield(1986) to estimate percentages per unit volume of magnetite in

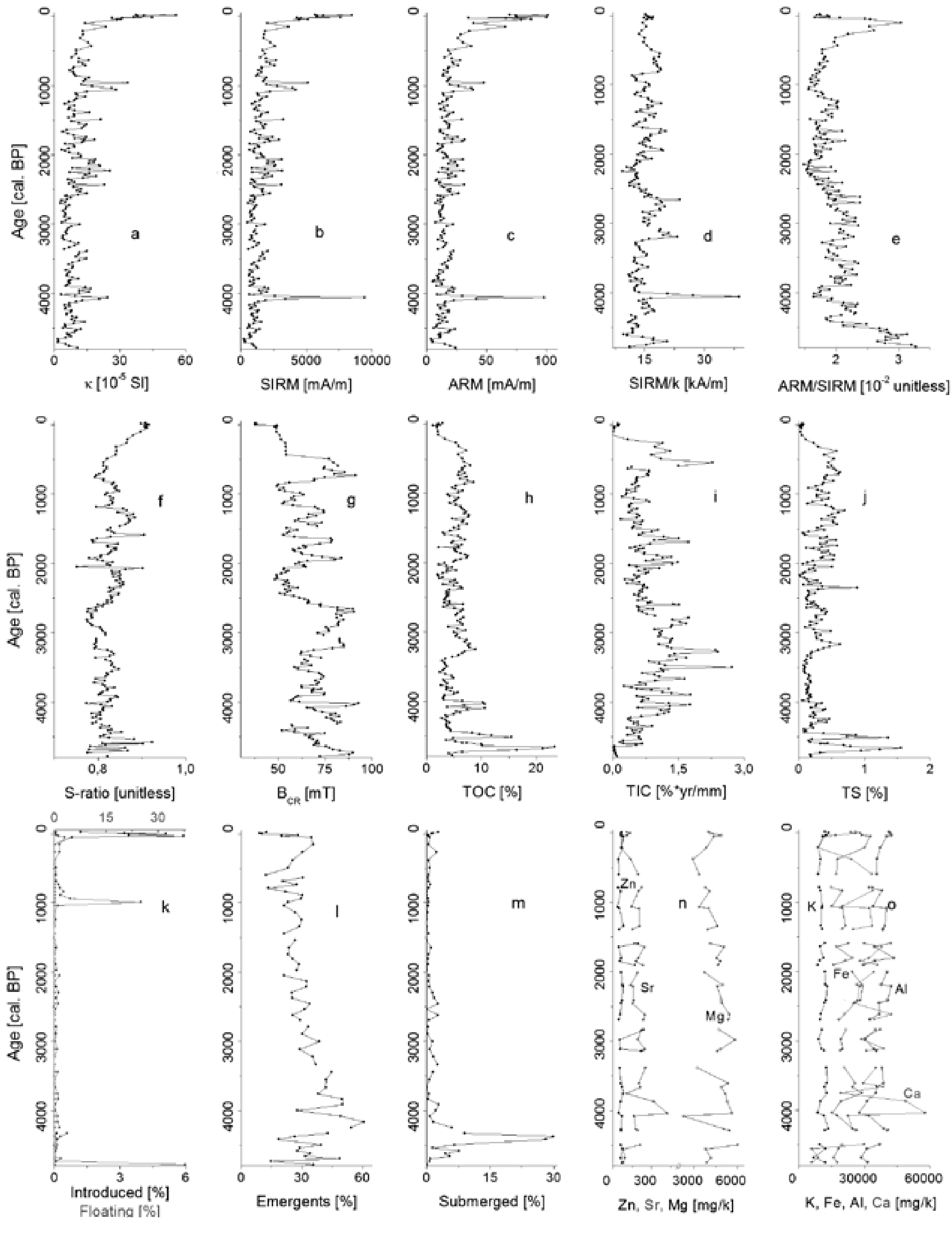

Figure 3. Logs of (a)κ, (b)SIRM, (c)ARM, (d) SIRM/k, (e)ARM/SIRM, (f) S-ratio, (g) BCR, (h)TOC, (i) TIC, (j) TS, (k) floating and introduced plants, (l) emergent plants,(m) submerged plants, (n) Zn, Sr and Mg, and (o) K, Fe, Al, Ca vs. age, in calibrated years before present.

the samples and to distinguish between grain sizes. The percentage of magnetite varies between0.003 and 0.02% and the magnetic grain size observed is between 2 and 8μm.The results obtained suggest that magnetic grain sizes are in the range of pseudo single-domain (PSD) magnetite (Thompson and Oldfield, 1986) which is probably due to a mixture of different magnetic grain sizes.Only two samples are finer than 2μm and correspond to the B_{CR} extreme values (Figure 3g) and one of them is in the region of greigite (Figure 4b).

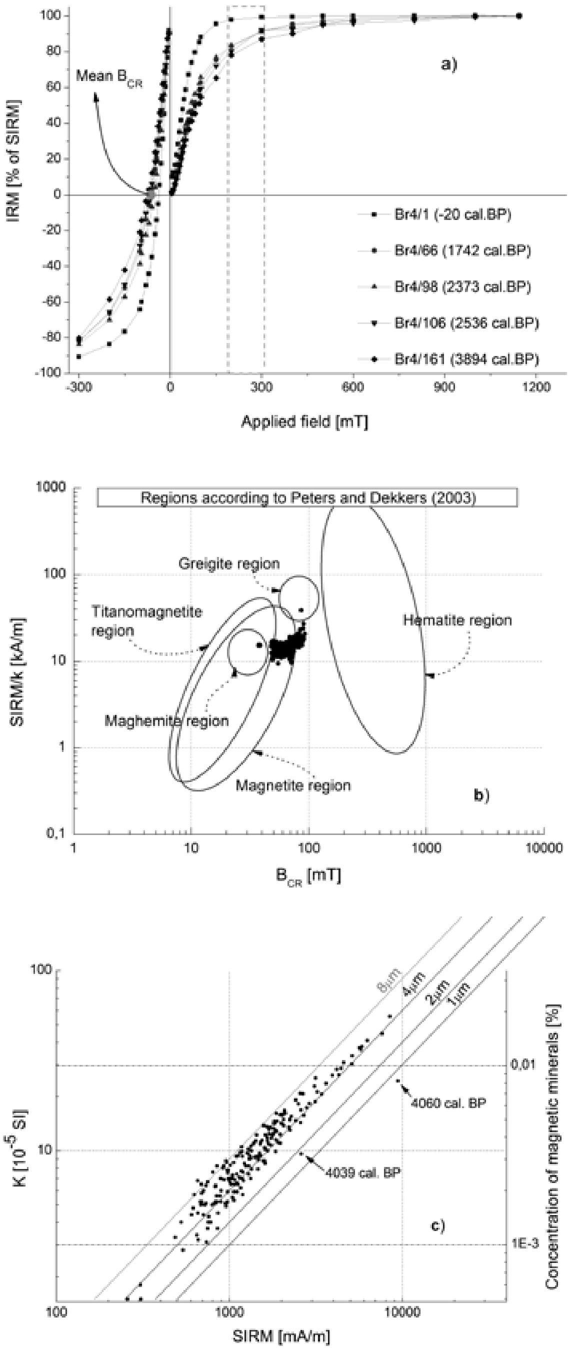

Inter-parametric ratios (SIRM/k andARM/SIRM, Figure 3d and 3e) generally increase with decreasing grain size and a higher proportion of single domain (SD) grains are present (Hunt *et al*., 1995; Turner, 1997). ARM is sensitive to fine ferromagnetic grains (0.02 – 0.1 mm) and the ratioARM/SIRM is independent of paramagnetic and diamagnetic grains because only remanences are involved (Turner, 1997). On the other hand, k also involves paramagnetic and diamagnetic grains and the ratio SIRM/k is also used to point out the presence of greigite (Roberts *et al*., 2011). The ratios show oscillating values around their mean values, 2 x 10^{-2} for ARM/SIRM and 15 for SIRM/k. The general behaviour belongs to a mixture of different sizes in the period 5000 - 4300 cal. BP and finer grain sizes between 3200 -2400 cal. BP and 300 – 50 cal. BP.According to SIRM/k, the finest magnetic grain size is observed at 4700, 4060, 3200 and 2660 cal. BP. But at 4700 and 4060 cal. BP ARM/SIRM show low relative values suggesting an apparent increase in magnetic grain size. High B_{CR} and S-ratio values between 0.77 and 0.87 suggest the presence of hard coercivity magnetic minerals for those samples. These results are in agreement with the results of Figure 4b for greigite. At 3200 and 2600 cal. BP ARM/SIRM shows also high values indicating fine magnetic grain sizes.

Figure 5 shows the result of thermal demagnetisation curves of SIRM and the obtained T_C. Sample 20 (Figure 5a) shows the behaviour of 85% of the samples. With two magnetic phases: a first magnetic phase with a characteristic temperature between 369 and 453 ºC. These temperatures correspond to the presence of (titano) magnetite with a low proportion of Ti (Dankers, 1978; Gogorza *et al*., 2004) or magnetite partially oxidised during the heating process (Dankers, 1978). The second phase is the principal magnetic phase, where more than 85% of remanence is lost at a mean value of T_C3 = 572 ºC (Figure 5d), indicating that magnetite is the principal magnetic carrier (Dankers, 1978; Hunt *et al*., 1995; Dunlop and *Özdemir*, 1997; Irurzun *et al*., 2009). Another two phases are found. According to a review

Figure 4. a) IRM acquisition curves of selected samples from the studied core. The grey dot is indicating the mean value obtained for B_{CR}. b) SIRM/k vs. B_{CR}. The regions on ellipses are the main sectors found by Peters & Dekkers (2003), most of the samples are located in the region for magnetite as main carrier. c) *k* vs. SIRM for all samples in order to estimate concentration and magnetic grain size according toThompson & Oldfield (1986).

made by Roberts *et al*. (2011), the Curie temperature of greigite is not exactly found but greater than 350°*C, but t*he shape of the heating curves shows an abrupt decrease between 290 and 320 °C. T_C1 between 266 and 342 °C (Figure 5c) could correspond to greigite samples (Krs *et al*., 1992; Dekkers *et al*., 2000; Sagnotti *et al*., 2005). T_C4 is found between 596 and 664ºC which correspond tosamples with the presence of antiferromagnetic minerals (Dankers, 1978). 10% of the samples have the same behaviour as the sample 186 (Figure 5b), were T_C2 and T_C4 are present. The samples from core Br4 hold a percentage of their magnetization after 580°C indicating the presence of a mix of magnetite with haematite materials (T_C =675ºC). This percentage oscillates between 0.2% for samples like 20 (Figure 5a) and 6.8% for samples like 186 (Figure 5b). Figure 5d shows the Curie temperatures as a function of the ages. Several peaks were found in the intervals 4690 - 4060 cal. BP and 2840 – 2070 cal. BP. Greigite is suggested at 4700 and 4060 cal. BP, consistent with high SIRM/k, high TOC and high TS (Figure 3). The high values of percentages of hematite were found at 4380, 2820 and 1290 cal. BP.

Geochemical analysis

The TOC record (Figure 3h) exhibits several fluctuations ranging between 1.2% and 23% and high values were determined between 4750 and 4450 cal. BP. TOC and TS (Figure 3j) show a significant positive correlation (R=0.84) and minima values between 4000 and 3500 cal. BP, 2600 and 2200 cal. BP and from 200 cal. BP, suggesting an organic origin for sulphur. TIC values (Figure 3i) range from 0 to 2.1%.

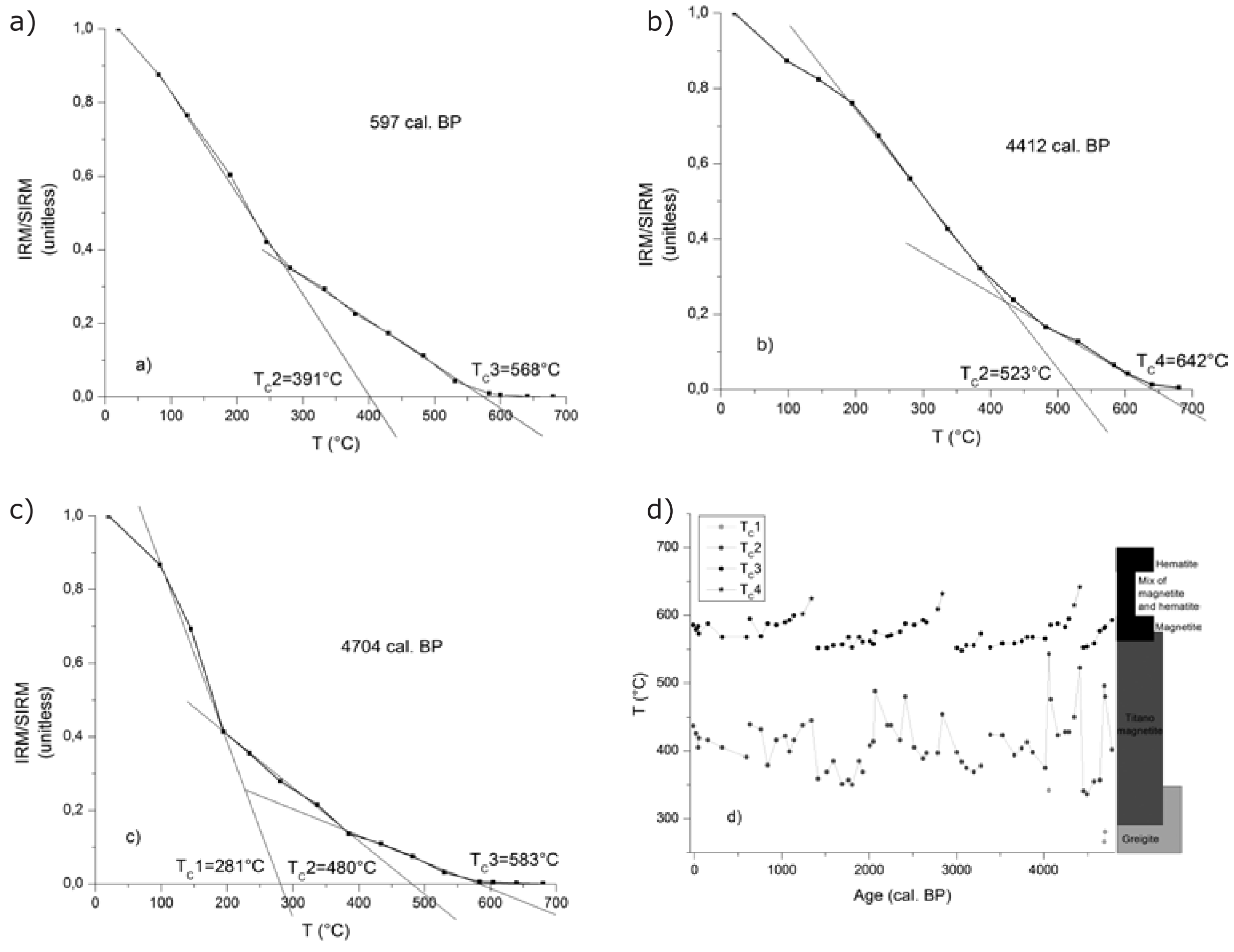

Figure 5. a) Thermal demagnetisation curves of SIRM:a) Sample 20 (54 cm, 597 cal. BP). b) Sample 186 (491 cm, 4412 cal. BP). c) Sample 201 (542 cm, 4704 cal. BP). d) Curie temperatures vs. age. T_C1 correspond to typical greigite temperatures, T_C2 to typical titano-magnetite temperatures, T_C3 to magnetite temperatures and T_C4 to hematite temperatures. The zone between magnetite and hematite was denominated as mix of magnetite and hematite region.

Values lower than 1% are found between 4800 and 4200 cal. BP, 2500 and 2100 cal. BP and from 1500 cal. BP, whereas maxima values were found at 4100,3800 cal. BP, 3500 cal. BP, 3250 cal. BP and around 2700 cal. BP.

Soft magnetic minerals are significant when TS has the lowest values. Around 4680 and 4510 cal. BP the maxima values of TS are found, but not so significant changes are found in κ. At 4020 cal. BP, κ has minima values consistent with TOC and TIC maxima values whereas TS is almost constant, indicating a low presence of any magnetic mineral. TOC logs display a general inverse behaviour to κ and S-ratio. TIC has an inverse relationship with κ in the period 400-4200 cal. BP, but both parameters have an increasing trend from 4800 to 4200 cal. BP and for the last 450 cal. BP.

The more significant results from elemental analyses are shown in Figure 3n and 3o. These elements show an oscillatory behaviour around their mean values,except Zn and Ca. Fe, Al and κ show similar behaviour between each other. There are increases in heavy metals and K at 4200, 3600, 2200 and around 200 cal. BP, which suggest a greater proportion of clay minerals at these ages (Abdul Aziz and Langereis, 2004), confirmed by grain size results. Ca, Mg and Sr show several coincident minima synchronized with high values of κ. There is a coincidence among the peaks of light metals, but Sr has less evident variations. The maxima in Ca coincide with maxima in TIC, suggesting that most of the inorganic carbon is in the form of calcium carbonate minerals. Low values of light metals coincide with high values of alkaline metals, pointing to the presence of eroded minerals from less-weathered depths in the catchment (Higgitt *et al*., 1991).

Pollen analysis

Local vegetation pollen record (Figure 3k, 3l and 3m) is dominated by emergent plants mostly characterized by Cyperaceae (*Schoenoplectus*), showing a general decreasing trend with a superimposed oscillating behaviour, with maxima at 347 cal. BP, and a decrease to the present. Between 4780 and 4160 cal. BP, emergent plants show fluctuating values from 20 to 60%. Floating plants (mainly *Azollafiliculoides*) are present along the record with values less than 3.7%, reaching two maxima, at 4780 cal. BP (36%) and 990 cal. BP (24%). Submerged plants (mainly *Myriophyllum*) have an increasing tendency between 4780 and 4370 cal. BP, reaching the highest value (30%) at 4400 cal. BP. Then, they decrease abruptly and present slight variations along the record. The last 50 cal. BP shows the impact of humans on the vegetation of the Lake La Brava region; an increase of introduced European weeds (*Rumex*, *Erodium* and *Carduus*-type) represent the agriculture and grazing activities developed in the last decades of the 20th-century which have modified the landscape surroundings of the shallow lake. *Eucalyptus* and *Pinus* pollen are related to the establishment of exotic arboreal vegetation near the farmer settlements.

Discussion

Lakes are “containers” of material coming from the atmosphere and the catchment area. A complete and continuous sediment sequence is indicated by not disturbed levels and it is reinforce by both the age-depth model as well as the smoothed total pollen concentration curve (Prieto, A.R. unpublished data) which indicate not significant change in the rate of sediment accumulation. Only a relatively higher rate of sedimentation occurs during anthropogenic settlement, probably due to larger external input of inorganic material into the lake owing to agricultural erosion.

The most frequently used parameter for lithostratigraphic correlation and preliminary palaeoclimatic assessment as rainfall indicator is κ (Maher and Thompson, 1999). When κ is high, higher concentration of magnetic minerals is expected. In this sense, lower TOC can be found because of a greater percentage of clastic influx during discharge into the lake owing to extreme flood events. Silt is almost constant in the sediments, so the opposite variation of clay and sand can be used as indicators of changes in the lake level as well. When the lake level is high, small particle size is expected in the centre of the lake (Nichols, 2009). If the lake level is low, then the shore is nearer of our coring site and coarser particles can be found. Inter-parametric ratios are used to determine periods of entrance of coarser or finer magnetic particles. As in the case of clay and sand, if high inter-parametric ratios (fine magnetic grain size) are found, then the shore is far from the coring site, indicating a high lake level or a wet period (Vázquez, 2012) and *vice versa*.

Another possible interpretation can be considered. Finer particles are easily transported by wind, whereas coarser particles need a more energetic transport way, like water, to reach the lake (Bagnold *et al.,* 1979). If a high energetic environment could transport coarse particles, then low inter-parametric ratios should be found during rainfall periods. This is also argued by Lascu *et al.* (2012). For TOC interpretations, lower values of TOC can be found during periods of higher amount of minerogenic materials as a consequence of a dryer environment and a lower lake level than today.

The trends in pollen percentages of emergent macrophytes could reflect temporal movements of vegetation belts toward the shore and could be interpreted as a gradual relative rising of the level lake since 4800 cal. BP. The spread of macrophytes towards the centre of the lake may result from a lake-level lowering, or the natural progressive infilling of the lake (Hannon and Gaillard, 1997).

The environmental interpretation of TIC is not so straightforward. TIC and Ca, Mg and Sr show positive correlation, and suggest that the TIC concentration reflects basically calcite occurrence. Assuming that TIC mainly represents calcite and given the relative low amount of calcareous fossils, most of the carbonates originate either from allochthonous sources or, more likely, are formed authigenically by precipitation (Shapley *et al*., 2005). As allochthonous source, El Peligro Creek is located at the highest sector of the basin, where quartzitic strata and quartzitic debris mixed with fine clastic sediments occur (Romanelli *et al*., 2010b). Since there is no carbonate outcrops in the basin, allochthonous sources of carbonates via surface influent El Peligro Creek can be dismissed. In fact, based on isotopic and geochemical data, El Peligro Creek can be considered as a "channeled" component of the groundwater (Romanelli *et al.*, 2010b). The high contribution of spring water(Romanelli *et al.*, 2011) indicates a direct and indirect wetland recharge *via* surface and subsurface runoff from the ranges, preferentially through the quartzite fracture system, and therefore they cannot be considered as a significant allochthonous source for carbonate or calcite ions to the lake water. Hence, in our model of authigenically carbonate origin, TIC minima imply a restriction of calcite precipitation, and TIC maxima imply favourable conditions of carbonate precipitation in the lake. In either case, the fluctuations in TIC indicate that Lake La Brava experienced significant environmental changes. Controls of authigenic carbonate burial include the rate of groundwater recharge, vegetation type, phytoproductivity and evaporation rate, which are in turn all linked to climate (Shapley *et al*., 2009). Except for the last 50 cal. BP, no evident changes in regional vegetation have been detected; authigenic carbonate production may be supported by groundwater exchange (Shapley *et al*., 2005) or by evaporation acting on water body.

In La Brava Lake, the relation between the lake and the aquifer is well known. In this way, the effluent- influent behaviour of la Brava Lake has been defined (Kruse, 1987; Romanelli *et al.*, 2010b). Mixing water estimation to identify the proportions in which recharge sources contribute to the lake water shows that 50.77 % of it corresponds to groundwater (Romanelli *et al.,* 2011). In turn, groundwater recharge function of the lake is of significant importance since it provides water to the aquifer system and contributes to the maintenance of phreatic levels (Romanelli *et al.*, 2011). Isotopic and hydrochemical data indicate that the recharge to the aquifer is influenced by the natural rainfall input, wetland discharge and the concentration of surface run-off from the range fringes to inter-range depressions (Romanelli *et al.*, 2011). Recharge areas coincide with the hills, with a magnesium- or calcium-bicarbonate water type and relative low pH and electrical conductivity values, in coincidence with the area of groundwater calcite undersaturation (Quiroz Londoño *et al.,* 2008). Afterwards, as a consequence of evaporation and promoted by higher pH, water lake evolves to a sodium bicarbonate water type as a consequence of calcite precipitation which preferentially removes Ca^{+2} and Mg^{+2} in a softening process (magnesium and calcium exchange for sodium) (Romanelli *et al.,* 2010a). Due to the shallowness of Lake La Brava its hydrology is highly dependent on *in situ* rainfall (Quirós *et al.*, 2002). As aquifer system recharge depends solely on rainwater infiltration, when precipitation decreases, groundwater recharge diminishes, lake level drops and higher pH and evaporative concentration promoted calcite precipitation in the lake. In conclusion, assuming that major proportion of carbonates has authigenic origin, increase amount of flux of TIC (percentage of TIC divided by sedimentation rate) in the central lake basin sediments could reflect periods of low lake level and vice versa.

Relatively insoluble metals like Ca, Sr, Mg, Ba, among others; tend to accumulate in the sediment. In periods with dilute conditions (wetter and high lake level) these same metals remain in solution and do not precipitate (Davison, 1992). Dry periods may occur during high evaporation rates. Increasing concentration of TS in the water and consequent precipitation of the solid phase mean the water level must be low, corresponding with low rainfall (Hillesheim *et al*., 2005).

Lake level variations and palaeoclimatic implications

Three intervals which integrate general behaviours can be considered. The first is estimated between 4800 and 4500 cal. BP (and an event at 4060 cal. BP), the second between 4500 and 260 cal. BP and the third between 260 cal. BP and the present.

Finer magnetic grain size particles according to inter-parametric ratios are found from 4800 to 4500 cal. BP and at around 4060. Advances of marginal vegetation between ca. 4780 and 4160 cal. BP are indicated by high percentages of emergent plants. Values up to 90% of Cyperaceae characterized the modern pollen data set from communities that represent flooded depressions and shallow lakes shores of the Pampa grasslands (Tonello and Prieto, 2008). Between 4700 and 4200 cal. BP some low lake levels are indicated by the floating fern which floats at the water surface in sheltered habitats because it is vulnerable to the destructive effects of wave action. At 4780 cal. BP, low values of TOC, moderate high κ and an extremely high percentage of floating fern were found indicating a very low lake levels or a dry event (Figure 6) in accordance with previous studies of Mancini *et al.* (2005)

High percentages of clay and in consequence high lake levels are found at around 4650 cal. BP. SIRM, κ and ARM have shown similar features, indicating that the signal of the magnetic parameters is dominated by changes in the concentration of magnetic minerals. The concentration parameters show opposite to TOC variations of less amplitude. Considering the aforementioned results, TOC variations at 4650 cal. BP are variations related to a period of more rainfall and mild temperatures (Figure 6). Warm temperatures were found by Tonni *et al*. (1999).

In general terms, the similarities between κ, Fe, K and Al indicate very little or no diagenetic overprinting (Riedinger *et al.*, 2005). At 4060 cal. BP a change in mineralogy is suggested by differences between κ and Fe and Al (Figure 3a and 3o) indicating autochthonous elements are responsible for the magnetic signal. As a consequence, the formation of authigenic phases like greigite could be considered. Temperature experiments suggest greigite (Figure 5c and 5d) in samples with high SIRM/k values (Figure 3d and e). From 4800 to 4500 cal. BP another two samples with greigite were found around 4700 cal. BP. A high organic matter and a low oxygenated environment of the bottom lake sediments due to eutrophication during quiet sediment conditions could be the reason for an intense reductive dissolution of the original magnetic particles (Maher and Thompson, 1999, Geiss *et al.,* 2003). Greigite can grow when dissolved iron and sulphide are available during diagenesis (Roberts *et al*., 2011) consistent with high TOC (Figure 3h) and high TS (Figure 3j). ARM/SIRM shows a relative decrease, suggesting coarser magnetic grain size in the greigite samples. So dissolution of the original magnetite to form greigite is possible (Geiss *et al*., 2004). According to Ariztegui and Dobson (1996) greigite is a well-defined palaeoenvironmental proxy as it is formed during a wet period in eutrophic lakes consistent with low flux of TIC. Pampean shallow lakes are not thermally stratified (Sosnovsky *et al*., 2010). Because of their shallowness, these lakes are strongly influenced by wind and are therefore polymictic (Rennella and Quirós, 2002, Miretzky *et al*., 2004). As a consequence, they lack chemical or thermal stratification (Quirós and Drago, 1999) and greigite cannot be formed unless there is a change in environmental conditions. In consequence, the greigite found may suggest particularly warm and wet times.

Greigite can preserve in sediments during a rapid sedimentation rate (Blanchet *et al.*, 2009). A relative high sedimentation rate is found at the beginning of the record, from 1.3mm/yr in average to 3 mm/yr at 4700 cal. BP, which might allow greigite preservation. In summary, the presence of greigite in the base indicates higher than present lake levels consistent with low TIC and submerged plants (Figure 3i and 3m) during probably warm temperatures (high TOC). This short episode of a probably relative high lake level was not found by other authors.

From 4500 to 300 cal. BP, ARM/SIRM varies in less than an order of magnitude indicating a broadly stable environment. Coarser magnetic grain size particles were found around 4350 and between 1040 and 960 cal. BP. Low ARM/SIRM could suggest either low lake level because the shore is near, or high lake level because of increased rainfall. At around 4330 and 1000 cal. BP, emergent pollen taxa are high indicating the climate conditions were humid and the lake level high.A contribution dominated by high energy sources, like fluvial sediment sources which reach the lake carrying coarse terrigenous elements from La Brava Hill and El Peligro Creek or strong winds can be considered. All these periods are consistent with relative high κ and low TIC, so it is more likely that the sediments were transported by fluvial sources. An unstable environment from 2000 cal. BP to the present was found by Laprida *et al* (2009a).

The taxa of submerged plants are more abundant at the centre of the lake when the body of water is reduced, suggesting a shallower lake level at maxima values. The variations suggested through submerged and emergent plants are consistent with the behaviour of κ,indicating that this magnetic parameter is a good recorder of lake level changes.Between 4430 and 4250 cal. BP, low TOC values suggest a dry environment in the catchment area of Lake La Brava.A low lake level suggested by submerged plants is found in this interval (4410 – 4370 cal. BP), coeval with the presence of haematite. Haematite is a significant proxy of arid climate, because it forms during dry episodes and lower rainfall in the catchment area (Torrent *et al.*, 2006). The presence of haematite in the samples was calculated as the remanent percentage of magnetization at 580°C in the thermal curves. The higher presence of different amount of haematite always precedes the wet periods (T_C4 from Figure 5d are between 5 to 6.8 %) and can reach the lake during times dominated by aeolian transport. The presence of haematite suggests an overall dry climate from 4420 to 260 cal. BP with episodic wet/rainy environment. Occasionally rain storm were also found by Stutz *et al* (2012) between 4840 and 1200 cal. BP in a lake located 90 km in the NE direction from Lake La Brava.

Meanwhile, from 3250 to 450 cal. BP, TOC values indicate broadly minor variations on rainfall and climate. During this period, TOC variations decrease when k increases, indicating high clastic input from the catchment. Ca, Sr and Mg indicate wetter periods at around 4000, 2500 – 2000, 1500 and the last 260 cal. BP, suggesting more humid conditions than in previous periods.High percentages of clay and in consequence high lake levels are found at around 4330 and between 4000 – 3530 and 2660 – 2170 cal. BP. A mostly dry period was found between 3100 and 2600 cal. BP, consistent with TS maxima, low κ and relative high ARM/SIRM. At 990 cal. BP another dry event is suggested for the magnetic grain size, concentration dependent parameters and a peak in floating fern. A summary of all lake level and climatic changes and a comparison with previous results is shown in Figure 6.

Finer magnetic grain size particles according to inter-parametric ratios are found from 260 cal. BP to the present, more noticeable in ARM/SIRM. κ is in an increasing trend region

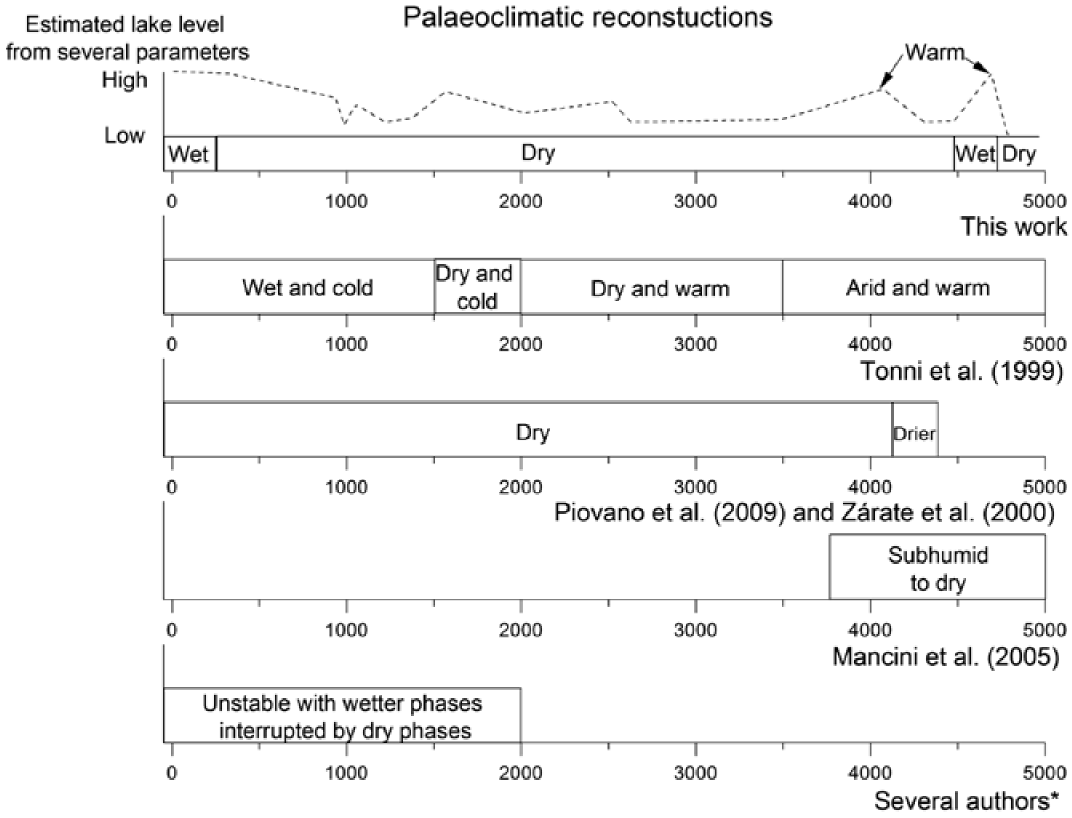

Figure 6. Summary of palaeoclimatic reconstructions for the last 5000 cal. BP in the Pampas Plain (other authors) and Lake La Brava (this work). All the ages are in calibrated years before present (cal. BP). * Cioccale (1999); Piovano *et al.* (2002); Stutz *et al.* (2002); Laprida *et al.* (2009a).

suggesting more erosion of unconsolidated material rich in magnetic minerals (Forester *et al.,* 1994; Dearing and Flower, 1982; Thorndycraft *et al*., 1998) from the catchment area. Clay reaches the maximum indicating a low energy environment at the centre of the lake. The flux of TIC is very low suggesting a high lake level. In summary, the most likely environment is a quiet climate where the coast was far from the coring site indicating a high lake level. The highest lake level was found for the last 260 cal. BP, consistent with the insoluble metals mentioned before. In summary, a high lake level, possibly flood episodes, and increased erosion are suggested in this period.

The last 50 cal. BP show a decrease in organic matter content consistent with a decrease in emergent plants. The highest values of κ from 25 cal. BP to the present are in agreement with the increasing trend of annual rainfall during the last eight decades (Irigoyen *et al.*, 2008). The logs of S-ratio and κ show an increase as well, but this magnetic enhancement is noticeable from 100 cal. BP to the present. This trend is similar to that reported for other lakes (Oldfield *et al*., 1978; Turner and Thompson, 1981; Zolitschka, 1998; Stockhausen and Zolitschka, 1999; Dearing *et al.,* 2001; Rolph *et al.,* 2004), suggesting changes in sediment delivery and depositional processes caused by human impact (agricultural activities implying different soil erosion). This trend is observed also in vegetation analysis with the appearance of different species (Morellón *et al.*, 2009). The proxy's record for the last decades suggests a mix of natural climate shift and anthropogenic activities. Considering that the values of κ are never that high, is more likely that the human disturbance is primarily responsible for these changes.

Conclusions

This study allowed us to obtain high-quality palaeoclimatic record for southeast Buenos Aires Province during the last 4800 cal. BP. The results from pollen analysis and sedimentology indicate that the lake never dried during this period. B_{CR}, SIRM/k and the combination of both are in the range of (titano) magnetite for most of the samples.The values of T_C and SIRM acquisition curves are consistent with sediments dominated by (titano) magnetite with different amount of Ti as the dominant magnetic carrier of remanence but not the only one present in the samples. S-ratio has its mean value at 0.86, suggesting the presence of magnetite with different percentages of antiferromagnetic minerals. The main magnetic carrier is magnetite with grain size into the PSD range(Thompson and Oldfield*,* 1986). This grain size is probably a combination of MD with small size ferrimagnetic particles (Stockhausen and Zolitschka, 1999). The concentration of magnetite varies from 0.003 and 0.02%.

In combination with geochemical and palynological studies, κ and ARM/SIRM are the better magnetic proxies to infer precipitation; low values of both parameters are found during high lake level or more rainfall. The general trend for all parameters indicates an overall dry environment since 4800 cal. BP. Based on magnetic and geochemical studies, a model for palaeoclimatic implications show some flood or high lake level events at 4700, 4060 and 1500 cal. BP and a period of high lake level from 2500 to 2100 cal. BP were found.Two moments of extremely dry environment were found at 4780 and 990 cal. BP.

All the results suggest that climate was the major forcing process of regional fluvial system behaviour (erosion and lake level changes) across the catchment area of Lake La Brava from 4800 cal. BP until the beginning of stable human settlement. It was established that anthropogenic influence is the main factor of the changes observed during the twentieth century over imposed to a more humid environment.

Acknowledgements

The authors wish to thank UNCPBA, IAA and CONICET. They are also grateful for funds provided by the CICYT project MEDEROCAR (CGL2008-0831), PIP-CONICET 1265/08 and the project PICT-O nº 13-11502. The authors wish to thanks Dr.C. Geiss for the comments and suggestions and to the anonymous reviewers for their comments which improve the paper.

References

Abbott M.B., Wolfe B.B., Wolfe AP, Seltzer G.O., Aravena R., Mark B.G., Polissar P.J., Rodbell D.T., Rowe H.D., Vuille M., 2003, Holocene paleohydrology and glacial history of the central Andes using multiproxy lake sediment studies. *Palaeogeography, Palaeoclimatology, Palaeoecology.,* 194, 123-138.

Abdul Aziz H., Langereis C.G., 2004, Astronomical tuning and duration of three new subchrons (C5r.2r-1n, C5r.2r-2n and C5r.3r-1n) recorded in a Middle Miocene continental sequence from NE Spain. In *Geophysical Monograph Series*, 145, AGU, 328 pp.

Ariztegui D., Dobson J., 1996, Magnetic investigations of framboidalgregigite formation: a record of anthropogenic environmental changes in eutrophic Lake St Moritz, Switzerland. *The Holocene,* 6, 2, 235 – 241.

Bagnold R.A., Rickwoods M.B., Edenbridge K.,1979, Sediment Transport by Wind and Water. *Nordic Hydrology,* 10, 309-322.

Bidegain J.C., Rico Y., Bartel A., Chaparro M.A.E., Jurado S., 2009, Magnetic parameters reflecting pedogenesis in Pleistocene loess deposits of Argentina. *Quaternary International*, 209, 1-2, 175-186.

Blanchet, C. L., N. Thouveny and L. Vidal, 2009. Formation and preservation of greigite (Fe_3S_4) in sediments from the Santa Barbara Basin: Implications for paleoenvironmental changes during the past 35 ka. *Paleoceanography,* 24, PA2224, doi:10.1029/2008PA001719.

Bronk Ramsey C., 2001, Development of the radiocarbon calibration program OxCal. *Radiocarbon., 43,* 2A, 355-363.

Bronk Ramsey C., 2008, Deposition models for chronological records. *Quaternary Science Reviews,* 27, 1-2, 42-60.

Chaparro M.A.E., 2006, Estudio de Parámetros Magnéticos de Distintos Ambientes Relativamente Contaminados en Argentina y Antártida.MONOGRAFIAS, Ed. Geofísica UNAM, Monografía No. 7, 107 pp. ISBN: 970323567-0. First edition, April 2006

Chaparro M.A.E., Böhnel H.N., Byrne R., Nowaczyk N.R., Molina-Garza R.S., Park J., Negendank J.F.W., 2008, Paleomagnetic secular variation and rock-magneticstudies of Holocenesedimentsfrom a maarlake (Hoya de San Nicolas) in Central Mexico. *Geophysical Journal International*, 175, 462–476.

Cioccale M.A., 1999, Climatic fluctuations in the Central Region of Argentina in the last 1000 years. *Quaternary International,* 62, 35-47.

Cordini R., 1942, Laguna La Brava (Prov. de Buenos Aires). *Revista Argentina de Zoogeografía*, II, 1, 3-53.

Dangavs N.V., 2005, Los ambientes acuáticos de la Provincia de Buenos Aires. In: Recursos Minerales de la Provincia de Buenos Aires. Geología y Relatorio XVL *Congreso Geológico Argentino*, pp 219-236, ed. Barrio, R.E., Etcheverry, R.O., Caballé M.F., Llambías E., La Plata, Argentina.

Dankers P.H., 1978, Magnetic properties of dispersed natural iron oxides of known grain size (3rd Ed.), Ph.D. Thesis, Univ. Utrecht. Netherlands.

Davison W., 1992, Iron and manganese in lakes. *Earth Sciences Reviews,* 34, 119-163.

Dearing J.A., Flower R.J., 1982, The magnetic susceptibility of sedimenting material trapped in Lough Neagh, Northern Ireland, and its erosional significance. *Limnology and Oceanography*, 27, 969-975.

Dearing J.A., Hu Y., Doody P., James P.A., Brauer A., 2001, Preliminary reconstruction of sediment-source linkages for the past 6000 yrs at the Petit Lac d'Annecy, France, based on mineral magnetic data. *Journal of Paleolimnology*, 25, 245–258.

Dekkers M.J., Passier H.F., Schoonen M.A.A., 2000, Magnetic properties of hydrothermally synthesized greigite (Fe3S4)—II. High- and low-temperature characteristics. *Geophys. J. Int.,* 141, 809–819.

Dunlop D.J., Özdemir Ö., 1997, Rock Magnetism. Fundamentals and Frontiers. 573 pp. Cambridge University Press, Cambridge.

Faegri K., Iversen J., 1989, Textbook of Pollen Analysis (Fourth Edition by K. Faegri, P.E. Kaland, and K. Krzywinski). John Wiley & Sons New York. 328 pp.

Forester R.M., Colman S.M., Reynols R.L., Keigwin L.D., 1994, Lake Michigan´s Late Quaternary limnological and climate history from ostracode, oxygen isotope, and magnetic susceptibility. *J. Great Lakes Res.,* 20, 99-107.

Geiss C.E., Umbanhowar C.E., Camill P., Banerjee S.K., 2003, Sediment magnetic properties reveal Holocene climate change along the Minnesota prairie-forest ecotone. *Journal of Paleolimnology*. *30: 151-166.*

Geiss C.E., Zanner C.W., Banerjee S.K., Joanna M., 2004, Signature of magnetic enhancement in a loessic soil in Nebraska, United States of America. *Earth and Planetary Science Letters,* 228, 355– 367.

Gogorza C.S.G., Lirio J.M., Nuñez H., Chaparro M., Vilas J.F., Bertorello H.R., Sinito A.M., 2004, Paleointensity studies on Holocene-Pleistocene sediments from lake Escondido, Argentina. *Physics of the Earth and Planetary Interiors,* 145, 219-238.

Gogorza C.S.G., Irurzun M.A., Chaparro M.A.E., Lirio J.M., Nuñez H., Bercoff P.G., Sinito A.M., 2006, Relative paleointensity of the geomagnetic field over the last 21,000 years BP from sediment cores, Lake El Trébol (Patagonia, Argentina). *Earth Planets Space*, 58, 1323–1332.

Gogorza C.S.G., Irurzun M.A., Sinito A.M., Lisé-Pronovost A., St-Onge G., 2012, High-resolution paleomagnetic records from Laguna PotrokAike (Patagonia, Argentina) for the last 16,000 years. *Geochem. Geophys. Geosyst.,* 13, 12, Q12Z37, doi: 10.1029/2011GC003900.

Hannon G.E., Gaillard M.J., 1997,The plant-macrofossil record of past lake-level changes. *Journal of Palaeolimnology,* 18, 15-28.

Higgitt S.R., Oldfield F., Appleby P.G., 1991, The record of land use change and soil erosion in the late Holocene sediments of the Petit Lac d'Annecy, eastern France.*The Holocene,* 1, 14-28.

Hillesheim M.B., Hodell D.A., Leyden B.W., Brenner M., Curtis J.H., Anselmetti F.S., Ariztegui D., Buck D.G., Guilderson T.P., Rosenmeier M.F., Schnurrenberger D.W., 2005, Climate change in lowland Central America during the late deglacial and early Holocene. *Journal of Quaternary Science*, 20, 4, 363-376.

Hunt C.P., Banerjee S.K., Han J., Solheid P.A., Oches E., Sun W., Liu T., 1995, Rock-magnetic proxies of climate change in the loess-paleosol sequences of the western Loess Plateau of China. *Geophys. J. Int.,* 123, 232–244.

INIDEP, 2001. Inf. Téc. INIDEP N°7. 06-03-01. 5 pp.

INTA. Instituto Nacional de Tecnología Agropecuaria. Informe Agropecuario (2008) http://www.inta.gob.ar/balcarce/info/documentos/econo/analisis/zonas/ZAHIIIFBalcarce.pdf.

Irigoyen A.I., Suero E.E., Gardiol J.M., 2008, Tendencia Y Estacionalidad De La Precipitación En Balcarce. Unidad Integrada: Facultad de Ciencias Agrarias UNMdP -EEA INTA Balcarce. Argentina.

Irurzun M.A., Gogorza C.S.G., Torcida S., Lirio J.M., Nuñez H., Chaparro M.A.E., Sinito A.M., 2009, Rock magnetic properties and relative paleointensity stack between 13 and 24 kyr B.P. calibrated ages from sediment cores, Lake Moreno (Patagonia, Argentina). *Physics of the Earth and Planetary Interiors*, 172, 157-168.

Krs M., Krsová M., Koulíková L., Pruner P., Valín F., 1992, On the applicability of oil shale to paleomagnetic investigations,*Phys. Earth Planet. Inter.,* 70, 178–186, doi:10.1016/0031-9201(92)90180-4.

Kruiver P.P., Dekkers M.J., Heslop D., 2001, Quantification of magnetic coercivity components by the analysis of acquisition curves of isothermal remanent magnetisation. *Earth and PlanetaryScience Letters*, 189, 269-276.

Kruse E., 1987, El agua subterránea en el régimen hidrológico de Laguna La Brava. Informe 40. Comisión de Investigaciones Científicas de la Provincia de Buenos Aires. 18 pp.

Laprida C., Valero-Garcés B., 2009a, Cambios ambientales de épocas históricas en la pampa bonaerense en base a ostrácodos: historia hidrológica de la laguna de Chascomús. *Ameghiniana*, 46, 95-111.

Laprida C., Orgeira M.J., GarciaChapori N., 2009b, El registro de la Pequeña Edad de Hielo en las lagunas pampeanas*. Revista de la Asociación Geológica Argentina*, 65, 4, 603 – 611.

Laprida C., Valero-Garcés B., Compagnucci R., Orgeira M.J., Navas A., Ito E., 2011, Cambios ambientales de la pampa bonaerense: memorias y olvidos de las lagunas pampeanas. En M. Caballero Miranda y B. Ortega Guerrero (eds.) Escenarios de Cambio Ambiental: Registros del Cuaternario en América Latina. Ed. Fondo de Cultura Económico, 38 p. México.

Lascu I., McLauchlan K., Myrbo A., Leavitt P.R. and Banerjee S.K., 2012, Sediment-magnetic evidence for last millennium drought conditions at the prairie–forest ecotone of northern United States, *Palaeogeography, Palaeoclimatology, Palaeoecology,* 337-338, 99-107.

Lirio J.M., Núñez H.J., Chaparro M.A., Sinito A.M., Irurzun A., Gogorza C.S., 2007, Laguna la brava, Provincia de Buenos Aires. Relaciones paleoclimáticas con Patagonia y Antartida. Actas del VI Simposio Argentino y III Latinoamericano sobre investigaciones Antárticas.

Maher B.A., Thompson R., 1999, Quaternary Climates, Environments and Magnetism. Cambridge Univ. Press, Cambridge. 390 pp.

McCormac F.G., Hogg A.G., Blackwell P.G., Buck C.E., Higham T.F.G., Reimer P.J., 2004, SHCal04 Southern Hemisphere calibration, 0–11.0 cal kyr BP. *Radiocarbon,* 46, 3, 1087–1092.

Mancini M.V., Paez M.M., Prieto A.R., Stutz S., Tonello M., Vilanova I., 2005, Mid-Holocene climatic variability reconstruction from pollen records (32°–52°S, Argentina). *Quaternary International*, 132, 47–59.

Miretzky P., Fernández Cirelli A., 2004, Silica dynamics in a pampean lake (Lake Chascomús, Argentina) *Chemical Geology,* 203, 1–2, 109-122.

Morellón M., Valero-Garcés B.L., González-Sampériz P., Vegas-Vilarrúbia T., Rubio E., Rieradevall M., Delgado-Huertas A., Mata P., Romero O., Engstrom D.R., López-Vicente M., Navas A., Soto J., 2009, Climate changes and human activities recorded in the sediments of Lake Estanya (NE Spain) during the Medieval Warm Period and Little Ice Age**.** *Journal of Paleolimnology,* 1-30.

Muhs D.R., Zárate M., 2001, Late Quaternary eolian records of the Americas and their paleoclimatic significance. *Interhemispheric climate linkages,* 12, 183-216.

Nabel P.E., Morrás H.J.M., Petersen N., Zech W., 1999, Correlation of magnetic and lithologic features of soils and Quaternary sediments from the Undulating Pampa, Argentina. *Journal of South American Earth Sciences,* 12, 3, 311-323.

Nichols G., 2009, Sedimentology and Stratigraphy. 2da ed., Ed. Wiley-Blackwell, United Kingdom, 419 pp.

Oldfield F., Dearing J.A., Thompson R., Garret-Jones S., 1978, Some magnetic properties of lake sediments and their possible links with erosion rates. *Pol. Arch. Hydrobiol.*, 25, 321-331.

Orgeira M.J., Walther A.M., Tófalo R.O., Vasquez C., Berquó T., FavierDobois C., Bohnel H., 2003, Environmental magnetism in fluvial and loessic Holocene sediments and paleosols from the Chacopampean plain (Argentina). *Journal of South American EarthSciences,* 16, 259–274.

Orgeira M.J., Pereyra F.X., Vásquez C., Castañeda E., Compagnucci R., 2004, Señal magnética en suelos actuales de la Provincia de Buenos Aires, Argentina: su relación con el clima. *GEO-TEMAS. Zaragoza: Sociedad Geológica de España,* 6, 311-314.

Orgeira M.J., Vásquez C.A., Compagnucci R.H., Raposo I., Pereyra F.X., 2009, Magnetismo de rocas en suelos actuales de la Pampa Ondulada, provincia de Buenos Aires, Argentina. Vinculación del clima con el comportamiento magnético. *Revista Mexicana de Ciencias Geológicas*, 26, 1, 65-78.

Peters C., Dekkers M.J., 2003, Selected room temperature magnetic parameters as a function of mineralogy, concentration and grain size. *Phys. Chem. Earth,* 28, 659–667.

Piovano E.L., Ariztegui D., Damatto Moreira S., 2002, Recent environmental changes in Laguna Mar Chiquita (central Argentina): a sedimentary model for a highly variable saline lake. *Sedimentology,* 49, 1371–1384.

Piovano E.L., Aristegui D., Cordoba F., Cioccale M., Sylvestre F., 2009, Hydrological Variability in South America below the Tropic of Capricorn (Pampas and Patagonia, Argentina) during the Last 13.0 Ka. In: F. Vimeux M. Khodri and F. Sylvestre (Eds). Past Climate Variability in South America and Surrounding Regions. From the Last Glacial Maximum to the Holocene. Springer, 14, 323-352.

Prieto A.R., 1996, Late Quaternary Vegetational and Climatic Changes in the Pampa Grassland of Argentina. *Quaternary Research*, 45, 73–88.

Prieto A.R., Blasi A.M., De Francesco C.G., Fernandez C., 2004, Environmental history since 11,000 14C yr B.P. of the northeastern Pampas, Argentina, from alluvial sequences of the Luján River.*Quaternary Research*, 62, 146–161.

Quirós R., 1988, Relationships between air temperature, depth, nutrients and chlorophyll in 103 Argentinian lakes. *Verh. Internat. Verein. Limnol.,* 23, 647-658.

Quirós S.R., Drago E., 1999, The environmental state of Argentinean lakes: an overview. Lakes&Reservoirs: Research and Management, 4, 55-64.

Quirós R., Rosso J.J., Rennella A., Sosnovsky A., Boveri M., 2002, Estudio sobre el estado trófico de las lagunas pampeanas. *Interciencia,* 27, 584-591.

Quirós R., 2004, Sobre la morfología de las lagunas pampeanas. Documento de Trabajo del Area de Sistemas de Producción Acuática Nº 3. Area de Sistemas de Producción Acuática, Departamento de Producción Animal, Facultad de Agronomía, Universidad de Buenos Aires.

Quiroz Londoño O.M., Martinez D.E., Dapena C., Massone H., 2008, Hydrogeochemistry and isotope analyses used to determine groundwater recharge and flow in low-gradient catchments of the province of Buenos Aires, Argentina. *Hydrogeology Journal,* 16, 1113-1127.

Rennella A. M. and Quirós R., 2002, Relations between planktivorous fish and zooplankton in two very shallow lakes of the Pampa Plain. *Verh. Internat. Verein. Limnol.,* 28, 1–5 Stuttgart, Germany.

Reynolds R.L., Tuttle M.L., Rice C.A., Fishman N.S., Karachewski J.A., Sherman D.M., 1994, Magnetization and geochemistry of greigite-bearing Cretaceous strata, North Slope Basin, Alaska. *Am. J. Sci*., 294, 485–528.

Riedinger N., Pfeifer K., Kasten S., Garming J.F.L., Vogt C., Hensen C., 2005, Diagenetic Alteration of Magnetic Signals by Anaerobic Oxidation of Methane Related to a Change in Sedimentation Rate.*Geochimicaet Cosmochimica Acta,* 69, 16, 4117–4126.

Roberts A.O., Turner G.M., 1993. Diagenetic formation of ferrimagnetic iron sulphide minerals in rapidly deposited marine sediments, South Island, New Zealand. *Earth Planet. Sci. Lett.,* 115, 257–273.

Roberts A.P., Chang L., Rowan C.J., Horng C. -S., Florindo F., 2011, Magnetic properties of sedimentary greigite (Fe_3S_4): An update, *Rev. Geophys*., 49, RG1002, doi:10.1029/2010RG000336.

Rolph T.C., Vigliotti L., Oldfield F., 2004, Mineral magnetism and geomagnetic secular variation of marine and lacustrine sediments from central Italy: timing and nature of local and regional Holocene environmental change. *Quaternary Science Reviews*, 23, 1699–1722.

Romanelli A., 2006, Estudio integral del área de laguna La Brava. Diagnóstico y perspectivas de gestión sustentable. Tesis de Grado. Facultad de Ciencias Exactas y Naturales, Universidad Nacional de Mar del Plata. 77 pp. (unpublished).

Romanelli A., Quiroz Londoño O.M., Massone H.E., Martinez D.E., Bocanegra E., 2010a, El agua subterránea en el funcionamiento hidrológico de los humedales del Sudeste Bonaerense, Provincia de Buenos Aires, Argentina. *Boletín Geológico y Minero,* 121, 4, 373-386.

Romanelli A., Quiroz Londoño O.M., Massone H.E., Escalante A. H., 2010b, Validación y ajuste del modelo hidrogeológico conceptual de un humedal de la Llanura Pampeana, Provincia de Buenos Aires, Argentina. *RevistaLimnetica.* Asociación Ibérica de Limnología, Madrid, España, 29, 2, 407-418.

Romanelli A., Massone H.E., Quiroz Londoño O. M., 2011, Integrated hydrogeological study of surface water and groundwater resources in the Southeastern of Buenos Aires Province, Argentina. *International Journal of Environmental Research,* 5, 4, 1053-1064.

Sagnotti L., Roberts A.P., Weaver R., Verosub K.L., Florindo F., Pike C.R., Clayton T., Wilson G.S., 2005, Apparent magneticpolarity reversals due to remagnetization resulting from latediagenetic growth of greigite from siderite, *Geophys. J. Int.*, 160, 89–100

Sandgren P., Risberg J., 1990, Magnetic mineralogy of the sediments in Lake Adran, E Sweden, and an interpretation of early Holocene water level changes. *Boreas*, 19, 57-68.

Schäbitz F., Liebricht H., 1998, Landscape and climate development in the south-eastern part of the ‘‘Arid Diagonal’’ during the last 13,000 years. *Bamberger Geographische Schriften,* 15, S, 371–388.

Shapley M.D., Ito E., Donovan J.J., 2005, Authienic calcium carbonate flux in groundwater-controled lakes: implications for lacustrine paleoclimate records. *Geochimica et Cosmochimica Acta,* 69, 10, 2517-2533.

Shapley M.D., Ito E., Donovan J.J., 2009, Lateglacial and Holocene hydroclimate inferred from a groundwater flow-through lake, Northern Rocky Mountains, USA. *The Holocene,* 19, 4, 523–535.

Sosnovsky A., Rosso J., Quirós R., 2010, Trophic interactions in shallow lakes of the Pampa plain (Argentina) and their effects on water transparency during two cold seasons of contrasting fish abundance. Limnetica, 29 (2): 233-246, Madrid. Spain. ISSN: 0213-8409

Stockhausen H., Zolitschka B., 1999, Environmental changes since 13,000 cal. BP reflected in magnetic and sedimentological properties of sediments from Lake Holzmaar (Germany). *Quaternary Science Reviews*, 18, 913-925.

Stutz S., Prieto A.R., Isla F.I., 2002, Historia de la vegetación del Holoceno de la laguna Hinojales, sudeste de la provincia de Buenos Aires, Argentina. *Ameghinina,* 39, 1, 85–94.

Stutz, S., Borel, C.M., Fontana, S.L., Tonello, S.M., 2012. Holocene changes in trophic states of shallow lakes from the Pampa plain of Argentina. *The Holocene,* 22, 11, 1263-1270.

Thompson R., Oldfield F., 1986, Environmental Magnetism. Allen &Unwin Ltd., London, U.K. 225 pp.

Thorndycraft V., Hu Y., Oldfield F., Crooks P.R.J., Appleby P.G., 1998, A high resolution flood event stratigraphy un the sediments of the Petit Lac d'Annecy. *Holocene*, 8, 741-746.

Tonello M.S.,Prieto A.R., 2008, Modern vegetation-pollen-climate relationships for the Pampa grasslands of Argentina. *Journal of Biogeography,* 35, 5, 926–938.

Tonello M.S., Prieto A.R., 2010, Tendencias climáticas para los pastizales pampeanos durante el Pleistoceno tardío-Holoceno: estimaciones cuantitativas basadas en secuencias polínicas fósiles. *Ameghiniana,* 47, 501-514.

Tonni E.P., Cione A.L., Figini A.J., 1999, Predominance of arid climates indicated by mammals in the pampas of Argentina during the Late Pleistocene and Holocene. *Palaeogeography, Palaeoclimatology, Palaeoecology*, 147, 257–281.

Torrent J., Barrón V., Liu Q., 2006, Magnetic enhancement is linked to and precedes hematite formation in aerobic soil. *Geophysical Research Letters,* 33, L02401, doi: 10.1029/2005GL024818.

Turner G.M., 1997, Environmental magnetism and magnetic correlation of high resolution lake sediment records from Nortern Hawke's Bay, New Zealand. *New Zealand Journal of Geology and Geophysics,* 40, 287-298.

Turner G.M., Thompson R., 1981, Lake sediment record of geomagnetic secular variation in Britain during Holocene times. *Geophys J. R. Soc,* 65, 703-725.

Vázquez G., 2012, Magnetismo Ambiental de los Últimos 17,000 años en el Lago Zirahuén, Michoacán, México. PhD. Thesis Universidad Nacional Autónoma de México, México. 222pp.

Zárate M., Kemp R.A., Espinosa M., Ferrero L., 2000, Pedosedimentary and palaeoenvironmental significance of a Holocene alluvial sequence in the southern Pampas Argentina. *The Holocene*, 10, 4), 481–488.

Zárate M., Kemp R., Toms P., 2009, Late Quaternary landscape reconstruction and geochronology in the northern Pampas of Buenos Aires province, Argentina. *Journal of South American Earth Science,* 27, 1, 88-99.

Zárate M.A., Tripaldi, A., 2012, The aeolian system of central Argentina. *Aeolian Research,* 3, 401-417.

Zolitschka B., 1998, A 14000 year sediment yield record from western Germany based on annually laminated sediments. *Geomorphology*, 22, 1-17.

Geofísica Internacional (2014) 53-4: 385-398

Original paper

Spectral Reflectance Analysis of the Caribbean Sea

Raúl Aguirre Gómez

Received: March 03, 2013; accepted: January 21, 2013; published on line: October 01, 2014

Resumen

En este trabajo se analizaron curvas de reflectancia espectral mediante el método de derivada. Los espectros de derivada de la reflectancia revelaron picos ocultos tanto en curvas de reflectancia y absorción del agua del Mar Caribe y de elementos contenidos en ella. Las curvas de reflectancia mostraron un predominio del color azul (400-500 nm), el cual es característico de aguas oligotróficas del Caribe, los picos de absorción están influenciados por las propiedades ópticas de la clorofila *a* y el agua de mar. Las curvas de reflectancia mostraron respuesta espectral similar. En este artículo se analizaron los espectros de reflectancia del agua marina en 31 estaciones en el Mar Caribe en el verano de 2001.

Palabras clave: Propiedades ópticas, Oceanografía óptica, análisis de derivada de la reflectancia, Mar Caribe.

Abstract

Reflectance spectral curves were analysed by a derivative method. Derivative reflectance spectra revealed concealed peaks of both reflectance and absorption curves of Caribbean seawater and elements contained within it. Reflectance curves showed a predominant blue colour (400-500 nm) characteristic of Caribbean oligotrophic waters, conspicuous peaks result from the optical properties of chlorophyll *a* and seawater. Reflectance curves had a similar spectral response. This paper analyses reflectance spectra of surface seawater at 31 stations in the Caribbean Sea during the summer of 2001.

Keywords: Optical properties, optical Oceanography, derivative reflectance analysis, Caribbean Sea.

Raúl Aguirre Gómez
Laboratorio de Análisis Geoespacial
Instituto de Geografía
Universidad Nacional Autónoma de México
Circuito Exterior, Ciudad Universitaria
04510, México D.F., México
Corresponding author: raguirre@igg.unam.mx

Introduction

Sea surface reflectance R(λ) is operationally defined as the ratio between upwelling irradiance $E_u(\lambda,0)$ and the downwelling irradiance $E_d(\lambda,0)$ at wavelength λ at the surface (depth $Z=0$) and is expressed as:

$$R(\lambda,0) = \frac{E_u(\lambda,0)}{E_d(\lambda,0)} \tag{1}$$

The parameter $E_u(\lambda,0)$ possesses information on the sea water and the dissolved and particulate matter contained within it, whilst $E_d(\lambda,0)$ stands for the total incoming irradiance. Changes of ocean colour are determined by the spectral variations of the reflectance $R(\lambda,0)$.

The operational expression of Equation (1) can be related to physical properties of water. Many models of radiative transfer are useful for establishing a relationship between $R(\lambda)$ and the absorption (a) and backscattering (b_b) coefficients (e.g. Morel and Prieur 1977, Gordon and Morel 1983). Both coefficients are influenced by the optical characteristics of pure sea water and those of the particulate and dissolved substances present in variable amounts in the sea. Thus, reflectance spectra are a consequence of absorption and backscattering processes due to water (w), phytoplankton ($phyto$), carbon dissolved organic matter or CDOM (y) and non-phytoplankton particles (x). Hence, any interpretation of the reflectance must consider the optical properties of these substances.

Morel and Prieur (1977) proposed a simple relationship for the reflectance of oceanic waters:

$$R = f\frac{b_b}{a} \tag{2}$$

Where f is a function of solar altitude and the scattering phase function (Gordon *et al*., 1988). Thus, f can take different values depending on the angle of measurement. Historically, it had the value of 0.33 at the zenith angle of incident light (Morel and Prieur, 1977; Kirk 1984); however, other authors have estimated the f value for different angle intervals (e. g. Hirata and Højerslev, 2008). Nonetheless, this equation is only valid for waters where $b_b \ll a$, and it is assumed that the coefficients a and b_b follow the principle of superposition (Sathyendranath and Morel 1983).

Experimental data and theory indicate that, under most conditions, values of $b_b(\lambda)$ are relatively small compared to values of $a(\lambda)$ and decrease monotonically with respect to wavelength (Gordon and Morel 1983).

In order to analyze reflectance spectra a number of techniques have been employed. Thus, ratios and differences have traditionally been used in ocean colour studies, although they are restricted to a small number of spectral bands.

Nowadays, the advent of high-spectral-resolution sensors requires the use of powerful analytical methods of study such as the derivative analysis. The derivative method undertakes many of the problems of quantitative analysis more effectively than ratios and differences by considering a larger amount of data, which stands for more information potentially available (Jia *et al.*, 2008). Derivative analysis has been applied to a different kind of spectra obtained by high spectral-resolution sensors (e. g., Evangelista *et al*., 2006). These sensors are characterised by having a bandwidth less than 5 nm and/or more than 100 spectral bands. Thus, high-spectral-resolution sensors can provide information about smaller spectral variations than coarse bands do. The derivative method has been used for minimizing low-frequency background noise and for resolving overlapping spectra (Butler and Hopkins 1970). This method has successfully been applied in aquatic remote sensing for studying suspended solids in water (Chen *et al*., 1992, Goodin *et al.,* 1993; Hunter *et al.,* 2008) and detecting photosynthetic algal pigments (Aguirre-Gómez *et al.,* 2001; Han, 2005), among other topics.

In general, data provided by high-spectral-resolution sensors mounted on an aircraft, on a satellite, and on a field spectroradiometer, can be useful for testing new types of algorithms designed to analyse the reflectance of seawater. Particularly, data provided by field spectroradiometers are important in remote sensing studies because they may simulate those obtained through sensors mounted on aircraft or satellites. Additionally, these measurements are essential for determining the atmospheric effect between the airborne or spaceborne remote sensor and the ground, instead of using models for removing atmospheric influences (Philpot, 1991). Finally, under certain circumstances, it could be better to use ship-based information because of higher confidence of in situ related data.

Consequently, the in situ optical properties, as calculated by equation (2), can be related to ocean colour observations through reflectance information on the marine surface as measured by equation (1).

The aim of this study is to assess the potential of derivative analysis applied to high-spectral-resolution ship-based spectroradiometer data for retrieving information about photosynthetic pigments. Due to the lack of simultaneous *in situ* measurements of pigments, satellite-derived chlorophyll-a concentration was estimated to validate the spectral reflectance curves.

Derivative reflectance spectra

According to equation (2), the solar radiation reflected from the sea surface depends on absorption and backscattering processes. Both processes are dependent on the water itself, phytoplankton, particulate and dissolved matter (Kirk, 2011). Thus, considering all of these components, the derivative reflectance spectra can be expressed as the rate of change of reflectance with wavelength dR(λ)/dλ. Therefore, by estimating the complete differentiation of $R = R(a_w, a_{phyto}, a_x, a_y, b_{bw}, b_{bphyto}, b_{bx}, \lambda)$, we obtain

$$\frac{dR(\lambda)}{d\lambda} = \frac{\partial R}{\partial a_w}\frac{da_w}{d\lambda} + \frac{\partial R}{\partial a_{phyto}}\frac{da_{phyto}}{d\lambda} + \frac{\partial R}{\partial a_x}\frac{da_x}{d\lambda} + \frac{\partial R}{\partial a_y}\frac{da_y}{d\lambda} + \frac{\partial R}{\partial b_{bw}}\frac{db_{bw}}{d\lambda} + \frac{\partial R}{\partial b_{bphyto}}\frac{db_{bphyto}}{d\lambda} + \frac{\partial R}{\partial b_{bx}}\frac{db_{bx}}{d\lambda} \tag{3}$$

where the partial derivatives are an implicit function of λ.

Assuming $R(\lambda) \approx b_b(\lambda)/a(\lambda)$ and by calculating the partial derivative for each component, and substituting in the equation (3), we get:

$$\frac{dR(\lambda)}{d\lambda} \approx \frac{b_b(\lambda)}{a(\lambda)^2}\left(\frac{da_w}{d\lambda} + \frac{da_{phyto}}{d\lambda} + \frac{da_x}{d\lambda} + \frac{da_y}{d\lambda}\right) + \frac{1}{a(\lambda)}\left(\frac{db_{bw}}{d\lambda} + \frac{db_{bphyto}}{d\lambda} + \frac{db_{bx}}{d\lambda}\right) \tag{4}$$

This equation relates the slope of a directly measured reflectance spectrum at any wavelength to each of the components. Consequently, it is possible to iteratively calculate high-order derivatives. Thus, in principle, the presence of phytoplankton pigments, suspended and organic matter within the sea water can be estimated by considering reflectance spectrum components as mutually independent.

Study area

The Caribbean Sea is the largest sea adjacent to the Atlantic Ocean. It has an upper mixed layer of about 50 m, which quickly responds to atmospheric forcing. Circulation at this layer is controlled by the Caribbean Current, which substantially contributes to heat advection from the tropic to mid-latitudes. The physical characteristics of the Caribbean Sea have been studied from various perspectives (e.g. Gordon, 1967; Etter *et al.*, 1987; Kinder *et al.*, 1985; Müller-Karger *et al.*, 1989). The Caribbean Sea is considered to be an oligotrophic area. This can be supported in terms of its efficiency of light utilisation. An areal efficiency e_A (ratio of areal photosynthetic rate to the total Photosynthetically Active Radiation), in a range of 0.02%-0.07%, was reported for the Caribbean Sea, which can be interpreted as a relatively low amount of phytoplankton within the euphotic zone (Morel, 1978). When the pycnocline is deeper than about 100 m, the deep chlorophyll maximum is extremely weak. However, the literature contains few studies of the bio-optical characteristics of the area, measured with spectral radiometers and apparently no reports of its reflectance properties (e.g. Clark and Ewing, 1974; Farmer *et al.,* 1993).

The reflectance characteristics of oceanic waters have been studies by a number of authors (e.g. Wilson and Kiefer, 1979; Morel *et al.,* 1995). With the advent of high spectral resolution sensors the analysis of reflectance properties has been significantly improved.

The Bi-directional Reflectance Factor (BDRF) method proposed by Milton (1987) has been widely used on lakes and lagoons (e.g. Dekker *et al.,* 1991; Aguirre-Gómez, 2001) and on oceanic sites (e.g. Bidigare *et al.,* 1989; Aguirre *et al.,* 2001). One of the advantages of using high spectral resolution sensors is the potential for applying sophisticated algorithms, such as the derivative method, to nearly continuous curves. Particularly, it is a powerful tool for detecting information concealed in spectral reflectance curves. Thus, the main objective of this study is to analyze the spectral reflectance characteristics of the Caribbean Sea through the derivative method.

Material And Methods

Hydrographical, meteorological and optical measurements were performed over the

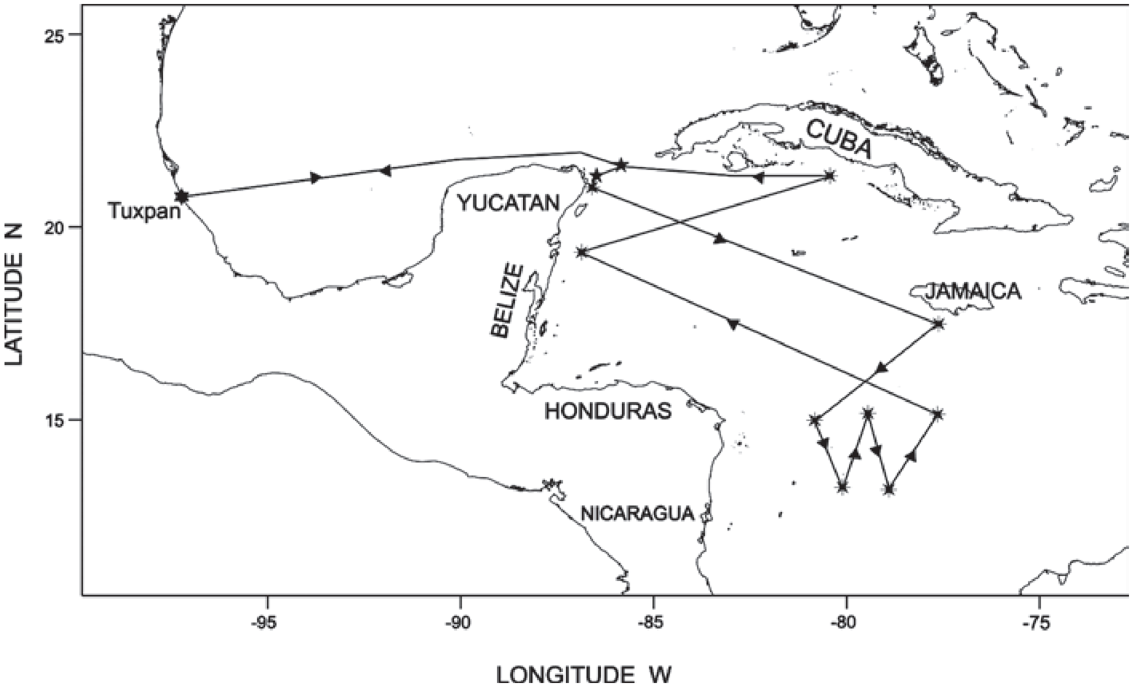

Figure 1. ECAC-3 cruise track from July 6 to 26, 2001.

Caribbean Sea during the oceanographic/meteorological cruise ECAC-3, onboard the R/V Justo Sierra (Universidad Nacional Autónoma de México, UNAM) from July 6 to 26, 2001.

The cruise track had three phases: outbound leg, main survey, and inbound leg (Figure 1). The outbound leg (from Tuxpan to Yucatan channel) was used for testing and training purposes. The cruise track for the main survey was determined by turning points that defined the nine cruise legs (Table I). The inbound leg (from Yucatan Channel to Tuxpan) was used for data processing and analysis, and database mergers.

Oceanic observations were focused on CTD casts made four or more times daily for temperature, salinity, density and dissolved oxygen (DO) depth profiles. Daytime fluorescence and reflectance measurements were carried out at 31 sampling stations located along of six cruise legs covering great extension of the Caribbean Sea (Figure 2). Chlorophyll *a* concentration at the 31 sampling stations was estimated by simultaneous derived SeaWiFs information.

Reflectance Measurements

Reflectance was measured by the BDRF method (Swain and Davis, 1978). The BDRF can be defined as:

$$R(\theta_i, \phi_i, \theta_r, \phi_r) = \frac{r_{ti}(\theta_i, \phi_i)}{r_{ci}(\theta_r, \phi_r)} k(\theta_i, \phi_i, \theta_r, \phi_r) \tag{5}$$

where r_{ti} is the flux reflected by a target under specified conditions of irradiation and viewing, r_{ci} is the flux reflected by a perfectly diffuse, completely reflecting Lambertian surface which is used as a reference and k is the panel correction factor which depends on the angular configuration and accounts for the non-Lambertian spectral reflectance of the panel. To measure r_{ti} the Spectroradiometer GER-1500 was placed over the sunny side of the ship to avoid the direct shadow of the ship, which may introduce an error of up to 30% (Gordon, 1985). Values of r_{ci} were obtained by comparison with a Spectralon reference panel (Labsphere). The panel is resistant and hydrophobic, characteristics that render it suitable for field-based research (Schutt *et al.,* 1981; Weidner and Hsia, 1981). The sensor was positioned to provide a nadir view of the water surface, reducing thus the unwanted irradiance of the specularly reflected light, which is independent of the optical properties of the water (Shifrin, 1988). This configuration guaranteed that light backscattered from the sea and the elements present within it would be the major contributor of the signal. Reflectance spectra were obtained by first scanning the water surface and then sequentially measuring over the reference

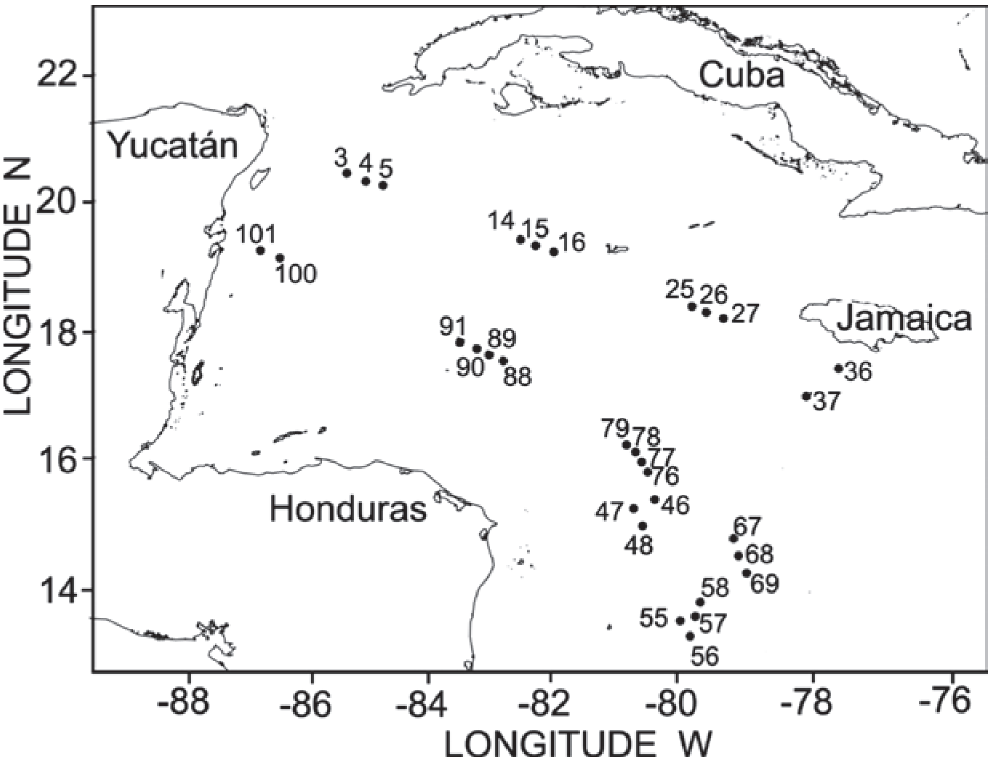

Figure 2. Location of 31 daytime sampling sites.

Table 1. Geographical positions of the nine transects sampled in the Caribbean Sea.

LEG	INITIAL POSITION	FINAL POSITION	ELAPSED TIME
I	21.0N; 86.7W	17.5N; 78.0W	0720 July 11 to 1210 July 14
II	17.5N, 78.0W	15.0N, 80.7W	1210 July 14 to 1730 July 15
III	15.0N, 80.7W	13.0N, 79.8W	1730 July 15 to 1525 July 16
IV	13.0N, 79.8W	15.0N, 79.5W	1525 July 16 to 0755 July 17
V	15.0N, 79.5W	13.0N, 79.08W	0755 July 17 to 0230 July 18
VI	13.0N, 79.1W	13.6N, 78.7W	0230 July 18 to 1210 July 18
VII	15.7N, 80.6W	19.2N, 86.4W	1420 July 19 to 1640 July 21
VIII	19.2N, 86.5W	21.2N, 81.1W	1640 July 21 to 0745 July 23
IX	21.2N, 81.1W	21.6N, 85.6W	0745 July 23 to 0800 July 24

panel. These observations were carried out while trying to keep the same viewing geometry by looking at nadir in both cases. However, since the calibration panel was onboard the target and reference observations were performed at different heights. Then, both scans were divided according to equation (5) and multiplied by a correction factor of k=0.99, following the manufacturer's instructions.

Spectroradiometric measurements were performed between 9:00 and 15:00 hrs for suitable solar conditions of illumination, that is, 45° around nadir view, as suggested by Jerlov, (1968).

Remote Sensing reflectance spectra were estimated through ad hoc formulas taken a Fresnel reflectance ρ = 0.028, which minimizes the effects of Sun glint and non-uniform sky radiance, avoids instrument shading problems and is reliable for wind speeds less than 5 m s^{-1} (Mobley, 1999). Additionally, according to SeaWiFS protocol (Mueller and Austin, 1995) and in order to remove residual surface reflectance due to wave facets, the spectra were corrected for sun/sky glint error by subtracting the reflectance measured at 750 nm from each spectrum.

Derivative Spectral Analysis

Atmospheric effects such as sky radiance, Rayleigh scattering, ozone absorption and Mie (or aerosol) scattering are unwanted signals in marine optics and in ocean colour studies (Sturm, 1981; Gordon, 1978). These effects must be considered in studies using remote sensing reflectance and have to be reduced if not eliminated. Atmospheric normalization algorithms can be used when analysing data for which there are no simultaneous atmospheric measurements. The derivative method is a kind of algorithm which makes insensitive to atmospheric effects some spectral features of the target. Generally, atmospheric normalization algorithms serve to parameterize the spectral shape (slope, curvature, etc) of the remote observations in an attempt to relate them to invariant spectra (Philpot, 1991). Grew (1981), developed a simple empirical algorithm for estimating oceanic chlorophyll from Multichannel Ocean Color Sensor (MOCS) data, the so-called "inflection ratio algorithm". This algorithm is a linear difference operator acting as a high pass filter. Thus, linear variations in λ are completely removed and high order variations are reduced to a constant. Hence, the filtering quality of derivatives together with is linear properties account for its sensitivity to chlorophyll and its capabilities for eliminating unrelated effects such as the atmospheric ones. In this study a fourth derivative filter was applied to reflectance spectra for locating and identifying ubiquitous peaks concealed in the spectral curves. Since differentiation tends to magnify effects of high-frequency noise in the spectra, a polynomial fit smoothing filter was applied over the data prior to calculation of the derivatives. Smoothed and derivative spectra were obtained with PeakFit program (AISN software, 1995). This program applies a convolution among the reflectance spectra and low and high -pass filters (smoothing and fourth derivative filters, respectively).

Particularly, the fourth derivative detects the presence of both maxima and minima peaks that correspond to reflectance and absorption regions, respectively, due to optical properties of seawater and elements contained within it. Interpretation of peaks was based on the physical and biological spectral properties of these constituents.

Seawifs Data

SeaWiFS data were utilised for associating reflectance and absorption peaks to chlorophyll *a* concentration. Daily images were not available due to cloud coverage in some of them, thus a set of existing of SeaWiFS imagery during the month was used for estimating the chlorophyll *a* concentration ([Chl-a]) at each sampling station. A monthly-averaged image, with a pixel of 1 km^2, was obtained. From this, [Chl-a] was estimated by using the empirical algorithm OC4 (O'Reilly *et al.*, 1998; O'Reilly *et al.,* 2000). In oligotrophic waters, the [Chl-a] and its co-varying derived products are considered to be the main contributors to the water reflectance. A simple relationship, with a sigmoid shape, links the log-transformed reflectance ratios or remote sensing reflectance (R_{rs}) to [Chl-a]. The OC4 algorithm uses a single set of coefficients applied to the blue-green ratio R_{BG} which is determined by the maximum band ratio approach.

Thus, for R equal to $\log_{10}(R_{BG})$:

$$OC4\_Chl_a = 10\left(0.366 - 3.067R + 1.93R^2 - 2.649R^3 - 1.532R^4\right) - 0.0414$$

SeaWiFS satellite data were processed with SeaDAS version 6.1. OC4 formulations and coefficients can be obtained from SeaDAS 6.1 documentation.

Results And Discussion

Meteorological conditions, measured on board during the cruise, were rather stable except for two days of adverse weather at mid July (Table II). Mean values of the parameters indicate the stability of weather conditions. Thus, wind vectors had a mean magnitude of 6.24(3.01) m s^{-1} at 138.42(64.04) degrees. Variability of the other meteorological parameters was less: Mean Relative humidity 80.48% (4.13); mean barometric pressure 1010.7 (1.59) mb; and air temperature 29.16 (0.85) (°C).

The spectral response of the Caribbean Sea is rather homogeneous. Most spectra profiles had a similar trend, with a relatively high reflectance between 0.04 and 0.06 at the blue end (400-500 nm), except for three cases showing higher values; an abrupt downward slope starting at around 500 nm due to water absorption, and lower values at the red end of the spectra (Figure 3). All spectra are modulated by the optical properties of oceanic water and, at a lesser extent, by phytoplankton, which is characteristic of oligotrophic conditions. These characteristics account for the typical blue coloration of Caribbean waters.

The derivative analysis provides a more accurate location of absorption and reflectance peaks. They slightly differ from analysis performed with conventional methods. The derivative method precisely locates and the actual inflexion points and, consequently, identifies absorption or reflection peaks. Thus, a fourth derivative filter was then applied to all spectra in order to detect hidden reflectance and absorption peaks. Each reflectance spectra showed similar reflectance and absorption peaks as maxima and minima values, respectively. Hence, instead of having the theoretical blue absorption peak of chlorophyll around 440 nm, with the derivative analysis this peak is found around 447 nm. A statistical analysis of all the peaks found through this method was performed for the reflectance curves of every sampling site. Consequently, a mean value of them was considered in the following derivative analysis (Table IV). When all reflectance spectra were normalised at 447.95 (mean value of the fourth derivative maxima), which corresponds to the absorption peak of chlorophyll *a* in the blue region, the differences and similarities among the spectra could be assessed (Figure 4). Major differences are apparent between 400 and 450 nm (blue), whilst similarities occur mainly in the 450 - 500 nm region (green). From 500 nm onwards all spectra have the same trend with slight variations between 650 and 700 nm.

However, it has been reported the presence also of cyanobacteria and green algae groups (Bidigare *et al.,* 1993). Mean absorption peaks at 597.12 and 659.02 nm are due to pure seawater. There is evidence that light absorption by pure water depends on its temperature, being apparent in absorption bands around 600 and 660 nm at 21°C (Pegau and Zaneveld, 1993). It has been found that the absorption maximum shifts towards lower wavelengths at increasing temperature (Hakvoort, 1994). This may account for the slight difference found between the two sets of data, since the sea surface temperature of Caribbean waters was around 29°C during the sampling.

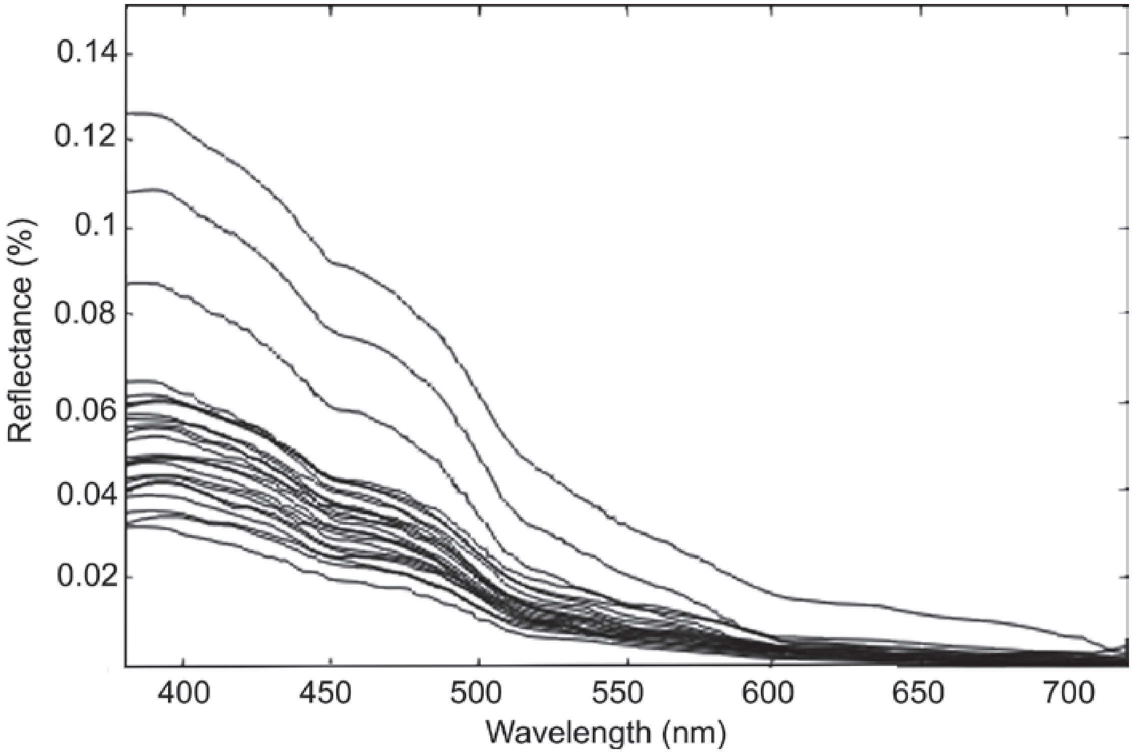

Figure 3. Reflectance profiles of 31 daytime sampling stations.

Table 2. Meteorological and biological parameters measured on board the RV Justo Sierra. S. P. (Sampling point); L (Cruise leg); Lat, (Latitude: °N); Lon, (Longitude: °W); W(d), Wind direction (°); W(r), Wind speed, (m s^{-1}); R. H., relative humidity (%); A.T., Air Temperature, (°C); B. P., barometric pressure, (mb); Chlorophyll concentration [Chl-a] (mg m^{-3}); time of reflectance measurements (*hh:min*); date (*ddmmyy*).

S.P	Leg	Lat	Lon	W(d)	W(r)	R.H.	A.T	B.P	[Chl a]	Time	Date
003	I	20:21	85.37	199	6.32	76	28.5	1012	0.072	08:58	110701
004	I	20.16	85.22	134	4.42	72	29.4	1012	0.060	12:45	110701
005	I	20.10	85.07	125	3.7	72	29.4	1011	0.077	14.20	110701
014	I	19.29	83.10	155	8.33	76	29.0	1013	0.098	08:15	120701
015	I	19.22	82.53	155	5.40	78	29.2	1014	0.094	10.52	120701
016	I	19.17	82.38	147	3.44	77	29.3	1013	0.082	13.10	120701
025	I	18.27	80.26	339	10.84	82	28.5	1013	0.101	09:15	130701
026	I	18.21	80.11	157	6.48	82	28.9	1013	0.108	13:25	130701
027	I	18.16	79.56	101	2.98	81	28.7	1012	0.105	13:25	130701
036	II	17.19	78.11	120	7.25	79	28.4	1010	0.158	09:20	140701
037	II	16.44	78.36	083	5.25	78	28.3	1009	0.101	13.30	140701
046	II	15.07	80.24	157	6.68	84	28.1	1009	0.116	09:15	150701
047	II	15.00	80.40	062	6.94	84	28.1	1009	0.112	12:40	150701
048	III	14.44	80.37	117	6.17	84	28.2	1008	XXX	15:00	150701
055	III	13.06	79.57	195	3.91	87	28.3	1010	0.116	08:16	160701
056	III	13.00	79.49	130	6.01	87	28.3	1010	0.120	10:00	160701
057	IV	13.15	79.47	333	7.30	87	28.3	1010	0.105	12:10	160701
058	IV	13.29	79.44	125	6.06	87	28.4	1009	0.153	14:30	160701
067	V	14.15	79.20	154	12.39	84	28.8	1010	XXX	10:00	170701
068	V	14.01	79.17	159	11.51	84	28.9	1009	XXX	11:50	170701
069	V	13.46	79.14	103	11.41	82	29.3	1008	XXX	14.17	170701
076	VI	15.44	80.38	139	12.13	79	29.5	1010	0.109	09:40	190701
077	VI	16.00	80.41	106	8.02	81	29.6	1011	0.116	11:15	190701
078	VI	16.15	80.49	125	8.02	82	29.8	1010	0.105	13:30	190701
079	VI	16.22	80.53	093	5.96	81	30.0	1010	0.156	14:30	190701
088	VI	17.35	83.23	015	4.21	80	29.9	1012	0.105	09:30	200701
089	VI	17.41	83.37	083	2.98	81	29.9	1012	0.116	10:57	200701
090	VI	17.47	83.52	107	2.36	79	30.2	1012	0.105	13:34	200701
091	VI	17.54	84.06	117	2.42	77	31.0	1010	0.138	15:39	200701
100	VI	19.02	86.08	128	2.57	75	31.1	1010	0.108	08:30	210701
101	VI	19.09	86.20	128	2.11	77	30.6	1010	0.098	09:55	210701

Table 3. Descriptive statistics (μ, mean: σ: standard deviation; min: minimum value; max: maximum value; V.C. Variation Coefficient; S.E. Standard error; P.S.E.: Percentual Standard error. W(d), Wind direction (°); W(r), Wind speed, (m s^{-1}); R. H., relative humidity (%); A.T., Air Temperature, (°C); B. P., barometric pressure, (mb); [Chl-a] Chlorophyll concentration (mg m^{-3})

	W(D)	**W(r)**	**R.H.**	**A.T**	**B.P**	**[Chl a]**
μ	138.42	6.24	80.48	29.16	1010.7	0.1087
σ	64.04	3.01	4.13	0.85	1.59	0.023
min	15	2.11	72	28.1	1008	0.06
max	339	12.39	87	31.1	1014	0.158
V.C. (%)	46.26	48.23	5.13	2.91	0.16	21.16
S.E.	11.50	0.54	0.74	0.15	0.29	0.0045
P.S.E. (%)	8.30	8.66	0.92	0.52	0.02	4.07

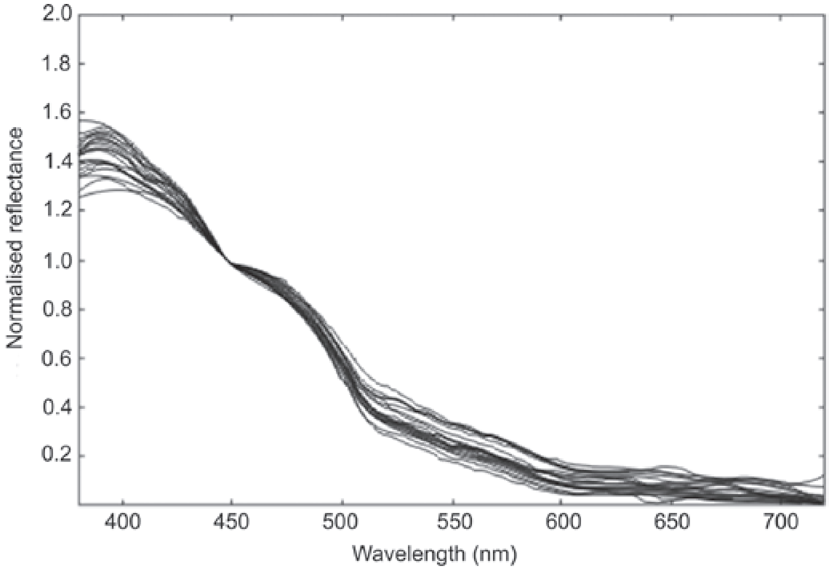

Figure 4. Reflectance spectra normalized at 447.98 nm, corresponding to the region of maximum chlorophyll *a* absorption.

A typical reflectance spectrum with its correspondent derivative peaks is shown in Figure 5. Peaks found through the derivative method can be associated with the optical properties of seawater. Mean reflectance peaks at 415.04 and 480.31 nm stands for the dominant colour of the water, which was mostly bluish over the entire zone. The peak at 685.82 nm is mainly due to the sum of irradiances produced through natural fluorescence emission by chlorophyll *a* and elastic scattering (Kirk, 2011). The mean reflectance peak at 546.92 nm has a physical explanation rather than a biological one because this peak marks the starting point of the strong water absorption, which reaches a maximum around 600 nm (Buiteveld *et al,* 1994).

On the other hand, absorption peaks found by the derivative process can be essentially related to optical properties of pigments and seawater (Prézelin and Bóczar, 1986; Aguirre et al, 2001). Thus, the peak at 447.95 nm is due to chlorophyll *a* absorption in the blue region. A carotenoid absorption peak at 513.01 nm can presumably be attributed to fucoxanthin-like pigments of brown algae, which are among the dominant groups in the zone (Taylor, 1959; Müller-Karger et al, 1989; Bidigare *et al*, 1993).

Satellite-estimated [Chl-a] at each sampling station is shown in Table II and had a mean value of 0.109 (0.023) mg m^{-3} (Table III). Values obtained are typical of oligotrophic waters, mainly at the northern sampling stations (3,

Table 4. Reflection (R_i) and Absorption (A_i) peaks found through derivative analysis.

S.P.	**R1**	**R2**	**R3**	**R4**	**R5**	**A1**	**A2**	**A3**	**A4**
003	414.92	479.01	544.94	637.62	696.50	446.06	512.01	605.35	666.41
004	418.18	480.66	544.94	624.75	680.70	449.35	513.66	595.60	652.05
005	414.92	482.31	546.58	636.02	698.08	447.7	512.01	602.11	668.30
014	411.65	479.01	546.58	631.19	688.61	447.7	512.01	600.48	660.03
015	416.55	480.66	544.94	627.97	680.70	449.30	512.01	597.23	653.65
016	419.82	480.66	544.94	621.52	675.94	449.35	512.01	592.36	647.25
025	411.65	480.66	546.58	634.41	691.77	446.06	512.01	598.86	664.81
026	413.29	479.01	544.94	627.97	683.86	446.06	512.01	595.61	653.65
027	418.80	480.66	544.94	626.36	675.94	447.70	513.66	595.60	652.05
036	406.77	480.66	546.58	634.41	691.70	447.7	512.01	592.36	659.59
037	419.82	474.06	543.29	640.83	679.11	442.77	512.01	559.70	663.22
046	414.92	479.01	548.22	632.80	690.19	447.70	513.66	598.86	663.22
047	418.18	480.66	544.94	634.40	680.70	447.70	513.66	606.97	660.03
048	411.65	480.66	548.22	632.80	694.92	447.70	513.66	600.48	661.63
055	414.92	480.66	558.06	631.19	691.77	449.35	515.31	600.48	660.03
056	413.29	482.31	546.58	627.97	671.18	447.70	512.01	597.23	652.05
057	419.82	480.66	541.65	645.64	691.79	449.35	512.01	558.06	647.25
058	413.29	480.66	546.58	627.58	675.94	447.70	512.01	595.61	652.05
067	411.65	480.66	548.22	632.80	691.77	449.35	513.66	603.73	663.22
068	408.40	482.31	559.70	642.44	696.50	452.64	515.31	597.23	672.77
069	414.92	480.66	546.58	629.58	680.70	447.70	513.66	600.48	656.84
076	414.92	480.66	551.30	632.80	688.81	447.70	513.66	600.48	663.22
077	414.92	482.31	546.58	619.91	672.77	449.35	515.31	592.36	645.64
078	416.55	480.66	544.94	629.58	682.28	447.70	513.66	602.11	655.24
079	410.02	480.66	546.58	623.14	671.18	449.35	513.66	597.23	645.64
089	418.18	480.66	544.94	627.97	682.28	447.70	512.01	600.48	655.24
100	414.92	479.01	544.94	632.80	693.35	449.35	512.01	602.11	661.63
101	413.29	479.01	546.48	632.80	694.92	447.70	512.01	600.48	664.81
102	418.18	480.66	544.94	626.36	675.94	447.70	513.66	600.48	652.05
103	421.45	479.01	548.22	644.04	694.92	447.70	513.66	600.48	671.18
112	414.92	479.01	546.58	631.19	685.45	447.70	513.66	600.48	660.03
113	418.18	480.66	546.58	639.23	694.92	446.06	513.66	611.83	669.59
114	413.29	482.31	546.58	632.80	687.03	447.70	512.01	602.11	663.22
m	415.04	480.31	546.92	631.90	685.82	447.95	513.01	597.12	659.02
s	03.43	1.54	3.51	6.09	8.19	1.60	1.09	10.67	7.59

4, 5, 14 and 15), the remaining sites showed a slight increment of [Chl-a] between 0.101 – 0.158 mg m^{-3} but still in the oligotrophic interval, according to the CZCS-NASA climatological monthly maps (Feldman *et al.*, 1989) as seen in Table II and Figure 2. Regions with the highest [Chl-a] values were found close to Jamaica island (sites 25, 26, 27, 36) and near Honduras (sites 58, 79 and 91).

Moreover, applying OC4 algorithm to SeaDAS data tends to over-estimates the chlorophyll concentrations in relatively chlorophyll-poor waters, where the relative part of the suspended matter and the CDOM in the optical properties of water is high. For such waters, benefit in accuracy by using one algorithm or the other seems negligible compared with the biases and the noises. However, we have chosen the OC4 band ratio as it is recommended in the literature for a larger variety of waters, including chlorophyll rich waters.

Conclusions

Reflectance characteristics of the Caribbean Sea were analysed with a high spectral resolution radiometer. Reflectance spectra show a typical coloration of tropical waters with maxima at the blue region of the electromagnetic spectrum. This response is mainly due to the oligotrophic characteristics of the zone, with a deep chlorophyll maximum at around 107 m. The presence of chlorophyll *a* can be established by two ways: a) via fluorescence, by observing the spectral behaviour which has an absorption peak at 447.9 nm (blue absorption) and a reflectance peak at 685.82 nm (fluorescence emission); b) via satellite derived information. Satellite information confirms both the homogenous distribution of [Chl-a] and the oligotrophic condition of the Caribbean Sea. Reflectance profiles are markedly influenced by seawater spectral properties from 600 nm onwards. Hence, even though the Caribbean Sea is oligotrophic, the derivative analysis detects the presence of algae in an amount sufficient to generate a relatively strong signal within reflectance spectra and satellite imagery. Additionally, it can be concluded that most Caribbean Sea waters show similar optical characteristics in open ocean, being higher close to Jamaica and Honduras. This paper contributes to a better understanding of the optical characteristics of the Caribbean Sea.

Acknowledgements

I thank the following: Dr. A. Gallegos for his kind invitation to participate in the ECAC-3 cruise; Dr. V. Magaña, coordinator of the project and the IAI for funding these campaigns; to Dr. Olivia Salmerón and Tania Fernández for support during the cruise; the technicians of the Institute of Geography for drawings; and the crew of RV Justo Sierra.

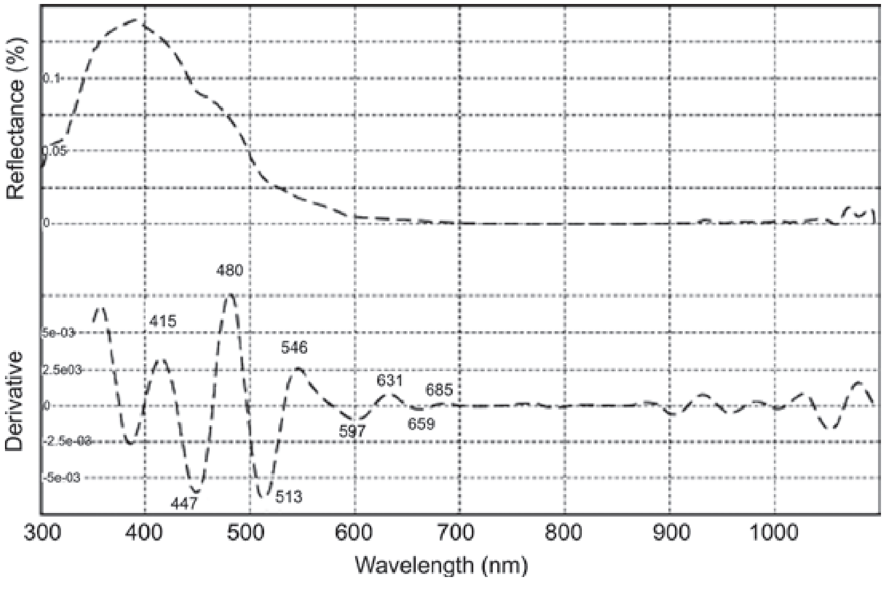

Figure 5. Typical reflectance profile with its derivative spectrum showing main reflectance and absorption peaks.

References

Aguirre-Gómez R., 2001, Caracterización óptica de la laguna costera de Coyuca de Benítez. *Investigaciones Geográficas*, 46, 78-97.

Aguirre-Gómez R., Weeks A.R., Boxall S.R., 2001, Detecting photosynthetic algal pigments in natural populations using a high-spectral resolution spectroradiometer. *Int. J. Remote Sens*., 22, 15, 2867-2884.

Bidigare R.R., Morrow J.H., Kiefer D.A., 1989, Derivative analysis of spectral absorption by photosynthetic pigments in the western Sargasso Sea. *J. Mar. Res.*, 47, 323-341.

Bidigare R.R., Ondrusek M.E., Brooks J.M., 1993, Influence of the Orinoco River outflow on distribution of algal pigments in the Caribbean Sea. *J. Geophys. Res*., 98, C2, 2259-2269.

Buiteveld H., Hakvoort J.H.M., Donze M., 1994, The optical properties of pure water. SP1E, 2258 Ocean Optics XlI: 174-183.

Butler W.L., Hopkins D.W., 1970, Higher derivative analysis of complex absorption spectra. *Photochem. Photobiol.*, 12, 439-450.

Chen Z., Curran P.J., Hansom J.D., 1992, Derivative reflectance spectroscopy to estimate suspended sediment concentration. *Remote Sens. Environ*., 40, 67-77.

Clark G.L., Ewing G.C., 1974, Remote spectroscopy of the sea for biological production studies. En N. G. Jerlov & E. S. Nielsen (eds.), Optical Aspects of Oceanography, London: Academic Press, pp. 389-413.

Dekker A.G., Malthus T.H., Seyhan E., 1991, Quantitative modeling of inland water quality for high-resolution MSS systems. *IEEE Trans. Geosci and Remote Sensing.*, 29, 89-95.

Etter P.C., Lamb P.J., Portis D.H., 1987, Heat and freshwater budgets of the Caribbean Sea with revised estimates for the Central American Seas, *J. Phys. Oceanogr.*, 17, 1232-1248.

Evangelista V., Frassanito A.M., Passarelli V., Barsanti L., Gualtieri P., 2006, Microspectroscopy of the Photosynthetic Compartment of Algae. *Photochem. Photobiol.*, 82, 4, 1039-1046.

Farmer C.T., Moore C.A., Zika R.G., Sikorski R.J., 1993, Effects of low and high Orinoco river flow on the underwater light field of the eastern Caribbean basin. *J. Geophys. Res*., 98, C2, 2279-2288.

Feldman G.C., Kuring N., Ng C., Esaias W., McClain C.R., Elrod Maynard N., Endres D., Evans R., Brown J., Walsh S., Carle M., Podesta G., 1989. Ocean color: availability of the global data set. EOS Trans. *Am. Geophys. Union,* 70, 634-641.

Gordon, A.L., 1967, Circulation of the Caribbean Sea, *J. Geophys. Res*., 72, 24, 6207-6223.

Gordon H.R., 1978, Removal of atmospheric effects from satellite imagery of the oceans. *Appl. Optics*, 17, 1631-1636.

Gordon H.R., 1985, Ship perturbation of radiance measurements at sea. 1: Monte Carlo simulations. *Appl. Optics*, 24, 4172-4182.

Goodin D.G., Han L., Fraser R.N., Rundquist D.C., Stebbins W.A., 1993, Analysis of suspended solids in water using remotely sensed high resolution derivative spectra. *Photogramm. Eng. Rem. S.*, 59, 505-510.

Gordon H.R, Morel A., 1983, Remote assessment of ocean color for interpretation of satellite visible imagery, a review. *Lectures. Notes on Coastal and Estuarine. Studies,* 4, Springer-Verlag New York.

Gordon H.R., Brown O.B., Evans R.H., Brown J.W, Smith R.C, Smith K.S., Baker K.S, Clark D.K., 1988, A semianalytical radiance model of ocean color. *J. Geophysical Res*. Vol., 93, 10 909-10924.

Grew G., 1981, Real-time test of MOCS algorithm during Superflux 1980, NASA Washington DC, CP-2188, 301-322.

Hakvoort J.H.M., 1994, *Absorption of light by surface water*. (Delft: Delft University Press).

Han L., 2005, Estimating chlorophyll-*a* concentration using first-derivative spectra in coastal water. *Int. J. Remote Sens*. Vol., 26, 23, 5235-5244.

Hirata T., Højerslev N.K., 2008, Relationship between the irradiance reflectance and inherent optical properties of seawater. *J. Geophys. Res*., 113, C03030.

Hunter P.D., Tyler A.N., Présing M., Kovács A.W., Preston T., 2008, Spectral discrimination of phytoplankton colour groups: The effect of suspended particulate matter and sensor spectral resolution. *Remote Sens. Environ*., 112, 4, 1527-1544.

Jerlov N.G., 1968, Optical oceanography: New York, American Elsevier Publishing Co., 194 pp.

Jia Y., Pengwu T., Hongyi Y., 2008, Peak Identification of Communication Signal Using Wavelet Packet Transform, *Wireless Communications, Networking and Mobile Computing, WiCOM '08. 4th International Conference on*, 1-4, doi: 10.1109/ WiCom.2008.449.

Kinder T.H., Heburn G.W., Green A.W., 1985, Some aspects of the Caribbean circulation, *Mar. Geol*., 68, 25-52.

Kirk J.T.O., 2011, *Light and photosynthesis in aquatic Ecosystems* (Cambridge: Cambridge University Press), Third Edition.

Kirk J.T.O., 1984, Dependence of relationship between inherent and apparent optical properties of water on solar altitude. *Limnol. Oceanogr*., 29, 350-356

Milton E.J., 1987, Principles of field spectroscopy. *Int. J. Remote Sens*., 8, 1807-1827.

Morel A., 1978, Available, usable and stored radiant energy in relation to marine photosynthesis. *Deep-Sea Res*., 25, 673-688.

Morel A., Prieur L., 1977, Analysis of variations in ocean color. *Limnol. Oceanogr*., 22, 709-722.

Morel A., Voss K.J., Gentili B., 1995, Bidirectional reflectance of oceanic waters: A comparison of modeled and measured upward radiance fields. *J. Geophys. Res*., 100, C7, 13143-13150.

Mueller J.L., Austin R.W., 1995, Ocean optics protocols for SeaWiFS validation, revision 1, SeaWiFS Technical Report Series, Vol. 25, NASA Tech. Memo. 104566, S. B. Hooker, E. R. Firestone, and J. G. Acker, eds. ~National Technical Information Service, Springfield, Va.

Müller-Karger F.E., McClain C.R., Fisher T.R., Esaias W.E., Varela R., 1989, Pigment distribution in the Caribbean Sea: Observations from Space. *Prog. Oceanogr*., 23, 23-64.

O'Reilly J.E., Maritorena S., Mitchell B.G., Siegel D.A., Carder K.L., Garver S.A., Kahru S.A., McClain C., 1998, Ocean color chlorophyll algorithms for SeaWiFS. *Journal of Geophysical Research*, 103, 24 937–24 953

O'Reilly J.E., Maritorena S., Siegel D., O'Brien M., Toole D.T., Mitchell B.G., Kahru M., Chavez F.P., Strutton P., Cota G.F., Hooker S.B., McClain C.R., Carder K.L., Muller-Karger F.E., Harding L., Magnuson A., Phinney D., Moore G.F., Aiken J., Arrigo K.R., Letelier R.M., Culver M.E., 2000, Ocean Color Chlorophyll a algorithms for SeaWiFS, OC2 and OC4: Version 4. SeaWiFS Postlaunch Calibration and Validation Analyses, Part 3. NASA/TM 206892, 11, 9-23.

Pegau W.S., Zaneveld J.R.V., 1993, Temperature-dependent absorption of water in the red and near infrared portion of the spectrum. *Limnol. Oceanogr*, 38, 188-192.

Philpot W.D., 1991, The derivative ratio algorithm: avoiding atmospheric effects in remote sensing. IEEE Transactions on Geoscience and Remote Sensing, 29, 3.

Prézelin B.B., Bóczar B.A., 1986, Molecular bases of cell absorption and fluorescence in phytoplankton: potential applications to studies in optical oceanography. In Round, F. E., and Chapman, D. J. (eds). Progress in *Phycological Research*, 4. Biopress Ltd., Bristol, pp: 349-464.

Sathyendranath S., Morel A., 1983, Light emerging from the sea-interpretation and uses in remote sensing. En A. P. Cracknell (Ed.) *Remote Sensing Applications in Marine Science and Technology*, Chapter 16, D. Reidel, Dordrecht).

Schutt J.B., Holben B.N., Shai L.M., Henninger J.H., 1981, Reflectivity of TFE –a washable surface- compared with that of $BaSO_4$. *Appl. Optics*, 20, 2033-2035.

Shiffrin K.S., 1988, *Physical Optics of Ocean Water* (New York: American Institute of Physics).

Sturm B., 1981, The atmospheric correction of remotely sensed data and the qualitative determination of suspended matter in marine water surface layer. In Cracknell, A. P. (ed). Remote Sensing in meteorology, oceanography and hydrology, Ellis Horwood Ltd., 163-197.

Swain P.H., Davis, S.M., 1978, *Remote Sensing: The Quantitative Approach.* New York: McGraw-Hill.

Taylor W.R., 1959, *Distribution in depth of Marine algae in the Caribbean and adjacent seas*. En Proceedings of the 9th International Botanical Congress. Canada: University of Toronto Press. Pp: 193-197.

Weidner D.L., Hsia J.J., 1981, Reflection properties of pressed polytetrafluorethylene powder. *J. Opt. Soc. Am*., 71, 856-861.

Wilson W.H. Kiefer D.A, 1979, Reflectance spectroscopy of marine phytoplankton. Part 2. A simple model of ocean color. *Limnol. Oceanogr*., 24, 4, 673-682.

Geofísica Internacional (2014) 53-4: 399-409

Original paper

Enhancing Geophysical Signals Through the Use of Savitzky-Golay filtering method

Khadija Baba*, Lahcen Bahi and Latifa Ouadif

Received: March 08, 2013; accepted: December 03, 2013; published on line: October 01, 2014

Resumen

En la cuenca de Sidi Chennane en Marruecos, existen inclusiones estériles de caliche que dificultan la extracción de las rocas fosfatadas y que son difíciles de detectar. La resistividad de los caliches excede un valor de 200 Ω-m contra 150 Ω-m para la roca fosfatada. Se realizó un trabajo de prospección eléctrica de tipo Schlumberger en una zona de 50 ha en la cuenca de fosfatos de Oulad Abdoun. Se obtuvieron modelos del perfil geológico mediante el filtro de Savitzky–Golay, y se logró localizar las inclusiones de caliche y las estimaciones de cálculo de las reservas de los fosfatos se encuentran muy circunscritas.

Palabras clave: Marruecos fosfatos, prospección geofísica, Schlumberger, eliminación de ruido, Savitzky-Golay.

Abstract

In the Sidi Chennane basin exploitation inclusions of sterile hardpan—so-called “derangements” — are hard to detect and interfere with phosphate extraction. A Schlumberger resistivity survey over an area of 50 hectares was carried out. The Savitzky-Golay filtering method was used as a tool for denoising the data.

Savitzky-Golay (S-G) filters are one of the filters which can smoothen out the signal without much destroying its original properties. Despite their exceptional features, they were rarely used so far in the geophysical signal processing. The aim of this paper is the investigation of their properties in detail from the geoelectrical signal processing aspect. The experimental results indicate that S-G filter is better for denoising geoelectrical signal. Models of the geology were successfully obtained from Savitzky-Golay filtering method, which help mapping the phosphate deposit inclusions and the estimations of phosphate reserves were improved and better constrained.

Keywords: Moroccan phosphate, geoelectric prospecting, electric Resistivity, Schlumberger, denoising, Savitzky-Golay.

Khadija Baba*
Lahcen Bahi
Latifa Ouadif
3GIE Laboratory
Mohammadia engineering School
Mohammed V- Agdal University
Rabat, Morocco
Corresponding author: baba.khadija@gmail.com

Introduction

Morocco is the world's third largest phosphate producer, after the USA and China. Total mine production recorded by the Ministry of Energy and Mines in 2003 was 29.39 Mt so more than 75% of world reserves. Four major phosphate basins are now known and are being exploited, three of which are located in central-northern Morocco. The four main deposits of phosphate are: the Oued Eddahab basin situated in Sahara, the central ganntour basin near Youssoufia, the Meskala basin at east of Essaouira and the Oulad Abdoun basin situated near Khouribga. The existence of morocco sedimentary phosphate rock has been known since 1908 in the Meskala basin, but it had not generated significant interest until the discovery, in 1917, of the Oulad Abdoun basin.

The geological investigations carried out in Sidi Chennane phosphatic deposit in the Oulad Abdoun basin revealed a phenomenon of sterile hardpan, these sterile bodies are formed by accumulations of silicified limestones or by limestone blocks within an argillaceous matrix (Michard, 2008) which interfere with phosphate extraction and their resistivity is higher than the phosphate-rich mineral resistivity. The application of the electric prospection methods constitutes a suitable means to map these sterile bodies in order to establish a model of their distribution and would permit the definition of these structures before the mining front reaches them.

Geological framework and methodology of work

The Ouled Abdoun basin is the largest phosphate basin in Morocco. It's located about 100 km in south-east of Casablanca. The phosphate deposits of Ouled Abdoun area belongs to the western Moroccan Meseta, commonly considered being stable. The local sedimentary deposits resulting from a large transgression occurred in mid-Cretaceous. It consists of (Kchikach; 2002) : marly limestone and gypsum of Cenomanian, Turonian white limestones, Senonian marl and yellow marly limestones, phosphatic series dated from Maastrichtian to Ypresian and Lutetian calcareous Thersitean slab. The Neogene continental deposits cover locally the marine series.

The loose phosphatic Levels exploited are cited according to their succession (Kchikach; 2002) Layer III: Maastrichtian, Layer II: Paleocene, Layers I and 0, "forrow" A and B: Ypresian. They are typically separated by phosphatic indurated limestone benches, more or less important and more or less regular called "infill", II / I layers infill, III / II layers infill, etc.

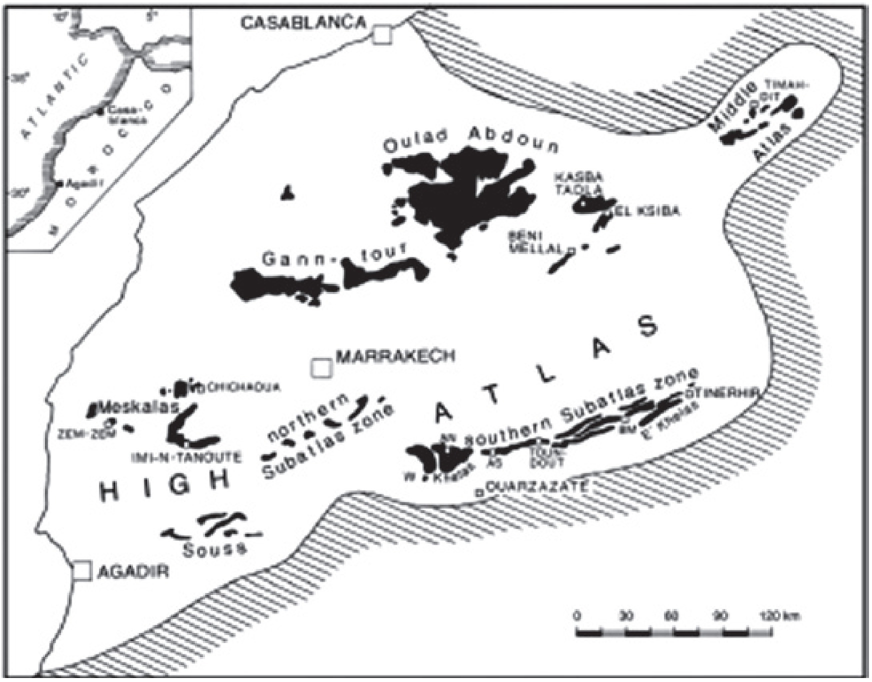

Figure 1. The central Moroccan phosphate basins (Ganntour, Oulad Abdoun and Meskala)

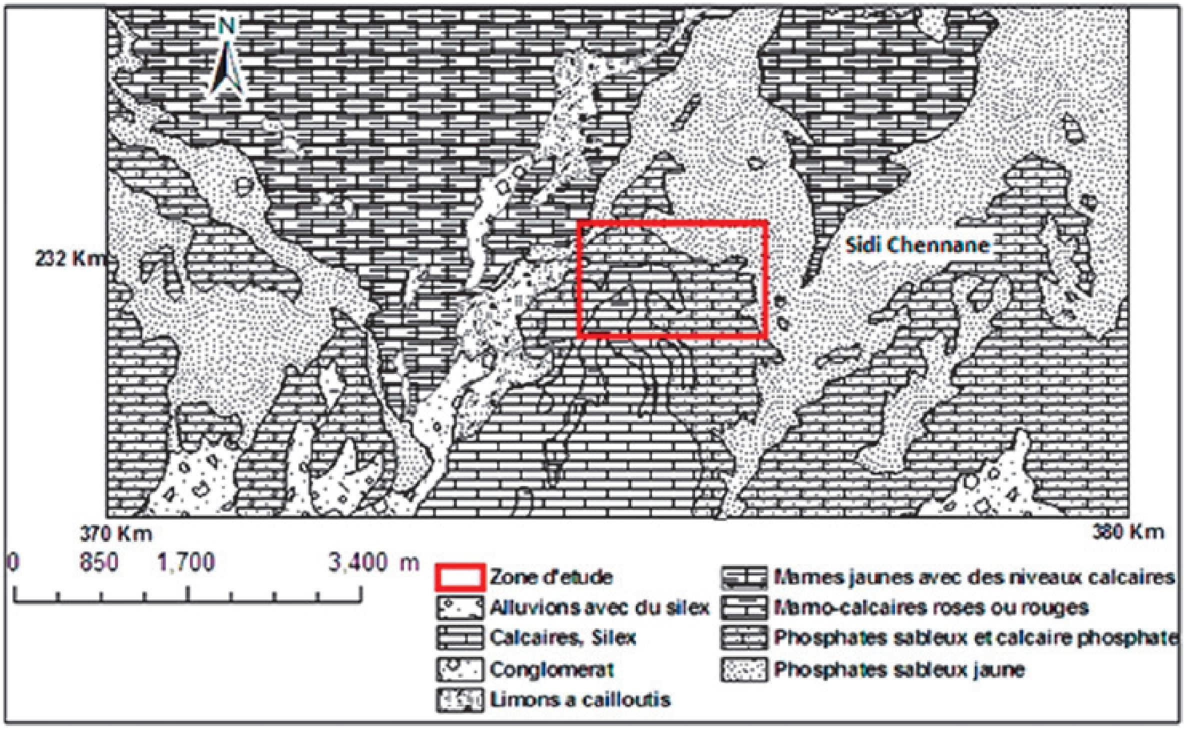

Figure 2. Localization map of the study area.

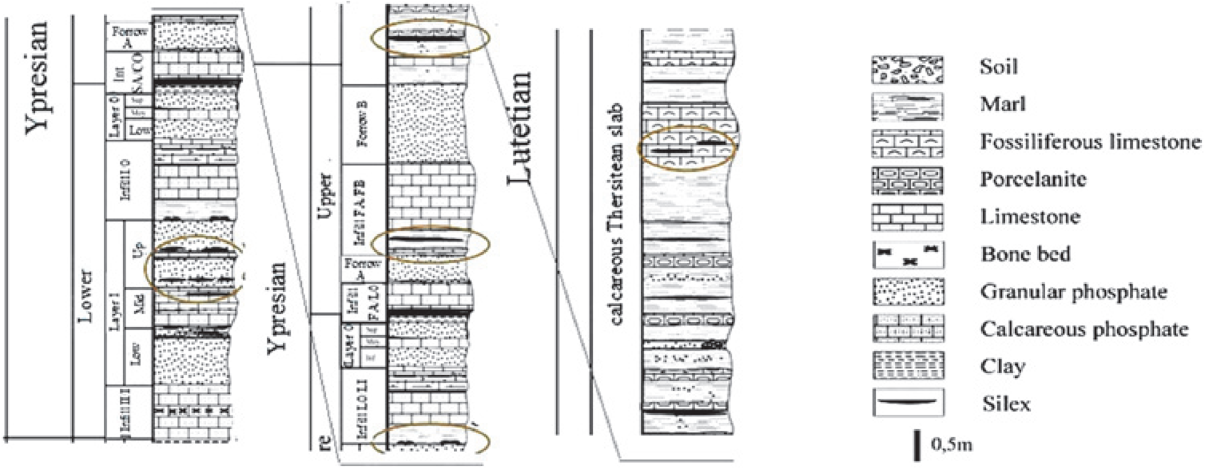

Figure 3. Stratigraphical log of the phosphatic series of Sidi Chennane

Data acquisition

Electrical sounding is a method to investigate the change in earth resistivity with depth at a particular location. Horizontal electrical profiling is a method to determine lateral variations in earth resistivity within a limited depth range. Traditionally, arrangements using four electrodes (two current-transmitting electrodes and two voltage-sensing electrodes) are used for either vertical soundings or horizontal profiling. For vertical soundings, the electrodes are arranged symmetrically according to a center, with increasing distances between electrodes used to explore deeper depths. In the profiling mode, the distance between the potential and current dipoles (a dipole consists of a pair of like electrodes) is maintained while the array is moved along the profile line for mapping lateral changes (Chouteau, 2001; Ouadif, 2011).

When using profiling techniques, an estimate of the earth resistivity is calculated by using the well-known relation between resistivity, an electric field, current density (called Ohm's Law), the geometry and spacing of the current and potential electrodes. When the earth is not homogeneous neither isotropic, this estimated value is called the apparent resistivity, ρ_{upp}, which is an average of the true resistivity in the measured section of the earth:

$$\rho_{upp} = K\frac{\Delta V}{1}$$

Where K is the geometrical factor that depends on the electrodes arrangement.

To cover all the zones being able to be disturbed, we carried out, during the geophysical prospection in a parcel of 50 ha, 41 vertical electrical soundings then 5151 resistivity measurements as horizontal profiling (SYSCAL-R2 resistivity instrument IRIS Instruments) using the well-known Schlumberger array, in order to map the spatial distribution of the sterile hardpan inclusions. The 5151 stations of the resistivity survey is a compilation of 51 profiles spaced at 20 m. For every profile, there were 101 stations separated by 5 m.

The VES (some of them have been done in old trenches of exploitation where these bodies are visible) helped us: (1) to determine the intrinsic resistivity for the different terms of the phosphatic series (Baba, 2012), indeed, the apparent resistivity values above the sterile bodies are between 200 and 250 Ωm and the observed values on normal phosphatic series are around 150 Ωm, (2) to select the appropriate length of the measurement device for the profiling survey. Anomalies are in the upper part of the phosphate layer 25 meters to 60 meters of depth, leading us to choose 120 m for the maximum device length of the resistivity profiling survey.

Data Analysis

To map resistivity contrasts, field data, apparent resistivity measurements obtained from horizontal profiling with 40m, 80m and 120m device length, are plotted on a map of the surveyed area, using Surfer desktop software. Kriging interpolation was used in order to create maps of the corresponding geophysical data.

Iso-resistivity map was prepared and interpreted in terms of resistivity and thickness of sub-surface layer and resistivity results were correlated with the existing lithology:

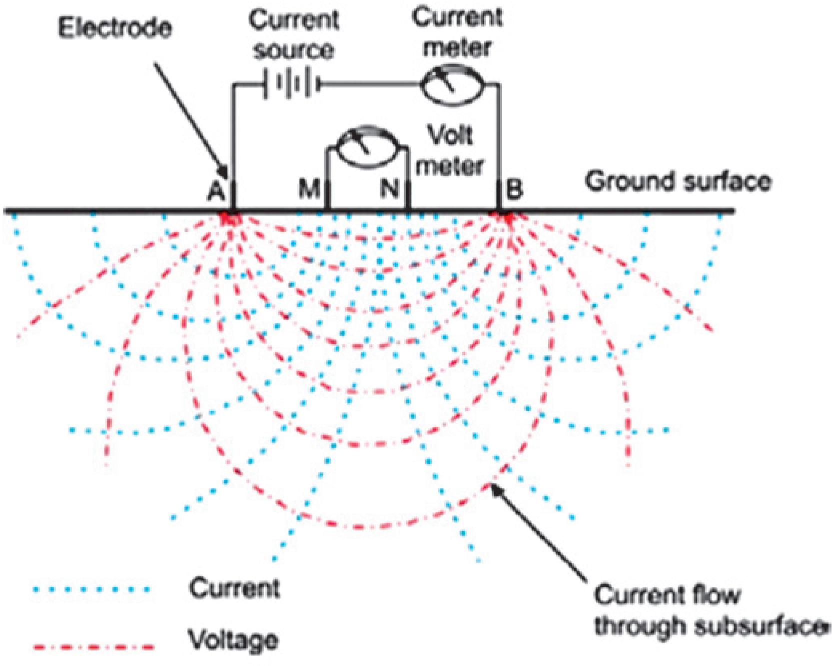

Figure 4. The basic principles of Schlumberger device

- The kriged maps of electrical resistivity distribution AB=40 denote a higher mean resistivity distribution representing the calcareous Thersitean slab effect.

- The kriged maps of electrical resistivity distribution AB=80 and AB=120 show anomalous zones of directions NE-SW located at an average depth of 60m. Thus, the majority of anomalies affect only the subsurface of the phosphate series.

Denoising geoelectrical data

Noise is often a significant issue in electrical resistivity data, field data rarely comes clean, thus robust processing methods is required, in order to remove non-geological noise and extract useful information from raw data.

As a result of the above processes, the maps resulting by the interpolation of the geophysical measurements often has poor quality, containing high percentages of random or systematic noise which hinder the valuable information related to the subsurface targets which are here essentially the inclusions. Therefore, the suppression of the noise levels and the enhancement of the signals carrying the useful information is an important process in any processing approach.

Savitzky-Golay

Savitzky and Golay (1964), interested in smoothing of noisy data obtained from chemical spectrum analyzers, demonstrated that fitting a polynomial to a set of input samples and then evaluating the resulting polynomial at a single point within the approximation interval is equivalent to discrete convolution with a fixed impulse response (Savitzky, 1964).

The least squares digital polynomial smoothing filters, popularized by Savitzky-Golay are widely used for smoothing and differentiation signal processing in many fields namely in Biomedical signals usually known as non-stationary such as electroencephalogram (EEG) and electrocardiogram (ECG) (Azami 2012), in elastography and magnetocardiogram and mainly in absorption spectroscopy (Hargittai 2005). ECG signal can potentially corrupted by various types of noise which lead to incorrect the diagnosis. Many types of filters are available to smoothing the noisy ECG signal Golay is one of the filter which can smoothen out the signal without destroying its original properties[(Hassanpour 2007; Orfanidis 2010; Schafer 2011; Hassanpour *et al*. 2012).

The filters are constructed to fit a particular polynomial to a windowed portion of the signal, with the least squares method, and then replace the central point of the window with the value of the polynomial at that point to produce a smoothed output. The Saviztky-Golay filtering can be considered as a generalized moving average.

The polynomial can be represented as:

$$\rho(x_i) = c_0 + c_1 x + \ldots + c_p x^p$$

Where ρ is the corresponding apparent resistivity data vector, x_i represent the north coordinate of a gidded point of the resistivity map.

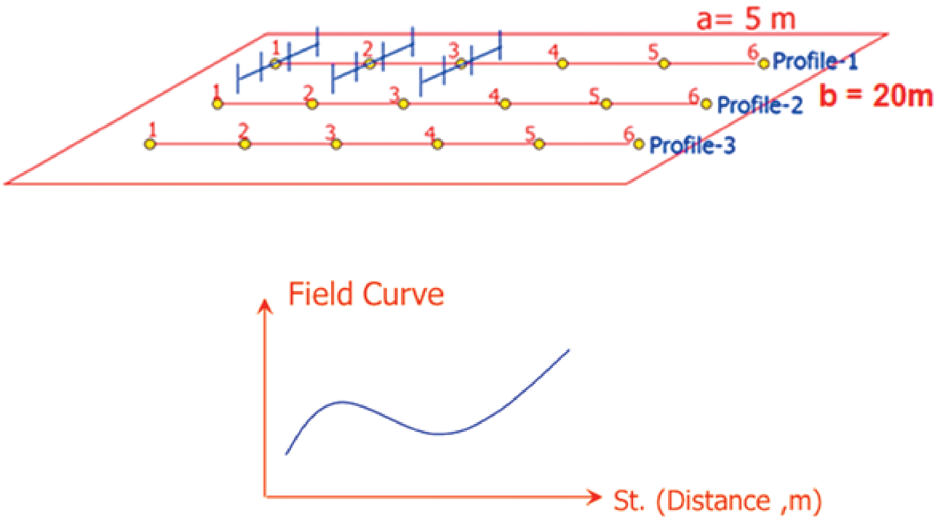

Figure 5. Profiling by schlumberger array

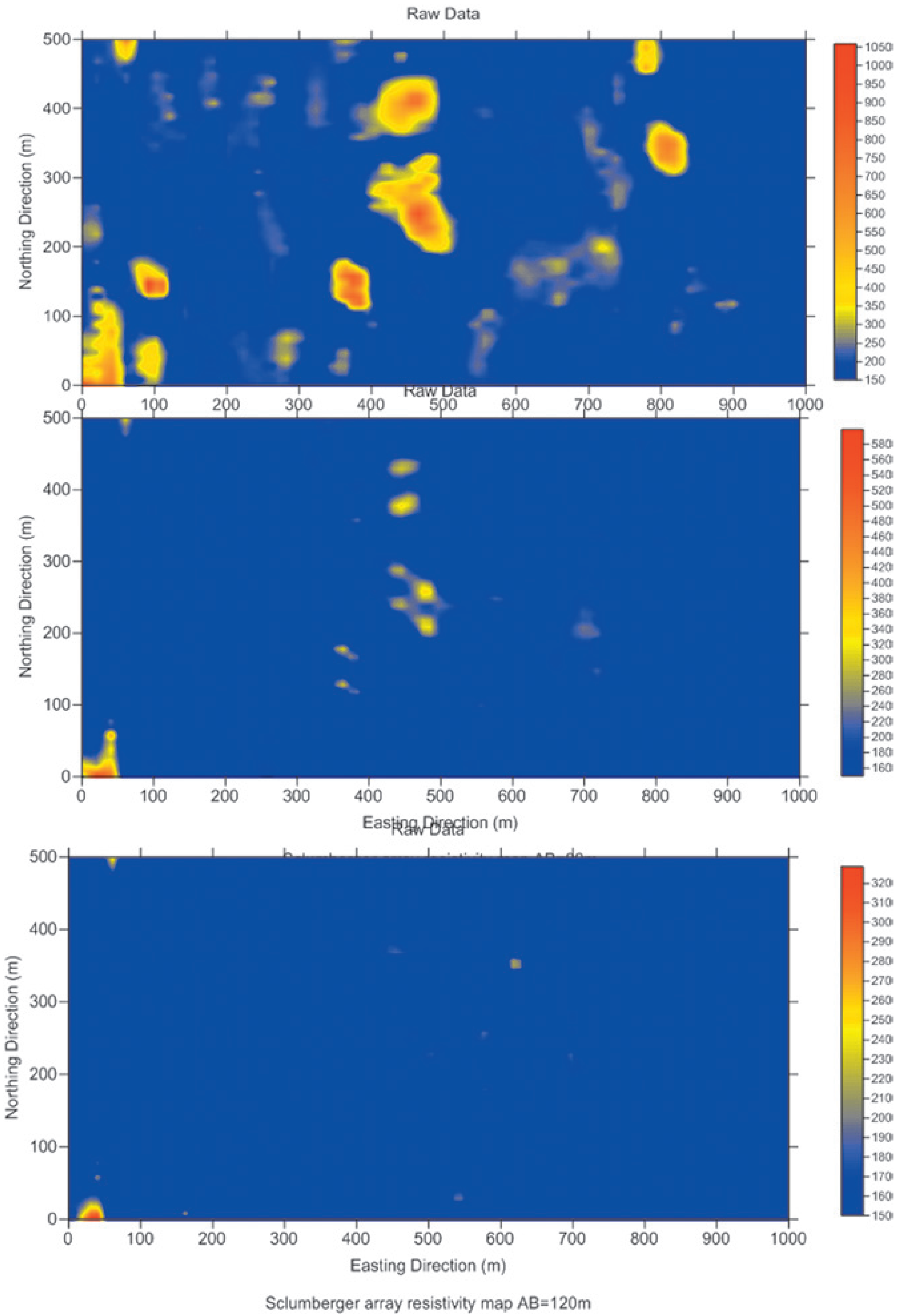

Figure 6. Maps of the apparent resistivity for various Schlumberger electrodes spacing (a) AB= 40 m (b) AB=80 m and (c) AB=120 m.

To design these filters, we have first to decide on the length of the filter k, order of polynomial p, order of derivative n and the size of the smoothing window N where N is odd, and $N \geq p+1$. The coefficients of a Savitzky-Golay filter, when applied to a signal, perform a polynomial is fitted to points $N=N_r+N_l+1$ of the signal. Nr and Nl are signal points in the right and signal points in the left of a current signal point, respectively.

To find these polynomial coefficients, we solve a least-squares inversion:

$$\mathrm{Mc} = \mathrm{d}$$

Where

$$M = \begin{pmatrix} 1 & (k-1)/2) & (-(k-1)/2)^2 & \dots\dots\dots\dots & \left(-(k-1)/2\right)^p \\ \dots\dots\dots\dots & \dots\dots\dots\dots & \dots\dots\dots & \dots\dots\dots\dots & \dots\dots\dots\dots \\ 1 & -1 & \left(-1\right)^2 & \dots\dots\dots\dots & \left(-1\right)^p \\ 1 & 0 & 0 & \dots\dots\dots\dots & 0 \\ 1 & 1 & 1^2 & \dots\dots\dots\dots & \left(1\right)^p \\ \dots\dots\dots\dots & \dots\dots\dots\dots & \dots\dots\dots & \dots\dots\dots\dots & \dots\dots\dots\dots \\ 1 & \left(k-1\right)^2 & \left((k-1)/2\right)^2 & & \left((k-1)/2\right)^p \end{pmatrix}$$

And $c = \begin{pmatrix} c_0 \\ c_1 \\ c_2 \\ \\ c_p \end{pmatrix}$ is the vector of polynomial coefficients of length (p + 1)

And $\rho = \left[\left(\begin{matrix} \rho-(k-1)/2 \\ \rho-(k-2)/2 \\ \\ \rho_0 \\ \\ \rho_{(K-1)/2} \end{matrix}\right)\right]$ is the vector of data values of length k.

We can find the vector of polynomial coefficients via least-squares solution of the matrix equation

$$\mathrm{c} = (\mathrm{M}^t\mathrm{M})^{-1}\mathrm{M}^t\rho$$

The matrix inversion expresses each of the polynomial coefficients in c as a linear combination of the rows of $(\mathrm{M}^t\mathrm{M})^{-1}\mathrm{M}^t\rho$.

Importantly, the value of the polynomial at point ρ_0 is simply given by c_0 (since all other values in the polynomial are zero). The Savitzky-Golay filter of derivative order 0 is given by the (time-reversed) coefficients of the central row of $(\mathrm{M}^t\mathrm{M})^{-1}\mathrm{M}^t\rho$. In general, the coefficients for the Savitzky-Golay filter of derivative order n will be given by the (time-reversed) row n + 1 of the matrix inverse.

FiltersResults From Denoised Data

To achieve a high level of smoothing without attenuating the extrema in the data, a Savitzky-Golay filter with a quartic (order 4) polynomial and the mean centering was applied.

To map resistivity contrasts, field data, apparent resistivity measurements obtained from smoothed data are plotted as a map of the surveyed area.

The resistivity maps generated by the Savitzky-Golay smoothed data allow enhancing the qualitative interpretation of iso-apparent resistivity, in figure 8,9 and 10, the postulated anomalies appear clearly delineated by the Savitzky-Golay filtered resistivity maps, thus a high order polynomial (n=4) allows a high level of smoothing without attenuation of data features.

Conclusion

A detailed geoelectric resistivity survey in a parcel of 50 ha was executed using the horizontal electrical profiling approach with Schlumberger array. Iso-apparent resistivity maps were constructed at electrode spacings equal 40, 80 and 120m in order to study the lateral variations in the geoelectric behavior in phosphatic series of Sidi Chennane.

In this paper, the Savitzky-Golay smoothing method is used to denoise geophysical data to detect anomalous zones of Sidi Chennane phosphatic series, their localisation would permit the mining engineers to get around them during the exploitation.

The Savitzky-Golay filter, method of least-squares-fit smoothing and differentiation of digital data, is versatile and extremely simple to use.

The qualitative interpretation of the smoothed resistivity maps allows defining resistivity contrast, consequently we have delimited the crossing dominate area from a "normal" into a "disturbed" area. We have also observed a best similarity to original signal and slightly denoised it; indeed, this filter is often preferred because, when it is appropriately designed to match the waveform of an oversampled signal corrupted by noise, it tends to preserve the width and height of peaks in the signal waveform. The efficiency of Savitzky-Golay noise reduction filtering estimation technique is shown to be significantly better.

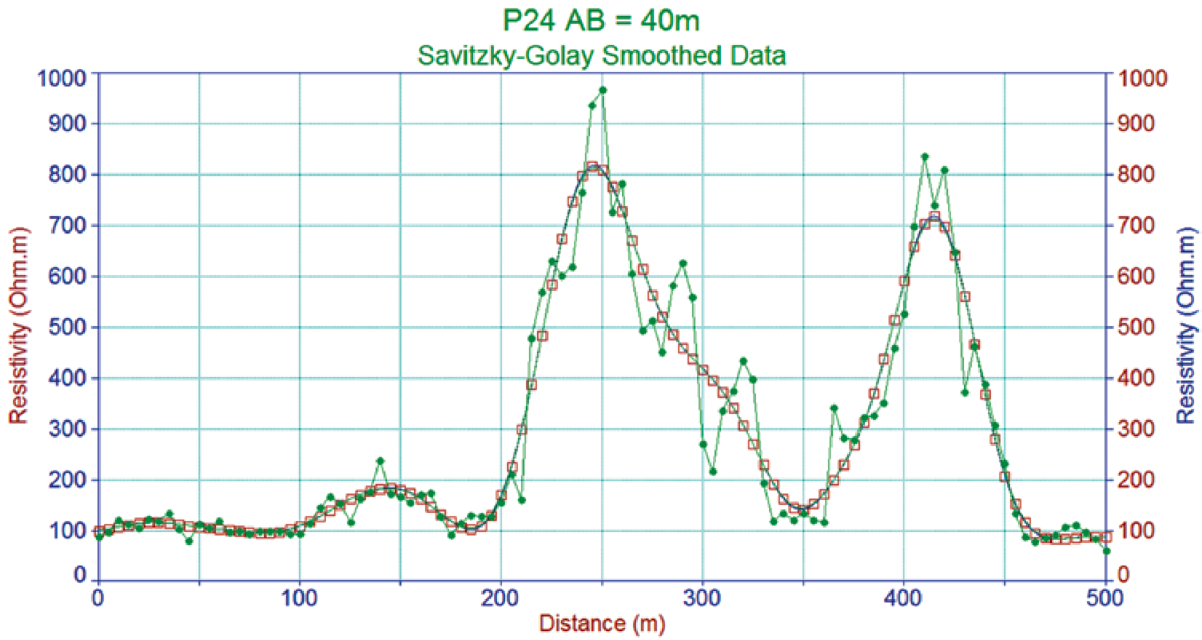
P24 AB = 40m

Savitzky-Golay Smoothed Data

Figure 7. Real noisy data (black) and Savitzky-Golay smoothed data (square)

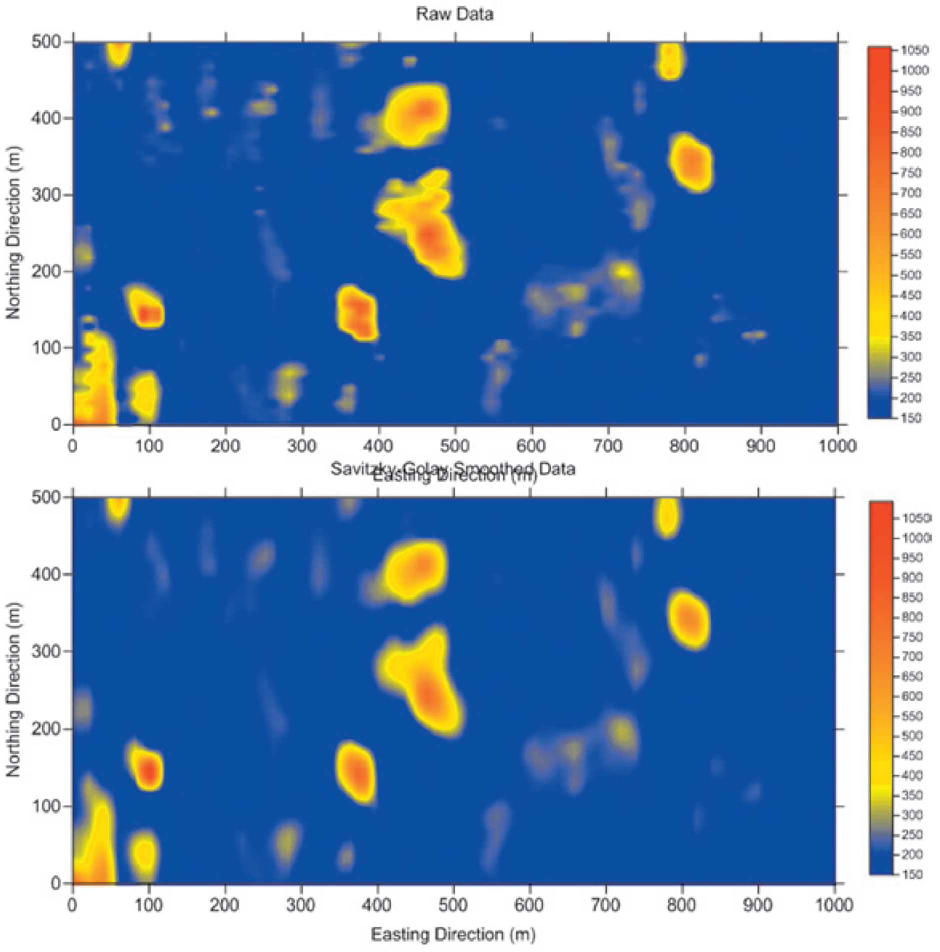
Raw Data

Savitzky-Golay Smoothed Data

Sclumberger array resistivity map AB=40m

Figure 8. Maps of the apparent resistivity, raw and smoothed data; for Schlumberger electrodes spacing AB= 40 m

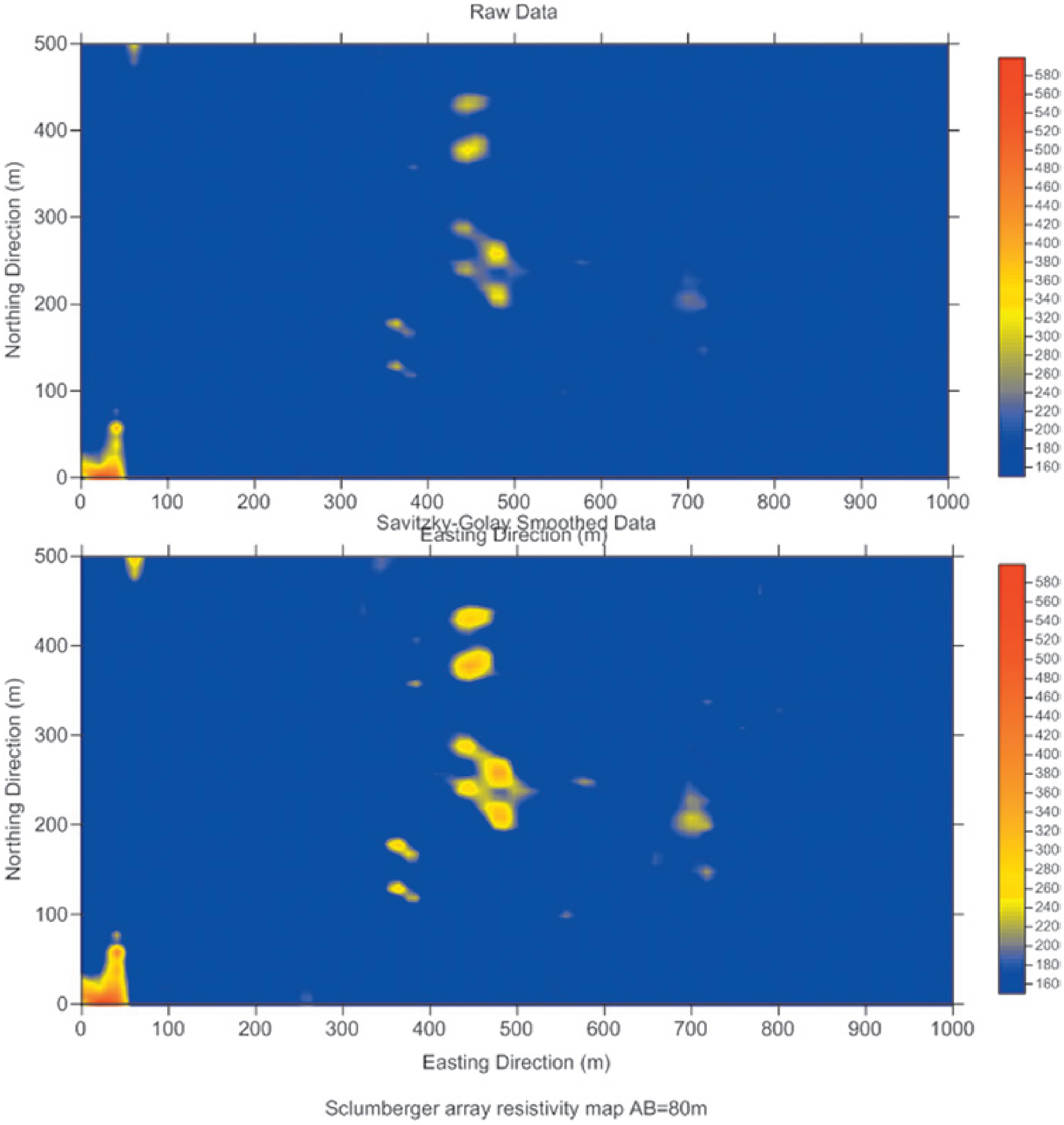

Figure 9. Maps of the apparent resistivity, raw and smoothed data; for Schlumberger electrodes spacing AB=80 m

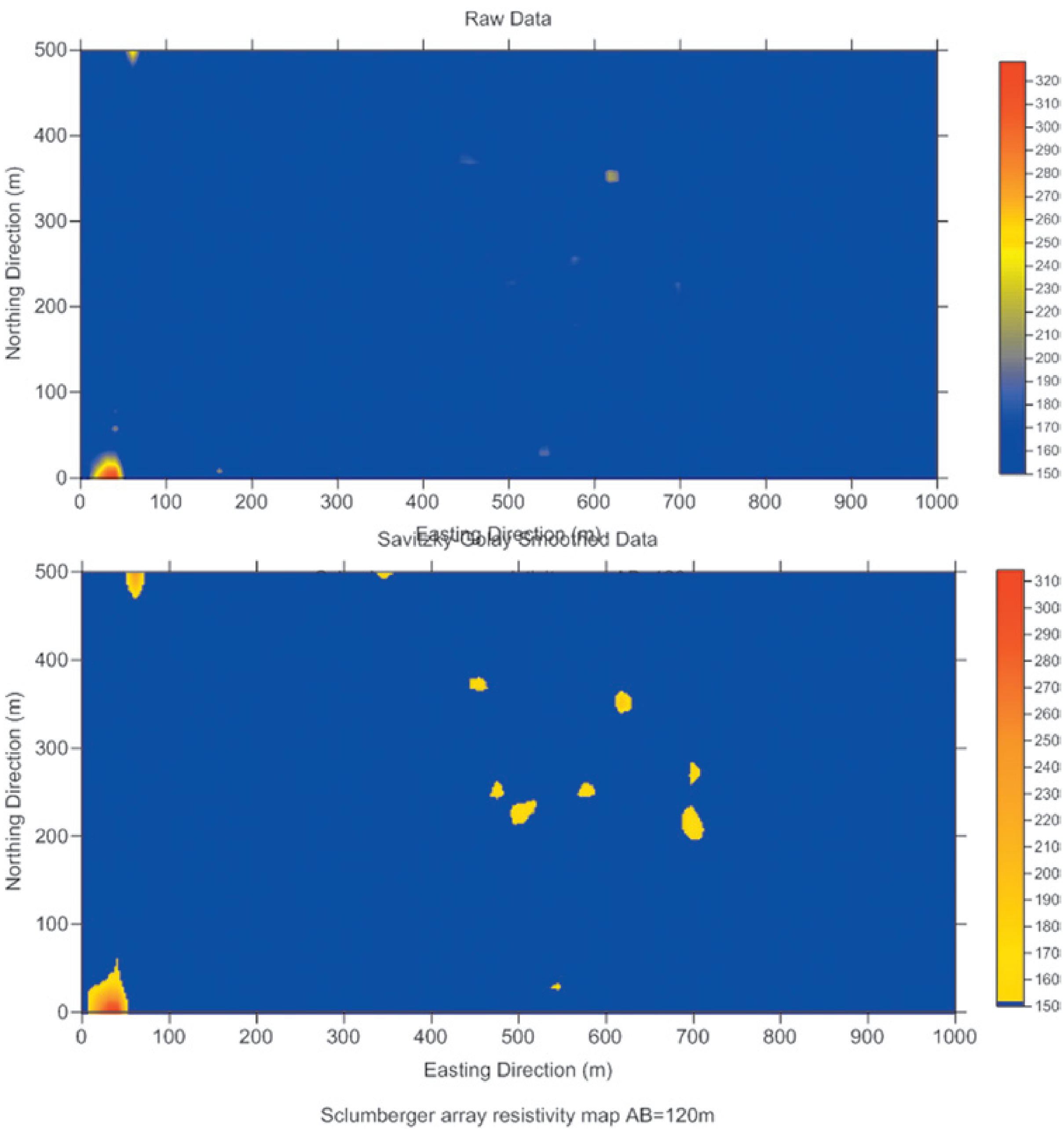

Figure 10. Maps of the apparent resistivity, raw and smoothed data; for Schlumberger electrodes spacing AB=120 m.

Bibliography

Azami H., Mohammadi K., Bozorgtabar B., 2012, An Improved Signal Segmentation Using Moving Average and Savitzky-Golay Filter, *Journal of Signal and Information Processing*, 3, 39-44 doi:10.4236/jsip.2012.31006.

Baba K., Bahi L., Ouadif L. , Akhssas A., 2012, Mapping Sterile Bodies in the Sidi Chennane phosphatic deposit (Morocco) using geoelectrical, *Investigations International Journal of Engineering Research and Applications* (IJERA), 2, 5, September-October, pp.2132-2136.

Chouteau T., 2001, Les méthodes électriques, Notes de cours, Publications Ecole Polytechnique, Montréal.

Hargittai S., Savitzky-Golay, 2005, least-squares polynomial filters in ECG signal processing, Computers in Cardiology, 32, 763−766.

Hassanpour H., 2007, Improved SVD-based technique for enhancing the time-frequency representation of signals. IEEE International Symposium on Circuits and Systems.

Hassanpour H., Zehtabian A., Sadati S.J., 2012, «Time domain signal enhancement based on an optimized singular vector denoising algorithm.» *Digital Signal Processing* 22, 5), pp. 786-794.

Kchikach A., Jaffala M., Aïfab T., Bahi L. Cartographie de corps stériles sous couverturequaternaire par méthode de résistivités électriquesdans le gisement phosphaté de Sidi Chennane (Maroc), *Geosciences* 334 (2002) 379–386

Michard A., Saddiqi O., Chalouan A., 2008, "Continental evolution: the geology of Morocco: structure, stratigraphy and ..." *Springer*.

Md. Abdul Awal, Sheikh Shanawaz Mostata, Mohiuddin Ahmed, Perfomance Analysis of Savitzky-Golay Smoothing Filter Using ECG signal" ISSN 2218-5224, 1, ISSUE 02.

Orfanidis S.J., 2010, Introduction to Signal Processing, Prentice Hall.

Ouadif L., Bahi L., Akhssas A., Baba K., Menzhi M., 2012, Contribution of Geophysics for the Determination of Aquifers with a Case Study. *International Journal of Geosciences*, 3 1, pp. 117-125. doi: 10.4236/ijg.2012.31014.

Savitzky A., Golay M.J.E., 1964, Smoothing and differentiation of data by simplified least squares procedures, *Analytical Chemistry*, 36, 2, p.1627–1639.

Schafer R.W., 2011, What is a Savitzky-Golay Filter?, *Signal Processing Magazine*, IEEE 28, 4, pp. 111-117.

Geofísica Internacional (2014) 53-4: 411-423

Original paper

Comparative study of top soil magnetic susceptibility variation based on some human activities

Kanu M. O.*, Meludu O. C. and Oniku S. A.

Received: June 10; 2013; accepted: November 11, 2013; published on line: October 01, 2014

Resumen

Se realizó una investigación sobre el efecto que tienen algunas actividades humanas en la susceptibilidad magnética y la susceptibilidad dependiente de la frecuencia: el estudio se realizó en Jalingo, estado de Taraba, Nigeria, en la superficie del suelo de una zona comercial, un estacionamiento de autos y una zona escolar. El objetivo fue evaluar la variación de la susceptibilidad magnética con distintos tipos de uso de la tierra y detectar los puntos más contaminados utilizando los parámetros de proxy magnéticos. Con ello se evaluó la contribución de superparamagnéticas (SP), del tamaño de un grano, a la susceptibilidad magnética del cálculo de la dependencia de la frecuencia de la susceptibilidad magnética (MS). Los resultados de las mediciones de masa específicos de susceptibilidad de baja frecuencia magnética mostraron una mejora significativa con valores que van desde 67,8 hasta 495,3 x 10^{-8} m^3kg^{-1}, con un valor medio de 191,61 x 10^{-8} m^3kg^{-1} para el Colegio Jalingo de Educación (datos JCOE); 520,1-1612,8 x 10^{-8} m^3kg^{-1} con un valor medio de 901,34 x 10^{-8} m^3kg^{-1} para el mercado principal de Jalingo (JMM) y 188.5- 1.203,6 x $10^{-8}m^3kg^{-1}$ con un valor promedio de 574 92 x 10^{-6} m^3kg^{-1} para el Motor Park Jalingo (JMP). La mejora magnética significativa indica una alta concentración de minerales ferrimagnéticos en el suelo y, por lo tanto, un aumento en la contaminación. La susceptibilidad magnética de los diferentes usos del suelo estudiados se redujo en la zona comercial (mercado)>, estacionamiento > e instalaciones escolares. Los resultados de la dependencia del porcentaje de la susceptibilidad dependiente de la frecuencia mostró que la mayoría de las muestras tenían una mezcla de SP y los granos gruesos o de dominio de múltiples granos SP <0.05µm. El valor de% χ_{fd}% rango 2,68 a 13,80%, con un valor medio de 8,67% en las muestras JCOE, 0,49 a 10,04%, con un promedio de 5,05% en las muestras JMM y 0,56 a 13,04%, con un valor promedio de 5.86% en las muestras de JMP.

Palabras clave: Contaminación del suelo, susceptibilidad magnética, susceptibilidad dependiente de la frecuencia, mineral magnético, ferrimagnético.

Abstract

An investigation of the effect of some human activities on the magnetic susceptibility and frequency dependent susceptibility was conducted on top soil samples from, a commercial area, a motor park and a school environment in Jalingo, Taraba State, N-E Nigeria. The purpose was to assess the variation of magnetic susceptibility with different land use, detect pollution hotspots using magnetic proxy parameters and evaluate the contribution of superparamagnetic (SP) grain size contribution to the magnetic susceptibility from calculation of the frequency dependence of magnetic susceptibility (MS). The results of the mass specific low frequency magnetic susceptibility measurements showed significant enhancement with values ranging from 67.8 - 495.3 x 10^{-8} m^3kg^{-1} with a mean value of 191.61 x 10^{-8} m^3kg^{-1} for the Jalingo College of Education (JCOE) data; 520.1 – 1612.8 x 10^{-8} m^3kg^{-1} with a mean value of 901.34 x 10^{-8} m^3kg^{-1} for the Jalingo main Market (JMM) and 188.5- 1203.6 x $10^{-8}m^3kg^{-1}$ with an average value of 574 92 x 10^{-6} m^3kg^{-1} for the Jalingo Motor Park (JMP). The significant magnetic enhancement indicates high concentration of ferrimagnetic minerals in the soil and hence increased pollution. The magnetic susceptibility of the different land use studied decreased in the order commercial area (market) > motor park > school premises. The results of the percentage frequency dependence susceptibility showed that most of the samples had a mixture of SP and coarse multi domain grains or SP grains < 0.05µm. The value of χ_{fd}% range from 2.68 to 13.80% with an average value of 8.67% in the JCOE samples, 0.49 to 10.04% with an a-verage of 5.05% in the JMM samples and 0.56 to 13.04% with an average value of 5.86% in the JMP samples.

Key words: Soil pollution, magnetic susceptibility, frequency dependent susceptibility, mineral magnetic, ferrimagnetic

---

M. O. Kanu*
Department of Physics
Taraba State University
P. M. B. 1167, Jalingo
Taraba State, Nigeria
*Corresponding author: maxiexpress007@gmail.com

O. C. Meludu
S. A. Oniku
Department of Physics
Modibbo Adama University of Technology
P.M.B. 2076, Yola
Adamawa State, Nigeria

Introduction

The adverse effect of human impact in the environment has increased in recent years and has become a subject of global concern. The type and intensity of human activity greatly impact on the environment. With increased urbanization, the urban environment is threatened by various pollution sources released into it. This pollution ranged from indiscriminate refuse dump, sewage disposal, industrial wastes, bush burning, and emissions from industries and automobile exhaust. So, pollution has become a subject widely investigated from several fields, such as geology, geophysics, chemistry, agriculture etc. Atmospheric pollution has been identified, as one of the most harmful factors for ecosystems (Petrovsky and Elwood, 1999). Usually, heavy metals and toxic elements from industrial, vehicular and domestic emissions are released into the atmosphere and are incorporated into the environment or in living organism such as vegetation, animals and human beings. These contaminants that are released into the atmosphere, soils and sediments are rich in magnetic particles, resulting in magnetic enhancement of the urban soils and sediments. A measure of the amount of magnetic enhancement is expressed by its magnetic susceptibility and in recent years, it has been successfully used to monitor anthropogenic pollution, especially heavy metal pollution in soils (example Gautam *et al.*, 2004, Petrovsky *et al.*, 2000, Strzyszcz and Magiera, 1998, etc.).

Magnetic susceptibility is defined as the ratio of the total magnetization induced in a sample to the intensity of the magnetic field that produces the magnetization Mullins (1977).

Magnetic susceptibility measures the concentration of magnetic crystals and also gives information on the type of magnetic minerals present in a sample. Magnetic minerals present in soils may either be obtained from the parent rocks (lithogenic origin), during pedogenesis or as a result of anthropogenic activities. The magnetic mineral content of the soil can broadly be expressed by its magnetic susceptibility. Magnetic susceptibility can be used to identify the type of mineral and the amount of iron bearing minerals contained in a material. Soils are sinks to anthropogenic pollutants released into the atmosphere. Accumulation of anthropogenic ferrimagnetic particles, originating from oxidation process during combustion of fossil fuels results in significant enhancement of topsoil magnetic susceptibility. The most important magnetic mineral is magnetite and in the atmosphere it can originate from combustion (and other industrial) processes (Petrovsky *et al.*, 2000).

The first evidence of magnetic enhancement was reported by Le Borgne (1955). Subsequent studies by Mullins (1977) confirmed this phenomenon. Thompson and Oldfield (1986) further reported that the soils near urban areas and industrial zones have an increased susceptibility due to deposition of magnetic particles such as, dust of the metallurgical industries and fly ashes of the coal combustion. Since then, extensive studies of pollution and magnetic proxies for pollution have been conducted for example Alagarsamy (2009), Canbay (2010), Gautam *et al*. (2005), Kapicka *et al*. (1999), Knab *et al*. (2006), Magiera *et al*. (2006), Petrovsky *et al*. (2000), Shen *et al*. (2008), Strzyszcz *et al.* (1996) etc. Magnetic measurement is a simple, rapid and non-destructive technique that can be applied on soil/sediment samples.

The purpose of this study was to assess the variation of magnetic susceptibility with different land use, detect pollution hotspots using magnetic proxy parameters and determine the grain size of the samples from calculation of the frequency dependence of magnetic susceptibility (MS).

Materials and Methods

Geographical and Geological setting of the Study Area

Jalingo, the study area is the administrative headquarters of Taraba State which is located between latitude 6º30’ and 8º30’ North of the equator and between 9º00’ and 12º00’ East of the Greenwich meridian (Figure 1). The state has a tropical wet and dry climate, dry season lasts for a minimum of five months (November to March) while the wet season spans from April to October. It has an annual rainfall of about 8000 mm. Jalingo is a rapidly growing city without significant industrial activity, the major pollution source is the emission from traffic and power generating sets and other human activities such as indiscriminate refuse dump, bush burning etc.

The study area is underlain by the undifferentiated Basement Complex rocks which consist mainly of the migmatites, gneisses and the Older Granites. Tertiary to Recent basalts also occurs in the area. The undifferentiated Basement Complex particularly the migmatites, generally vary from coarsely mixed gneisses to

Figure 1. Map of study area (insert: map of Nigeria, showing study area).

diffused textured rocks of variable grain size and are frequently porphyroblastic (Macleod *et al*., 1971).

The Pan African Older Granites are equally widespread in the area. They occur either as basic or intermediate intrusives (Turner, 1964). Different kinds of textures ranging from fine to medium to coarse grains can be noticed on the Older Granites (McCurry, 1976). Other localized occurrences of minor rock types include some doleritic and pegmatitic rocks mostly occurring as intrusive dykes and vein bodies. These occurrences are common to both the undifferentiated Basement Complex and the Older Granite rocks (Carter *et al*., 1963, McCurry, 1976). The Tertiary basalts on the other hand are found in the Mambila Plateau mostly formed by trachytic lavas and extensive basalts which occur around Nguroje (du Preez and Barber, 1965).

Sampling and Analysis

Topsoil samples (0- 2 cm) were collected from three different locations using a plastic material to avoid contamination. The samples locations were determined using a 12 Channel Garmin Global Positioning System (GPS 12). A total of 59 samples were randomly collected, 15 samples from a school environment, 10 samples from a motor park, 11 samples from a commercial area and 23 samples from an unpolluted rural area with the same geology to serve as control. The Jalingo College of Education (JCOE) which has been in existence for more than 25 years was chosen to represent a school environment. The Jalingo Motor Park (JMP) has been in operation for more than 15 years with a land area of about 250 square meters with more than 500 vehicles moving in and out daily. The Jalingo Main Market (JMM), which is the major commercial centre of the city has an area of about 500 square meters and was built more than two decades ago. A lot of commercial activities take place in this market and vehicular movement around the market area has been on the increase over the years.

The samples were air dried at a temperature of 30ºC in the laboratory for some days to avoid any chemical reactions. They were then ground using agate mortar and sieved using a 1 mm sieve mesh (Kim *et al*., 1999) and stored in a plastic container for further laboratory measurements. The mass specific magnetic susceptibility measurements were then carried out on the sieved samples packaged in a 10 ml plastic container at laboratory temperature. Measurements of magnetic susceptibility were made at both low (0.47 kHz) and high (4.7 kHz) frequencies using MS2 dual frequency susceptibility meter. All measurements were conducted at the 1.0 sensitivity setting. Each sample was measured three times with an air reading before and after each series for drift correction. The mass specific frequency dependence susceptibility χ_{fd} was obtained from the relation:

$$\chi_{fd} = \chi_{lf} - \chi_{hf} \tag{1}$$

Where χ_{lf} and χ_{hf} are the low and high frequencies susceptibility respectively.

Table 1. Jalingo College of Education (JCOE) data

Sample	Mass (g)	Latitude (N)	Longitude (E)	χ_{lf} x 10^{-8} m^3kg^{-1}	χ_{hf} x 10^{-8} m^3kg^{-1}	χ_{fd} x 10^{-8} m^3kg^{-1}	χ_{fd} (%)
JCOE 1	16.29	8º54.080′	11º19.052′	226.7	197.0	29.7	13.10
JCOE 2	17.91	8º54.067′	11º19.078′	359.5	309.9	48.6	13.80
JCOE 3	18.31	8º54.104′	11º19.078′	175.7	171.0	4.7	2.68
JCOE 4	17.94	8º54.119′	11º19.044′	132.8	123.4	9.4	7.08
JCOE 5	18.58	8º54.129′	11º19.021′	200.8	182.4	18.4	9.16
JCOE 6	17.03	8º54.135′	11º19.009′	136.9	125.2	11.7	8.55
JCOE 7	19.72	8º54.111′	11º18.992′	156.7	149.7	7.0	4.47
JCOE 8	18.96	8º54.122′	11º18.962′	131.1	122.7	8.4	6.41
JCOE 9	17.70	8º54.078′	11º19.005′	495.3	437.2	58.1	11.73
JCOE 10	19.62	8º54.162′	11º19.087′	309.6	286.1	23.5	7.59
JCOE 11	18.95	8º54.186′	11º19.102′	81.0	74.0	8.6	9.31
JCOE 12	19.07	8º54.193′	11º19.072′	67.8	62.0	5.8	8.55
JCOE 13	18.26	8º54.191′	11º19.038′	110.8	96.8	14.0	12.64
JCOE 14	19.20	8º54.165′	11º19.049′	141.7	136.4	5.3	3.74
JCOE 15	17.11	8º54.220′	11º18.961′	147.1	130.5	16.6	11.28

Table 2. Jalingo Main Market (JMM) data.

Sample	Mass (g)	Latitude (N)	Longitude (E)	χ_{lf} x10^{-8} m^3kg^{-1}	χ_{hf} x 10^{-8} m^3kg^{-1}	χ_{fd} x 10^{-8} m^3kg^{-1}	χ_{fd} (%)
JMM 1	16.63	8º53.714′	11º21.605′	658.3	622.3	36.0	5.47
JM M 2	18.06	8º53.711′	11º21.526′	520.1	510.0	10.1	1.94
JMM 3	18.05	8º53.678′	11º21.547′	1182.7	1115.9	66.8	5.65
JMM 4	16.87	8º53.703′	11º21.555′	1321.4	1229.2	92.2	6.98
JMM 5	15.79	8º53.692′	11º21.607′	623.5	599.8	23.7	3.80
JMM 6	17.44	8º53.689′	11º21.603′	571.5	568.7	2.8	0.49
JMM 7	17.13	8º53.690′	11º21.600′	556.1	549.7	6.4	1.15
JMM 8	17.17	8o53.651′	11º21.578′	1612.8	1503.4	109.4	6.78
JMM 9	16.28	8º53.619′	11º21.601′	656.6	611.9	44.7	6.81
JMM 10	17.41	8º53.591′	11º21.610′	1120.9	1008.4	112.5	10.04
JMM 11	18.10	8º53.548′	11º21.631′	1090.8	1020.3	70.5	6.46

Table 3. Jalingo Motor Park (JMP) data.

Sample	Mass (g)	Latitude (N)	Longitude (E)	χ_{lf} x 10^{-8} m^3kg^{-1}	χ_{hf} x 10^{-8} m^3kg^{-1}	χ_{fd} x 10^{-8} m^3kg^{-1}	χ_{fd} (%)
JMP1	17.86	8º56.267′	11º20.328′	401.7	349.3	52.4	13.04
JMP 2	18.15	8º56.301′	11º20.323′	842.4	811.8	30.6	3.63
JMP 3	18.57	8º56.306′	11º20.305′	444.3	418.7	25.6	5.76
JMP 4	16.90	8º56.300′	11º20.283′	286.0	261.5	24.5	8.57
JMP 5	18.38	8º56.290′	11º20.303′	442.6	440.1	2.5	0.56
JMP 6	17.46	8º56.277′	11º20.286′	188.5	167.7	21.8	11.03
JMP 7	18.34	8º56.265′	11º20.281′	466.7	453.3	13.4	2.87
JMP 8	17.86	8º56.274′	11º20.301′	903.9	855.3	48.6	5.38
JMP 9	18.94	8º56.257′	11º20.317′	1203.6	1149.9	53.7	4.46
JMP 10	17.71	8º56.242′	11º20.300′	569.5	550.5	19.0	3.34

This parameter is sensitive only to a very narrow grain size region crossing the superparamagnetic/single domain threshold (~ 20 – 25 nm for maghemite) (Worm and Jackson, 1999). For natural samples which generally exhibit a continuous and nearly constant grain size distribution, χ_{fd} can be used as a proxy for relative changes in concentration in pedogenic fined – grained magnetic particles (Liu *et al.*, 2005). The relative χ_{fd} also called Percentage frequency dependent susceptibility ($\chi_{fd}\%$) was then calculated following Dearing (1999) as:

$$\chi fd\% = \left(\frac{\chi_{lf} - \chi_{hf}}{\chi_{lf}}\right) \times 100 \qquad (2)$$

Results and Discussion

The results of the mass specific low field magnetic susceptibility, frequency dependence and percentage frequency dependence of the samples are displayed in tables 1 - 3. The value of low frequency mass specific magnetic susceptibility ranges from 67.8 to 495.3 x 10^{-8} m^3kg^{-1} with a mean value of 191.61 x 10^{-8} m^3kg^{-1} for the JCOE data. The JMM has low frequency magnetic susceptibility values ranging from 520.1 to 1612.8 x 10^{-8} m^3kg^{-1} with a mean value of 901.34 x 10^{-8} m^3kg^{-1}, while the JMP has value of low frequency magnetic susceptibility ranging from 188.5 to 1203.6 x10^{-8} m^3kg^{-1} with an average value of 574.92 x 10^{-8} m^3kg^{-1}. The magnetic susceptibility of the different land use studied decreased in the order: commercial area (market) > motor park > official area. Differences in the values of magnetic susceptibility are a result of difference in the type and strength of human activity in the different areas. The high magnetic susceptibility values of the JMM may be attributed to the high commercial activity in the market rusted of pieces of metals that might be thrown on the soils and emissions from the high volume of traffic around the market area.

Gautam *et al.* (2004) classified soils into three broad categories based on their magnetic susceptibility (MS) values as follows: ‘normal’ (MS < 10 x 10^{-8} m^3kg^{-1}), ‘moderately magnetic’ (MS 10 – 100 x 10^{-8} m^3kg^{-1}) and ‘highly magnetic’ (MS >100 x 10-8 m^3kg^{-1}). From the above classification, the soils from JMM and JMP can be said to be highly magnetic, while that of JCOE ranges from moderate to highly magnetic. The high values indicate high concentration of ferrimagnetic minerals in the soil. Previous studies showed that magnetic susceptibility variations are caused by differences in geology (lithogenic/geogenic), soil forming processes (pedogenesis) and anthropogenic input of magnetic material (Dearing *et al.*, 1996 and Thompson and Oldfield, 1986). The higher magnetic enhancement in JMM and JMP is attributed to anthropogenic inputs of magnetic minerals. The anthropogenic magnetic particles may likely come from vehicle emissions (vehicular exhaust, abrasion of tyres and brake linings) and waste products. Vehicular emissions comprises of different fractions of particles formed in the exhaust pipes and released into the environment. These emissions have magnetic character which is determined by the increase in the MS. The moderate values of MS obtained from JCOE samples are expected since the area is an academic environment with less traffic and with proper waste disposal system. The results obtained for the JCOE are similar to that obtained for a school in Xi'an city, China (263.45 -531.28 x 10^{-8} m^{3}kg^{-1}) (Li *et al.*, 2010). The high values obtained in some samples are attributed to emissions from vehicles and power generating sets as there is insufficient power supply in this city. Most businesses are operated using private alternating current generators.

The values of low frequency mass specific magnetic susceptibility of the unpolluted site range from 35.4 to 92.8 x 10^{-8} m^{3}kg^{-1} with a mean value of 64.56 x 10^{-8} m^{3}kg^{-1}. These values are lower than the signal from urban topsoil samples. The average magnetic susceptibility value in JCOE, JMM and JMP respectively increased by about 3, 14 and 9 times those of the unpolluted site, suggesting magnetic enhancement derived from anthropogenic activities in urban soils.

The values of magnetic susceptibility measured at high frequencies (4.7 kHz) are usually lower than the values obtained from the low frequency (0.47 kHz) magnetic susceptibility measurements (Dearing *et al.*, 1996; Dearing, 1999). This is further confirmed for soils in Jalingo as shown in Figures 2 to 4. Measurements made at these two frequencies at a constant applied field are generally used to detect the presence of ultrafine ferrimagnetic (also called super paramagnetic fraction of less than 0.03 μm) minerals occurring as crystals and to some extent the single domain (approximately greater than 0.03 to less than 0.06 μm fractions) (Sangode *et al.*, 2010). Higher frequency measurements do not allow super paramagnetic grains to react with the applied magnetic field, as it changes more quickly than the required relaxation time for super paramagnetic grains. As a result, in higher frequency, lower values of MS are encountered and the difference is used to estimate the super paramagnetic ferrimagnetic particles (Sangode *et al.*, 2010). When super paramagnetic minerals are present in a soil sample, the MS values at high frequency are slightly lower than the values of MS at low frequency. If there are no super paramagnetic (SP) minerals the two measurements are identical (Dearing, 1999).

There is wide difference between measured values of χ_{LF} and χ_{HF} which indicates the presence of admixture of SP minerals in the studied soil. This difference is expressed by the frequency dependent MS (χ_{fd}) shown in Tables 1-3.

The values of χ_{fd} varied between 4.7 and 58.1 x 10^{-8} m^{3}kg^{-1} with an average of 17.99 x 10^{-8} m^{3}kg^{-1} for the JCOE, 2.8 and 112.5 x 10^{-8} m^{3}kg^{-1} with a mean value of 52.28 x 10^{-8} m^{3}kg^{-1} for JMM and 2.5 and 53.7 x 10^{-8} m^{3}kg^{-1} with a mean of 29.21 x 10^{-8} m^{3}kg^{-1} for the JMP. According to Dearing (1999), the mass specific frequency dependent susceptibility χ_{fd} ranges from ~30 x 10^{-8} m^{3}kg^{-1} in stable single domain (SSD) grains to 75 – 160 x 10^{-8} m^{3}kg^{-1} in the SP range. From this information, the majority

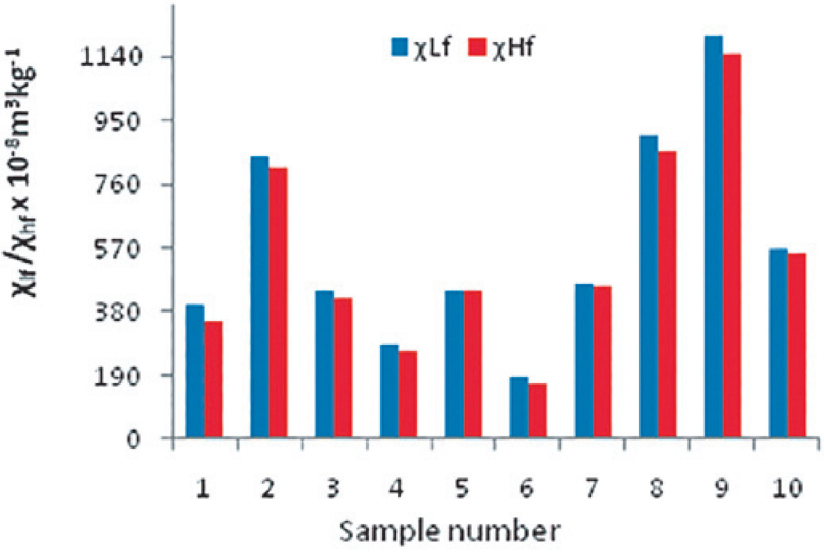

Figure 2. χ_{lf} / χ_{hf} x10^{-8} m^{3}kg^{-1} values of JMP samples both at high and low frequency

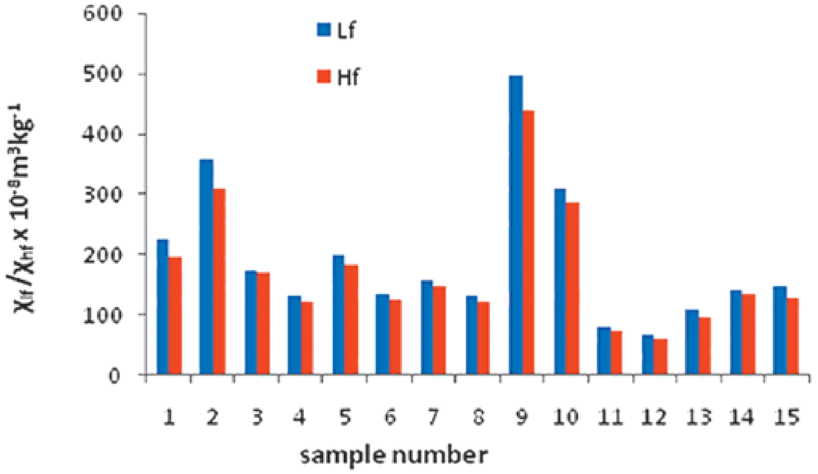

Figure 3. χlf/χhf x10-8 m3kg-1 values of JCOE samples both at high and low frequency.

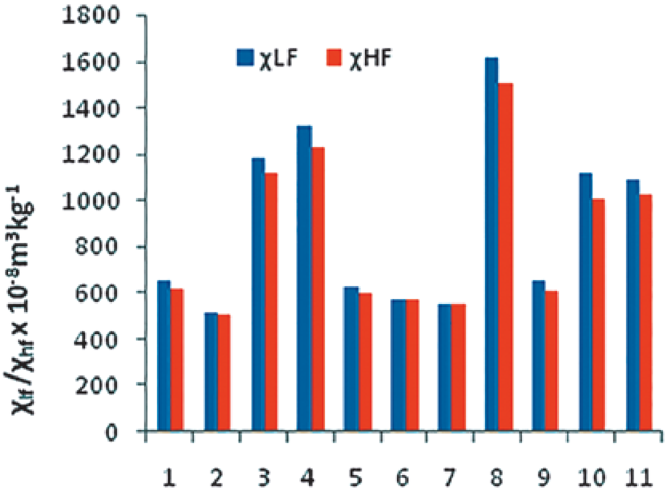

Figure 4. χ_{lf} / χ_{hf} x10^{-8} m^3kg^{-1} values of JMM samples both at high and low frequency

of the samples studied falls within the SSD range while only about 20% from the JMM are in the SP range.

Figure 5 relate the χ_{LF} and χ_{HF} values in the topsoil samples of JMP. The graph shows a linear relationship between χ_{lf} and χHF with very significant correlation coefficient and a slope less than one indicating evidence of superparamagnetic minerals.

Figures 6 - 8 compares the χ_{fd} and χ_{LF} values in the topsoil samples. An increase in MS appears to be related with an increase in theχ_{fd}. According to Forster *et al.* (1994), such linear correlation indicates that with increasing magnitude the susceptibility is more controlled by the contribution from the fine pedogenic magnetic fraction. The linear relationship also indicates high homogeneity in the magnetic mineralogy of the soils corresponding with the mineral size. Similar result was obtained by Sadiki *et al*. (2009). The JMM and JCOE are more correlated with correlation coefficients of 0.84 and 0.85 respectively. The graph of χ_{lf} against χ_{fd} can be used to obtain the background low magnetic susceptibility χ_B (Forster *et al.*, 1994). This corresponds to the intercept on the χlf axis where χ_{fd} is zero. From Figures 9-11, the values of the background magnetic susceptibility are 176.0 x10^{-8} m^3kg^1, 72.89 x10^{-8} m^3kg^{-1}, 457.1 x10^{-8} m^3kg^{-1} respectively for JMP, JCOE and JMM. From these values, it was observed that all the samples except JCOE 12 had magnetic susceptibility values above the background value, implying an enhancement in the MS values. The MS enhancement can be attributed to either pedogenesis or anthropogenic sources. This observation seems to agree with our earlier observation using the classification of Gautam *et al.* (2004). The MS enhancement of sample JCOE 12 was attributed to lithogenesis.

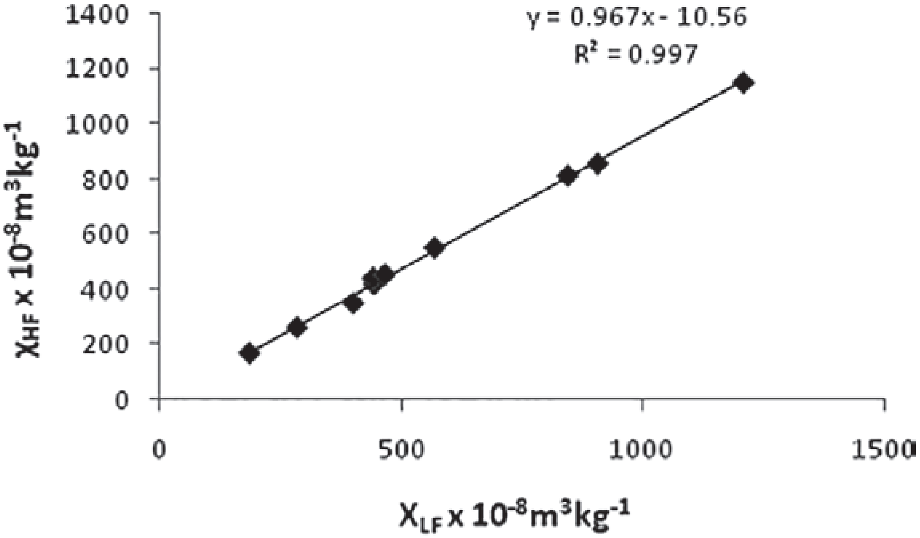

Figure 5. Relation between low frequency and high frequency susceptibility for JMP samples.

Percentage frequency dependent susceptibility $\chi_{fd}\%$ is used to approximate the total concentration of SP grains, while coarse multi domain (MD) magnetic grains are frequency independent as they show similar susceptibility values at low and high frequencies. Dearing (1999) proposed a model for the interpretation of frequency dependence as follows:

χ_{fd} (%)	value	Interpretation
Low χ_{fd} (%)	< 2.0%	Virtually no SP grains
Medium χ_{fd} (%)	2.0– 10.0 %	Admixture of SP and coarser non-SP grains or SP grains < 0.005µm
High χ_{fd} (%)	10.0 – 14.0%	Virtually all (> 75%) SP grains
Very high χ_{fd} (%)	>14 %	Rare values, erroneous measurements, weak samples or contamination

Based on the semi quantitative model above, the results of this work demonstrated that most of the samples (about 67%) have a mixture of SP and coarse grains or SP grains < 0.005µm. In the JCOE samples, the value of $\chi_{fd}\%$ ranges from 2.68 to 13.80% with an average value of 8.67%. Five samples (that is about 30%) are virtually all SP grains as they have $\chi_{fd}\%$ in the

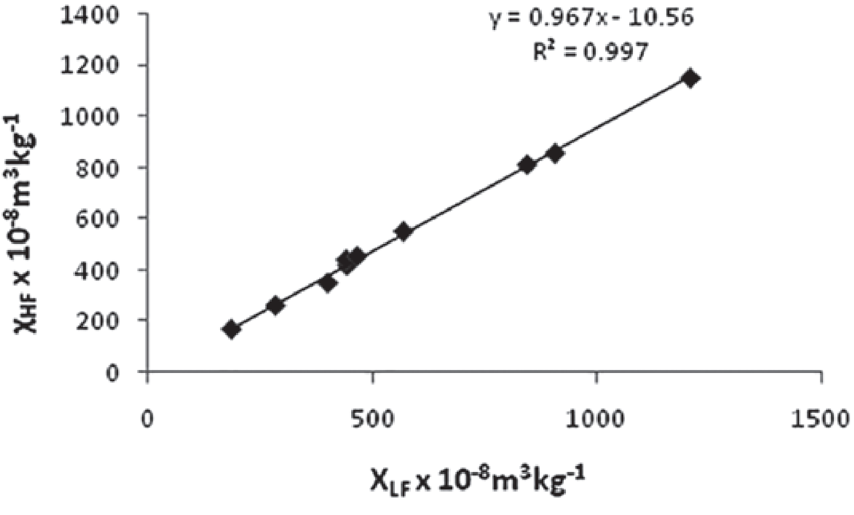

Figure 6. Linear regression between χ_{fd} and n χ_{LF} fo JMP.

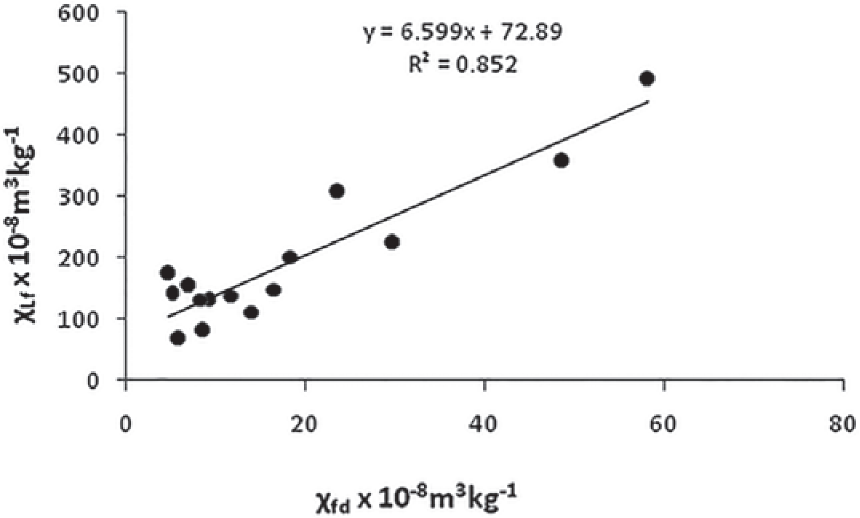

Figure 7. Linear regression between x_{fd} and χLf for JCOE samples

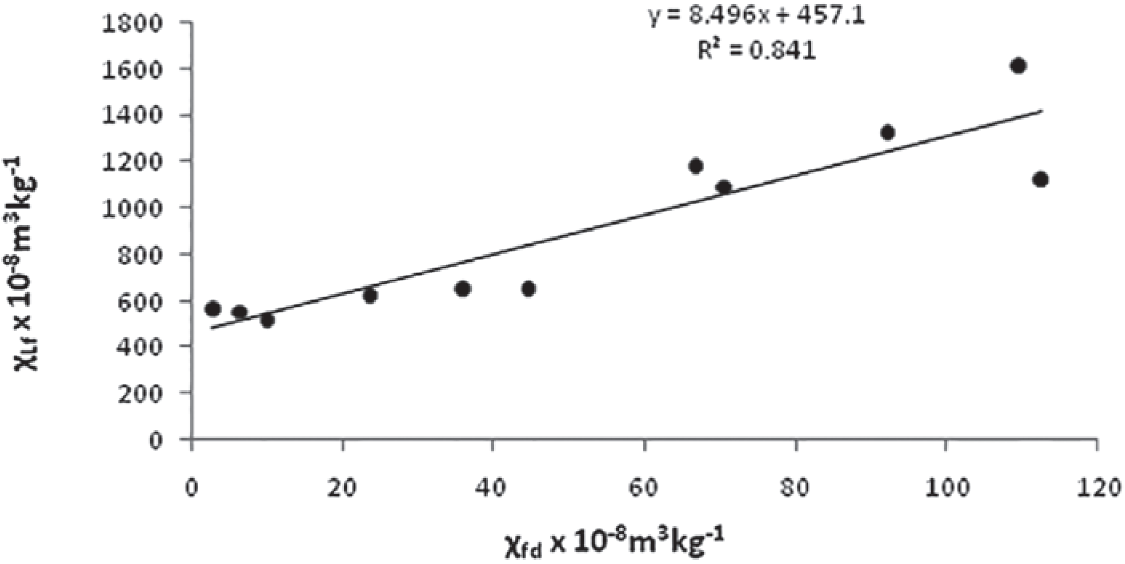

Figure 8. Linear regression between χ_{fd} and χ_{LF} JMM samples

range of 12 – 14 %, while other samples have values in the range of 2 – 10 % indicating the presence of a mixture of SP and MD magnetic grains. In the JMM samples, seven samples falls within the medium range of 2 – 10 % and may be said to have a mixture of SP and coarse MD grains, three samples have low χ_{fd}% of < 2% implying that they have no SP grains while only one sample has high χ_{fd}% of 10.04 % meaning that the dominant magnetic component of this soil are SP ferrimagnetic grains. For the JMP samples, about 70% of the samples have χ_{fd}% value in the medium range and this can be interpreted as soils with admixture of SP and coarser non SP grains or < 0.005µm SP grains. About 20% of the JMP samples are soils where virtually all the iron component are SP grains, while about 10% of the samples contains no SP grains. Generally, most of the samples in the studied area contain a mixture of SP and MD magnetic grains.

Figures 9 – 11 are the respective scattergram of χ_{lf} - χ_{fd} % for JMP, JCOE and JMM showing typical sample positions for the various domains and sources. The JMP samples showed negative correlation between χ_{lf} and χ_{fd} % while the JCOE and JMM samples showed positive correlation. The negative correlation observed in the JMP samples indicates that the main susceptibility variations are due to magnetic enhancement as a result of industrial and anthropogenic pollution. The negative correlation between χ_{lf} and $\chi_{fd}\%$ further shows that pedogenic SP grains contribute little to the magnetic enhancement of urban soils, the magnetic enhancement is mainly contributed by coarse magnetic grains from industrial and anthropogenic pollution. Similar results were also obtained by Lu *et al.* (2007) for urban topsoils from Luoyang and Lu and Bai (2008) for urban soils from Hangzhou. The positive correlation of the JMM and JCOE samples indicates that the MS enhancement is due to SP ferrimagnetic grains. The MS of soils derived from sedimentary rocks usually increase with an increase in frequency dependent susceptibility (Lu, 2003). Many authors (example Wang *et al*., 2003, Zhu *et al.*, 2001) also reported positive correlation between $\chi_{(lf)}$ and $\chi_{fd}\%$ for Chinese loess and paleosol. The combination of both positive and negative correlation within the study area is attributed to a combination of anthropogenic and pedogenic contribution to the magnetic susceptibility enhancement.

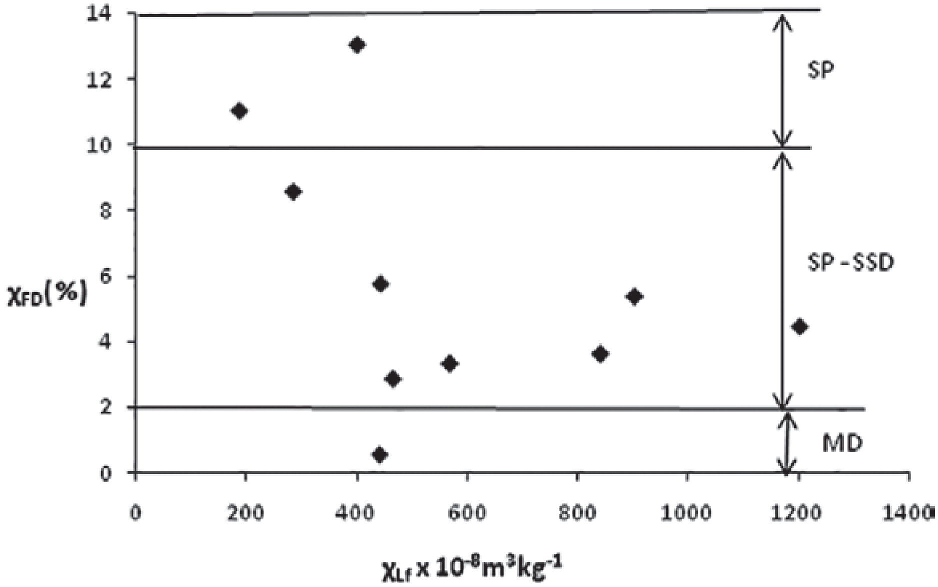

Figure 9. A schematic χ_{if} - χ_{fd} % scattering diagram showing typical positions of samples from JMP.

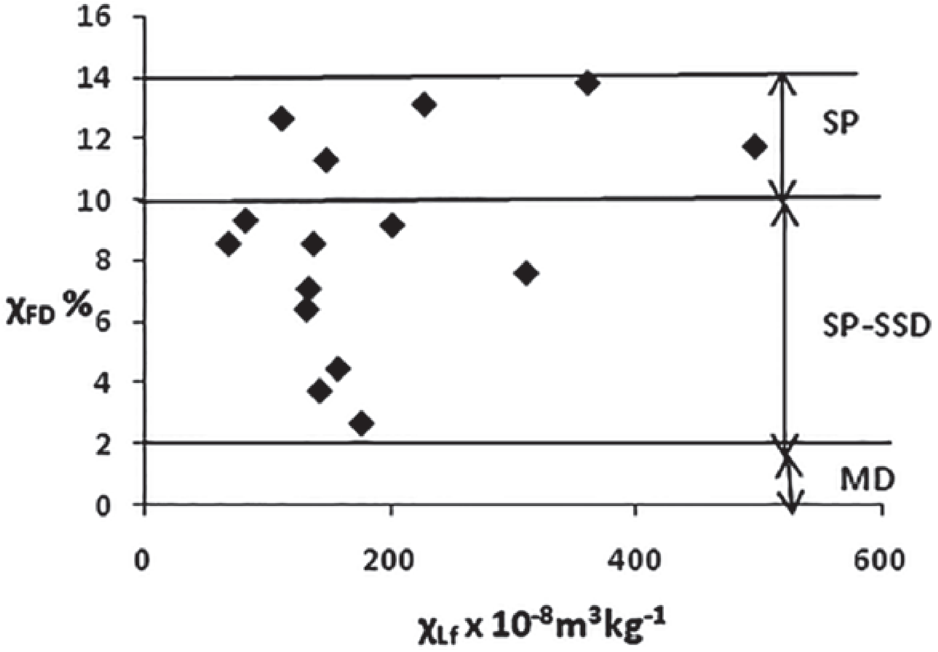

Figure 10. A schematic χ_{if} - χ_{fd} % scattering diagram showing typical positions of samples from JCOE.

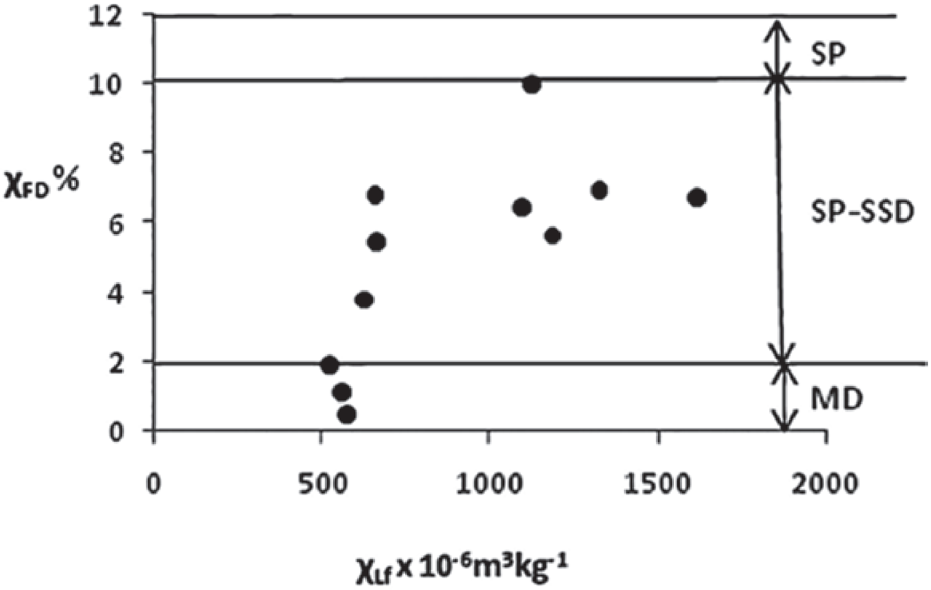

Figure 11. A schematic χ_{if} - χ_{fd}% scattering diagram showing typical positions of samples from JMM.

Conclusion

This paper presents the result of magnetic susceptibility measurements of topsoils in different areas of Jalingo based on different types of human activities undertaken. The results shows significant magnetic enhancement which indicates the high concentration of ferrimagnetic minerals in the soil. The magnetic susceptibility of the different land use studied decreased in the order commercial area (market) > motor park > school premises. The significant magnetic enhancement also implied that the soils in the studied areas were polluted. Pollution distribution can be known by measurement of MS. Since the MS method is cheap, fast and capable of covering wide area in a short time, it can be used as preliminary tool to detect pollution hotspots before the application of the time consuming and expensive geochemical methods to selected samples.

Evaluation of the background MS from the graph of χ_{lf} and χ_{fd} reveal that all the samples had MS value beyond the background values, indicating significant enhancement in the soils caused by the different land use.

The results of the percentage frequency dependence showed that most of the samples have a mixture of SP and coarser non SP grains or SP grains < 0.05µm. This implied that the observed magnetic susceptibility values results from a combination of pedogenic and anthropogenic sources.

References

Alagarsamy R., 2009, Environmental Magnetism and Application in the Continental Shelf of Sediments of India. *Mar. Environ. Res*., 68, 2, pp 49 – 58.

Canbay M., 2010, Investigation of the Relationship between Heavy metal Contamination of soils and its Magnetic Susceptibility. *International Journ. of Physical Sciences,* 5, 5, pp.393 – 400.

Carter J.D., Barber W., Tait E.A., 1963, The Geology of parts of Adamawa, Bauchi and Bornu Provinces in Northeastern Nigeria. Bull. No. 30, *Geological Survey of Nigeria,* 108.

Dearing J.A., 1999, Environmental Magnetic Susceptibility, Using the Bartington MS2 System. Second edition, England: *Chi Publishing.*

Dearing J.A., Dann R.J.L., Hay K., Lees J.A., Loveland P.J., Maher B.A, O'Grady K., 1996, Frequency Dependent Susceptibility Measurements of Environmental Materials. *Geophys. J. Int.*, 124, 228 – 240.

du Preez J.W., Barber W., 1965, The Distinction of Chemical Quality of Ground Water in Northern Nigeria. Bull. 36, *Geological Survey of Nigeria,* 93.

Forster T.H., Evans M.E., Heller F., 1994, The Frequency Dependence of Low Field Susceptibility in Loess Sediments, *Geophys. J. Int.*, 118, 636 – 642.

Gautam P., Blaha U., Appel E., 2004, Integration of Magnetic Properties and Heavy Metal Chemistry to Quantify Environmental Pollution in Urban Soils, Kathmandu, Nepal. Extended Abstract: 19th Himalaya-Karakoram –Tibet Workshop, Niseko, Japan.

Gautam P., Blaha U., Appel E., 2005, Magnetic Susceptibility of Dust Loaded Leaves as a Proxy of Traffic -Related Heavy Metal Pollution in Kathmandu, Nepal. *Phy. Chem. Earth*, 29, 2201 -2211.

Kapicka A., Petrovsky E., Ustjak S., Macháćková K., 1999, Proxy Mapping of Fly-ash Pollution of soils around a Coal- burning Power Plant: A Case Study in the Czech Republic. *J. Geochem. Explor*., 66, 291 – 297.

Kim W., Doh S.J., Yu Y., 1999, Anthropogenic contribution of magnetic particulates in urban roadside dust. *Atmospheric Environment*, 43, 3137-3144.

Knab M., Hoffmann V., Petrovsky A. Kapicka A., Jordanova N., Appel E., 2006, Surveying the anthropogenic impact of the Moldan River Sediments and Nearby Soils using Magnetic Susceptibility. *Environ. Geol.,* 49, 527–535.

Le Borgne E., 1955, Susceptibité Magnétiqué anormale du Soil Superficiel. Ann. *Geophys.,* 11, 399 -419.

Li P., Qiang X.K., Xu X.W., Li X.B., Sun Y.F., 2010, Magnetic properties of street dust: A case in Xi'an city, Shaanxi province, China. *Chinese Journal of Geophysics,* 53, 1, pp 113-120.

Liu Q.S., Maher B.A., Yu Y., Deng C.I., Zhu R.X., Zhao X.X., 2005, Quantifying Grain Size Distribution of Pedogenic Magnetite Particles in Chinese Loess and its Significance for Pedogenesis. *J. Geophys. Res*., 110, B11102, doi: 10.1029/2005JB003726.

Lu S.G., 2003, Chinese Soil Magnetism and Environment. Higher Education Press, Beijing (in Chinese).

Lu S.G., Bai S.Q., Xue Q.F., 2007, Magnetic Particles as Indicators of Heavy Metals Pollution in Urban Soils: A case Study from the City of Luoyang, China. *Geophys. Journ. Inter.,* 171, 603 – 612.

Lu S.G., Bai S.Q., 2008, Magnetic Characterization and Magnetic Mineralogy of the Hangzhou Urban Soils and its Environmental Implications. *Chinese Journal of Geophys.,* 51, 3, pp. 549 – 557.

Magiera T., Strzyszcz Z., Kapicka A., Petrovsky E., MAGPROX TEAM, 2006, Discrimination of Lithogenic and Anthropogenic Influences on Topsoil Magnetic Susceptibility in Central Europe. *Geoderma*, 130, 299 – 311.

Macleod W.N., Turner D.C., Wright E.P., 1971, *The Geology of the Jos Plateau. Geological Survey of Nigeria, Bull.* No. 32, 18.

McCurry P., 1976, A Generalized Review of the Geology of the Precambrian to lower Paleozoic Rocks, Northern Nigeria: In Kogbe, C. A. (ed.), Geology of Nigeria, Elizabethan Press, Lagos. Pp. 13 -38.

Mullins C.E., 1977, Magnetic Suscep tibility of the Soil and its significance in Soil Science: a Review, *J. Soil Sci.*, 28, 223 – 246.

Petrovsky E., Ellwood B.B., 1999, Magnetic Monitoring of Air, Land and Water pollution. In: Maher, B. A. and Thompson, R. (eds.) Quaternary Climates, Environments and Magnetism. UK: Cambridge University Press, pp. 279 – 319.

Petrovsky E., Kapicka A., Jordanova N., Knab M., Hoffmann V., 2000, Low Field Magnetic Susceptibility: A Proxy Method in Estimating increased Pollution of different Environmental Systems. *Environ. Geol.,* 39, 312 – 318.

Sadiki A., Faleh A., Navas A., Bouhlassa S., 2009, Using magnetic susceptibility to asses soil degradation in the Eastrn Rif, Morocco. *Earth Surface Processes and Landforms,* 34, 15, 2057-2069.

Sangode S.J., Vhatkar K., Patil S.K., Meshram D.C., Pawar N.J., Gudadhe S.S., Badekar A.G., Kumaravel V., 2010, Magnetic Susceptibility Distribution in the Soils of Pune Metropolitan Region: Implications to Soil Magnetometry of Anthropogenic Loading. *Current Science,* 98, 4, PP. 516 -527.

Shen M., Hu S., Blaha U., Yan H., Roster W., Appel E., Hoffmann V., 2008, Magnetic Properties of Urban Soil Profiles and their Significance for traffic Pollution- Case Study of the Capital Airport Expressway in Beijing. Front. *Earth Sci. China*, 2, 4, 400 – 407.

Strzyszcz Z.T., Magiera T., Heller F., 1996, The Influence of Industrial Immsions on the Magnetic Susceptibility of Soils in Upper Silesia. *Stud. Geoph. Geod*., 40, 276 – 286.

Strzyszcz Z.T., Magiera T., 1998, Magneic Susceptibility and Heavy Metals Contamination in Soils of Southern Poland. *Phys. Chem. Earth,* 23, 1127 -1131.

Thompson R., Oldfield F., 1986, Environmental Magnetism. *Allen and Unwin*, London.

Turner D.C., 1964, Notes on Fieldwork of the Basement Rocks of 1: 250,000 Sheets 7 and 8. *Geol. Survey of Nigeria Report* No. 5503.

Wang X.Y., Lu Z., Deng C.L., Tan H.B., Song Y.G., 2003, Paleoclimate Significance of Mineral Magnetic Properties of Loess Sediments in Northern Qingai-Tibetan Plateau. *Chinese Sci. Bull.* 48, 2126 – 2133.

Worm H.U., Jackson M., 1999, The Superparamagnetism of Yucca Mountain Tuff. *J. Geophys. Res.* 104, 25415 – 25425.

Zhu R.X., Deng C.I., Jackson M.J., 2001, A Magnetic Investigation along a NW-SE transect of the Chinese Loess Plateau and its Implications. *Phys. Chem. Earth.* 26, 867 - 872.

Geofísica Internacional (2014) 53-4: 425-434

Original paper

Special 3D electric resistivity tomography (ERT) array applied to detect buried fractures on urban areas: San Antonio Tecómitl, Milpa Alta, México

René E. Chávez*, Gerardo Cifuentes-Nava, Andrés Tejero, J. Esteban Hernández-Quintero, and Diana Vargas

Received: June 21, 2013; accepted: May 20, 2014; published on line: October 01, 2014

Resumen

Las técnicas geofísicas se pueden emplear para entender las características físicas del subsuelo en áreas densamente pobladas, donde los asentamientos urbanos presentan problemas estructurales. Un ejemplo interesante se presenta en esta investigación, donde se aplica en tres dimensiones el método de Tomografía de Resistividad Eléctrica (TRE-3D) empleando arreglos alternativos que permiten investigar el subsuelo bajo las construcciones afectadas.
Se estudia un pequeño barrio compuesto por un bloque de casas dentro del pueblo de San Antonio Tecomitl. El área se encuentra hacia la planicie de la Sierra del Chichinautzin, en el límite sur de la Cuenca de México. Este asentamiento sufre de fuertes daños estructurales debido a fracturamientos y hundimientos en el subsuelo. El método TRE-3D se realizó para caracterizar el subsuelo bajo este complejo urbano. Se utilizó un arreglo de resistividad especial (geometría de ‹*herradura*‵) empleando una combinación de arreglos en "*L*", los métodos ecuatorial -dipolo y de Mínimo de Acoplamiento para ‹ *iluminar* ‵ en su totalidad el subsuelo que se encuentra debajo de la manzana de casas. Los modelos de resistividad calculados presentan un patrón de valores de alta resistividad, que coincide con las viviendas afectadas. Tal rasgo parece extenderse más allá de los límites de la región estudiada, y es probablemente parte de un sistema de fracturas más complejas. Es muy probable que las fracturas se produjeron debido al suelo pobremente consolidado, el cual es parte de una zona de transición; la intensa extracción de agua, que forman vacíos en el subsuelo provocando subsidencia y, finalmente, la existencia de fallas regionales de mayor extensión y profundidad que podrían controlar estas estructuras superficiales.

Palabras clave: tomografía de resistividad eléctrica 3-D, Geofísica urbana, fracturamientos, hundimientos.

R. E. Chávez*
G. Cifuentes-Nava
J. E. Hernández-Quintero
D. Vargas

Abstract

Geophysical techniques can be employed to understand the physical characteristics of the subsurface in highly populated areas, where urban settlements present structural problems. An interesting example is presented in this investigation, where three-dimensional Electric Resistivity Tomography (ERT-3D) is applied employing alternative arrays that allow investigating the subsoil beneath the affected constructions.
A small neighborhood comprised by a block of houses within the town of San Antonio Tecómitl is studied. The area is found towards the outskirts of the Chichinautzin range, in the southern limit of the Mexican Basin. This settlement suffers of strong damage in their structures due to fractures and subsidence within the subsoil. ERT-3D was carried out to characterize the subsoil beneath this urban complex. A special resistivity array (‵*horse-shoe*′ geometry) employing a combination of ‵*L*′, *equatorial-dipole* and *minimum-coupling* methods was carried out to fully ‵*illuminate*′ the subsoil beneath the block of houses. Computed resistivity models depicted a high resistivity pattern that coincides with the affected houses. Such pattern seems to extend beyond the limits of the surveyed areas, and is probably part of a more complex fracture system. It is very likely that fractures have been produced due to the poorly consolidated soil, which is part of a transition zone; the intense water extraction, that form ‵voids′ in the subsoil causing subsidence effects and finally the existence of regional faults to greater extent that might control these shallow features.

Keywords: electric resistivity tomography 3-D, urban Geophysics, fractures, subsidence.

Instituto de Geofísica
Universidad Nacional Autónoma de México
Del. Coyoacán, 04510
México D.F., México

Andrés Tejero
División de Ciencias de la Tierra
Facultad de Ingeniería
Universidad Nacional Autónoma de México
Del. Coyoacán, 04510
México D.F., México

Introduction

Urban development in modern cities requires of a more integral knowledge of the subsurface, mainly on those areas, where human concentrations increase. Mexico City is one example, where this megacity constitutes one of the largest concentrations of human activities in the world. Most of the urban area is underlain by lacustrine sediments of the former lakes, and confined by important volcanic ranges. Such sediments offer poor foundation conditions for constructive purposes. Therefore, high risk areas have to be identified to prevent accidents and disastrous events.

In the last three decades ERT-3D techniques have been developed, like the Roll-Along method to acquire 3D data (Dahlin and Bernstone, 1997). Such methodology consists on setting parallel lines that cover the study area. Observations are made in the 'x' and 'y' directions, which commonly employ the Pole-Pole array. An important amount of data can be obtained by using this technique, however data processing is cumbersome and sometimes data inversion takes too much time.

Loke and Barker (1996) designed a processing approach to decrease the number of data maintaining resolution and quality of the modeled data. This technique was named 'cross-diagonal survey', where the potential (V) observations are made in the electrodes lying in the horizontal, vertical and diagonal transects crossing the current electrode. The amount of data is reduced to the half, keeping significant quality and resolution. Aizebeokhai, *et al*. (2009) recommends a maximum separation between profiles of 4*a* in designing the survey grids, being *a* the electrode separation. Such rule guaranties good quality and resolution of the 3D resistive image of the subsoil. These techniques are suitable to open areas, as the example provided by Dahlin *et al.* (2002), when investigating karstic zones.

However, cities and in general urbanized zones present a different challenge. In this case, the urban spots extend towards the already scarce open spaces, leaving the streets to carry out geophysical observations in terms of 2D profiles. Therefore, the already mentioned 3D techniques cannot be applied. However, geophysical transects are not ideal to obtain a complete cover of the studied area (Deceuster and Kaufmann, 2003). On the other hand, the distance between parallel streets can be larger than the distance recommended by Aizebeokhai, *et al.* (2009), if grids or Quasi-3D methods are considered. Thus, interpretation of such sets of data cannot be reliable. Geophysical prospecting methods are challenged, when applied on highly urbanized areas, where habitation complexes (Trogu *et al*., 2011; Chávez *et al*., 2014), schools, historical monuments (Chávez *et al*., 2010; Argote *et al.*, 2013), prevent the positioning of profiles in parallel to form grids. In order to overcome this problem, an alternative technique is employed, that allows acquiring reliable distribution of resistivity data at depth beneath the affected area without the need of parallel transects across the constructions

An example of one of such heavily urbanized sectors within the Mexican Basin is found in Tecomitl, a small town belonging to Milpa Alta County, towards the southeastern limits of the Country's capital, which is part of the so called transition zone (Marzal and Massari, 1969). This is a small neighborhood possessing a high concentration of low- to middle-class houses comprised by one- and two-story edifications, where some of these dwellings are being affected by cracks and fissures in their constructions. County authorities are worried about the possibility of a soil collapse in this area and its disastrous effects on this community. Therefore a three dimensional Electric Resistivity Tomography (ERT-3D) was carried out to characterize the subsoil beneath the buildings, as a project to allow the authorities to establish a plan to remediate the vulnerable zones.

ERT-3D Methodology

Unfortunately, there is no sufficient space to deploy the geophysical transects through the dwellings and settlements composing this locality due to the heavy urbanization this neighborhood possesses. Therefore, a special array type (*Horse-Shoe* geometry) was employed (Argote *et al.*, 2013; Tejero *et al.,* 2014). The so named *horse-shoe* array employed in this investigation is a combination of different special arrays designed to cover the subsurface by means of a series of apparent resistivity observations at depth. These arrays are the '*L*-array' (Chávez *et al*., 2011; Tejero *et al.,* 2014), the equatorial (*EQ*) and the minimum coupling (*MC*) settings (Argote *et al.*, 2013).

This special geometry attempts to cover the subsurface with resistivity observations underneath the neighborhood. ERT-3D data was acquired employing a Syscal-Pro resistivimeter (IRIS Instruments) with 48 channels. Electrodes were inserted deep enough (~0.6 m) to make contact with the '*natural*' soil, with a separation of 4m. Cables and electrodes were deployed along the narrow streets surrounding the neighborhood studied. The *horse-shoe* dispositive designed to survey the area possesses a length on each side of 80 m long, approximately. Display of apparent resistivities at depth were computed with the help of the software Electre-Pro (Iris Instruments, 2010), which computes the attribution point of each apparent resistivity measured at depth

The *L*-array

This ERT array was explained in detail by Chávez *et al.* (2011) and Argote *et al.* (2013). In this case, two perpendicular ERT profiles are needed. The horseshoe arrangement employed in this investigation is depicted in Figure 1. This array allows surrounding the structure to be studied. In this particular example three 'L's are carried out. The WS array is employed; the current electrodes (in red) are moved one electrode as well as the potential electrodes (Figure 1A), where the arrows define the direction of movement. Figure 1B depicts the distribution at depth of the apparent resistivities measured. Separation between current electrodes is increased by two electrode positions and the procedure is repeated once more. The process ends when the all electrodes in this geometry are used.

Dipole-Equatorial (*EQ*) array.

Such an array needs two parallel ERT lines (Figure 2A), where the current electrodes are kept fixed at the corner of each ERT line. The potential electrodes (M, N) will move in the direction of arrows until the total number of electrodes in each line is completed. Then, the current electrodes (A, B) move one electrode up (A). The resulting subsurface resistivity observations are displayed in (Figure 2B). It is possible to observe that each point at depth as well as the shallow line of observations is generated for each electrode change along the parallel transects (P1 and P2).

Minimum Coupling (*MC*) array.

Two parallel lines are also needed to carry out the apparent resistivity observations, as mentioned above. The current electrodes are set at the corners of each ERT. In this array (Figure 3A), the current electrodes are fixed (A, B), whereas the potential (M, N) electrodes move along the P1-P1' line in the S-N direction. Such process continues until the last electrode is reached. Then, the current electrodes move one electrode space up and the process start again. The progression is over when the last electrode is reached. Then, the same procedure follows with the next line (P2-P2') and everything goes exactly the same. Observe the apparent resistivity distribution at depth obtained with this process. Two different resistivity patterns are obtained.

Area Of Study

The area under study is found towards the southern portion of the Basin of Mexico, within the San Antonio Tecómitl town (Figure 4A). Geologically speaking, the area belongs to a transition zone identified by Marsal and Mazzari (1969). These authors divided the Basin of Mexico in three different regions. Zone I (Hilly zone) is formed by harder materials products of past eruptive events and found in the high

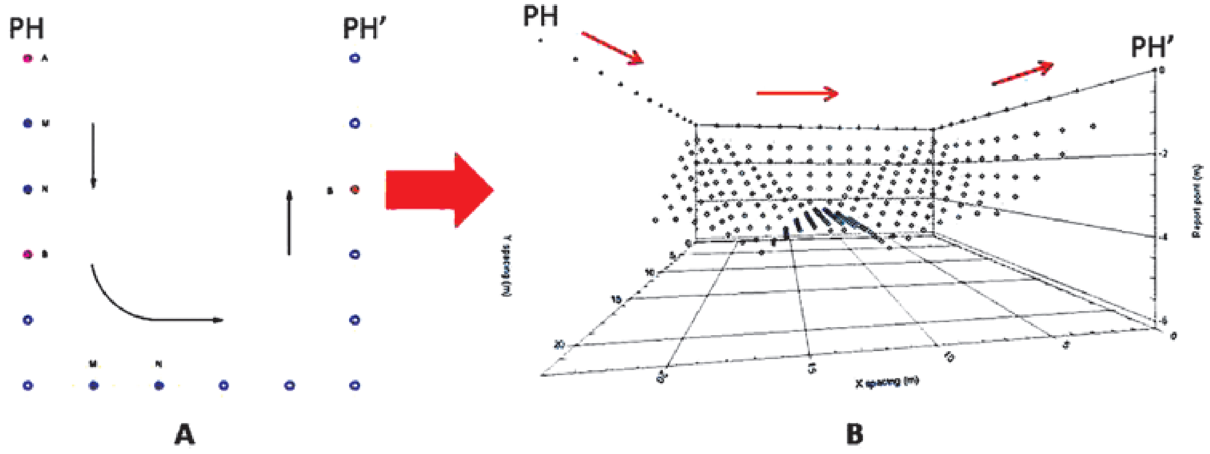

Figure 1. Sequence designed to calculate the '*L*' array (A), A and B indicate the current electrodes and M and N the potential electrodes. The computed distribution of observed apparent resistivities as measured by the resistivimeter is shown (B).

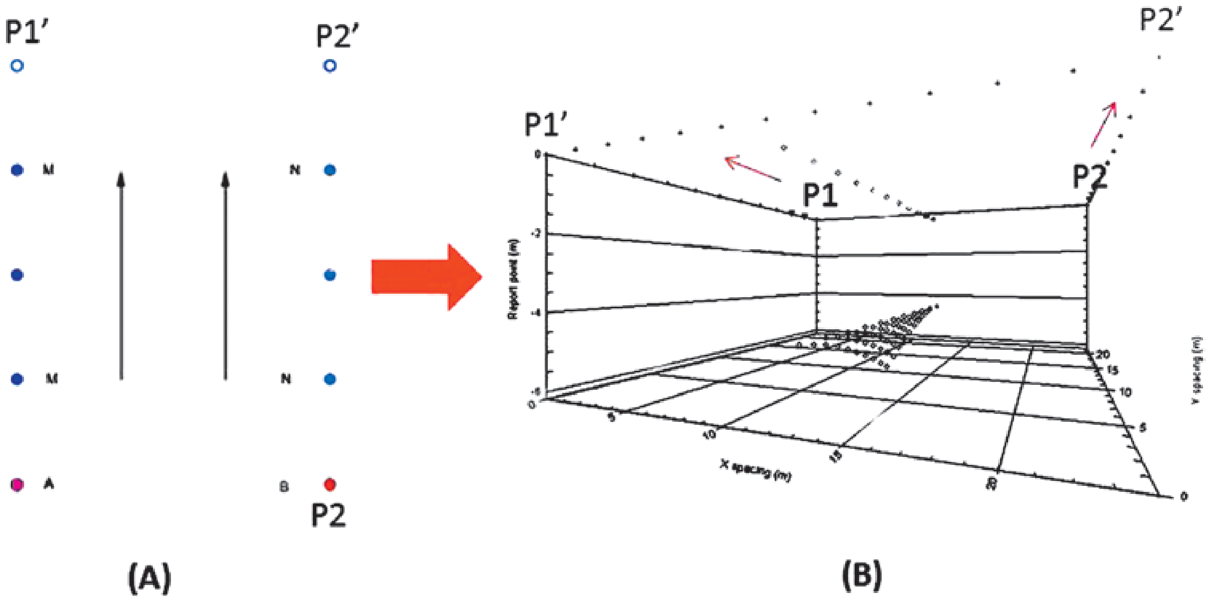

Figure 2. Sequence designed for the Equatorial Dipole dispositive (A) and the distribution of measured apparent resistivities at depth (B) are depicted.

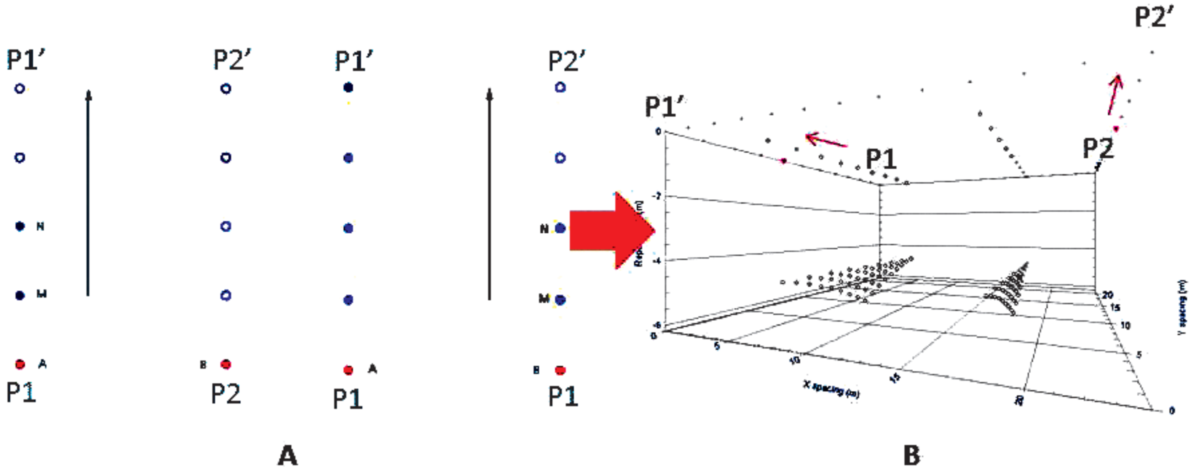

Figure 3. Sequence designed for the Minimum Coupling (MC) (A) and distribution at depth of apparent resistivities (B) are displayed.

ranges surrounding the basin. They have good load capacity and negligible compressibility. Zone II is a region that possesses poor stability, suffering of differential subsidence effects. Finally, Zone III ((Lacustrine Zone) is composed mainly by clayey sediments, and poorly consolidated materials that once were the bottom of the ancient lake of Texcoco in pre-Hispanic times. This small urbanized region is found on top of clays and sand lenses interbedded with soft eruptive materials (volcanic tuffs).

Some of the dwellings composing the studied area present important damages in their foundations, walls and roofs. Images depicted by Figures 4B and 4C show part of the damage found in the constructions located in this neighborhood. Subsidence effects and fractures observed in many portions of the dwellings are possibly produced by the ground water extraction; rain water flows from the highlands that undermine the shallow sedimentary layers at depth, and possible problems of anthropogenic origin, like water leaks from the water distribution network and so on.

ERT-3D Investigation

The geophysical study was carried out within the boundaries of a block of houses to characterize the subsoil beneath this settlement. Figure 5A outlines the horse-shoe array. Each circle and number depicts the position of every electrode along the streets surrounding the neighborhood. The main goal is to detect a fracture that crosses underneath, where evidence of such a feature can be observed in several homes, in terms of fissures in walls, and small fractures on the paved roads.

Figure 5B depicts the observations at depth as calculated by using the program ElectrePro (IRIS, 2010). A total of 824 resistivity observations at depth can be estimated, depicted as black dots. A good coverage towards the northern portion of the working cube is attained. Black squares in the image depict the location of the 48 electrodes deployed partially surrounding the neighborhood. Unfortunately, the southern portion of the measured square could not be closed, due to the heavy traffic found in 5 de Mayo Avenue. We could not get permission by the local authorities to close the traffic in that street.

It is possible to observe the measured apparent resistivities calculated by the program Electre-Pro and visualized with a special representation program. Figure 6 displays the 824 apparent resistivities at depth. Each color determines the resistivity value measured with the resistivimeter, note that negative values are present. Such type of data is due to the methodology employed to compute every data point at depth. Yellow circles define the position of the electrodes. The highest variation in these values is found towards the northwestern portion of the *horseshoe* array, where low (~10 Ohm-m) to high (>200 Ohm-m) apparent resistivity values have been measured. In general, apparent resistivity values are around 100 Ohm-m, which suggests that this is the average resistive value for the subsoil. Even if high resistive values are found in the deepest line provided by the MC array, it is clear that resolution at that depth with the array employed will be poor. Therefore, the array presented in this investigation may resolve anomalous resistivities located up to a depth of 20 m, approximately. Deeper resistive structures will have no meaning, and then a constraint can be added to the inversion process in terms of the maximum depth to be investigated.

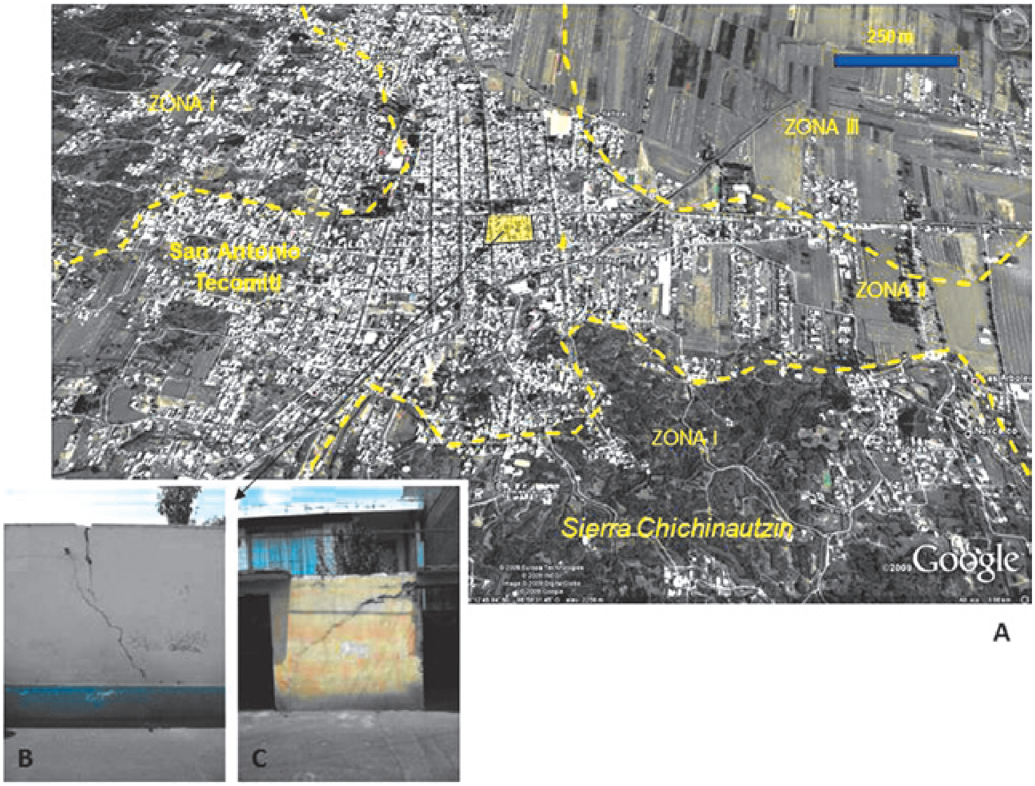

Figure 4. The satellite image (Google, 2012) displays the San Antonio Tecomitl town. The inset depicts the different damages (B) and (C) observed in the study area. Note fissures and cracks on walls.

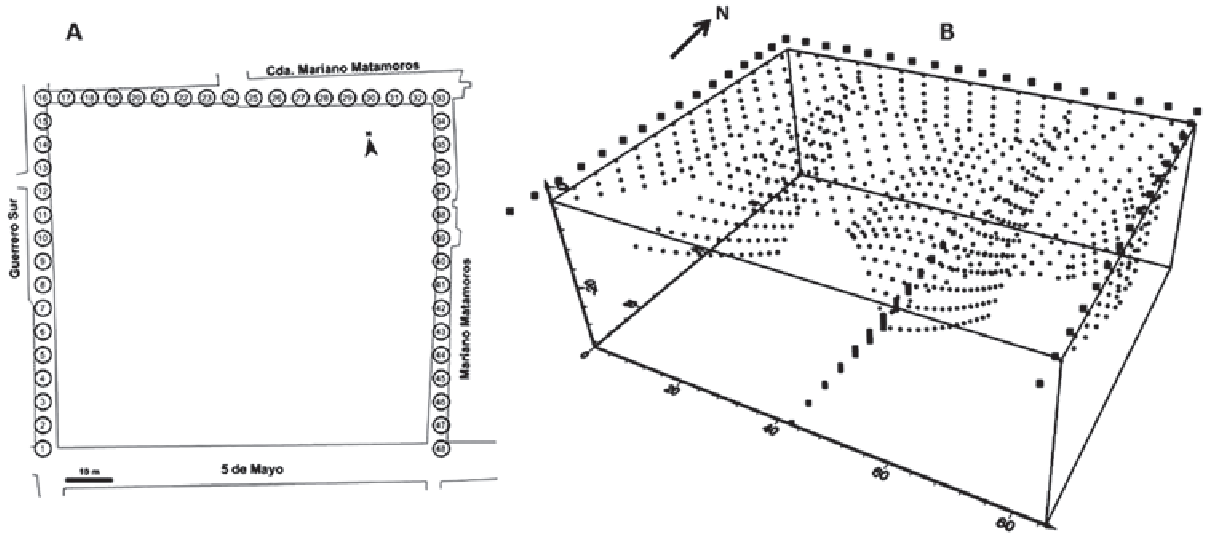

Figure 5. The *horse-shoe* array designed to study the affected block of houses. Circles and numbers indicate the location of the electrodes (A). The computed distribution of apparent resistivities at depth is depicted (B). 824 quadripoles are computed with a maximum penetration depth of 20 m.

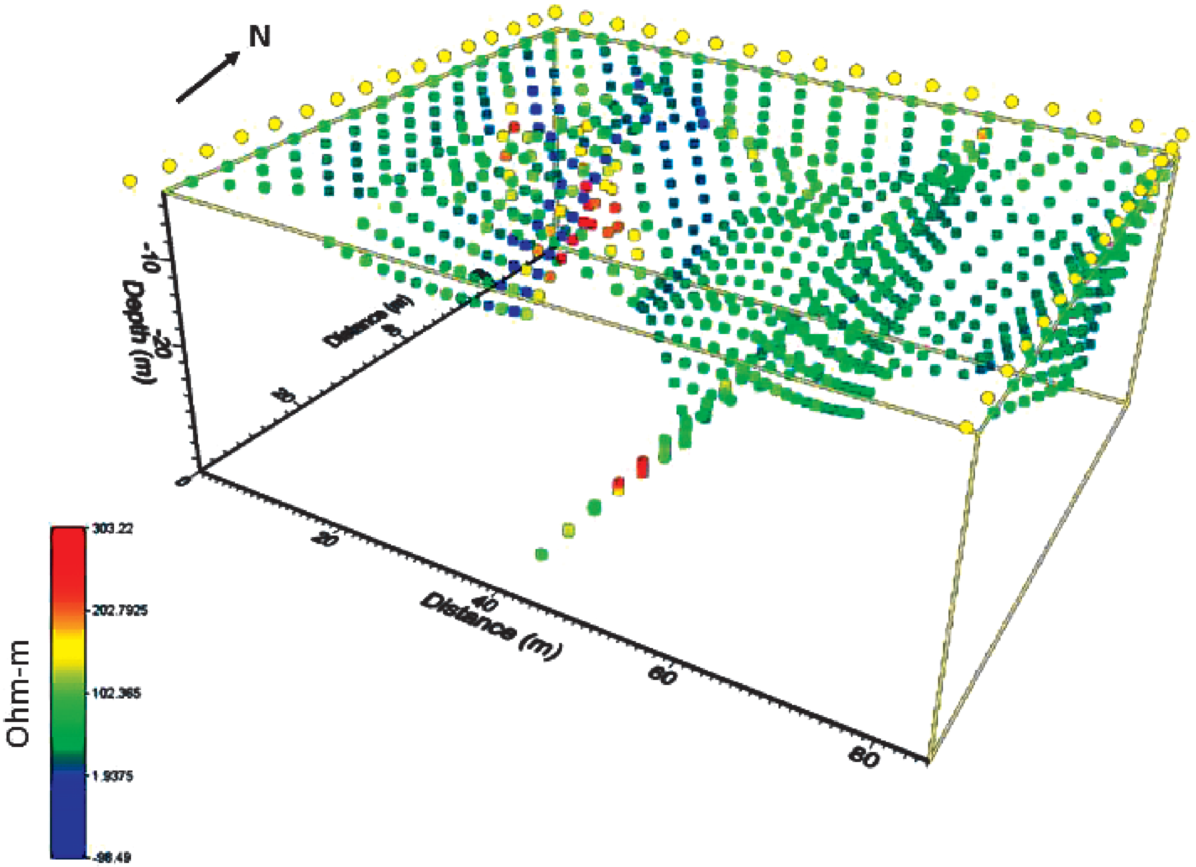

Figure 6. Measured resistivities at depth obtained from the field survey. Colors indicate the observed apparent resistivity value.

The inversion process carried out to compute the three dimensional resistivity model is an important module of the EarthImager3D (AGI, 2012) commercial package. This is based on the methodology described by Loke and Barker (1996), which is explained in detail by Tejero *et al.* (2002). The mathematical modelling of the real resistivities at depth includes several steps to arrive to a final solution. Initially, a starting model is constructed based on a given apparent resistivity distribution at depth. In this case, a half-space with a constant resistivity is assumed. Then, a selection of a non-linear optimization technique can be performed. Such a procedure must include the solution of a linearized inverse problem based on the current model and data misfit for a model update. Therefore, the elements of a Jacobean matrix must be assessed to finally solving the system of equations. It is important to mention that the underdetermined and ill-posed nature of the 3D resistivity data, which generally speaking, most of the geophysical data share; makes the inverse solution non-unique and ambiguous. Therefore, additional constraints or other type of criteria must be imposed to obtain a reasonable solution. In this investigation, we have employed the smooth model inversion, which is also known as Occam's inversion (Lines and Treitel, 1988; DeGroot-Hedlin and Constable, 1990). This type of process assumes that errors follow a Gaussian distribution (Tejero *et al.*, 2002).

The misfit between the observed and computed values can be represented as the dispersion of the computed resistivity values in terms of the observed apparent resistivities. Figure 7A depicts the cross-plot calculated by the commercial program employed (EarthImager3D), which allowed to keep track of every inverted step. An initial RMS value of 20% is obtained for the first iteration process, where 8 iterations followed to reach a final solution. The corresponding cross-plot shows a much better fit between the observed and computed data (Figure 7B), with the corresponding RMS error computed of 8.9%.

The inverted solution shows a high resistive alignment, which could be associated to a possible fracture (Figure 8A). As expected, the southern portion of the resistivity cube lacks of resolution. Figure 7B depicts the working cube from the top, and Figure 7C from the bottom, selecting a high resistivity (160 Ohm-m to 1,000 Ohm-m) interval. It is clear the high resistivity values depicting a NE-SW feature. Such an alignment can be associated to the presence of a fracture.

These high resistive values (~1000 Ohm-m) can be explained by assuming that the low consolidated materials forming this lacustrine basin (mainly clays) may fill the fracture, increasing its apparent resistivity, which is proportional to their porosity. It is expected that pores within the clays are mostly occupied by air, which behaves as a dielectric fluid, during the dry season (Ovando-Shelley *et al*., 2007).

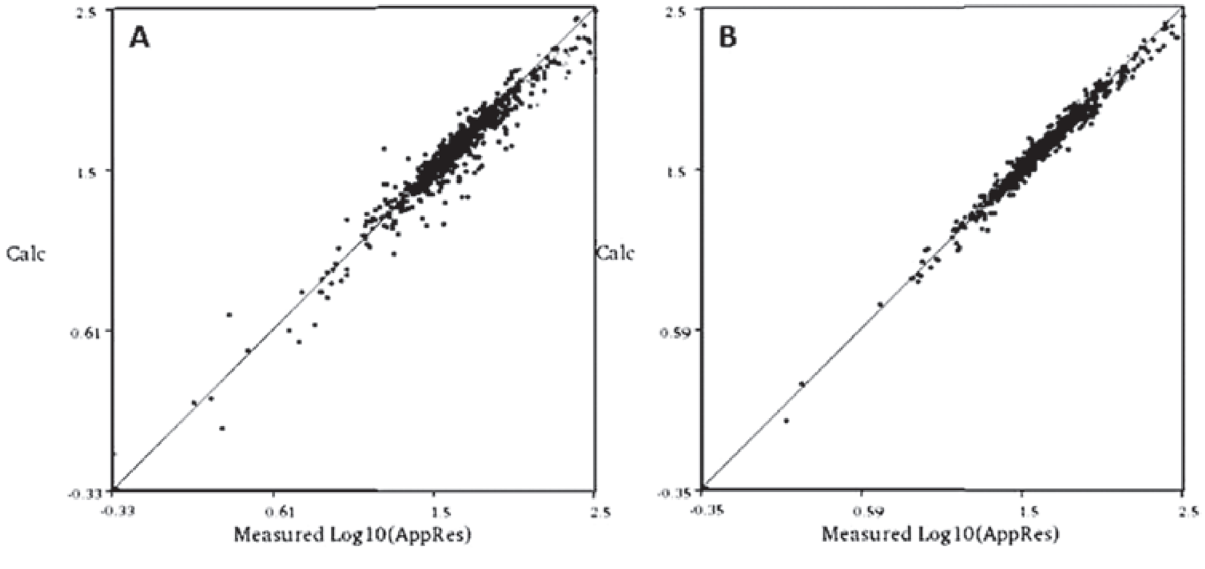

Figure 7. Apparent resistivity cross-plots calculated for the initial iteration (A) and the final iteration (B). 8 iterations were needed to come up to a final inverted resistivity model.

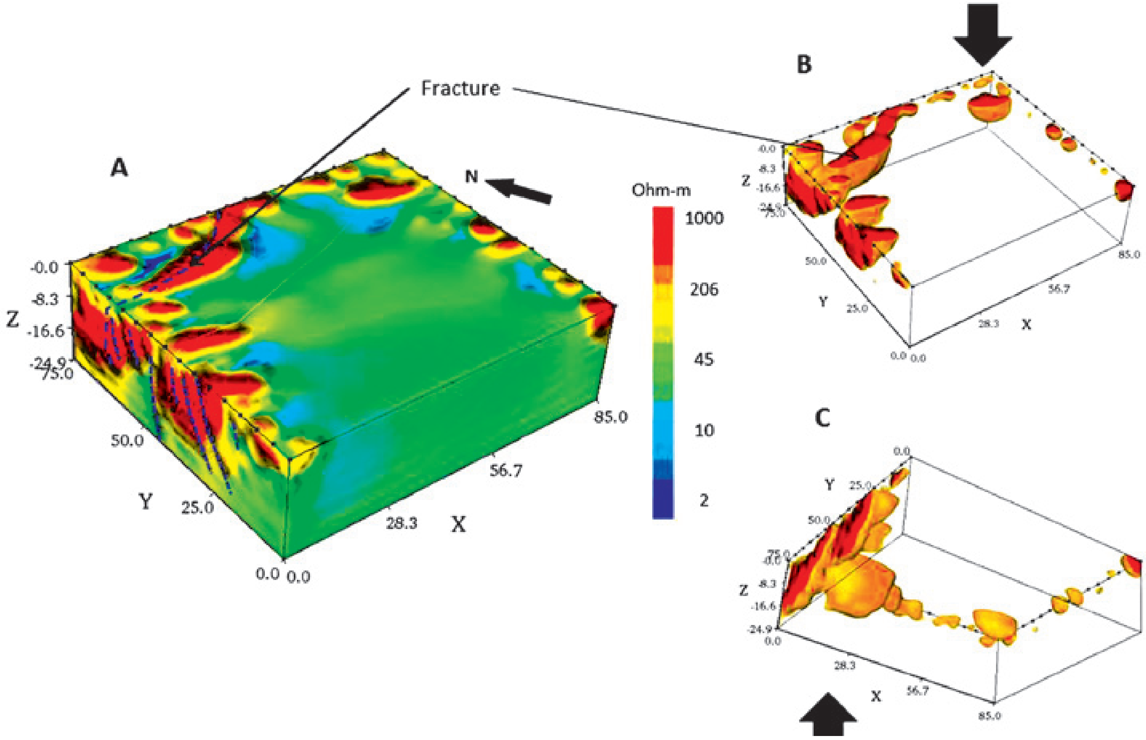

Figure 8. The inverted cube is shown (A). High resistivity values can be associated to a fracture. Images to the right depict the working cube from the top (B) and from the bottom (C). Only high resistive values (~1000 ohm-m) are depicted to observe clearly the resistive anomaly.

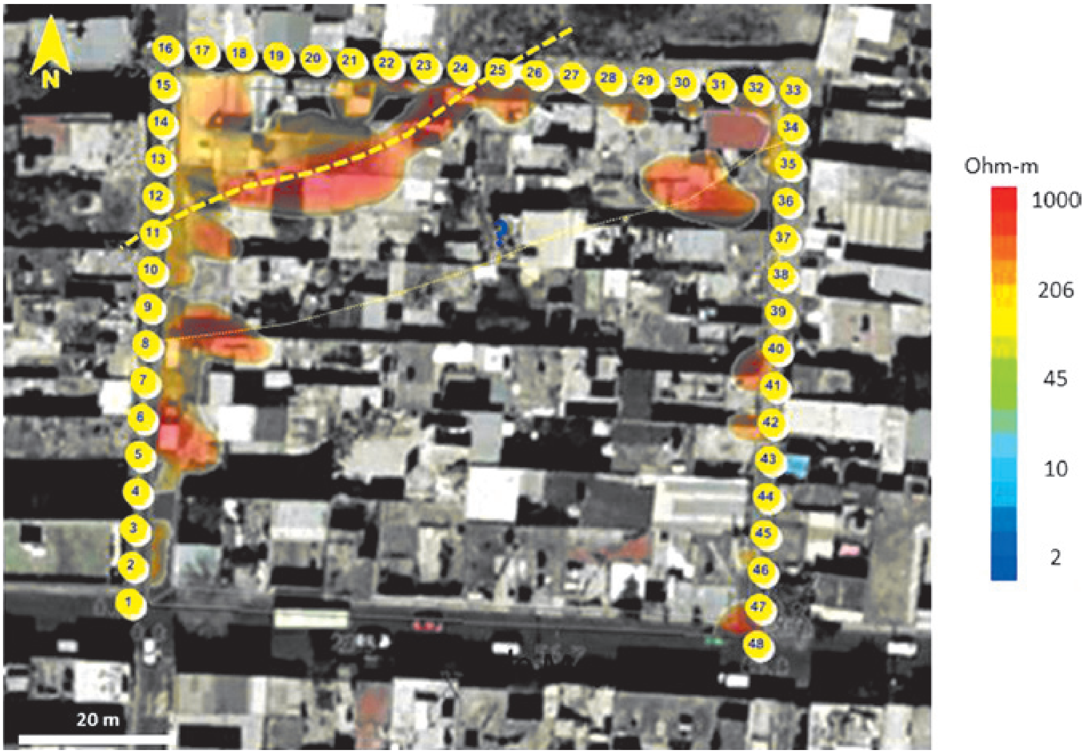

Figure 9. The working cube is observed from the top. The Google image (Google, 2012) is superimposed on top of the resitivity anomalies. Observe the fracture in the NE-SW direction.

The 3D model has been superimposed over the satellite image (Google-Earth, 2012) in Figure 8. It is possible to observe that the high resistive alignment crosses in the NE-SW direction a series of houses within the studied neighborhood. Some of the fissures and cracks observed on the pavement and walls of houses coincide with the detected structure (Figure 4B and Figure 4C). These problems in the subsoil can be attributed to differences in water content leading to subsidence problems beneath houses or a differential compaction of sands and clays comprising the materials forming the Zone II.

Conclusions

The 3D methodology employed with the '*horse-shoe*' array discussed in this investigation resolves adequately the characteristics of the subsurface. This methodology loose shallow information, due to the missing data points at the central and southern portions of the array, where no-electrodic line could be set, nevertheless, reliable information up to a depth of 20 m can be attained.

Computed resistivity models depicted the buried fracture pattern affecting the urban complexes. Such pattern seems to extend beyond the limits of the surveyed areas, and is probably part of a more complex fracture system. It is very likely that fractures have been produced due to the poorly consolidated soil, which is part of a transition zone (Zone II, according to Marssal and Massari, 1969); the intense water extraction, that form 'voids' in the subsoil causing subsidence effects and finally the existence of regional faults to greater extent that might control these shallow features.

Results provided useful information about the resistivity distribution beneath the areas studied, leaving to the corresponding authorities to define the remediation process to be carried out in this section of San Antonio Tecomitl to avoid possible collapses of the subsoil.

This methodology provides of a new alternative tool to investigate the subsurface beneath constructions, where it is not possible to set a traditional ERT-3D array in urban populated areas or buildings.

Aknowledgments

We thank the authorities of the Milpa Alta County, Dirección de Protección Civil for allowing us to carry out the field survey within the San Antonio Tecomitl urban zone. We are also grateful to the Engineering Geophysics students from the Faculty of Engineering UNAM for helping us in the field work. This study was financed by the Mexico City's Secretaría de Ciencia, Tecnología e Inovación agreement # PINV11-6. D. Vargas received a scholarship from this project.

References

AGI, 2010, EarthImagerTM 2D and 3D, Resistivity and IP inversion software: Advanced Geosciences Incorporated, www.agiusa.com.

Aizebeokhai A.P., Olayinka A.I., Singh V.S., 2009, Numerical evaluation of 3D geoelectrical resistivity imaging for environmental and engineering investigations using orthogonal profiles, SEG *Expanded Abstracts*, 1440, doi:10.1190/1.3255120.

Argote-Espino D., Tejero-Andrade A., Cifuentes-Nava G., Iriarte L., Farías S., Chávez RE., López F. 2013. 3D electrical prospection in the archaeological site El Pahñu, Hidalgo State, Central Mexico: *Journal of Archaeological Science*, 40, 1213-1223.

Chávez G., Tejero A., Alcantara M.A., Chavez R.E., 2011. The 'L-Array', a tool to characterize a fracture pattern in an urban zone: Extended Abstracts of the 2011 Near Surface Geophysics meeting, *European Section Meeting* (Printed in CD), Leicester, UK.

Chávez R.E., Tejero A., Cifuentes G., Hernández E., Aguilar D., 2014, Imaging fractures beneath a residential complex using novel 3D electrical resistivity arrays: *Journal of Environmental and Engineering Geophysics*. In revision.

Dahlin T., Bernstone C., 1997, A roll-along technique for 3D resistivity data acquisition with multi-electrode arrays: 10th *Annual Meeting of the Symposium on the Application of Geophysics to Engineering and Enviromental Problems*, 927-35.

Dahlin T., Bernstone C., Loke M.H., 2002, A 3-D resistivity investigation of a contaminated site at Leernaken, Sweden, *Geophysics*, 67, 1692-1700.

Deceuster J., Kaufmann O., 2003, Applications des tomographies en résistivité électrique 3D à la reconnaissance de zones Karstifiées, Belgique, *Actes du 4ème Colloque GEOFCAN*, 143-150.

DeGroot-Hedlin D., Constable S., 1990, Occam's inversion to generate smooth, two-dimensional models from magnetotelluric data, *Geophysics*, 55, 1613-1624.

Google-Earth, 2012, www.google.com.mx/intl/es/earth/.

IRIS, 2010, ElectrePro@ software: User manual. www.iris-instruments.com.

Lines R.L., Treitel S., 1988, Tutorial: A review of least-squares inversion and its application to geophysical problems, *Geophysical Prospecting*, 32, 159-186.

Loke M.H., Barker R.D., 1996, Practical techniques for 3D resistivity surveys and data inversion. *Geophysical Prospecting*, 44, 449-523.

Tejero A., Chávez R.E., Urbieta J., Flores-Márquez E.L., 2002, Cavity detection in the south-western hilly portion of Mexico City by resistivity imaging: *Journal of Engineering and Environmental Geophysics*, 7-3, 130-139.

Tejero A., Cifuentes G., Chávez R.E., López-González A., Delgado-Solorzano C., 2014, "L" and "Corner" arrays for 3D electrical resistivity tomography: An alternative for urban zones: *Near Surface Geophysics*. In press.

Trogu A., Ranieri G., Fischanger F., 2011, 3D electrical resistivity tomography to improve the knowledge of the subsoil below existing buildings: *Environmental Semeiotics*, 4-4, 63-70.

Geofísica Internacional (2014) 53-4: 435-456

Original paper

Ca. 13 Ma strike-slip deformation in coastal Sonora from a large-scale, *en-echelon*, brittle-ductile, dextral shear indicator: implications for the evolution of the California rift

David García-Martínez*, Roberto Stanley Molina Garza, Jaime Roldán Quintana, Hector Mendívil-Quijada

Received: September 02; 2013; accepted: February 18, 2014; published on line: October 01, 2014

Resumen

La estructura semicircular Rancho Nuevo es una estructura geomorfológica definida por patrones de drenaje en la planicie costera de Sonora, localizada a 160 kilómetros al noroeste de Hermosillo. Su extensión es de 15 por 30 kilómetros y está compuesta por un núcleo de plutones de composición félsica-intermedia (granodiorita, monzogranito, cuarzo pórfido y granito), cubiertos por rocas volcánicas del Mioceno. Este trabajo está enfocado a la deformación de los intrusivos que abarcan casi la totalidad del área de estudio. Los plutones consisten en una serie co-magmática fechada entre 71 ± 1.1 y 67.9 ± 1.0Ma (U-Pb en circones, LA-ICP-MS). La unidad más voluminosa es una granodiorita caracterizada por un fracturamiento conspicuo de forma sigmoidal visible a escala de imágenes de satélite de alta resolución, a lo largo del cual se emplazaron diques de composición riolítica de 13.2 Ma (U-Pb en circones, LA-ICP-MS). La fabrica magnética (AMS) y los datos paleomagnéticos fueron colectados en 27 sitios en la unidad granodiorita. La fábrica magnética es débil pero bien definida y se caracteriza por contener planos de foliación en la roca bien desarrollados con rumbos que siguen el patrón de fracturamiento sigmoidal sugiriendo un aplanamiento NE-SW a NW-SE, posterior al emplazamiento. La magnetización característica es de polaridad dual, pero dominantemente inversa y consistente con un emplazamiento durante el cron C31r. La magnetización prevalente es suroeste y moderadamente negativa (10 sitios), mostrando una rotación en sentido horario alrededor de 41º ± 11 con respecto a la dirección de referencia esperada del Cretácico Tardío. Sin embargo, existe evidencia paleomagnética que sugiere que la estructura Rancho Nuevo no rotó como un cuerpo rígido, sino que en su lugar se deformó internamente. Estos datos indican que la estructura semicircular Rancho Nuevo registra cizallamiento, dextral, frágil-dúctil, a gran escala. La edad de los diques y su relación discordante por rocas asignadas a la Toba San Felipe indican que el movimiento dextral de la península de Baja California (y por lo tanto la placa del Pacífico) afectó la costa de Sonora hace aproximadamente 13 Ma.

Palabras clave: Mioceno, Golfo de California, Sonora, rumbo de desplazamiento, paleomagnetismo

---

D. García-Martínez*
J. Roldán Quintana
H. Mendívil-Quijada
Posgrado en Ciencias de la Tierra
Universidad Nacional Autónoma de México
sede Hermosillo
Boulevard Colosio y Madrid, s/n
83000, Col. Centro
Hermosillo, Sonora, México
Corresponding author: davidgm1964@yahoo.com.mx

R. Stanley Molina Garza
Centro de Geociencias
Universidad Nacional Autónoma de México
Campus Juriquilla, 76230
Querétaro, México

Abstract

The Rancho Nuevo semi-circular structure is a geomorphological structure defined by drainage patterns in coastal Sonora, about 160 km NW of Hermosillo. The structure is about 15 by 30 km, and it is cored by felsic to intermediate plutons (granodiorite, monzogranite, quartz-porphyry) covered by Miocene volcanic rocks. This work is focused on the deformation of the intrusives which cover most of study area.The plutons are a co-magmatic suite dated between 71±1.1 and 67.9±1.0Ma (U-Pb zircon, LA-ICPMS). The most voluminous unit is a granodiorite characterized by conspicuous sigmoidal fractures at the scale of high resolution satellite images, along which rhyolite dikes were emplaced about 13.2 Ma. Magnetic fabric (AMS) and paleomagnetic data were collected from 27 sites in the granodiorite. Magnetic fabrics are weak but well developed, and are characterized by steep foliation planes with strikes that follow the sigmoidal fracture pattern and suggest NE-SW to NW-SE flattening after emplacement. The characteristic magnetization is of dual polarity, but it is dominantly reverse consistent with emplacement during chron C31r. The prevalent magnetization is southwest and moderately steep negative (ten sites), a discordant direction rotated clockwise about 41º±11 with respect to the expected Late Cretaceous reference direction, also indicating gentle southward tilt. There is, however, paleomagnetic evidence suggesting that the structure did not rotate as a rigid body, but it deformed internally instead. These data are interpreted to indicate that the Rancho Nuevo semicircular structure is a large-scale, dextral, brittle-ductile shear indicator. The age of the dikes and the fact that they are covered discordantly by rocks assigned to the tuff of San Felipe indicate that northwest, srike-slip, motion of Baja California peninsula (and thus the Pacific plate relative to North America) was accommodated by faults in coastal Sonora about 13 Ma ago.

Key words: Miocene, Gulf of California, Sonora, strike-slip, paleomagnetism

Introduction

Western North America is perhaps the best studied convergent margin in the world, and possibly the best suited to study oceanic plate-continent interactions. The arrival of the spreading center that existed between the Farallon and Pacific plates to the convergent margin of western North America by the end of Oligocene gave rise to major plate reorganization that subsequently resulted in deformation in the plate boundary region. The margin changed from subduction of the Farallon plate under North America to a dextral oblique transform between the Pacific plate and North America. This resulted, eventually, in rifting between Baja California and North America in the Miocene as this block was transferred to the Pacific plate. There is disagreement among the authors working in the region, however, on the timing and the geodynamics of the changes described above. One of the most contentious issues is whether the initial rifting process between Baja California and North America, between about 13 and 6 Ma, was orthogonal or dextral-oblique strike slip. Answering this question requires field studies, to determine the timing and kinematics of the faults along the plate boundary region.

Before the arrival of the Farallon-Pacific ridge to the continental margin, the plate boundary evolved as a compressional Cretaceous to Paleogene continental arc where subduction consumed the Farallon plate forming the Peninsular Ranges and the coastal Sonoran batholith.The semicircular structure Rancho Nuevo (RNSS) is part of the coastal Sonoran batholiths. This paper focus is on the deformation of the granitoids of the RNSS in the central coast of Sonora. New field work, geochronology, and paleomagnetic data show that Late Cretaceous intrusives were rotated about a vertical axis and deformed in a dextral-shear couple. This rotation and deformation of the RNSS are interpreted in terms of plate interactions, and contribute to better understanding the Gulf of California history. Here we interpret the semi-circular Rancho Nuevo structure as a feature produced by dextral shear *ca*. 13 Ma. The RNSS is a dextral, *en-echelon system*, with brittle-ductile structures associated to right-lateral faults that accommodated motion between Baja California (Pacific plate) and Sonora (North America plate).

Tectonic model for Cenozoic evolution of NW Mexico

The geologic evolution of NW Mexico is closely linked to oceanic plate-continent interactions. Subduction of the Farallon plate produced voluminous arc magmatism, and was also the main driver of the Late Cretaceous-Paleogene Laramide orogeny. The Laramide thickened the crust and created significant topography. This event was followed by the basin and range extensional episode along western North America; extension led to crustal thinning. Although the mechanisms for extension and crustal thinning in the basin and range are under debate, these include gravitational collapse of over thickened crust, lithospheric delamination by a mantle plume, and plate boundary interactions such as a slow-down of the plate convergence rate.

The basin and range event is also associated with emplacement of large volumes of felsic and mafic volcanic products (bimodal volcanism). Damon *et al*. (1981) showed that the position of the magmatic front migrated eastward during the Laramide orogeny, from Sonora to central Coahuila, migrating back to the west during the basin and range extensional event to reach the longitude of the Gulf of California by mid-Miocene time. This evolution can be explained by subduction dynamics: flattening of the slab during the Laramide orogeny and later slab roll-back.

A Late Oligocene to Middle Miocene volcanic arc (27-16 Ma) was established between the Peninsular Ranges and coastal Sonoran batholiths, the region that today is occupied by the Gulf of California Umhoefer *et al.,* (2001). Arc magmatism culminated by the end of middle Miocene, marking the end of the subduction process between Farallon and North American plates at the latitude of the Gulf of California. At this latitude subduction was oblique, and relative plate motion in the plate boundary region was partly accommodated by a dextral transtensional system. The time of the tectonic transition from orthogonal basin and range style extension to dextral transtension in the Gulf extensional province (GEP, Figure 1) is, however, controversial.

In general terms, the distinction between the Gulf extensional province from the basin and range proper has not been defined. The GEP is the area between the SMO and coastal Sonora and Baja California (Stock& Hodges, 1989). This region experienced crustal extension in wide-rift mode and core complex formation between 25 and 16 Ma (Wong and Gans, 2008; Nourse *et al*., 1994; Vega-Granillo and Calmus, 2003). Subsequent minor extension continued until 12 Ma and after (McDowell *et al.*, 1997). This extensional episode is coeval with subduction of the Farallon its fragmentation into other microplates, and arc volcanism in Baja California and Sonora. In Baja California, stratigraphic relationships at Sierra San Felipe indicate that transtentional faulting initiated synchronously as a kinematically linked fault system before ~ 7 Ma. This is based on the timing of footwall exhumation, during a phase of rifting that has been called "proto-Gulf"(Seiler *et al.,* 2010).

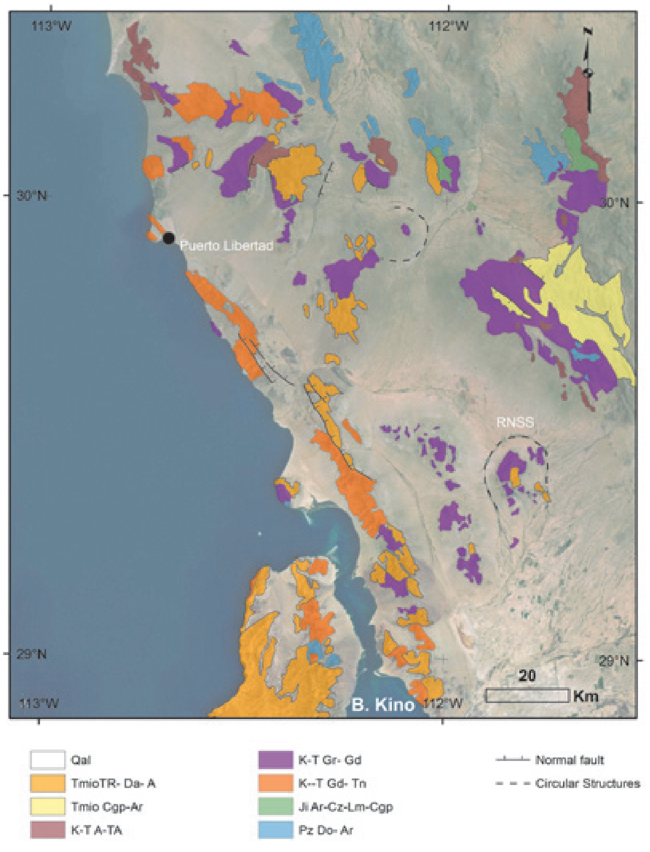

Figure 1. Geologic map of central-coastal Sonora, showing the location of the Rancho Nuevo semi-circular structure. The inset shows the distribution of plutonic rocks assigned to the Peninsular Ranges and the Sonoran Laramide batholithsas well as the Gulf of California extensional province. Modified from Servicio Geológico Mexicano (SGM), 2008. KsGd-Tn=Upper Cretaceous granodiorite and tonalite; KsTpaGr-Gd= Upper Cretaceous-Paleocene granite and granodiorite; JiAr-Cz-Lm-Cgp=Lower Jurassic sedimentary rocks; pTsDo-Ar=Neoproterozoic metasedimentary sedimentary rocks.

The coastal Sonora region hosts the onshore portion of the transform boundary between the Upper Tiburón and Adair-Tepoca marine basins, two early-formed oblique rift segments. Extension commenced here between 11.5 and 7 Ma(Bennett *et al*., 2013). Based on structural, ^{40}Ar/^{39}Ar geochronology, and a palinspastic reconstruction Gans (1997) proposed the onset of transtension and relative motion of Baja California together with the Pacific plate shortly after the ~11 Ma termination of subduction.

Correlation of geologic features on both sides of the Gulf of California (Oskin and Stock, 2003a) indicates about 280 km of slip along faults in the gulf, from 6 Ma to present (Atwater and Stock, 1998; Oskin *et al*., 2001). Nonetheless, there are 300 km of dextral motion between the Pacific plate and North America that must be accommodated during the proto-Gulf episode between ~12 and 6 Ma (Stock, 1989; Stock and Hodges, 1989; Stock and Molnar, 1988). Relative plate motion during the proto-Gulf event may have been accommodated west of Baja California by the San Benito and Tosco-Abreojos faults (Stock and Hodges, 1989), east of Baja California along coastal Sonora, or in both (Gans, 1997; Fletcher *et al*., 2007; Bennett *et al*., 2013).

Methodology

This work is based on 1:10,000 field mapping of the RNSS, and detailed petrographic analysis of 50 samples, 16 of which were point-counted for modal analysis (with a minimum of 600 points) for later classification in a Streickeinsen diagram (Streickeinsen, 1976). Structural data were collected at 148 stations, including foliation, lineation, dike orientation, bedding attitude, brittle fault plane, and pitch of striations. Five rock samples were dated using U-Pb geochronological analysis by LA-ICP-MS (Laser Ablation-Inductively Coupled Plasma-Mass Spectrometry). Three samples (T-83, T-91, T-92) were prepared, processed, and analyzed at the University of Arizona, Tucson, using standard techniques that include crushing, sieving, magnetic separation and high-density liquids for final extraction of heavy minerals. Zircon separates were mounted manually in epoxy and polished. Zircons were analyzed in a VGI isoprobe multi-collector ICP-MS, equipped with nine Faraday collectors, an axial Daly detector, and four ion counting channels (Gehrels *et al*., 2006). Two samples (T-205 y TR-46) were processed for zircon separation at the Centro de Geociencias, UNAM Juriquilla Campus, where they were first crushed and sieved, and then subjected to magnetic separation and heavy liquids extraction (MEI). Zircon separates were then manually mounted in epoxy resin and polished. These two samples were analyzed with an ICP-MS Thermo X series "quadrupole" at Centro de Geociencias in Juriquilla Mexico. (Solariet *et al*., 2010).

We collected samples in 27 paleomagnetic sites, all in granodiorite, for a total of 162 samples; the samples have a cylinder shape with 1 inch of diameter and 1 inch high. The same samples were used for anisotropy of magnetic susceptibility measurements (AMS) with the objective of observing if there are changes in the magnetic fabric related to post-emplacement deformation. The sampling was performed with a portable drill using diamond tip drillbits; samples were oriented with magnetic and sun compasses. As with all other field stations, sites were located using a portable GPS device. For magnetic susceptibility measurements we used a KLY-3 Kappabridge susceptibilimeter, using 15 positions. For remanence measurements we used a JR-5 Spinner magnetometer. All samples were subjected to progressive demagnetization, either alternating field demagnetization using an ASC LDA-3 up to inductions of 100 mT or thermal demagnetization using an ASC-TD48 furnace up to temperatures of 590 ºC. The main objective of the paleomagnetic part of this study was to determine a possible rotation or tilt within the RNSS by comparing observed directions with the expected direction from the North America craton reference pole for the Late Cretaceous. All magnetic measurements were performed at the Paleomagnetic Laboratory of the Centro de Geociencias, UNAM Juriquilla Campus. Orthogonal demagnetization diagrams were used to interpret the vectorial composition of the natural remanent magnetization (NRM), and characteristic directions were computed using principal component analysis (Kirschvink, 1980). Site mean directions were calculated using Fisher statistics.

Regional geology

The stratigraphy of western Sonora includes a basement unit composed of various Paleozoic metasedimentary units, with protoliths that range in age from the Cambrian to the Devonian (Gastil and Krummenacher, 1977; Stewart, 1988; Ávila-Ángulo, 1987; Poole, 1993). This assemblage was thrusted over an Upper Paleozoic basin, late in the Ouachita orogeny (Poole *et al*., 2005). Late Cretaceous plutonic rocks of the Sonoran Laramide batholith intruded the entire basement assemblage (Anderson and Silver, 1969; Gastil and Krummenacher, 1977; Valencia Moreno *et al*., 2003; Ramos-Velázquez *et al*., 2008).

The supracrustal units in the GEP in Sonora include four groups after (Oskin and Stock; 2003b, Bennet, 2009; 2013). The oldest, Group I, consists of continental sedimentary rocks of Oligocene-Miocene age. It includes coarse to fine sandstone and conglomerate with basement clasts and clasts of intermediate volcanic rocks. These rocks were deposited by immature fluvial systems and rest unconformably on basement. Group I represents an erosional episode perhaps linked to Basin and Range tectonics within the Gulf of California extensional province.

Group II rocks are likely related to arc volcanic activity associated with the Early- to Middle- Miocene Comondú arc, and subduction of progressively younger Farallon oceanic lithosphere (Umhoefer *et al*., 2001; Gastil *et al*., 1979; Hausback, 1984; Oskin and Stock, 2003b; Bennett, 2009).It consists of volcanic flows and pyroclastic deposits of intermediate composition. Although the tuff of San Felipe is included in Group II, and represents the onset of extension in the northern GEP, and it clearly postdates the end of subduction and arc volcanism (Stock *et al*., 1999; Vidal Solano *et al*., 2007; 2008). The tuff of San Felipe (Ttsf) is a regional stratigraphic marker that covered an approximate surface of >4000 km^2 on both margins of the Gulf of California. Distribution of the Ttsf has been used as a piercing point for reconstruction of the peninsula to its pre-opening position because the age of Ttsf is 12.5 Ma (Oskin, 2002; Oskin and Stock 2003a). The Ttsf crops out in the RNSS with a thickness of 60 m (Figure 2).

Group III consists of basaltic and rhyolitic rocks interstratified with non-marine strata. It is Middle Miocene to Late Miocene (11.47-6.39 Ma), (Oskin *et al*., 2003b; Bennett etal., 2007). The upper age of Group III is considered late Miocene, based on the age of the Mesa Cuadrada tuff of 6.39 ± 0.02 Ma, ^{40}Ar^{39}Ar, in plagioclase, published by Bennett *et al*. (2007). Group III includes ignimbrites regionally distributed over an area >2100 km^2 on both margins of the Gulf, in Isla Tiburón, (Oskin and Stock, 2003a, b), and in coastal Sonora (Oskin *et al.*, 2001). Mesa Cuadrada tuff deposits are thin, about 30 m. Characteristics of this unit that makes it easily recognizable are that it changes laterally from non-welded to poorly welded, and it presents a conspicuous salmon color. The series of rocks deposited between the San Felipe and Mesa Cuadrada tuffs, between 12.5-6.4 Ma (Stock *et al*., 1999),may contain the geologic record of transtension in the Gulf of California. Finally, Group IV consists of sedimentary rocks, characterized by non-marine strata with local intercalations of pyroclastic deposits such as air-fall tuffs. These strata were deposited during the latest proto-Gulf stages (Pliocene-Holocene). Coastal eolian and beach deposits, as well as alluvial and fluvial strata also included in Group IV.

Geology of Rancho Nuevo Semicircular Structure

The RNSS is located in the Sonoran coastal plain, about 160 km NW of the city of Hermosillo and about 40 km from the coast. RNSS is composed of granitic rocks that intrude an andesite unit mapped as part of the Sonoran Laramide batholith. The RNSS is a domo shaped geomorphic feature defined by conspicuous drainage patterns. The dome may have been produced by a magmatic chamber, or with later erosion. The structure is an elongated dome, with a 30 km long axis, oriented nearly N-S, and it is about 15 km wide. The arroyos (ephemeral streams) draining small and apparently disorganized sierras outside the structure run into a loop that surrounds the structure, whilst drainage runs radially away from the core of the structure into the same loop. Drainages eventually collect south of the RNSS and flow into playa San Bartolo. The RNSS is cored by suite of Late Cretaceous intrusive rocks (Figure 2). For the description of the geology of the RNSS, we grouped rocks chronologically associated with the Late Cretaceous intrusive suite, and rocks associated with the Miocene volcanic and volcaniclastic sequence.

Late Cretaceous intrusive and volcanic rocks at Rancho Nuevo

The Cretaceous suite at the RNSS is composed of plutonic rocks and their host rock. The host rocks are Late Cretaceous, greenish gray andesite flows. These lava flows crop out primarily in the south-central sector of the structure, forming low-standing hills (Figure 2). The andesite unit is intruded by plutonic rocks which include four units: (1) granodiorite-monzogranite, (2) monzogranite, (3) quartz-feldspathic porphyry, and (4) quartz-rich granitoid, aplitic and pegmatite dikes. Near the contact with the intrusions the andesite unit it develops neoformations zones, or andesite breccias at greater distance from the contact. The mineralogy of andesite flows consists of plagioclase > pyroxene + chlorite and Fe-oxides.

The granodiorite-monzogranite unit is the largest of the intrusive suite because of its volume and areal extend. It is also important because this unit has a sigmoidal fracture pattern, which is described in the next section. This pattern is further emphasized by the intrusion of a series of Miocene rhyolitic dikes (Figure 2). Outcrops of the granodiorite-monzogranite unit form valleys between minor and discontinuous north-south ranges where plutons of more felsic composition crop out. The granodiorite-mozogranite unit is light to dark gray depending on mafic mineral content. Microscopically, the quartz presents undulatory extinction, and

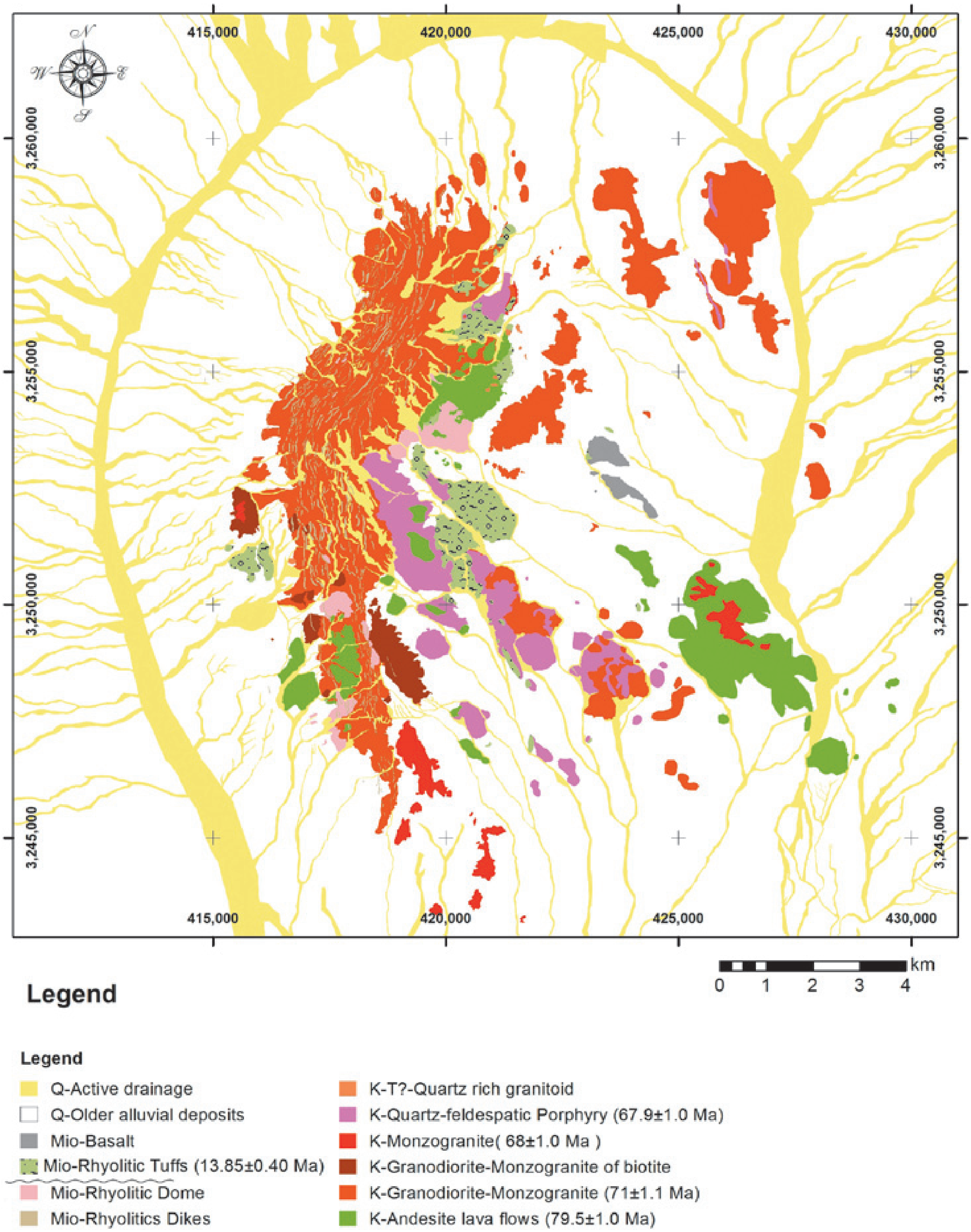

Figure 2. Generalized geologic map of Sierra Rancho Nuevo.

the plagioclases are often fractured or broken forming a matrix of small crystals with quartz and feldspar recrystallization. The biotite abundance increases in zones of hydrothermal alteration. Amphiboles are often corroded, and also altered to chlorite and epidote. Potassium feldspar content gradually increases to the east of the RNSS, where the composition changes transitionally from granodiorite to monzogranite. (Figure 3 and Appendix I).

The granodiorite-monzogranite unit is intruded by coarse-grained monzogranite unit. Characterized by a distinctive texture of large feldspars phenocrytals and marked mineral lineation and in outcrop it presents a pinkish coloration due to K-feldspar content and biotite oxidation. The monzogranite crops out on the southern and western sides of the structure (Figure 2). The monzogranite presents various families of fractures with different orientations, which are often filled by aplitic dikes and pegmatites. Locally, the monzogranite includes granodiorite xenoliths, which lack reaction rims and do not present preferential orientation. Xenoliths may be as much as 20 cm in diameter but are generally between 5 and 10 cm. In thin section, this rock is composed of quartz with undulatory extinction, both microclines and orthoclases are 1 to 2 cm in length, plagioclase crystals are not zoned but a number of them are broken up or deformed as kink-bands. Plagioclase rims are often corroded and show quartz-feldspar recrystallization. This is often a feature produced by crystal-plastic deformation (Vernon, 1975). Many biotite and amphibole crystals are altered to chlorite, epidote and Fe-oxides.

The quartz-feldespatic porphyry unit crops out in the south-central part of the RNSS, forming small hills. To the northeast of the structure, the porphyry intrudes the granodiorite-monzogranite unit in the form of dikes with a preferred orientation 10° to 20° NW (Figure 2). Quartz and K-feldspar crystals are embedded in an aphanitic matrix. Potassium-feldspar (orthoclase) is commonly broken up and shows sericitic alteration. Many plagioclase crystals are zoned. Biotite grains are euhedral; most of them are fractured, corroded, oxidized and sericitized. There are small amounts of hornblende altered to epidote, chlorite and Fe-oxides.

The granite rich in quartz, aplite and pegmatite dikes unit is the kind of facies typically associated with late crystallization phases in the magma chamber. The granite bodies are scarce within the RNSS, cropping

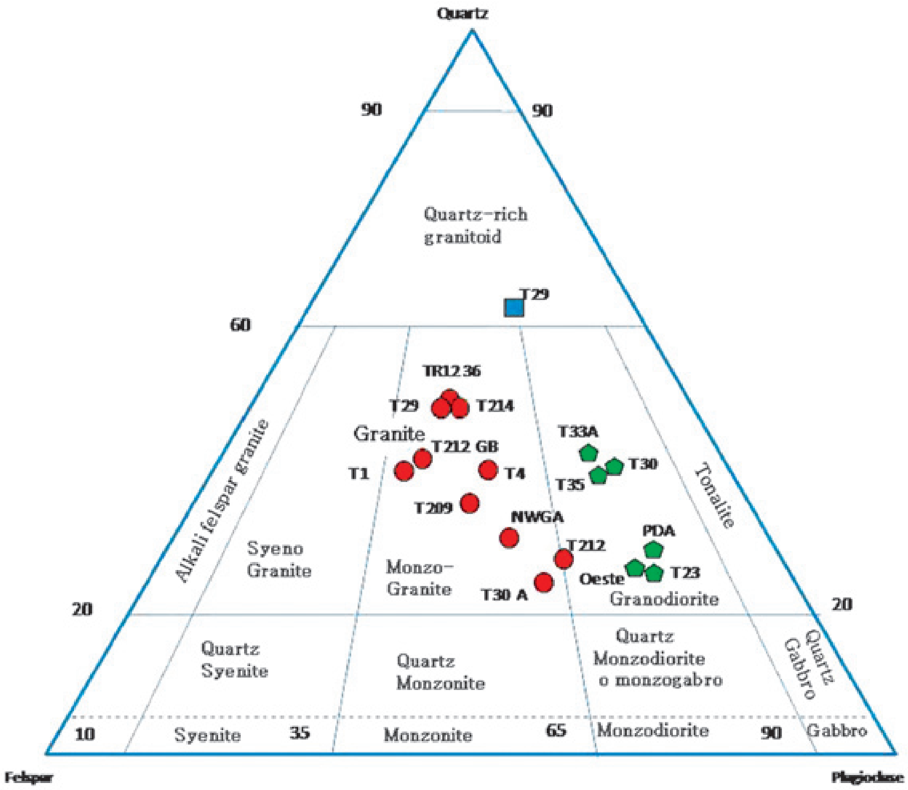

Figure 3. Intrusive rocks classification diagram, Streickeisen (1976), shows the representative samples distribution of RNSS units. The original data are summarized in Appendix I.

out as scattered apophyses not larger than ~100 m in diameter. They are light gray and of fine-grained texture. The aplitic and pegmatites dikes are generally less than 1 m thick, and show no preferred orientation. More common mineralogical association in these dikes is quartz, potassium-feldspar, plagioclase, mica, and accessory tourmaline.

The Miocene volcanic and sedimentary rocks

Miocene volcanic and intrusive rocks in the RNSS either unconformably overlie the Cretaceous plutons or intrude in to them. They were mapped as three compositional units: rhyolite lava, rhyolitic tuffs, and basalts flows. The rhyolite unit includes dikes filling sigmoidal fractures within the granodiorite-monzogranite main pluton, as well as associated domes which are coeval. The rhyolite dikes occur mostly in the western side of the RNSS, but dikes cut the entire structure from north to south; they also occur in the central-eastern side and cut quartz feldspatic porphyry (Figure 2). The dikes form as discontinuous prominent ridges, rising tens of meters above their surroundings. As mentioned earlier, rhyolites dikes follow sigmoidal trends striking N-S in the north, NE-SW in the center, and NNW in the south. The sigmoidal fracture pattern that they intrude was developed earlier or during the emplacement of the rhyolitic dikes within the granodiorite-monzogranite. The rhyolite dikes are ~ 2 km long, but they are narrow (2-4 m). The rhyolite unit also includes domes up to 400 m in diameter. Generally they are pink to reddish-gray because of the presence of Fe-oxides. They have an aphanitic texture, containing <5% of quartz, feldspar or plagioclase phenocrysts.The rhyolite also contain small crystals of fayalite, aegirine (<1%), and arfvedsonite (<1%), which are indicators of high alkaline composition (Vidal-Solano, personal communication 2012).

Dispersed across the RNSS, there are outcrops of volcanic and volcaniclastic rocks mapped as the rhyolitic tuff unit. These rocks generally occur as small remnants, filling paleo-valleys between minor ranges composed of granitoid. The largest outcrops are about 3 km^2 in the east-central side of the RNSS. The base of the volcaniclastic sequence is formed by tuffaceous breccias, which include clasts of the volcanic and granitic older units, overlain by a well-stratified volcanic sequence. This sequence is composed of ~18m thick a black vitrophyre, lapilli tuffsof rhyolithic composition, ~20 m of pinkish lithic tuff of rhyolitic composition, about 3m of clear fine-grained tuff (pumicite), and a second vitrophyre 4m thick. The sequence overlies ~18m of pinkish and yellowish tuff for a total thickness of about 60 m. This unit is gently tilted, 5°-18° to the west, probably produced by the paleo-geography. The petrological characteristics of this unit suggest that it may correlate with the tuff of San Felipe. The basalt unit in the map (Figure 2) is restricted, to isolated outcrops scattered along the RNSS; however, the contact with the underlying intrusions is not well exposed. In the central part of the structure basalts flows dip gently ~10° to the northeast.

Geochronology

Five samples within the RNSS were selected for U-Pb zircon dating. Analytical results are summarized in Appendix 2, and results are summarized in Figure 4 and Table 1. An isotopic age of 79.5±1.0 Ma (Campanian) was obtained for sample T205 of the andesite unit, host rock to the Rancho Nuevo intrusive suite. The age is based on the average of 11 concordant grains. The zircon analysis of the intrusive rocks yielded ages of 71±1.1 Ma (sample T92, from granodiorite-monzogranite, average of 27 concordant grains), 68±1.0 Ma (sample T91, monzogranite, average of 24 concordant grains), and 67.9±1.0 Ma (sample T83, quartz-feldspar porphyry, average of 24 concordant grains). The ages obtained are consistent with field relations, as the granodiorite-monzogranite is intruded by the younger granitic and subvolcanic units. A rhyolitic feeder dike yielded a crystallization age of 13.2±0.4 Ma (Figure 4, and Table 1) based on the average of 10 concordant grains.

Structural observations

The Rancho Nuevo granodiorite-monzogranite unit contains sigmoidal fractures hundreds to tens of meters long, where most of the fractures were filled by viscous rhyolite. These fractures were clearly formed after pluton emplacement. The sigmoidal pattern of fractures and rhyolite dikes is clearly visible on satellite images of high resolution. Figure 5. The fractures and dikes are nearly vertical (79°-90°). In the north, fractures and dikes strikes are predominantly 20°-30° to NE (Figure 6a), and change orientation to 0°-10° NNE in the central portion of the range (Figure 6b), whilst in the south fractures and dikes strike 0°-10°NNW (Figure 6c). Figure 6d shows the strike of the complete data set, with a resultant strike. The geometry of the fractures and dikes in the RNSS resembles an *en-echelon,* dextral-shear indicator, formed in a brittle-ductile environment. Apparently, the continuation of the Rancho Nuevo sigmoidal struture is buried by alluvial deposits south and north of the RNSS (Figure 2).

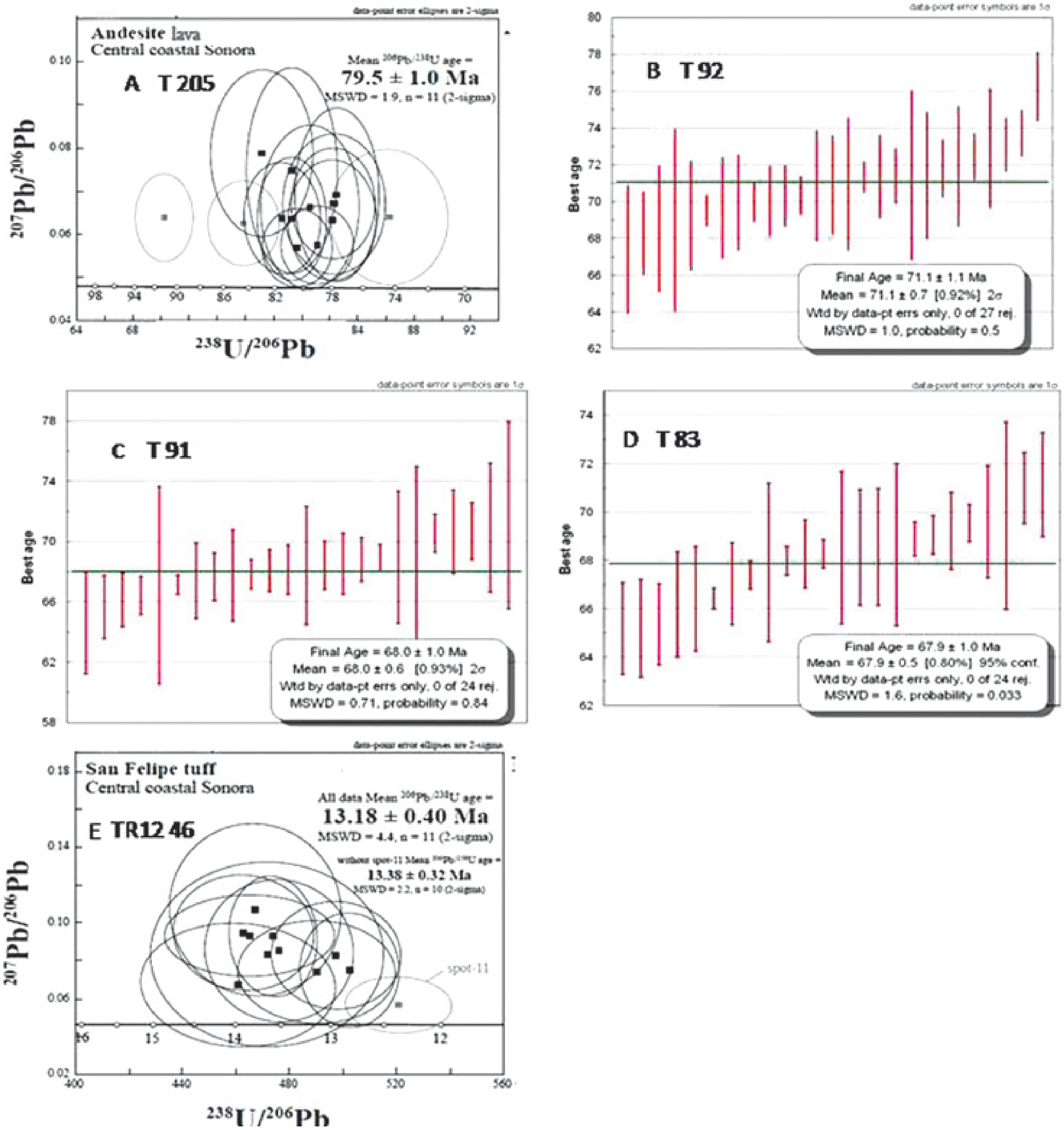

Figure 4. Geochronology results of samples from Sierra Rancho Nuevo by U-Pb LASER ablation method in zircon. the samples (T-92, T83, and T91) were analyzed at Arizona University. The samples (T-205, TR12 46) were processed at Universidad Nacional Autónoma de México, Campus Juriquilla.

Table 1. Summary of geochronological data.

Sample	E Coordinate	N Coordinate	Unit	Age (Ma)
T-205	419812	3243269	Kand	79.5+/-1.0
T-92	425877	3257407	Gd-mzgr	71.1+/-1.0
T-91	425404	3257313	Kpor	67.9+/-1.0
T-83	420614	3243460	KMz	68.0+/-1.0
TR12-46	423440	3253799	Dike	13.2+/-0.4

The granodiorite-monzogranite body does not display a macroscopic foliation or mineral lineation, nor ductile shear zones. Other kinematic indicators are striations in the internal faces of the factures where rhyolite dikes were emplaced. These observations combined with observations of microscopic brittle deformation and plagioclase recrystallization, suggest that deformation occurred at relatively shallow crustal levels. The coarse-grained granite unit in the southern extreme of the RNSS is characterized by variable but nearly N-S magmatic foliation defined by feldspatic phenocrystals that deep steeply >70º to the east.

Anisotropy of magnetic susceptibility

Because of the scarcity of kinematic indicators and the homogeneity of the Cretaceous granitoids, we employed anisotropy of magnetic susceptibility (AMS) as an estimate of strain recorded by intrusive rocks of the RNSS. AMS fabric often parallels the orientation of the strain ellipsoid, but interpretation may not be straightforward. AMS fabrics are represented by an ellipsoid defined by the axis of maximum, intermediate and minimum susceptibility (kmax, kint, and kmin). The maximum and intermediate axes define the magnetic foliation plane, while the shape of the ellipsoid is described using relations between the axes in terms of the parameter T (T<0 for prolate ellipses, and T>0 for oblate ellipses). The intensity of the fabric is evaluated with the percentage of anisotropy (Pj) parameter (Table 2).

AMS studies have been applied to the systematic study of plutonic rocks, which generally have relatively simple magnetic mineralogy (Borradaile, 1988; Borradaile and Henry, 1997). The interpretation of these data, however, can be difficult because the magnetic susceptibility ellipsoid often reflects the combination of emplacement related strain (due to magma flow or interaction with the host rock), regional strain during emplacement, as well as solid-state deformation after emplacement.

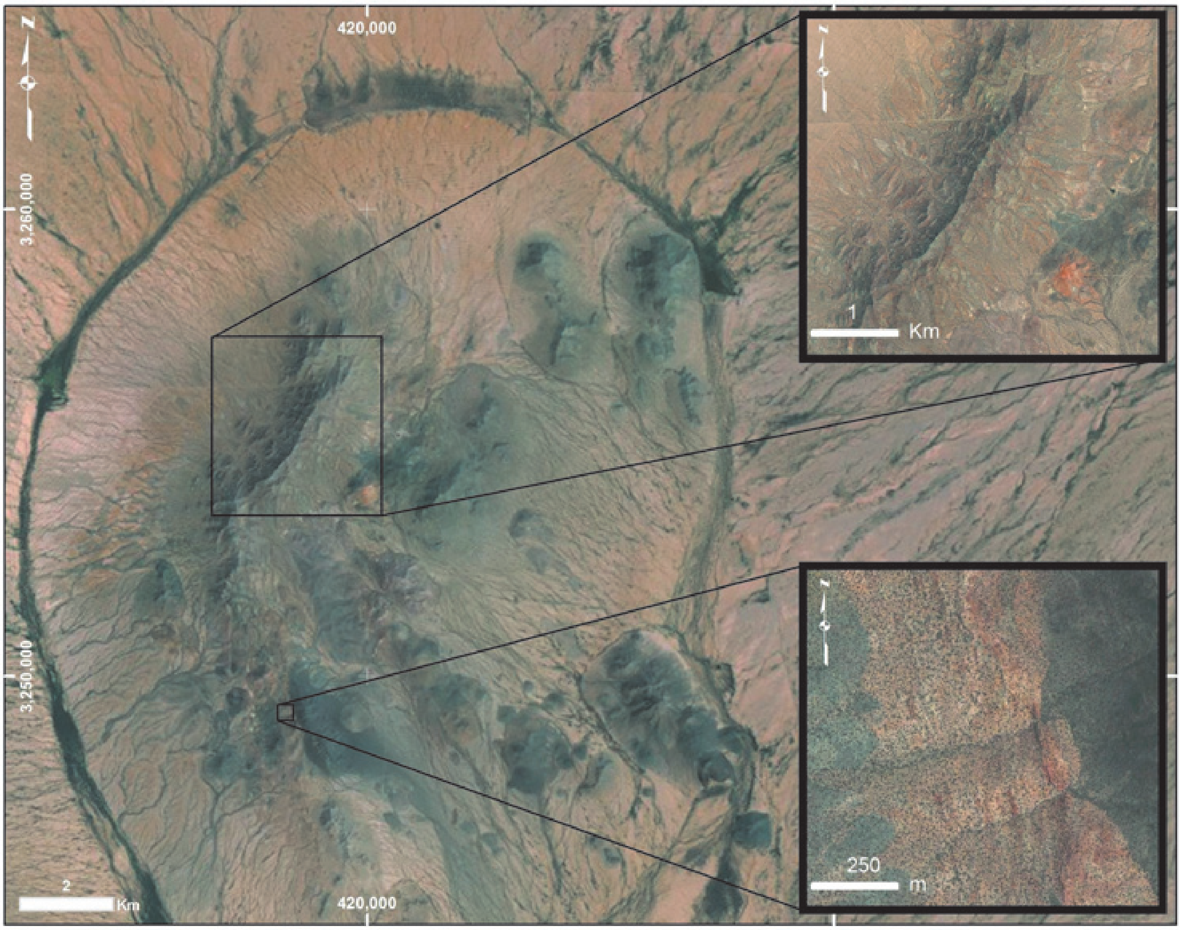

Figure 5. Shows the RNSS and the system of fractures filled of rhylitic composition dikes. Two detailed images of the dikes in the northern and southern portion are presented. Images taken of Google Earth.

Table 2. Summary AMS data of RNSS.

Site	N	Kmean	K1	K2	K3	Dec K1	Dec k2	Dec k3	Inc k1	Inck2	Inck3	L	F	P	Pj	T	U
RN1	12	1.18 e-2	1.004	1.001	0.995	339.7	79.1	242.3	8.4	47.7	41.1	1.003	1.007	1.01	1.01	0.385	0.383
RN2	9	2.91 e-2	1.066	1.056	0.878	46.9	315.2	139.8	2.2	37.4	52.5	1.009	1.204	1.215	1.246	0.907	0.898
RN3	6	2-66 e-2	1.023	1.015	0.962	50.9	161.3	315.6	10.7	61.4	26.1	1.008	1.0055	1.063	1.069	0.741	0.734
RN4	9	1.09 e-2	1.014	1.004	0.982	222.4	45.7	313.5	35.6	54.3	1.6	1.01	1.022	1.032	1.033	0.389	0.383
RN5	12	6.58 e-3	1.016	0.998	0.986	53.7	173.9	320.1	11	68.9	17.8	1.018	1.012	1.03	1.03	-0.213	-0.220
RN6	13	2.03 e-2	1.017	1.008	0.975	6.4	248.4	99.6	9.9	69.5	17.8	1.01	1.033	1.043	1.045	0.547	0.54
RN7	9	1.81 e-4	1.006	1.002	0.992	100.1	241.7	8.2	11.7	75.2	8.9	1.003	1.01	1.013	1.014	0.488	0.485
RN8	10	1.82 e-2	1.028	1	0.972	167.3	76.3	333.9	15.3	3.4	74.3	1.028	1.028	1.058	1.058	-0.002	-0.016
RN9	7	2.94 e-2	1.019	1.003	0.978	262.8	170.8	75.6	31.9	3.2	57.9	1.016	1.025	1.042	1.042	0.222	0.212
RN10	9	3.06 e-2	1.04	0.993	0.967	207.9	69.2	327.9	54.4	28.6	19.9	1.047	1.027	1.075	1.076	-0.226	-0.283
RN11	7	5.57 e-2	1.027	0.989	0.984	190.8	100.5	283	0.08	20.2	69.8	1.038	1.006	1.044	1.047	-0.74	-0.745
RN12	7	1.53 e-2	1.017	0.997	0.986	40	298.4	180.4	29.8	19.3	53.4	1.019	1.011	1.031	1.031	-0.252	-0.259
RN13	7	1.75 e-2	1.011	1.004	0.984	169	289.4	76.7	8.7	73.2	14.3	1.007	1.021	1.028	1.029	0.497	0.492
RN14	6	1.19 e-2	1.017	1.003	0.98	9	244.9	129.8	39.5	34.3	31.9	1.014	1.023	1.038	1.038	0.224	0.215
RN15	10	1.68 e-2	1.032	1.001	0.966	74.5	225.1	323.4	56	30.5	13.7	1.031	1.037	1.069	1.069	0.081	0.064
RN16	7	1.72 e-2	1.026	0.998	0.976	41.3	282	133.1	7.2	74.6	13.6	1.028	1.022	1.051	1.051	-0.11	-0.122
RN17	9	1.67 e-2	1.026	0.999	0.975	196.6	303.6	94.5	14.9	47.8	38.4	1.027	1.024	1.053	1.053	-0.057	-0.07
RN18	8	2.1 e-2	1.028	0.999	0.973	111.3	4.7	263.4	48.6	14.1	37.9	1.028	1.027	1.056	1.056	-0.031	-0.044
RN19	8	9.12 e-4	1.01	0.998	0.992	168.8	69.5	265	7.7	50.3	38.6	1.012	1.006	1.018	1.018	-0.342	-0.346
RN20	8	1.99 e-2	1.032	1.017	0.95	113.9	258.2	354	63.4	22.1	14	1.014	1.071	1.086	1.092	0.653	0.641
RN21	6	1.24 e-2	1.013	0.994	0.993	92.2	329.2	213.1	38.6	34.3	32.8	1.019	1.001	1.02	1.023	-0.864	-0.865
RN22	6	2.2 e-2	1.015	0.998	0.987	195.7	311.5	80.3	28.6	38.6	38.2	1.017	1.011	1.029	1.029	-0.229	-0.236
RN23	7	4.74 e-3	1.011	1.005	0.983	150.5	35.2	301.5	67.5	10	20	1.006	1.023	1.029	1.03	0.578	0.573
RN24	7	6.97 e-3	1.011	1.003	0.987	199.1	353.1	94	48	39	13.1	1.008	1.016	1.024	1.025	0.337	0.331
RN25	7	5.45 e-3	1.011	1.007	0.982	178.9	357.8	88	69.7	20.3	0.3	1.003	1.026	1.03	1.032	0.772	0.769
RN26	6	1.24 e-2	1.02	0.999	0.981	354	120.6	211.2	82.2	4.7	6.2	1.021	1.018	1.039	1.039	-0.06	-0.069
RN27	6		1.006	1.002	0.991	291.5	142.4	36.2	41.4	44.3	16.1	1.004	1.011	1.015	1.016	0.452	0.449

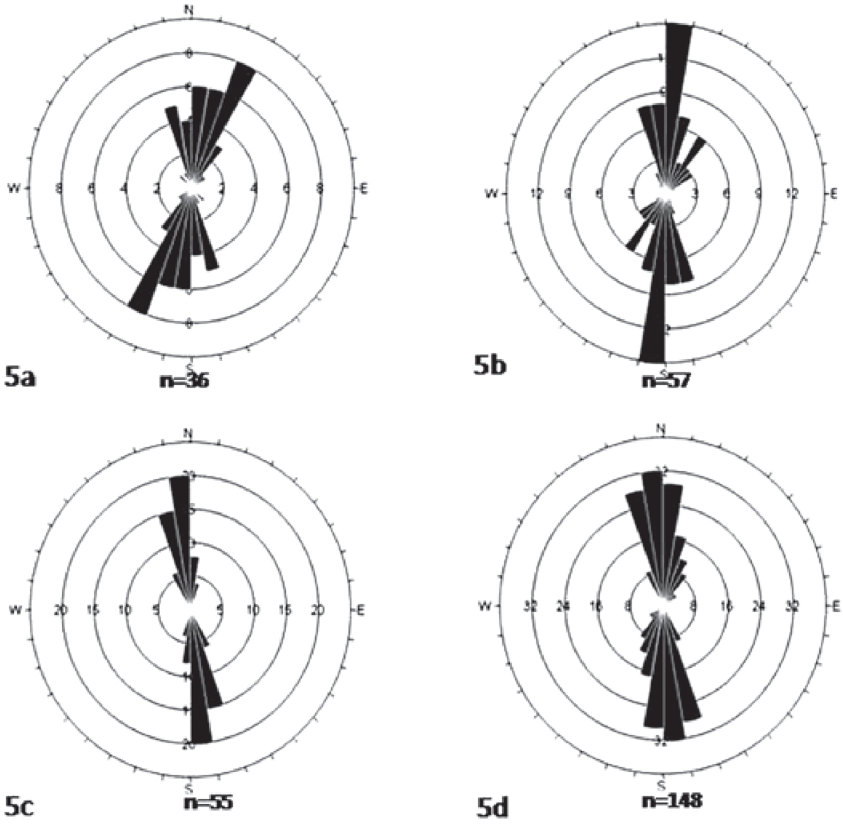

Figure 6. Diagrams of representations main strikes (rhyolitic compositions dikes) about different sectors in RNSS.5a) North sector, 5b) Central sector, 5c) South sector, and 5d) all data sectors.n=collected number data.

AMS data were obtained in all 27 drilled sites. The samples were measured prior to beging demagnetized, Magnetic susceptibility for samples of the granodiorite-monzogranite are high, with the mean of the samples ranging between about 5 x10^{-3} and 6 x10^{-2} SI units, except for sites 7 and 19 that have significantly lower values (between 1 and 9 x10^{-4}). The high susceptibility values suggest that the magnetic fabric is dominated by the ferromagnetic mineral phases (Ellwood and Wenner, 1981). Despite the fact that the granodiorite-monzogranite unit does not display a visible fabric, there is a weak but well-defined magnetic fabric. Percentage anisotropy is relatively low, with an average value of 1.048 (typical of undeformed to weakly deformed granitoids), but with a wide range between 1.010 and 1.246; the high values suggest that high strain is recorded at some sites. The highest values of percent anisotropy (Pj>1.06) were observed in the northern and eastern sides of the mountain range. The shape parameter T varies within the Rancho Nuevo sigmoidal structure. Four sites in the central part of the RNSS have a range of T between -0.002 and -0.11, indicating nearly tridimensional to weakly prolate ellipsoids (Figure 7, Table 2). In the northern and southern sectors of the structure, ellipsoids are dominantly prolate (at six sites T ranges between -0.252 and -0.864). Nonetheless, at rest of the sites T typically has positive values indicating ellipsoids of oblate shape. Oblate ellipsoids suggest generally SE-NW to NE-SW compression.

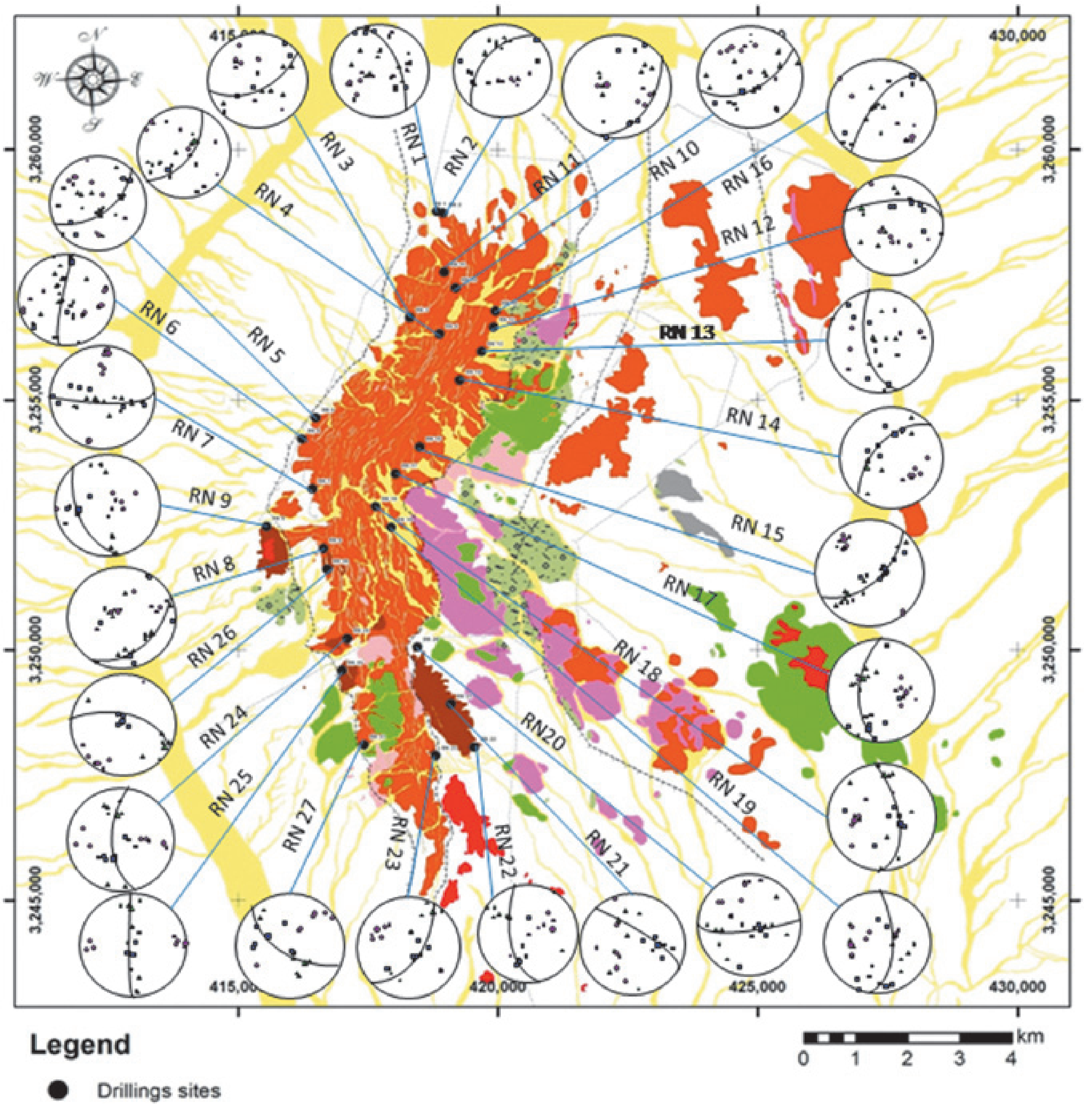

Figure 7. Drilling sites for paleomagnetism and magnetic fabric, the stereograms represent the graphics (AMS) in lower hemisphere. Squares correspond to maximum, triangles to intermediate, and circle to minimum susceptibility axes. The black line symbolize average magnetic folitation plane for each particular site in granodiorite-monzogranite unit.

The orientation of kmax, kint and kmin is displayed in Figure 7. The orientation of the AMS foliation in the granodiorite-monzogranite unit is generally parallel to the dike orientations, such as in sites 13 through 17 in the NE side of the sigmoid, sites 6 and 11 in the northern side, and sites 21 to 25 in the southern sector of the sigmoid (Figure 7). There are, however, significant deviations with foliation planes oblique to the structure, such as sites 20 and 21, as well as 7. These sites generally show the lowest percentage anisotropy values (<1.015), suggesting they were not affected significantly by deformation after emplacement. Magnetic lineation, interpreted from kmax, suggests roughly a NNE-SSW direction and small elongation in the northern part of the RNSS, and N-S and moderately steep in the southern part.

Paleomagnetism

Samples of the granodiorite-monzogranite collected at Rancho Nuevo generally have moderately strong magnetizations, and relatively straightforward demagnetization behavior. The NRM is typically the sum of two magnetizations. A low coercivity magnetization is removed with inductions of about 12 mT (Figure 8). The directions of the low coercivity component show no prevalent within-site orientation. A moderate-coercivity (20-80 mT) magnetization is defined by linear trajectories to the origin, and it is considered the characteristic magnetization (ChRM). The direction of the ChRM is typically to the SW and moderately steep negative, or antipodal to this direction, but it is to the southwest and shallow at three sites in the north and the west sides of the structure and to the NW (SE) and moderately steep positive (negative) at sites 9 and 19 (Figure 8, Table 3). A ChRM was identified at 16 sites, but in one of them the statistic is poor. Within-site dispersion of the ChRM is low, with precision parameter generally higher than 50. At eleven sites no stable magnetization was observed. In some of these sites the NRM is of very low coercivity, and directions within a site have high dispersion; in others demagnetization behavior is erratic. The ChRMin 15 sites are predominantly of reverse

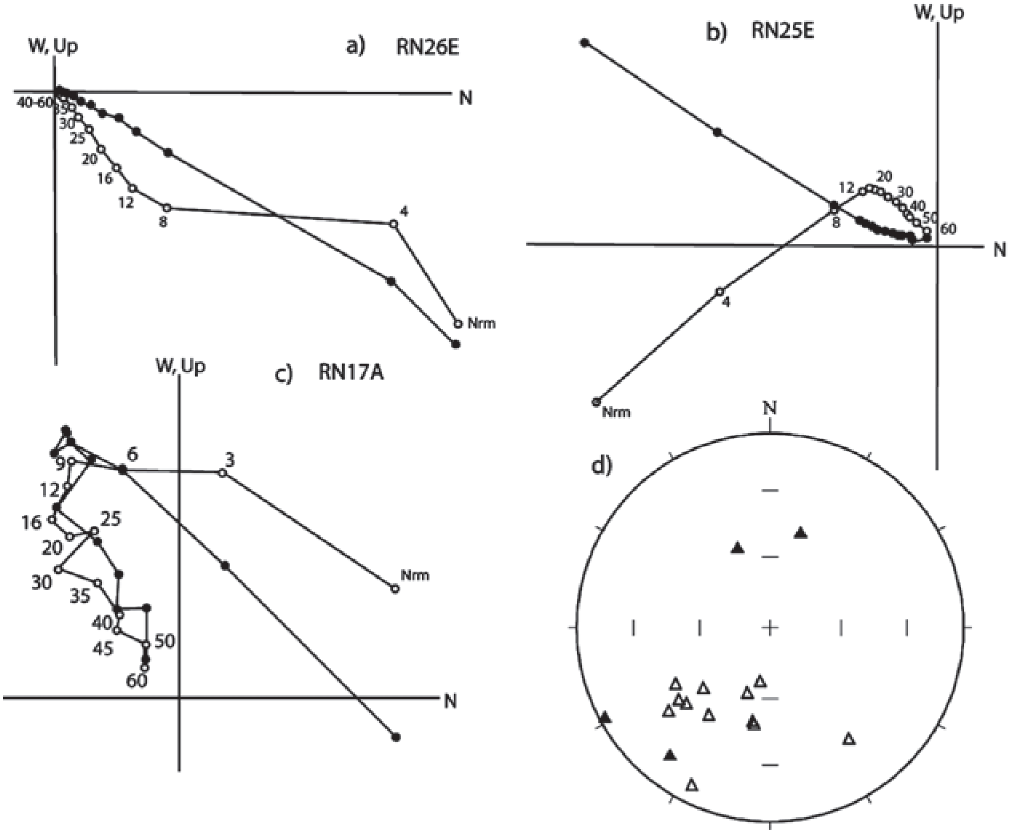

Figure 8. Paleomagnetic data. (a-c) Orthogonal demagnetization diagrams of selected samples. Open (closed) symbols are projections on the vertical (horizontal) plane. (d) Stereographic projection of the characteristic magnetization (in situ), here open (closed) symbols are projections on the upper (lower) hemisphere.

Table 3. Paleomagnetic data and statistical parameters.

Site	**n**	**Dec (º)**	**Inc (º)**	**k**	a95	**Dec (º)**	**Inc (º)**
rn1	1	204.9	-13.7			202.6	-12.6
rn5	3	233	2.4	76.9	14.2	233.1	-1.5
rn6	4	211.6	16.7	162.6	7.2	214.6	16.2
rn9	3	146.8	-37.4	44	18.8	144	-28
rn15	3	247.3	-41.1	76.3	23.4	240.1	-46.4
rn16	5	236.4	-35.1	20.0	17.5	229.4	-39
rn17	6	233.9	-49.5	288.7	3.9	222.1	-52.6
rn18	6	231.5	-48.4	46.0	10.0	220.1	-51.1
rn19	2	341	55.1			333.5	47.1
rn20*	6	185.4	-68.3	10.9	21.3	167.1	-62.7
rn21	6	233.7	-59.6	393.2	3.4	216.2	-62.2
rn22	4	199.5	-62.4	54.7	12.4	182.5	-59.1
rn24	6	197.5	-49.3	152.9	5.4	187	-46.2
rn25	6	196.8	-47.1	505.6	3.0	187.1	-44
rn26	6	21.3	44.6	498.7	3.0	12.1	42.3
rn27	3	211.4	-43.3	203.8	8.7	202.1	-42.7
Mean	**10**	**219.7**	**-49.5**	**28.4**	**9.2**	**207.9**	**-50.2**

Here n is the number of samples used in the calculation of the site mean.
Dec and Inc are the declination and inclination, with statistical parameters k and alpha 95. Dec+ and Inc+ correspond to tilt corrected directions.

polarity, consistent with emplacement during C31r. based on the average age of ~70 Ma, for granitoids.

Between-site dispersion appears high, but a group of ten sites yields a well defined mean direction of D=219.7º and I=-49.5º (k=28.4 andα_{95}=9.2º); this calculation includes most of the sites in the southern and eastern sides of the structure. Corrected for the gentle westward tilt of the Miocene tuffs near El Volteadero ranch in the center of the structure, the direction is D = 207.9º and I = -50.2º. The ChRM is discordant with respect to the direction calculated for the sampling locality from the North America reference pole, which is D = 166.1º and I = -56.9º (based on Besse and Courtillot, 2002). The mean direction indicates clockwise rotation of 41.8º+/-11.6º, with small flattening (F=6.7º+/-3.4º). For individual sites, calculations of R(rotation) range between about 16º and 74º. It appears, however, unlikely that the RNSS rotated as a rigid body, as sites in the north and west with southwesterly and shallow ChRM indicate a combination of rotation and tilt (southward), and two sites (9 and 19) do not record significant rotation.

Discussion

To our knowledge, this is the first study where the deformation of intrusive rocks in the extensional province of the gulf is analyzed. The most evident indication of deformation in the RNSS is the presence of a sigmoidal structure, which later on was filled by viscous rhyolite as dikes.The sigmoidal structure appears to have been produced by the gash extensional fractures (σ3) which are perpendicular to the maximum stress (σ1, Figure 9). The fractures may be rotated by ductile deformation either during or after formation. As gash fractures develop at different times of ductile shearing they show different amounts of rotation. This deformation coincides with the results of the paleomagnetic study.

The AMS is a technique that defines the orientation and intensity of the magnetic fabric in the rocks. The AMS in the granodiorita-mozogranite unit of the RNSS shows that considerable changes in the orientation of the magnetic fabric exist in the rock, indicating that they record significant strain. Also, the characteristic magnetization of the granodiorite-monzogranite is discordant with respect to the expected direction; the discordance is best explained by rotation about a local nearly vertical axis of about 40º. As mentioned above, not all sites record the same amount of rotation. For instance, sites 5 and 6 in the western side of the structure require a combination of rotation and tilt. This suggests that the structure did not behave as a rigid body during deformation. Based on the crystallization age (U-Pb) for the dikes of rhyolite, which are considered coeval or little younger than the dextral transtentional deformation, we conclude strike-slip deformation occurred by about 13 Ma.

Prior to ~16 Ma, the southwestern edge of the North American plate along northwestern Mexico was a subduction boundary (Fig. 2A; Atwater, 1970). By ~12.5 Ma, the Rivera-Pacific-North America triple junction jumped southeastward, setting the stage for transfer of the Baja peninsula to the Pacific plate. Karig and Jensky (1972) proposed that prior to the gulf existed in the area in the earliest stages of rifting from ca. 14 to 6 Ma a simple orthogonal extensional regime. Gastil and Krummenacher (1977), as well as Gastil *et al.*(1999), by means of reconnaissance mapping with geochronologic data determined that the timing of extensional faulting along coastal Sonora, between Puerto Lobos and Bahia Kino, occurred between 10-7 Ma but more likely before 9 Ma.

Stock and Hodges (1989) first proposed the 'strain partitioning' model for the Pacific-North America plate boundary. The model was supported by estimations of the timing and direction of extensional structures during proto-Gulf time, along with estimations of the direction and amount of Pacific-North America plate motion throughout Miocene time. Neuhaus (1989) studied volcanic rocks in Isla Tiburón with ages between 19 and 15 Ma that were tilted between about 13 and 11 Ma. Based on refined geochronology, additional structural observations, and paleomagnetic data, Oskin *et al*. (2001), as well as Oskin and Stock (2003a), proposed that dextral motion of Baja California was accommodated by faults within the gulf between about 6-7 Ma and the present. Bennett (2013), used paleomagnetic, geochronological and structural data to conclude that the extension in coastal Sonora commenced between 11.5 Ma and 7 Ma**.**

Dextral slip oriented parallel to the Gulf of California (roughly NNW) in the coast of Sonora is inferred from the geometry of the Rancho Nuevo semicircular structure. The geometry is consistent with a very large-scale, *en-echelon*, brittle-ductile shear zone, and this geometry is supported by deformation recorded by AMS fabric and paleomagnetically determined clockwise rotation of about 40º; the model is illustrated in Figure 9. Rhyolite dikes and domes emplaced along sigmoidal fractures in the RNSS are hyperalcaline (Vidal Solano *et al*., 2007).They are related to extension, and their crystallization age is ~13 Ma, and they are

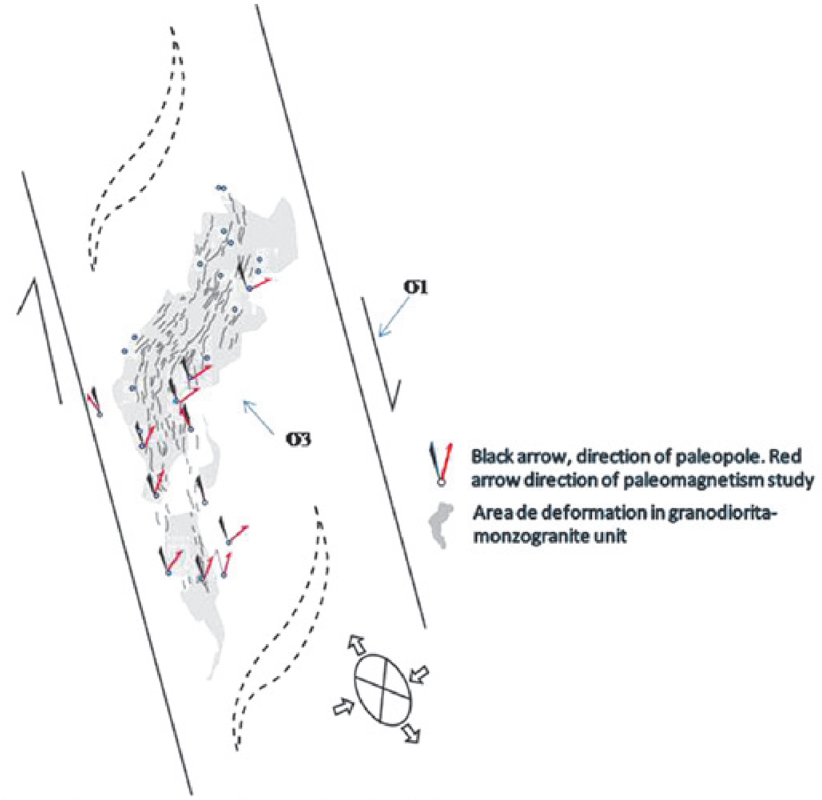

Where, σ1 is a maximun stress and σ3 is minimun stress

Figure 9. Schematic model of a right-lateral, brittle-ductile, en-echelon pattern of fractures developed in the Rancho Nuevo granitoids and filled by Miocene hyperalkaline dikes. Also indicate the gash fractures formed as extensional fractures that are perpendicular to the minimum compressive stress, Where, σ1 is a maximun stress and σ3 is minimun stress.

discordantly covered by the tuff of San Felipe dated at 12.5 Ma by Vidal Solano *et al.* (2007) and Stock *et al.* (1999).

Our findings suggest that deformation of Cretaceous plutonic rocks at Rancho Nuevo is driven by transtensional shearing along dextral strike-slip faults north and south of the structure, such as the Sacrificio, Infiernillo, and Kino bay faults (Bennett and Oskin, 2007); these faults are most likely related to transtensional motion of Baja California peninsula, and thus the Pacific plate. Some authors (e.g., Oskin and Stock, 2003a,b; Bennett, 2009; and Darin *et al*., 2012) have proposed that right-lateral slip of the peninsula is limited to 7-0 Ma, based on studies of the Miocene volcanic sequence of coastal Sonora. Nonetheless, in this study we recognized the emplacement of hyperalkaline dikes with crystallization ages of ~13 Ma, in plutonic rocks defining an *en-echelon* dextral geometry. The structural observations, such as the presence of striations, crushed plagioclase at microscopic scale, and the magnetic fabric are consistent with a brittle-ductile setting. The deformation is dated at about 13 Ma based on the overlap relationship between tuff San Felipe and rhyolite dikes. Magnetic anisotropy is also consistent with ENE flattening linked to NNE right-lateral shear. We notice that the prolate AMS fabrics at the extremes of the RNSS are also consistent with elongation caused by right-lateral shear. The most convincing evidence of dextral slip and transtensional shearing in late Middle Miocene time is provided, however, by the clockwise rotation observed in the central and southern part of the Rancho Nuevo sigmoid structure. This transtensional deformation is thus related to North America-Pacific plate motion early during the capture of the Baja California Peninsula by the Pacific Plate. may record similar deformation. They include a rhomboidal structure at playa San Bartolo, 27 km to the southwest of Sierra Rancho Nuevo, and a series of dikes located 30 km to the north of the of it, these dikes have a length of the 17 km oriented NNW, suggesting strong structural control by Miocene faults.

Conclusions

The semi-circular Rancho Nuevo structure is a structural dome exposing a Late Cretaceous Plutonic suite partially covered by the ~12.5 Ma tuff of San Felipe. The core of the structure includes granodiorite-monzogranite, monzogranite, quartz-feldespathic porphyry, and granite rich in aplitic dikes and pegmatites. This suite has crystallization age between about 71 and 68 Ma. The plutonic suite is intruded by ~13 Ma (U-Pb zircon) Miocene dikes and disconformably covered by Miocene volcanic rocks.

A sigmoidal fracture pattern affected the plutonic rocks of the RNSS, and it is best developed in the granodiorite-monzogranite body. The fractures were filled by Miocene hyperalkaline dikes, defining an *en-echelon*, brittle-ductile, dextral shear indicator of kilometric scale. Magnetic anisotropy in the plutonic rocks shows a foliation that commonly follows the strike of the dikes, and thus records post-emplacement crystal plastic deformation. In thin section, this deformation is observed as crushed plagioclase grains, undulatory extinction in quartz, and kink-bands. Magnetic fabric suggests elongation to the NNW-ESE, and NW-SE to NE-SW flattening.

The characteristic magnetization in granodiorite of the RNSS is to the southwest and moderately steep negative, indicating (when compared to the expected reference direction) ~40º horizontal rotation about a vertical axis. Rotation is unlikely to have occurred as a simple rigid block. Instead, paleomagnetic data suggest internal deformation of the structure within a zone of dominant right-lateral strain. Therefore, we propose that NNW trending right-lateral faults bound the Rancho Nuevo crystalline block and were active during emplacement of *ca*. 13 Ma hyperalkaline dikes in the RNSS. This suggests that strain was localized. We also propose that these faults accommodated part of the NW motion of Baja California peninsula during the proto-Gulf event.

Acknowledgements

We thank CONACYT who supported the research of D.García and R. Molina with CB grant 12982. We also thank Thierry Calmus, José Luis Rodriguez C, and Sergio Salgado S. for their comments and support. Alexander Iriondo provided direction and support in U-Pb determinations at Centro de Geociencias, Juriquilla. We also thank Aimée Orci Romero for thin section preparation, Pablo Peñaflor Escárcega for help in sample preparation, and Jesús Vidal Solano for valuable comments to previous version of this manuscript and discussion of hyperalcaline magmas. We thank Mr. Pilo Galáz y Mr. Miguel Robles for access to their properties, as well as Gonzalo Ibarra for his assistance in the field. We thank Dr. Garcia y Barragán, for his detailed review of the paper. The comments of K. Busby and treewo anonymous reviewers served to improve this article and are greatly appreciated.

References

Ávila–Ángulo R., 1987, Consideraciones geológicas y estratigráficas de la porción NW de Hermosillo: México: Hermosillo, Son., Universidad de Sonora, Departamento de Geología, Tesis de licenciatura, 78 p.

Atwater T., 1970, Implications of plate tectonics for the Cenozoic evolution of western North America: *Geological Society of America Bulletin,* 81, p. 3513–3536.

Atwater T., Stock J.M., 1998, Pacific–North America plate tectonics of the Neogene southwestern United States: An update: *International Geology Review,* 40, p. 375–402.

Atwater T., 1989, Plate tectonic, history of northeastern Pacific and western North America: In Wintered E. L., Hussong, D. M, and Decker R. W., (Eds.) The eastern Pacific ocean and Hawaii: Geological Society of America, *The geology of North America,* N, p. 21-72.

Bennett S.E.K., Oskin M., 2007, Transition from Proto-Gulf Extension to Transtension. Coastal Sonora, México: *Eos Transactions American Geophysical Union*, 88; P.Abstract S31A-10.

Bennett S.E.K., 2009, Transtensional Rifting in the late Proto-Gulf of California Near Bahia Kino, Sonora Mexico. Thesis Master Sciences, Department of Geological Sciences, North Caroline University at Chapel Hill, 122 p.

Bennett S.E.K., Oskin M.E., Iriondo A., 2013, Transtensional rifting in the proto–Gulf of California near Bahía Kino, Sonora, México. *Geological Society of America Bulletin.*

Besse J., Courtillot V., 2002, Apparent and true polar wanderand the geometry of the geomagnetic field over the last200 Myr. *Journal of Geophysical Research-Solid Earth,* 107, B11.

Borradaile, G.J. 1988, *Magnetic Susceptibility, petrofabrics and strain, Tectonophysics,* v. 156,p.1-20.

Borradaile G.J., Henry B., 1997, Tectonic application of magnetic susceptibility and its anisotropy. *Earths Sci.* Review 4, 49-93.

Damon P.E., Shafiqullah M., Clark K.F., 1981, Evolución de los arcos magmáticos en México y su relación con la metalogenesis, *Revista Mexicana de Ciencias Geológicas*, 5, 223-238.

Darin M.H., Dorsey, R. J., Bennett, S.E.K., Oskin, M. and Iriondo, A., 2012, Late Miocene extension in the Sierra Bacha, coastal Sonora, Mexico: implications for the kinematic evolution of the Proto-Gulf of California. Cordilleran Section - 108th GSA *Annual Meeting Abstracts with Programs* (29–31), Juriquilla Querétaro.

Ellwood B.B., Wenner D.B., 1981, Correlation of magnetitic susceptibility with18O/16O data in late orogenic granites of the southern Appalachian Piedmont, *Earth and Planetary Science Letters,* 54, 200-202.

Fletcher J.M., Grove M., Kimbrough D., Lovera O., Gehrels G.E., 2007, Ridge-trench interactions and the Neogene tectonic evolution of the Magdalena shelf and southern Gulf of California: In sigthts from the detrital zircon U-Pb ages from the Magdalena fan adjacent areas; *Geological Society of America, Bulletin,* 119, 1313-1336.

Gans P.B., 1997, Large-magnitude Oligo-Miocene extension in southern Sonora: *Implications for the tectonic evolution of northwest Mexico, Tectonics,* 16, 338-408.

Gastil G., Krummenacher D., 1974, Reconnaissance geology map of coastal Sonora between Puerto Lobos and Bahia Kino, *Geological Society of America* Map and Chart Series MC-16 scala 1:150,000.

Gastil G., Krummenacher D., 1977, Reconnaissance geology of coastal Sonora between Puerto Lobos and Bahia Kino: *Geological Society of America Bulletin,* 88, 189–198.

Gastil G.R., Neuhaus J., Cassidy M., Smith J.T, Ingle J.C., Krummenancher D., 1999, Geology and paleontology of southwestern Isla Tiburon Sonora Mexico. *Revista Mexicana de Ciencias Geologicas,* 16 p. 1-34.

Gehrels G, Valencia V., Pullen A., 2006, Detrital zircon Geochronology by Laser Ablation Multicollector, ICPMS at Arizona LaserChron Center in Olszewszki.T.D. (ed).

Geochronology emerging opportunities: Paleontological Society papers, 12, 67-76.

Hausback B.P., 1984, Cenozoic volcanic and tectonic evolution of Baja California Sur, Mexico, in Frizell, V. A; Jr; ed; *Geology of the Baja California Peninsula,* Volume 39; los Angeles, California, Pacific Section of the Economic Paleontologists and Mineralogist. P. 219-236.

Karig D.E., Jensky W., 1972, The proto-Gulf of California, *Earth and Planetary Science Letters*, 17, p. 169–174.

Kirschvink J., 1980, The least-squares line and plane and the analysis of palaeomagnetic data, *Geophys. J. Int.*, 62, 699-718.

Lewis C.J., 1996, Stratigraphy and geochronology of Miocene and Pliocene volcanic rocks in the Sierra San Fermin and Southern Sierra San Felipe, Baja California, Mexico, *Geofísica Internacional*, 36, 1-31.

McDowell F.W., Roldán-Quintana J.J., Amaya-Martínez R., 1997, Interrelationship of sedimentary and volcanic deposits associated with Tertiary extension in Sonora, Mexico,*Geological Society of America Bulletin*, 109, p. 1349–1360.

Neuhaus J.R., 1989, Volcanic and non marine stratigraphy of southwest Isla Tiburón, Gulf of California, Thesis: San Diego California, San Diego California State University, 170 p.

Nourse J.A., Anderson T.H., Silver L.T., 1994, Tertiary metamorphic core complexes in Sonora, northwestern Mexico:Tectonics, 13, p. 1161–1182.

Oskin M., Stock J., Martin-Barajas A., 2001, Rapid localization of Pacific-North America plate motions in the Gulf of California,29, p. 459-462.

Oskin M., 2002, Tectonic evolution of the northern Gulf of California, Mexico deduce from conjugated rifted margins of the Upper Delfin Basin (Ph. Thesis): Pasadena California Institute of Technology, 481 P.

Oskin M., Stock J.M, 2003a, Pacific-North America plate motion and opening of the Upper Delfin basin, northern Gulf of California: *Geological Society of America Bulletin,* 115, p. 1173-1190.

Oskin M., Stock J., 2003b, Cenozoic volcanism and tectonics of the continental margins of the Delfin basin, northern Gulf of California, Mexico, Johnson, S. *et al*., eds. Tectonic Evolution of Northwestern México and Southwestern USA: Boulder, Colorado, *Geological Society of America Special Paper,* 374, p. 421-438.

Poole F.G., 1993, Ordovician eugeoclinal rocks in Turner Island, in the Gulf of California, Sonora, Mexico. Universidad Autónoma de México, Instituto de Geología and Universidad de Sonora, departamento de Geología. Simposio de la geología de Sonora y areas adyacentes 3rd, Hermosillo, Sonora; México. Resumenes. P. 103.

Poole F.G., William J. Jr., Madrid R.J., Amaya-Martinez R., 2005, Tectonic synthesis of the Ouachita-Marathon-Sonora orogenic margin of southern Laurentia: Stratigraphic and structural implications for timing of deformational events and plate-tectonic model.

Ramos-Velázquez E., Calmus T., Valencia V., Iriondo A., Valencia-Moreno M., Bellon H., 2008, U-Pb and 40Ar/39Ar geochronology of the Coastal Sonora Batholith: new insights on Laramide continental arc magmatism. *Revista Mexicana de Ciencias Geológicas,* 25, 2 p. 314-333.

Seilers C., Fletcher J.M, Quigley M.C, Gleadow A.J, Kohn. B. P. 2010. Neogene structural evolution of the Sierra San Felipe, Baja California: *Evidence for proto-gulf transtension in the Gulf Extensional Province?Tectonophysics,* 488, 1–4, 5 June 2010, Pages 87–109

Servicio Geológico Mexicano, 2008, Carta Geológica Minera Estado de Sonora, 1:500,000., Boulevard Felipe Ángeles Km. 93.5-4, Col. Venta Prieta, C.P. 42080 Pachuca, Hidalgo.

Solari L.A., Gómez-Tuena A., Bernal J.P., Pérez-Arvizu O., Tanner M., 2010, U-Pb Zircon Geochronology with an Integrated LA-ICP-MS Microanalytical Workstation, Achievements in Precision and Accuracy Geostandards and Geoanalytical Research, 34, 5-18.

Stewart J.H., 1988,Latest Proterozoic and Paleozoic southern margin of North America and the accretion of Mexico, *Geology*, 16 P. 186-189.

Stock J.M., 1989, Sequence and geochronology of Miocene rocks adjacent to the main Gulf escarpment: Southern Valle Chico, Baja California Norte, Mexico: *Geofísica Internacional,* 28, 851-896.

Stock J.M., Hodges K.V., 1989, Pre-Pliocene Extension around the Gulf of California and the transfer of Baja California to the Pacific: Tectonics, 8, 99-115. *Relative to the Farallon, Kula, and Pacific plates: Tectonics*, 6, p. 1339-1384.

Stock J.M., Molnar P., 1988, Uncertainties and implications of the Late Cretaceous and Tertiary position of North America.

Streickeisen A.L., 1976, Classification of the common igneous rocks by means of their chemical composition: a provisional attempt. Neues Jahrbuch fur Mineralogie, Monatshefte, 1976, H.l, 1-15.

Valencia-Moreno J. Ruiz, Ochoa-Landín L., Martínez-Serrano R., Vargas-Navarro P., 2003, Geochemistry of the Coastal batholith, Northwestern México**.** *Canadian Journal of Earth Sciences,* 40, 819-831.

Vega-Granillo R., Calmus T., 2003, Mazatán metamorphic core complex (Sonora, Mexico) Structures along the detachment fault and its exhumation evolution: *Journal of South American Earth Sciences,* 16, 4, p. 193–204.

Vernon R.H., 1975, Deformation and recrystallization of a plagioclase grain. *American Mineralogist*, 60, 884-888.

Vidal-Solano J., Paz Moreno F.A., Demant A., López-Martínez M., 2007, Ignimbritas hiperalcalinas del Mioceno medio en Sonora Central—Revaluación de la estratigrafía y significa do del volcanismo terciario: *Revista Mexicana de Ciencias Geológicas,* 24, p. 47–67.

Wong M.S., Gans P.B., 2008, Geologic, structural, and thermochronologic constraints on the tectonic evolution of the Sierra Mazatán core complex, Sonora, Mexico: *New insights into metamorphic core complex formation. Tectonics*, 27, 4, TC4013.

Umhoefer P.J., Dorsey R.J., Sillsey S., Mayer L., Renne P., 2001, Stratigraphy and geochronology of the Comondú Group near Loreto, Baja California sur, Mexico, *Sedimentary Geology*, 144, 125-147.

Appendix 1. Table of Percentages of quartz, feldspar and plagioclase, and classification of the major intrusive units in RNSS. Nomenclature: Unidad Gd-Mzgr = granodiorite-monzogranite, UnidadGrG = monzogranite GrC = granite rich in quartz, aplitic dikes and pegmatites. And location in UTM WGS84, Zone 12.

Sample name	Unit	Coord E	Coord N	Quartz%	K-Feld-spar%	Plagioclase %	Classification
T 23	Gd-Mzgr	419178	3249104	17.34	25.16	57.50	Gd
Oeste	Gd-Mzgr	417124	3250151	17.64	25.40	56.94	Gd
PdA	Gd-Mzgr	421360	3252144	16.55	27.35	56.10	Gd
T 35	Gd-Mzgr	422750	3255818	14.69	39.30	46.01	Gd
T 30	Gd-Mzgr	416533	3253342	29.78	23.27	46.93	Gd
T 33a	Gd-Mzgr	421297	3253474	16.28	41.20	42.50	Gd
T 212	Gd-Mzgr	418797	3253613	27.52	27.52	49.94	Gd-Mzgr
T 30 A	Gd-Mzgr	417126	3252972	13.78	35.42	41.88	Mzgr
NWGA	Gd-Mzgr	427007	3259018	31.11	28.90	39.95	Mzgr
T 209	Gd-Mzgr	418206	3253914	31.64	33.67	34.68	Mzgr
T 21 2 GB	Gd-Mzgr	418853	3253558	34.70	40.78	24.51	Mzgr
T 214	Gd-Mzgr	418511	3253372	25.28	49.66	27.04	Mzgr
TR 12 36	Gd-Mzgr	424988	3248395	26.86	47.71	25.42	Mzgr
T 4	GrG	419832	3243410	28.23	39.30	32.47	Mzgr
T 1	GrG	420614	3243460	38.69	39.43	21.88	Mzgr
T 29	Grc	416289	3252218	13.78	61.87	24.40	Grcz

Appendix 2. Tables a,b,c,d,e, U-Pb isotopic relations of zircon analyzes in major RNSS units.

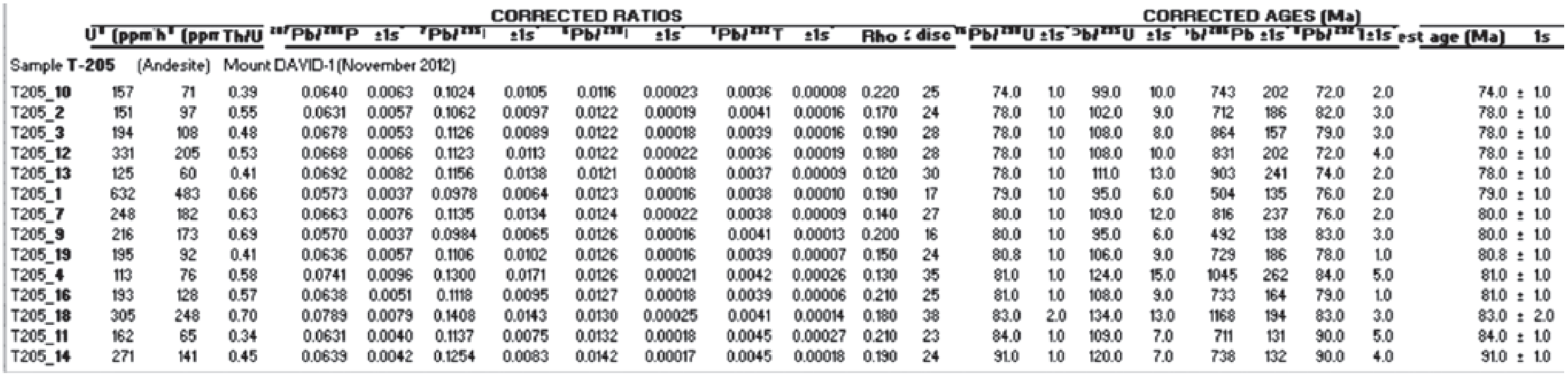

Tabla 2a

				CORRECTED RATIOS										CORRECTED AGES (Ma)									
	U (ppm)	Th (ppm)	Th/U	^{207}Pb/^{206}Pb	±1s	^{207}Pb/^{235}U	±1s	^{206}Pb/^{238}U	±1s	^{208}Pb/^{232}Th	±1s	Rho	% disc	^{206}Pb/^{238}U	±1s	^{207}Pb/^{235}U	±1s	^{207}Pb/^{206}Pb	±1s	^{208}Pb/^{232}Th	±1s	Best age (Ma)	1s
Sample **T-205**	(Andesite)	Mount DAVID-1 (November 2012)																					
T205_**10**	157	71	0.39	0.0640	0.0063	0.1024	0.0105	0.0116	0.00023	0.0036	0.00008	0.220	25	74.0	1.0	99.0	10.0	743	202	72.0	2.0	74.0	± 1.0
T205_**2**	151	97	0.55	0.0631	0.0057	0.1062	0.0097	0.0122	0.00019	0.0041	0.00016	0.170	24	78.0	1.0	102.0	9.0	712	186	82.0	3.0	78.0	± 1.0
T205_**3**	194	108	0.48	0.0678	0.0053	0.1126	0.0089	0.0122	0.00018	0.0039	0.00016	0.190	28	78.0	1.0	108.0	8.0	864	157	79.0	3.0	78.0	± 1.0
T205_**12**	331	205	0.53	0.0668	0.0066	0.1123	0.0113	0.0122	0.00022	0.0036	0.00019	0.180	28	78.0	1.0	108.0	10.0	831	202	72.0	4.0	78.0	± 1.0
T205_**13**	125	60	0.41	0.0692	0.0082	0.1156	0.0138	0.0121	0.00018	0.0037	0.00009	0.120	30	78.0	1.0	111.0	13.0	903	241	74.0	2.0	78.0	± 1.0
T205_**1**	632	483	0.66	0.0573	0.0037	0.0978	0.0064	0.0123	0.00016	0.0038	0.00010	0.190	17	79.0	1.0	95.0	6.0	504	135	76.0	2.0	79.0	± 1.0
T205_**7**	248	182	0.63	0.0663	0.0076	0.1135	0.0134	0.0124	0.00022	0.0038	0.00009	0.140	27	80.0	1.0	109.0	12.0	816	237	76.0	2.0	80.0	± 1.0
T205_**9**	216	173	0.69	0.0570	0.0037	0.0984	0.0065	0.0126	0.00016	0.0041	0.00013	0.200	16	80.0	1.0	95.0	6.0	492	138	83.0	3.0	80.0	± 1.0
T205_**19**	195	92	0.41	0.0636	0.0057	0.1106	0.0102	0.0126	0.00016	0.0039	0.00007	0.150	24	80.8	1.0	106.0	9.0	729	186	78.0	1.0	80.8	± 1.0
T205_**4**	113	76	0.58	0.0741	0.0096	0.1300	0.0171	0.0126	0.00021	0.0042	0.00026	0.130	35	81.0	1.0	124.0	15.0	1045	262	84.0	5.0	81.0	± 1.0
T205_**16**	193	128	0.57	0.0638	0.0051	0.1118	0.0095	0.0127	0.00018	0.0039	0.00006	0.210	25	81.0	1.0	108.0	9.0	733	164	79.0	1.0	81.0	± 1.0
T205_**18**	305	248	0.70	0.0789	0.0079	0.1408	0.0143	0.0130	0.00025	0.0041	0.00014	0.180	38	83.0	2.0	134.0	13.0	1168	194	83.0	3.0	83.0	± 2.0
T205_**11**	162	65	0.34	0.0631	0.0040	0.1137	0.0075	0.0132	0.00018	0.0045	0.00027	0.210	23	84.0	1.0	109.0	7.0	711	131	90.0	5.0	84.0	± 1.0
T205_**14**	271	141	0.45	0.0639	0.0042	0.1254	0.0083	0.0142	0.00017	0.0045	0.00018	0.190	24	91.0	1.0	120.0	7.0	738	132	90.0	4.0	91.0	± 1.0

Weighted ^{206}Pb/^{238}U mean age = 79.5 ± 1.0

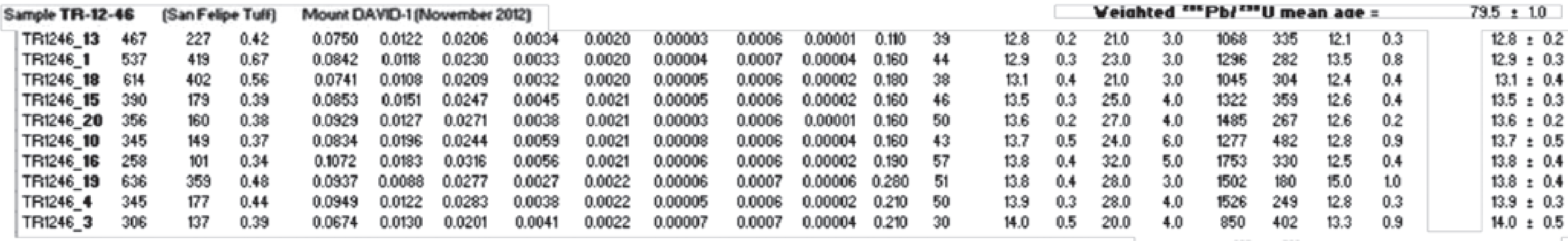

Tabla 2b

Sample **TR-12-46**	(San Felipe Tuff)	Mount DAVID-1 (November 2012)																					
TR1246_**13**	467	227	0.42	0.0750	0.0122	0.0206	0.0034	0.0020	0.00003	0.0006	0.00001	0.110	39	12.8	0.2	21.0	3.0	1068	335	12.1	0.3	12.8	± 0.2
TR1246_**1**	537	419	0.67	0.0842	0.0118	0.0230	0.0033	0.0020	0.00004	0.0007	0.00004	0.160	44	12.9	0.3	23.0	3.0	1296	282	13.5	0.8	12.9	± 0.3
TR1246_**18**	614	402	0.56	0.0741	0.0108	0.0209	0.0032	0.0020	0.00005	0.0006	0.00002	0.180	38	13.1	0.4	21.0	3.0	1045	304	12.4	0.4	13.1	± 0.4
TR1246_**15**	390	179	0.39	0.0853	0.0151	0.0247	0.0045	0.0021	0.00005	0.0006	0.00002	0.160	46	13.5	0.3	25.0	4.0	1322	359	12.6	0.4	13.5	± 0.3
TR1246_**20**	356	160	0.38	0.0929	0.0127	0.0271	0.0038	0.0021	0.00003	0.0006	0.00001	0.160	50	13.6	0.2	27.0	4.0	1485	267	12.6	0.2	13.6	± 0.2
TR1246_**10**	345	149	0.37	0.0834	0.0196	0.0244	0.0059	0.0021	0.00008	0.0006	0.00004	0.160	43	13.7	0.5	24.0	6.0	1277	482	12.8	0.9	13.7	± 0.5
TR1246_**16**	258	101	0.34	0.1072	0.0183	0.0316	0.0056	0.0021	0.00006	0.0006	0.00002	0.190	57	13.8	0.4	32.0	5.0	1753	330	12.5	0.4	13.8	± 0.4
TR1246_**19**	636	359	0.48	0.0937	0.0088	0.0277	0.0027	0.0022	0.00006	0.0007	0.00006	0.280	51	13.8	0.4	28.0	3.0	1502	180	15.0	1.0	13.8	± 0.4
TR1246_**4**	345	177	0.44	0.0949	0.0122	0.0283	0.0038	0.0022	0.00005	0.0006	0.00002	0.210	50	13.9	0.3	28.0	4.0	1526	249	12.8	0.3	13.9	± 0.3
TR1246_**3**	306	137	0.39	0.0674	0.0130	0.0201	0.0041	0.0022	0.00007	0.0007	0.00004	0.210	30	14.0	0.5	20.0	4.0	850	402	13.3	0.9	14.0	± 0.5

Weighted ^{206}Pb/^{238}U mean age = 13.38 ± 0.32

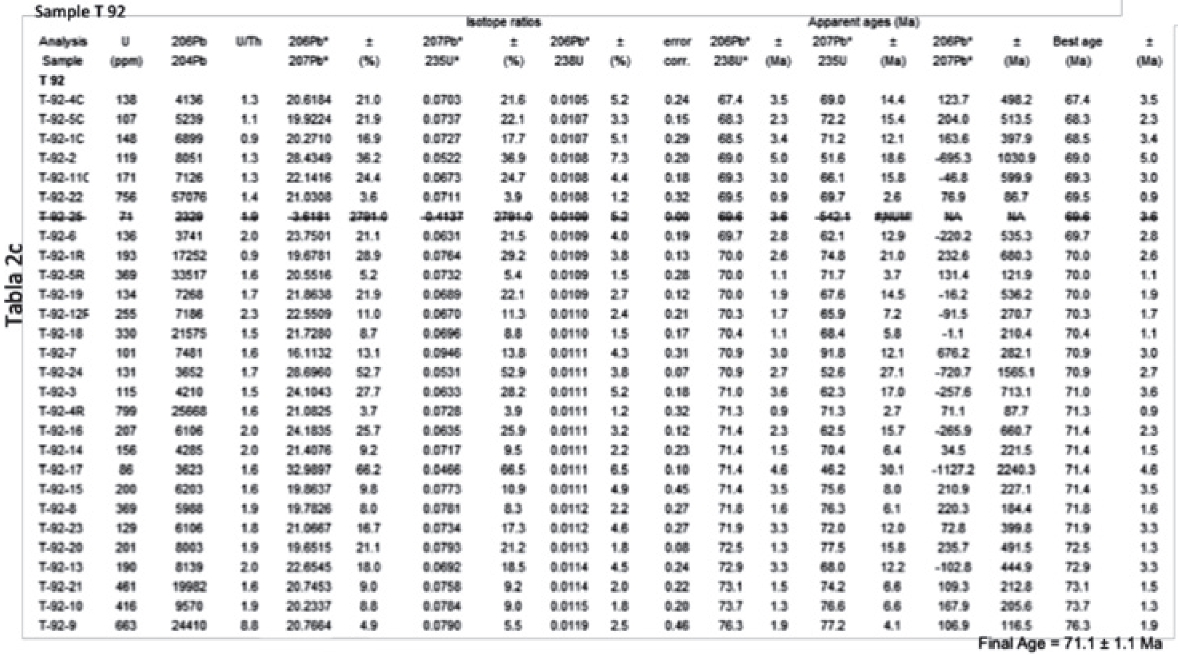

Tabla 2c

Sample T 92

				Isotope ratios							Apparent ages (Ma)							
Analysis Sample	U (ppm)	206Pb 204Pb	U/Th	206Pb* 207Pb*	± (%)	207Pb* 235U*	± (%)	206Pb* 238U	± (%)	error corr.	206Pb* 238U*	± (Ma)	207Pb* 235U	± (Ma)	206Pb* 207Pb*	± (Ma)	Best age (Ma)	± (Ma)
T 92																		
T-92-4C	138	4136	1.3	20.6184	21.0	0.0703	21.6	0.0105	5.2	0.24	67.4	3.5	69.0	14.4	123.7	498.2	67.4	3.5
T-92-5C	107	5239	1.1	19.9224	21.9	0.0737	22.1	0.0107	3.3	0.15	68.3	2.3	72.2	15.4	204.0	513.5	68.3	2.3
T-92-1C	148	6899	0.9	20.2710	16.9	0.0727	17.7	0.0107	5.1	0.29	68.5	3.4	71.2	12.1	163.6	397.9	68.5	3.4
T-92-2	119	8051	1.3	28.4349	36.2	0.0522	36.9	0.0108	7.3	0.20	69.0	5.0	51.6	18.6	-695.3	1030.9	69.0	5.0
T-92-11C	171	7126	1.3	22.1416	24.4	0.0673	24.7	0.0108	4.4	0.18	69.3	3.0	66.1	15.8	-46.8	599.9	69.3	3.0
T-92-22	756	57076	1.4	21.0308	3.6	0.0711	3.9	0.0108	1.2	0.32	69.5	0.9	69.7	2.6	76.9	86.7	69.5	0.9
~~T-92-25~~	~~71~~	~~2329~~	~~4.9~~	~~-3.6181~~	~~2791.0~~	~~-0.4137~~	~~2791.0~~	~~0.0109~~	~~5.2~~	~~0.00~~	~~69.6~~	~~3.6~~	~~-542.1~~	~~#NUM!~~	~~NA~~	~~NA~~	~~69.6~~	~~3.6~~
T-92-6	136	3741	2.0	23.7501	21.1	0.0631	21.5	0.0109	4.0	0.19	69.7	2.8	62.1	12.9	-220.2	535.3	69.7	2.8
T-92-1R	193	17252	0.9	19.6781	28.9	0.0764	29.2	0.0109	3.8	0.13	70.0	2.6	74.8	21.0	232.6	680.3	70.0	2.6
T-92-5R	369	33517	1.6	20.5516	5.2	0.0732	5.4	0.0109	1.5	0.28	70.0	1.1	71.7	3.7	131.4	121.9	70.0	1.1
T-92-19	134	7268	1.7	21.8638	21.9	0.0689	22.1	0.0109	2.7	0.12	70.0	1.9	67.6	14.5	-16.2	536.2	70.0	1.9
T-92-12F	255	7186	2.3	22.5509	11.0	0.0670	11.3	0.0110	2.4	0.21	70.3	1.7	65.9	7.2	-91.5	270.7	70.3	1.7
T-92-18	330	21575	1.5	21.7280	8.7	0.0696	8.8	0.0110	1.5	0.17	70.4	1.1	68.4	5.8	-1.1	210.4	70.4	1.1
T-92-7	101	7481	1.6	16.1132	13.1	0.0946	13.8	0.0111	4.3	0.31	70.9	3.0	91.8	12.1	676.2	282.1	70.9	3.0
T-92-24	131	3652	1.7	28.6960	52.7	0.0531	52.9	0.0111	3.8	0.07	70.9	2.7	52.6	27.1	-720.7	1565.1	70.9	2.7
T-92-3	115	4210	1.5	24.1043	27.7	0.0633	28.2	0.0111	5.2	0.18	71.0	3.6	62.3	17.0	-257.6	713.1	71.0	3.6
T-92-4R	799	25668	1.6	21.0825	3.7	0.0728	3.9	0.0111	1.2	0.32	71.3	0.9	71.3	2.7	71.1	87.7	71.3	0.9
T-92-16	207	6106	2.0	24.1835	25.7	0.0635	25.9	0.0111	3.2	0.12	71.4	2.3	62.5	15.7	-265.9	660.7	71.4	2.3
T-92-14	156	4285	2.0	21.4076	9.2	0.0717	9.5	0.0111	2.2	0.23	71.4	1.5	70.4	6.4	34.5	221.5	71.4	1.5
T-92-17	86	3623	1.6	32.9897	66.2	0.0466	66.5	0.0111	6.5	0.10	71.4	4.6	46.2	30.1	-1127.2	2240.3	71.4	4.6
T-92-15	200	6203	1.6	19.8637	9.8	0.0773	10.9	0.0111	4.9	0.45	71.4	3.5	75.6	8.0	210.9	227.1	71.4	3.5
T-92-8	369	5988	1.9	19.7826	8.0	0.0781	8.3	0.0112	2.2	0.27	71.8	1.6	76.3	6.1	220.3	184.4	71.8	1.6
T-92-23	129	6106	1.8	21.0667	16.7	0.0734	17.3	0.0112	4.6	0.27	71.9	3.3	72.0	12.0	72.8	399.8	71.9	3.3
T-92-20	201	8003	1.9	19.6515	21.1	0.0793	21.2	0.0113	1.8	0.08	72.5	1.3	77.5	15.8	235.7	491.5	72.5	1.3
T-92-13	190	8139	2.0	22.6545	18.0	0.0692	18.5	0.0114	4.5	0.24	72.9	3.3	68.0	12.2	-102.8	444.9	72.9	3.3
T-92-21	461	19982	1.6	20.7453	9.0	0.0758	9.2	0.0114	2.0	0.22	73.1	1.5	74.2	6.6	109.3	212.8	73.1	1.5
T-92-10	416	9570	1.9	20.2337	8.8	0.0784	9.0	0.0115	1.8	0.20	73.7	1.3	76.6	6.6	167.9	205.6	73.7	1.3
T-92-9	663	24410	8.8	20.7664	4.9	0.0790	5.5	0.0119	2.5	0.46	76.3	1.9	77.2	4.1	106.9	116.5	76.3	1.9

Final Age = 71.1 ± 1.1 Ma

Tabla d

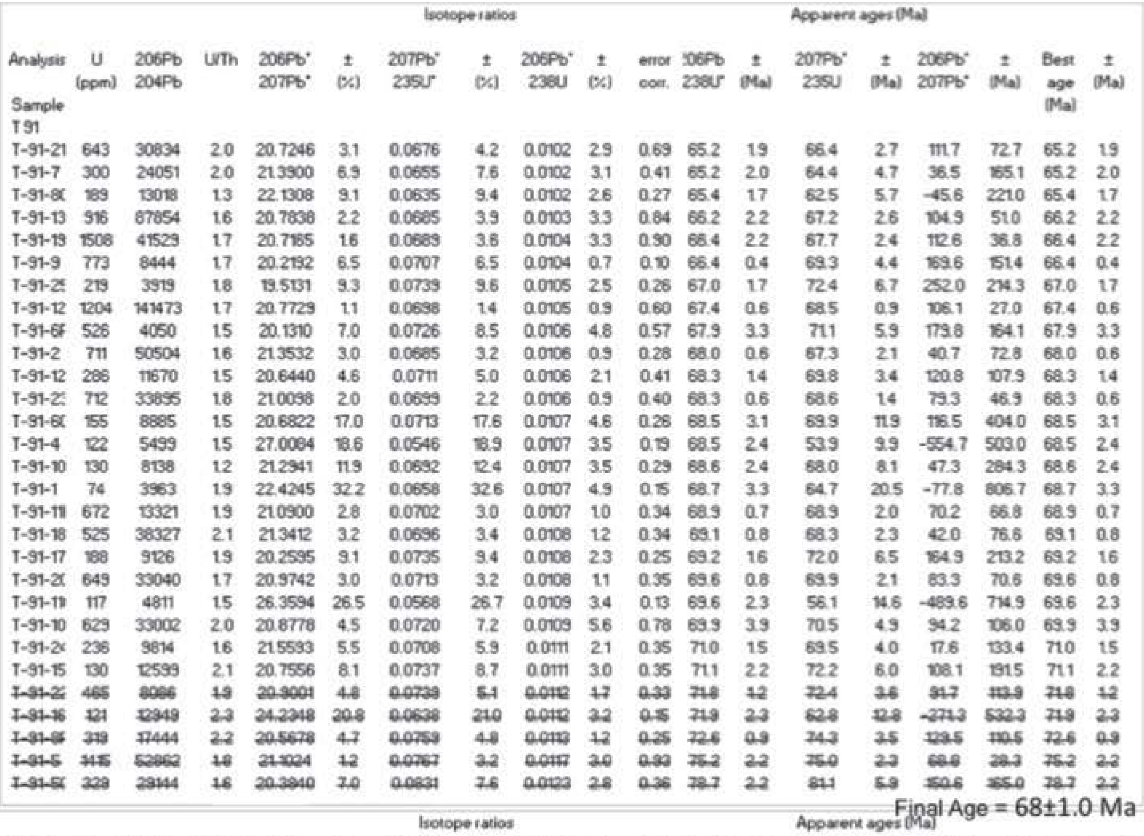

				Isotope ratios							Apparent ages (Ma)							
Analysis	U (ppm)	206Pb 204Pb	U/Th	206Pb* 207Pb*	± (%)	207Pb* 235U*	± (%)	206Pb* 238U	± (%)	error corr.	06Pb 238U*	± (Ma)	207Pb* 235U	± (Ma)	206Pb* 207Pb*	± (Ma)	Best age (Ma)	± (Ma)
Sample																		
T 91																		
T-91-21	643	30834	2.0	20.7246	3.1	0.0676	4.2	0.0102	2.9	0.69	65.2	1.9	66.4	2.7	111.7	72.7	65.2	1.9
T-91-7	300	24051	2.0	21.3900	6.9	0.0655	7.6	0.0102	3.1	0.41	65.2	2.0	64.4	4.7	36.5	165.1	65.2	2.0
T-91-8	189	13018	1.3	22.1308	9.1	0.0635	9.4	0.0102	2.6	0.27	65.4	1.7	62.5	5.7	-45.6	221.0	65.4	1.7
T-91-13	916	87854	1.6	20.7838	2.2	0.0685	3.9	0.0103	3.3	0.84	66.2	2.2	67.2	2.6	104.9	51.0	66.2	2.2
T-91-13	1508	41529	1.7	20.7165	1.6	0.0683	3.6	0.0104	3.3	0.90	66.4	2.2	67.7	2.4	112.6	36.8	66.4	2.2
T-91-9	773	8444	1.7	20.2192	6.5	0.0707	6.5	0.0104	0.7	0.10	66.4	0.4	69.3	4.4	169.6	151.4	66.4	0.4
T-91-2	219	3919	1.8	19.5131	9.3	0.0739	9.6	0.0105	2.5	0.26	67.0	1.7	72.4	6.7	252.0	214.3	67.0	1.7
T-91-12	1204	141473	1.7	20.7729	1.1	0.0698	1.4	0.0105	0.9	0.60	67.4	0.6	68.5	0.9	106.1	27.0	67.4	0.6
T-91-6	526	4050	1.5	20.1310	7.0	0.0726	8.5	0.0106	4.8	0.57	67.9	3.3	71.1	5.9	173.8	164.1	67.9	3.3
T-91-2	711	50504	1.6	21.3532	3.0	0.0685	3.2	0.0106	0.9	0.28	68.0	0.6	67.3	2.1	40.7	72.8	68.0	0.6
T-91-12	286	11670	1.5	20.6440	4.6	0.0711	5.0	0.0106	2.1	0.41	68.3	1.4	69.8	3.4	120.8	107.9	68.3	1.4
T-91-2	712	33895	1.8	21.0098	2.0	0.0699	2.2	0.0106	0.9	0.40	68.3	0.6	68.6	1.4	79.3	46.9	68.3	0.6
T-91-6	155	8885	1.5	20.6822	17.0	0.0713	17.6	0.0107	4.6	0.26	68.5	3.1	69.9	11.9	116.5	404.0	68.5	3.1
T-91-4	122	5499	1.5	27.0084	18.6	0.0546	18.9	0.0107	3.5	0.19	68.5	2.4	53.9	9.9	-554.7	503.0	68.5	2.4
T-91-10	130	8138	1.2	21.2941	11.9	0.0692	12.4	0.0107	3.5	0.29	68.6	2.4	68.0	8.1	47.3	284.3	68.6	2.4
T-91-1	74	3963	1.9	22.4245	32.2	0.0658	32.6	0.0107	4.9	0.15	68.7	3.3	64.7	20.5	-77.8	806.7	68.7	3.3
T-91-11	672	13321	1.9	21.0900	2.8	0.0702	3.0	0.0107	1.0	0.34	68.9	0.7	68.9	2.0	70.2	66.8	68.9	0.7
T-91-18	525	38327	2.1	21.3412	3.2	0.0696	3.4	0.0108	1.2	0.34	69.1	0.8	68.3	2.3	42.0	76.6	69.1	0.8
T-91-17	188	9126	1.9	20.2595	9.1	0.0735	9.4	0.0108	2.3	0.25	69.2	1.6	72.0	6.5	164.9	213.2	69.2	1.6
T-91-2	649	33040	1.7	20.9742	3.0	0.0713	3.2	0.0108	1.1	0.35	69.6	0.8	69.9	2.1	83.3	70.6	69.6	0.8
T-91-1	117	4811	1.5	26.3594	26.5	0.0568	26.7	0.0109	3.4	0.13	69.6	2.3	56.1	14.6	-489.6	714.9	69.6	2.3
T-91-10	629	33002	2.0	20.8778	4.5	0.0720	7.2	0.0109	5.6	0.78	69.9	3.9	70.5	4.9	94.2	106.0	69.9	3.9
T-91-2	236	9814	1.6	21.5593	5.5	0.0708	5.9	0.0111	2.1	0.35	71.0	1.5	69.5	4.0	17.6	133.4	71.0	1.5
T-91-15	130	12599	2.1	20.7556	8.1	0.0737	8.7	0.0111	3.0	0.35	71.1	2.2	72.2	6.0	108.1	191.5	71.1	2.2
~~T-91-2~~	~~465~~	~~8086~~	~~1.9~~	~~20.9001~~	~~4.8~~	~~0.0739~~	~~5.1~~	~~0.0112~~	~~1.7~~	~~0.33~~	~~71.8~~	~~1.2~~	~~72.4~~	~~3.6~~	~~91.7~~	~~113.9~~	~~71.8~~	~~1.2~~
~~T-91-16~~	~~121~~	~~12949~~	~~2.3~~	~~24.2348~~	~~20.8~~	~~0.0638~~	~~21.0~~	~~0.0112~~	~~3.2~~	~~0.15~~	~~71.9~~	~~2.3~~	~~62.8~~	~~12.8~~	~~-271.3~~	~~532.3~~	~~71.9~~	~~2.3~~
~~T-91-8~~	~~319~~	~~17444~~	~~2.2~~	~~20.5678~~	~~4.7~~	~~0.0759~~	~~4.8~~	~~0.0113~~	~~1.2~~	~~0.25~~	~~72.6~~	~~0.9~~	~~74.3~~	~~3.5~~	~~129.5~~	~~110.5~~	~~72.6~~	~~0.9~~
~~T-91-5~~	~~1415~~	~~52862~~	~~1.8~~	~~21.1024~~	~~1.2~~	~~0.0767~~	~~3.2~~	~~0.0117~~	~~3.0~~	~~0.93~~	~~75.2~~	~~2.2~~	~~75.0~~	~~2.3~~	~~68.6~~	~~28.3~~	~~75.2~~	~~2.2~~
~~T-91-5~~	~~328~~	~~29144~~	~~1.6~~	~~20.3840~~	~~7.0~~	~~0.0831~~	~~7.6~~	~~0.0123~~	~~2.8~~	~~0.36~~	~~78.7~~	~~2.2~~	~~81.1~~	~~5.9~~	~~350.6~~	~~365.0~~	~~78.7~~	~~2.2~~

Final Age = 68±1.0 Ma

Tabla e

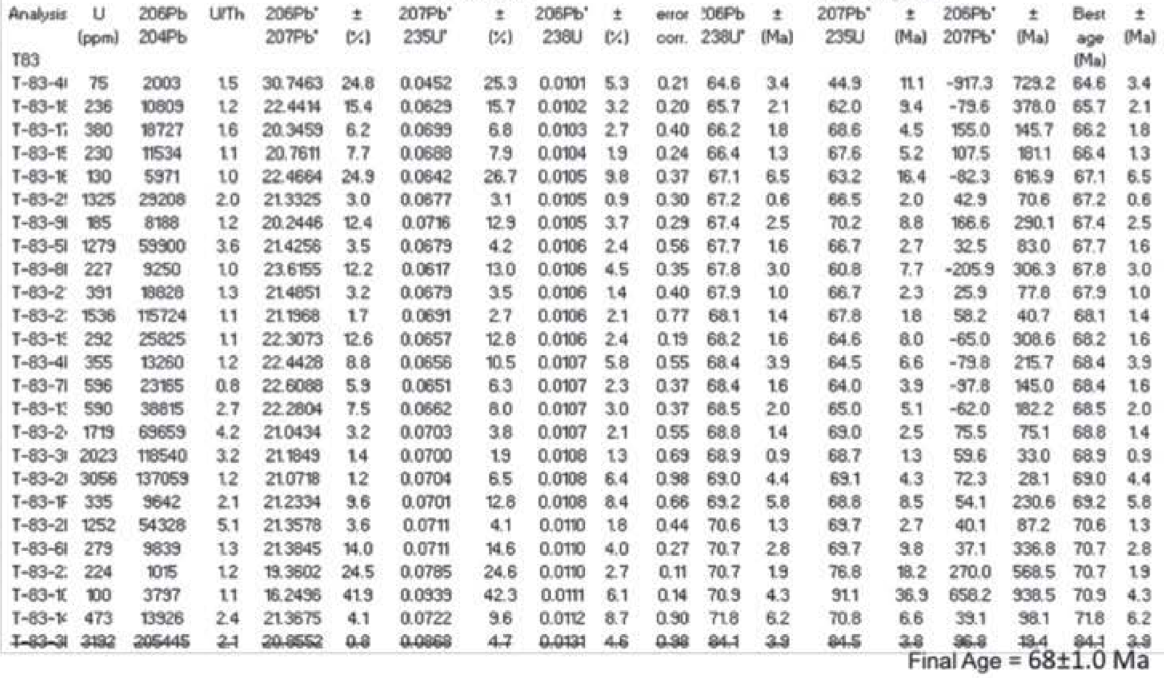

				Isotope ratios							Apparent ages (Ma)							
Analysis	U (ppm)	206Pb 204Pb	U/Th	206Pb* 207Pb*	± (%)	207Pb* 235U*	± (%)	206Pb* 238U	± (%)	error corr.	06Pb 238U*	± (Ma)	207Pb* 235U	± (Ma)	206Pb* 207Pb*	± (Ma)	Best age (Ma)	± (Ma)
T83																		
T-83-4	75	2003	1.5	30.7463	24.8	0.0452	25.3	0.0101	5.3	0.21	64.6	3.4	44.9	11.1	-917.3	729.2	64.6	3.4
T-83-1	236	10809	1.2	22.4414	15.4	0.0629	15.7	0.0102	3.2	0.20	65.7	2.1	62.0	9.4	-79.6	378.0	65.7	2.1
T-83-1	380	18727	1.6	20.3459	6.2	0.0699	6.8	0.0103	2.7	0.40	66.2	1.8	68.6	4.5	155.0	145.7	66.2	1.8
T-83-1	230	11534	1.1	20.7611	7.7	0.0688	7.9	0.0104	1.9	0.24	66.4	1.3	67.6	5.2	107.5	181.1	66.4	1.3
T-83-1	130	5971	1.0	22.4664	24.9	0.0642	26.7	0.0105	9.8	0.37	67.1	6.5	63.2	16.4	-82.3	616.9	67.1	6.5
T-83-2	1325	29208	2.0	21.3325	3.0	0.0677	3.1	0.0105	0.9	0.30	67.2	0.6	66.5	2.0	42.9	70.6	67.2	0.6
T-83-9	185	8188	1.2	20.2446	12.4	0.0716	12.9	0.0105	3.7	0.29	67.4	2.5	70.2	8.8	166.6	290.1	67.4	2.5
T-83-5	1279	59900	3.6	21.4256	3.5	0.0679	4.2	0.0106	2.4	0.56	67.7	1.6	66.7	2.7	32.5	83.0	67.7	1.6
T-83-8	227	9250	1.0	23.6155	12.2	0.0617	13.0	0.0106	4.5	0.35	67.8	3.0	60.8	7.7	-205.9	306.3	67.8	3.0
T-83-2	391	18828	1.3	21.4851	3.2	0.0679	3.5	0.0106	1.4	0.40	67.9	1.0	66.7	2.3	25.9	77.8	67.9	1.0
T-83-2	1536	115724	1.1	21.1968	1.7	0.0691	2.7	0.0106	2.1	0.77	68.1	1.4	67.8	1.8	58.2	40.7	68.1	1.4
T-83-1	292	25825	1.1	22.3073	12.6	0.0657	12.8	0.0106	2.4	0.19	68.2	1.6	64.6	8.0	-65.0	308.6	68.2	1.6
T-83-4	355	13260	1.2	22.4428	8.8	0.0656	10.5	0.0107	5.8	0.55	68.4	3.9	64.5	6.6	-79.8	215.7	68.4	3.9
T-83-7	596	23165	0.8	22.6088	5.9	0.0651	6.3	0.0107	2.3	0.37	68.4	1.6	64.0	3.9	-97.8	145.0	68.4	1.6
T-83-1	590	38815	2.7	22.2804	7.5	0.0662	8.0	0.0107	3.0	0.37	68.5	2.0	65.0	5.1	-62.0	182.2	68.5	2.0
T-83-2	1719	69659	4.2	21.0434	3.2	0.0703	3.8	0.0107	2.1	0.55	68.8	1.4	69.0	2.5	75.5	75.1	68.8	1.4
T-83-3	2023	118540	3.2	21.1849	1.4	0.0700	1.9	0.0108	1.3	0.69	68.9	0.9	68.7	1.3	59.6	33.0	68.9	0.9
T-83-2	3056	137059	1.2	21.0718	1.2	0.0704	6.5	0.0108	6.4	0.98	69.0	4.4	69.1	4.3	72.3	28.1	69.0	4.4
T-83-1	335	9642	2.1	21.2334	9.6	0.0701	12.8	0.0108	8.4	0.66	69.2	5.8	68.8	8.5	54.1	230.6	69.2	5.8
T-83-2	1252	54328	5.1	21.3578	3.6	0.0711	4.1	0.0110	1.8	0.44	70.6	1.3	69.7	2.7	40.1	87.2	70.6	1.3
T-83-6	279	9839	1.3	21.3845	14.0	0.0711	14.6	0.0110	4.0	0.27	70.7	2.8	69.7	9.8	37.1	336.8	70.7	2.8
T-83-2	224	1015	1.2	19.3602	24.5	0.0785	24.6	0.0110	2.7	0.11	70.7	1.9	76.8	18.2	270.0	568.5	70.7	1.9
T-83-1	100	3797	1.1	16.2496	41.9	0.0939	42.3	0.0111	6.1	0.14	70.9	4.3	91.1	36.9	658.2	938.5	70.9	4.3
T-83-1	473	13926	2.4	21.3675	4.1	0.0722	9.6	0.0112	8.7	0.90	71.8	6.2	70.8	6.6	39.1	98.1	71.8	6.2
~~T-83-3~~	~~3192~~	~~205445~~	~~2.1~~	~~20.8552~~	~~0.8~~	~~0.0868~~	~~4.7~~	~~0.0131~~	~~4.6~~	~~0.98~~	~~84.1~~	~~3.9~~	~~84.5~~	~~3.8~~	~~86.8~~	~~19.4~~	~~84.1~~	~~3.9~~

Final Age = 68±1.0 Ma

Geofísica Internacional (2014) 53-4: 457-471

Original paper

AVOA techniques for fracture characterization

Vladimir Sabinin

Received: September 02, 2013; accepted: December 05, 2013; published on line: October 01, 2014

Resumen

Se tomaron en consideración distintos aspectos de algunas técnicas computacionales para el análisis AVOA (Amplitud Versus Offset y Azimut), para la composición de fracturas, en particular: utilizando amplitudes en lugar de coeficientes de refección, suavizando los datos sísmicos y el método de la estimación numérica para calcular la dirección. Se estimó un nuevo método de cálculo y se indica un nuevo método suavizado. Se compararan distintos métodos de cálculo en los datos sintéticos de superficie de reflección, con y sin ruido. Se obtuvieron propiedades de los métodos numéricos, dependientes de conjuntos distintos de los azimut y los offset. Se muestra una superioridad del nuevo método.

Palabras clave: AVOA, medio HTI, anisotropía sísmica, caracterización de yacimientos fracturados.

Abstract

Different aspects of computational techniques for AVOA analysis (Amplitude Versus Offset and Azimuth) for fracture characterization are considered, in particular: using amplitudes instead of reflection coefficients, smoothing seismic data, and numerical methods for estimation of fracture directions. A new computational method and a new filter for smoothing are suggested. The different computational methods are compared in synthetic reflection surface data with noise, and without noise. Properties of the numerical methods in dependence on different sets of azimuths and offsets are obtained. It is shown a superiority of the new method.

Key words: AVOA, HTI medium, seismic anisotropy, fracture-reservoir characterization.

V. Sabinin*
Instituto Mexicano del Petróleo
Eje Central Lázaro Cárdenas 152
Col. San Bartolo Atepehuacan
C.P. 07730
México D.F., México.
*Corresponding author: vsabinin@yahoo.com

Introduction

The analysis of azimuthal variation in reflection coefficients, or AVOA analysis (Amplitude Versus Offset and Azimuth), is widely applied for detecting and mapping highly fractured zones with azimuthally-oriented vertical cracks (Mallik *et al*., 1998; Jenner, 2002; Sabinin & Chichinina, 2008). The AVOA techniques are based on the Rüger (1998) approximation for the reflection coefficients in HTI medium, and give principal symmetry directions of HTI medium.

Here, the computational aspects of AVOA techniques are considered, namely, applying amplitudes instead of reflection coefficients, smoothing the amplitudes, an incidence angle estimation, methods for obtaining the symmetry-axis angle, synthetic data for testing techniques, and a numerical experiment for investigating properties of the techniques. A new computational method for obtaining the symmetry-axis angle and a new filter for smoothing are suggested. All considered techniques are compared in synthetic anisotropic seismic data with noise, and without noise. The suggested new technique proved better than the others.

Background

The methodology of AVOA analysis is based on the concept of azimuthal anisotropy caused for the most part by parallel vertical fractures. It leads to the azimuthal anisotropy of amplitudes, in particular, to azimuthal variation in reflection coefficients. Let a fractured reservoir be represented by a model of a transversely isotropic medium with horizontal symmetry axis (HTI medium). The PP-wave reflection coefficient R at the interface (or at the reflecting boundary) between weakly anisotropic HTI media (or between an isotropic medium and an anisotropic HTI medium) is defined by the approximate formula (Rüger, 1998):

$$R(\theta, \phi)= A + B(\phi)\sin^2\theta + C(\phi)\sin^2\theta\tan^2\theta, \tag{1}$$

where θ is the incidence angle, and ϕ is the source-receiver-line azimuth with respect to the coordinate axis x. The term A is the normal-incidence reflection coefficient

$$A = \Delta Z/(2\bar{Z}) \tag{2}$$

where $Z \equiv \rho V_P^{\parallel}$ is the vertical P-wave impedance, $V_P^{\parallel}$ is the vertical velocity (or velocity in the isotropy plane) of the P-wave, ρ is density, Δ denotes the difference between the values of a parameter below and above the reflecting boundary, and the bar $\overline{\ldots}$ indicates average of these values. $V_P^{\parallel} = V_P$ in the isotropic media.

The coefficient $B(\phi)$ is a so-called AVO gradient, which can be written (Rüger, 1998) as

$$B(\phi) = B_{iso} + B_{ani}\cos^2(\phi-\phi_0), \tag{3}$$

where ϕ_0 is the angle of the symmetry axis with the x--axis. The term B_{iso} is the AVO-gradient isotropic part (equal to the AVO gradient for isotropic media), and B_{ani} is the anisotropic part of the AVO gradient.

The coefficient $C(\phi)$ can be written (Rüger, 1998) as,

$$C(\phi) = \alpha+\beta\cos^4(\phi-\phi_0) + \gamma\sin^2(\phi-\phi_0)\cos^2(\phi-\phi_0), \tag{4}$$

where $\alpha \equiv \Delta V_P^{\parallel}/(2\bar{V}_P^{\parallel})$, $\beta = \frac{1}{2}\Delta\varepsilon^{(V)}$, and $\gamma = \frac{1}{2}\Delta\delta^{(V)}$.

Above, Thomsen-style anisotropy parameters $\varepsilon^{(V)}$, and $\delta^{(V)}$ are negative for HTI media, and they are equal to zero for isotropic media.

The main problem of AVOA analysis is to estimate the symmetry-axis angle ϕ_0 from surface seismic data of amplitudes using numerical techniques.

The techniques of AVOA are based on equations (1) - (4). Note that equation (1) is intended for calculation of reflection coefficients, while in real data, one operates with amplitudes of reflected waves, not with reflection coefficients. This brings some problems which are discussed in the next section.

Using amplitudes instead of reflection coefficients

While the background of AVOA analysis is based on Rüger's equation for the reflection coefficient (1), in real data, AVOA analysis should use signal amplitudes. It is true that the amplitude is not equal to the reflection coefficient. Moreover, no picked instantaneous amplitude (sample) in the signal can be used instead of the reflection coefficient because the signal changes its form during propagation for many reasons. It seems that one should use an integral amplitude characteristic of the signal which adequately corresponds to the reflection coefficient. Let's call this characteristic simply by amplitude and denote it as P.

The estimated value of ϕ_0 is very sensitive to the definition of P, especially for data with noise. I suggest the following procedure for definition of P which gives good and stable results. The procedure calculates an average value of a signal envelope in a time window. In calculating the envelope, the Fourier transform of this signal is used: $F = F_+ + F_-$, where F is spectrum, F_+ is the part of spectrum corresponding to positive frequencies ($\omega \geq 0$), and F_- is the part of negative frequencies. The envelope of the signal is given by the absolute value of inverse Fourier transform of the spectrum with double F_+, and $F_- \equiv 0$ (Sheriff & Geldart, 1983).

The sign of envelope is positive; therefore this approach is applicable only to seismograms with the constant sign of reflection coefficient in dependence on offset.

For data with noise, the envelope is noisy, too (see Figure 1). Therefore, smoothing is necessary.

For smoothing, an algorithm of discrete transformations of wavelet by filters is applied. Four symmetric filters are constructed for it: the low-pass (h_0) and high-pass (h_1) analysis filters, and the low-pass (h_2) and high-pass (h_3) synthesis filters. The right-hand part of h_0 consists from the filter derived by Abdelnour & Selesnick (2004). The left-hand part of h_0 is symmetric to it. That is

$$h_0(\{-n,...,n\})=\{b,b,-a,a,b,b,a,-a,c,\\ -a,a,b,b,a,-a,b,b\}, \qquad (5)$$

where $a = M/32, M = \sqrt{2}/2, b = 4a$, and $n = 8$. The central value is $c = 1-M$.

The high-pass analysis filter is constructed by formula $h_1(i) = (-1)^i h_0(n-i+1)$ for $i \neq 0$, and $h_1(0) = 0$. The synthesis filters are calculated by formula $h_2(i) = (-1)^i h_1(i)$, $h_3(i) = (-1)^i h_0(i)$, see (Abdelnour & Selesnick, 2005). The central values are $h_2(0) = c$ and $h_3(0) = 0$.

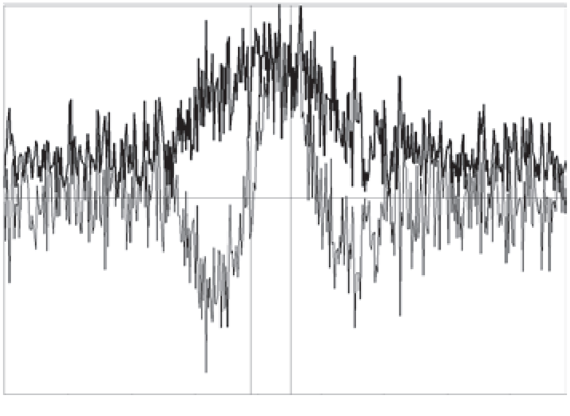

Figure 1. A signal with noise (thin line) in time, and its envelope.

The smoothed signal is obtained by the decomposition algorithm; see Figure 2 (WSBP, 2012).

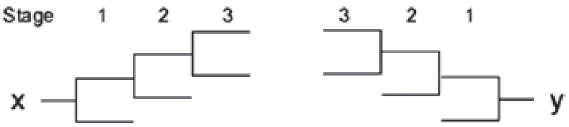

Figure 2. The 3-stage decomposition algorithm.

The input signal is $x(j)$, $j=1,\ldots,m$, $m>>2n$. It is decomposed into low and high components $lo_1(j)$ and $hi_1(j)$ in the first stage:

$$lo_1(j) = \sum_{i=-n}^{n} h_0(i)x(i+j),$$

$$hi_1(j) = \sum_{i=-n}^{n} h_1(i)x(i+j),$$

$$j = 1,...,m \; .$$

In the next stages ($s = 2,\ldots, S$), the each low component $lo_{s-1}(j)$ is decomposed by the same analysis filters.

After all stages of decomposition finishing, the stages of applying the synthesis filters are fulfilled in reverse order ($s=S, S-1,\ldots,1$):

$$lo_{s-1}(j) = \sum_{i=-n}^{n} h_2(i)lo_s(i+j) + \sum_{i=-n}^{n} h_3(i)hi_s(i+j),$$

$$j = 1,...,m \, .$$

The output signal $y(j)$ is obtained finally:

$$y(j) = lo_0(j)p,$$

where the fitting amplitude coefficient p can be approximately estimated by the formula $p = 1+0.057S$, where S is the number of stages.

The advantage of this variant of discrete transformation algorithm in comparison with (WSBP, 2012) is the absence of shift functions in it due to applying the fully symmetric filters ($i=-n,\ldots,n$).

It must be noted that the algorithm gives unsatisfactory results at the edges of the signal because of truncating the filters in $2n$ edge points. Therefore, it is necessary $m>>2n$.

The result of smoothing the signal of Figure 1 by the 3-stage algorithm is presented in Figure 3. The smoothness of resulting curve increases with increasing S. Also with increasing S, the algorithm slightly deforms the resulting impulse in comparison with the parent impulse without noise. Optimum in the smoothness and in the conservation of form is observed at the value $S = 3$.

The limits of time window for calculating P with the help of envelope can be chosen by different ways. I use the following way. From the envelope of signal $e(t)$, the maximum e_m and nearest local minimums, left e_l and right e_r, are calculated. The left limit of the time window is set in the point where $e = e_l + 0.15(e_m - e_l)$, and the right limit – where $e = e_r + 0.15(e_m - e_l)$, see vertical lines in Figures 1, 3. Obviously, this algorithm correctly works only with smoothed signals.

Equation (1) should be rewritten for using the amplitudes. If the source and the receivers are at the earth surface, then the amplitude of reflected PP-wave can be expressed as

$$P = c_g^2 R P_{ini} \,,$$

where c_g is the coefficient of geometrical spreading (divergence) from source to reflection point for this wave, $c_g = c_g(\theta, \phi)$, P_{ini} is the amplitude of the source (the initial amplitude), and R is the reflection coefficient, $R = R(\theta, \phi)$ in the equation (1).

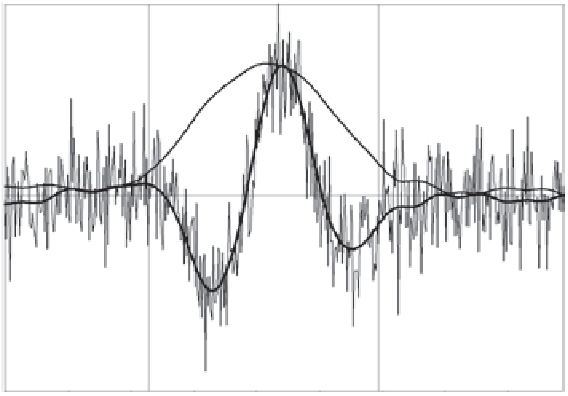

Figure 3. The signal with noise (thin line), the smoothed signal (thick line), and the envelope of smoothed signal.

The amplitude for the normal-incidence wave can be written as

$$P_0 = c_{g0}^2 A P_{ini} \,,$$

where c_{g0} is the normal-incidence coefficient of geometrical spreading, which does not depend on (θ, ϕ), and A is the normal-incidence reflection coefficient, $A = const$, see equations (1) - (2). Then the reflection coefficient can be expressed as

$$R = A \frac{c_{g0}^2 P}{c_g^2 P_0} \,.$$

Therefore the equation (1) for the reflection coefficient R transforms into the following equation for the amplitude P:

$$r_g P(\theta, \phi) = P_0 + mB(\phi)\sin^2\theta + mC(\phi)\sin^2\theta \tan^2\theta, \tag{6}$$

where $m = P_0/A$, and $r_g \equiv (c_{g0} / c_g)^2$. This equation should be used in the AVOA techniques instead of (1).

Note that c_g can be expressed as $c_g = c(\theta, \phi)/r$ in 3D space, where r is a half of travel path from source to receiver, and c depends on the direction of wave propagation (for isotropic media, $c = const$). In assuming a weak anisotropy, one may assume a weak dependence of geometrical spreading on incidence angle: $c \approx const$ for a given source-to-receiver line with azimuth ϕ. Then, for a homogeneous medium above the reflecting boundary,

$$r_g = \frac{c_{g0}^2}{c_g^2} = \frac{r^2}{z^2} = \frac{1}{\cos^2\theta} \,, \tag{7}$$

where z is the normal-incidence ray path, and $c_{g0} \equiv c / z$. It is the approximate formula for divergent correction.

Also for multilayered media, the expressions for divergence correction can be found from Newman (1973). A practical methodology for the P-wave geometrical-spreading correction in layered azimuthally anisotropic media can be found from Xu & Tsvankin (2004).

The incidence angle estimation

In the case of n isotropic layers above the reflecting boundary, one can obtain the incidence angle $\theta = \theta_n$ from a solution of the following non-linear equation for a:

$$x_0 = a\sum_{i=1}^{n}\frac{z_i V_i}{\sqrt{1-a^2V_i^2}}\,, \qquad (8)$$

where x_0 is the half of offset, z_i is the thickness of i-th layer, V_i is the velocity in i-th layer, and $\sin(\theta_n) = aV_n$. For calculating the geometrical spreading, the travel path $r = \sum_{i=1}^{n}\frac{z_i}{\sqrt{1-a^2V_i^2}}$.

In the case of the reflecting boundary being the lower boundary of anisotropic layer, the problem is more complicated because the last layer is anisotropic, and the velocity V_n depends on θ_n in it and is not known beforehand.

The problem can be solved by Sabinin (2012). An advantage of his method is that the value V_n in the anisotropic layer is unnecessary for calculating angle θ_n and path r. However, it uses additionally the impulse from the upper boundary of anisotropic layer what complicates the technique. It gives results not sufficiently better than the method (8). Therefore, I use the simple method (8) here with setting an approximate value of V_n.

The methods for estimation of symmetry axis angle by AVOA

Usually, 3D seismic data used in AVOA analysis are received from a system of receivers and sources spacing in nodes of a rectangle grid at the surface. The symmetry axis angle is calculated for a small square (for a bin) including a node of the grid, by using seismic traces which have the Common Middle Point (CMP) located in this bin. If such traces are few, then neighbor bins are combined into a superbin, and calculations are made for it. Therefore, a preliminary stage of the estimation is an extraction of seismic traces of the superbin from the seismic data for taking them into consideration.

For numerical methods of estimation of symmetry axis angle, one can use equation (6) as in Rüger's form:

$$T_* = a + (b_* + ct)s + (d_* + e_*t + ft^2)s^2/(1-s), \qquad (9a)$$

as in the power form:

$$T = a + s(b + ct) + s^2\,(d + et + ft^2), \qquad (9b)$$

where $T_* = r_g\,P(\theta, \phi)$, $T = (1-s)T_*$, $s = \sin^2\theta$, $t = \cos^2(\phi-\phi_0)$, $a = P_0$, $b_* = mB_{iso}$, $b = b_*-a$, $c = mB_{ani}$, $d_* = m\alpha$, $d = d_*-b_*$, $e_* = m\Delta\delta^{(V)}/2$, $e = e_*-c$, $f = m\Delta\varepsilon^{(V)}/2-e_*$ and $m = P_0/A$.

The methods vary by simplifying ways applied, and can be separated into Sectored methods (S and SR), Linear methods (L and LR), and General method (G), where the letter 'R' denotes that the Rüger's form (9a) is used instead of (9b).

Sectored methods

The method SR was suggested by Mallik *et al*. (1998) for the case of three azimuths with using equations (1), and (3). It took its perfect form in the work by Sabinin & Chichinina (2008) who used equations (6), (3), and (4). For this method, the traces of superbin are sorted by *n* azimuthal sectors. It is adopted that all traces of the sector have the same value of azimuth equal to the middle azimuth of the sector. Because of this, sectored methods introduce in ϕ_0 an own error no more than a half of the sector size.

Here, the method S applied to equation (9b) is presented. If in the sector of azimuth ϕ_j $(j = 1, \ldots, n)$, there are k_j traces with incidence angles θ_j $(i = 1, \ldots, k_j)$ in the last layer above the target boundary, then one can write from (9b) for this sector *j*:

$$T_{ij} = P_j + B_j^1 s_i + C_j^1 s_i^2\,, \qquad (10)$$

where T_{ij} is the value T calculated from the trace *i* in the sector *j*. In each sector, $B_j^1 = m_jB_j$, $C_j^1 = m_jC_j$, where $m_j = P_j/A$, and P_j, B_j^1, C_j^1 are the fitting constants.

Having T_{ij} and θ_i for all *i* in the sector *j* ($k_j \geq 3$), one can calculate $s_i = \sin^2\theta i$, and then P_j, B_j^1, and C_j^1 from (10) by the least-squares method. For this, it is minimized the functional of error for each sector *j*:

$$F_j = \sum_{i=1}^{k_j}(P_j + B_j^1 s_i + C_j^1 s_i^2 - T_{ij})^2\,.$$

For minimizing F_j, it is necessary to solve the system of three equations:

$$\partial F_j / \partial P_j = 0\,,\ \partial F_j / \partial B_j^1 = 0\,,\ \partial F_j / \partial C_j^1 = 0\,.$$

It gives: $C_j^1 = \frac{b_1f_1 - a_1g_1}{b_1^2 - a_1c_1}$, $B_j^1 = (f_1-C_j^1\,b_1)/a_1$, and $P_j = (u_0-BC_j^1-AB_j^1)/k_j$, where $a_1 = A^2-Bk_j$, $b_1 = AB-Ck_j$, $c_1 = B^2-Dk_j$, $f_1 = Au_0-u_1k_j$, $g_1 = Bu_0-u_2k_j$, ,

$$A = \sum_{i=1}^{k_j} s_i\,,\ B = \sum_{i=1}^{k_j} s_i^2\,,\ C = \sum_{i=1}^{k_j} s_i^3\,,\ D = \sum_{i=1}^{k_j} s_i^4\,,$$

$$u_0 = \sum_{i=1}^{k_j} T_{ij}\ ,\ u_1 = \sum_{i=1}^{k_j} s_i T_{ij}\ , \text{ and } u_2 = \sum_{i=1}^{k_j} s_i^2 T_{ij}\ .$$

These calculations should be made for all sectors.

Then, the unknown value ϕ_0 can be obtained from the system of equations of type (3), see (9b):

$$B_j^1 / P_j = b^1 + c^1 t_j, \tag{11}$$

where $j = 1, ..., n$, and $t_j = \cos^2(\phi - \phi_0)$. The unknown constants b^1, and c^1 have a sense: $b^1 A = B_{iso} - A$, and $c^1 A = B_{ani}$.

Equation (11) is transformed into more convenient form:

$$U_j = b_0 + c_0 g g_j + c_0 h h_j, \tag{12}$$

where $U_j = B_j^1 / P_j$, $b_0 = b^1 + 0.5c^1$, $c_0 = 0.5c^1$, $g = \cos(2\phi_0)$, $h = \sin(2\phi_0)$, $g_j = \cos(2\phi_j)$ and $h_j = \sin(2\phi_j)$.

The system (12) has three unknowns (b_0, c_0, and ϕ_0), therefore it should be $n \geq 3$ for obtaining solution. The system (12) has two solutions (two ϕ_0 differing in $\pi/2$, and two c_0 of opposite signs, correspondently), and is solved by the least-squares method, too. It is minimized the functional of error:

$$F = \sum_{j=1}^{n} (b_0 + c_0 g g_j + c_0 h h_j - U_j)^2. \tag{13}$$

The following system of three equations should be solved:

$$\partial F / \partial b_0 = 0, \partial F / \partial c_0 = 0, \partial F / \partial \phi_0 = 0.$$

It gives: $\tan(2\varphi_0) \equiv \frac{h}{g} = \frac{b_1 f_1 - a_1 f_2}{b_1 f_2 - c_1 f_1}$, $c_0 = f_1 / (g a_1 + h b_1)$, and $b_0 = [u_0 - c_0(Ag + Bh)]/n$, where

$a_1 = A^2 - Cn$, $b_1 = AB - Dn$, $c_1 = B^2 - En$, $f_1 = Au_0 - u_1 n$, $f_2 = Bu_0 - u_2 n$, $A = \sum_{j=1}^{n} g_j$, $B = \sum_{j=1}^{n} h_j$, $C = \sum_{j=1}^{n} g_j^2$, $D = \sum_{j=1}^{n} g_j h_j$, $E = \sum_{j=1}^{n} h_j^2$, $u_0 = \sum_{j=1}^{n} U_j$, $u_1 = \sum_{j=1}^{n} g_j U_j$, and $u_2 = \sum_{j=1}^{n} h_j U_j$.

The condition for distinguishing symmetry-axis from fracture-strike directions is derived by Sabinin & Chichinina (2008), and uses equation (4). Here it is presented in more general form.

In terms of equations (9b), (10), and (11), equation (4) can be written as

$$C_j^1 / P_j = d^1 + e^1 t_j + f^1 t_j^2\ , \tag{14}$$

where $j = 1, ..., n$, $d^1 = (\alpha - B_{iso})/A$, $e^1 = (\Delta\delta^{(V)}/2 - B_{ani})/A$, and $f^1 = (\Delta\varepsilon^{(V)} - \Delta\delta^{(V)})/(2A)$.

When substituting the value $\varphi_0 \pm \frac{\pi}{2}$ instead of ϕ_0 into equation (14), the sign of the second term $e^1 t_j$ switches to the opposite sign, because equation (14) takes the form

$$C_j^1 / P_j = (d^1 + e^1) - e^1 t_j + f^1 t_j^2\ .$$

The last term of equation (11) $c^1 t_j$ switches its sign, too. One can combine $\Delta\delta^{(V)} = 2A(c1 + e^1)$ from definitions to equations (11), (14), and conclude that the sign of $\Delta\delta^{(V)}$ is switched, too. For calculating $\Delta\delta^{(V)}$, it should be solved system (14) which is similar to (10) by the method of solution.

If the HTI layer is situated between isotropic layers then $\Delta\delta^{(V)}$ must be negative *for upper reflecting boundary* of the HTI layer, and positive *for lower boundary*. If the calculated value of $\Delta\delta^{(V)}$ has this sign then ϕ_0 is the symmetry-axis angle. In opposite case, it is the fracture-strike direction.

It must be noted that $\Delta\varepsilon^{(V)} = 2A(c^1 + e^1 + f^1)$, and also can be used for distinguishing solutions because $\varepsilon^{(V)}$ and $\delta^{(V)}$ have the same sign.

The formal condition that the second derivative of functional (13) must be positive in the minimum of functional can also be applied. Because of errors in data, it should be used as an additional condition to previous ones, and should have a form $\partial^2 F / \partial \phi_0^2 >$ a small value.

Linear methods

The method LR was suggested by Jenner (2002) for equation (1). It is not needed in sectoring data. All traces of superbin are taken into consideration together.

Here, it is applied to equation (9b), the method L. Equation (9b) is truncated after a line part respecting s. If the superbin has n traces($i = 1, ..., n$), with incidence angles θ_i at the target boundary, and with azimuthal angles

ϕ_i, then one can write the result of truncation in the form:

$$T_i = a + s_i\,(b_0 + c_0 g g_i + c_0 h h i). \qquad (15)$$

where T_i is the value T calculated from the trace i, $s_i = \sin^2\theta_i$, $b_0 = \mathrm{b} + 0.5c$, $c_0 = 0.5c$, $g = \cos(2\phi_0)$, $h = \sin(2\phi_0)$, $g_i = \cos(2\phi_i)$, and $h_i = \sin(2\phi_i)$.

The values s_i, g_i, and h_i are known because they can be calculated from headers of seismograms and parameters of medium. Let us consider the functional of error:

$$F = \sum_{i=1}^{n} (a + b_0 s_i + c_0 g s_i g_i + c_0 h s_i h_i - T_i)^2 . \qquad (16)$$

Functional F must be minimized over parameters a, b_0, c_0, and ϕ_0. For this, it is necessary to solve the system of four equations:

$$\partial F/\partial a = 0,\ \partial F/\partial b_0 = 0,\ \partial F/\partial c_0 = 0,\ \partial F/\partial \phi_0 = 0. \qquad (17)$$

Solution of system (17) gives the equation for obtaining ϕ_0:

$$\tan(2\varphi_0) = \frac{h}{g} = \frac{A_2 H_1 - A_1 H_2}{A_2 H_2 - B_1 H_1}, \qquad (18)$$

where $A_1 = a_1 b_1 - a_2^2$, $B_1 = a_1 c_1 - a_3^2$, $A_2 = a_1 b_2 - a_2 a_3$, $H_1 = F_2 a_1 - F_1 a_2$, and $H_2 = F_3 a_1 - F_1 a_3$ in which $a_1 = nB - A^2$, $b_1 = nI - D^2$, $c_1 = nJ - E^2$, $a_2 = nG - AD$, $b_2 = nK - ED$, $a_3 = nH - AE$, $F_1 = nf_1 - Af_0$, $F_2 = nf_2 - Df_0$, and $F_3 = nf_3 - Ef_0$, and finally: $A = \sum_{i=1}^{n} s_i$, $B = \sum_{i=1}^{n} s_i^2$, $D = \sum_{i=1}^{n} g_i s_i$, $E = \sum_{i=1}^{n} h_i s_i$, $G = \sum_{i=1}^{n} g_i s_i^2$, $H = \sum_{i=1}^{n} h_i s_i^2$, $I = \sum_{i=1}^{n} g_i^2 s_i^2$, $J = \sum_{i=1}^{n} h_i^2 s_i^2$, $K = \sum_{i=1}^{n} g_i h_i s_i^2$, $f_0 = \sum_{i=1}^{n} T_i$, $f_1 = \sum_{i=1}^{n} s_i T_i$, $f_2 = \sum_{i=1}^{n} g_i s_i T_i$, and $f_3 = \sum_{i=1}^{n} h_i s_i T_i$.

The other parameters are:

$$c_0 = \frac{A_2 H_1 - A_1 H_2}{h(A_2^2 - A_1 B_1)}, \quad b_0 = (F_1 - c_0 g a_2 - c_0 h a_3)/a_1,$$

and $a = (f_0 - b_0 A - c_0 g D - c_0 h E)/n$.

From (18), one can see that the solution ϕ_0 has a period of $\frac{\pi}{2}$. This value of the period means that we must use an additional condition for understanding what value ϕ_0 is the symmetry-axis azimuth. This condition may be $B_{ani} > 0$ if $V_S / V_P > 0.56$ (Chichinina *et al*., 2003). In general case, it can be the condition $\partial^2 F/\partial \phi_0^2 >$ a small positive value, where F is the functional of error (16).

General method (G)

The method is constructed by analogy with the GM method by Sabinin (2013). It is not needed in sectoring, too. All traces of superbin are taken into consideration together. If the superbin has n traces ($i = 1, ..., n$), with incidence angles θ_i at the target boundary, and with azimuthal angles ϕ_i, then equation (9b) can be written as:

$$T_i = a + bs_i + cs_i t_i + ds_i^2 + es_i^2 t_i + fs_i^2 t_i^2 ,$$

where T_i is the value T calculated from the trace i, $s_i = \sin^2\theta_i$, and $t_i = \cos^2(\phi_i - \phi_0)$.

Let us consider the functional of error:

$$F = \sum_{i=1}^{n} (a + bs_i + cs_i t_i + ds_i^2 + es_i^2 t_i + fs_i^2 t_i^2 - T_i)^2 . \qquad (19)$$

Functional F must be minimized over parameters a, b, c, d, e, f, and ϕ_0. For this, it is necessary to solve the system of seven equations:

$$\partial F/\partial a = 0, \partial F/\partial b = 0, \partial F/\partial c = 0, \partial F/\partial d = 0,$$
$$\partial F/\partial e = 0, \partial F/\partial f = 0, \partial F/\partial \phi_0 = 0. \qquad (20)$$

The six first equations of system (20) give a line system for deriving expressions for the parameters a, b, c, d, e, and f (for details, see Appendix).

The last equation of (20) can be transformed into a non-linear equation for obtaining ϕ_0 (for details, see Appendix).

Thus, system (20) is non-linear on ϕ_0, and is solved by the method of bisecting. It has more than one solution usually. From these local solutions, one chooses that one which gives a minimum for functional (19).

As was observed from calculations, the solutions of system (20) near the symmetry axis angle, and near the fracture strike angle give close values of functional (19). It means that additional criterions are practically needed for separating these directions. For the case of HTI layer situated between isotropic layers, it can be the condition of negative values for calculated $\varepsilon^{(V)}$ and $\delta^{(V)}$ in the anisotropic layer, as above. For this, from definitions to equations (9b) and (2), one can calculate from the solution of (20) at the interface:

$$\Delta\varepsilon^{(V)} = 2A(c + e + f)/a, \tag{21}$$

$$\Delta\delta^{(V)} = 2A(c + e)/a. \tag{22}$$

In the case of interface between anisotropic layers, it is needed additionally to know the predefined signs of $\Delta\varepsilon^{(V)}$, and $\Delta\delta^{(V)}$ for comparison.

The additional criterion can also be the maximum of second derivative of functional (19), $\partial F/\partial\phi_0$.

Comparing the AVOA techniques

The techniques using the methods above for estimation of symmetry axis angle were compared in ability to give the most precise value of ϕ_0 for HTI medium. At present, reliable field methods of obtaining ϕ_0 do not exist. Therefore, I generated synthetic seismograms for an artificial three-layer medium with the anisotropic layer in the middle by applying the technique by Sabinin (2012) of 2D wave modeling. I set ϕ_0 =60º, and derived models of the anisotropic layer for different values of ϕ_j by rotating the stiffness tensor for anisotropic HTI layer (MacBeth, 1999) around z axis relatively to ϕ_0. Anisotropic parameters e_n = 0.35, and e_t = 0.2 (see MacBeth, 1999) were used in the stiffness tensor.

Host rock velocity V_P in three layers from above had the values 3200, 4000, and 4800 (the other variant was 3200), *m/s*, V_S was twice less, densities were equal, and thicknesses of two first layers were 1600, and 400 *m*. A source of explosion type generated one Ricker impulse of frequency 30 *Hz.* Receivers were spaced over every 100 *m* beginning from the source, and they measured z-component of velocity. There were 50 offsets, and 50 traces in each seismogram.

There were three goals: to investigate how the techniques behave on different sets of incidence angles, how the techniques are influenced by non-symmetry in ϕ_j relatively to ϕ_0, and how the techniques are influenced by noise.

Therefore, for the first goal, I made calculations of ϕ_0 for different intervals of offsets: from a minimum offset till a maximum offset, provided the minimum offset was fixed at the number one, and the number of maximum offset was changed from number 50 down to 3 in one set of the intervals; and the maximum offset was fixed at the 50-th, and the minimum offset was changed from number 1 to 48 in the other set of the intervals. Naturally, the maximum incidence angle $\theta_{\max}$ corresponding to the maximum offset, and the minimum incidence angle $\theta_{\min}$ corresponding to the minimum offset was also correspondently changed in these sets of offsets.

For the second goal, I obtained different sets of the synthetic seismograms corresponding to different azimuths, one seismogram for each azimuth. The sets of azimuths were uniform, and differed by symmetry. I did not aim to find the best or the worst set from them. I only supposed that a symmetric set can be better than an asymmetric one. I kept for testing the symmetric set of azimuths $\phi_j = \{-150^\circ, -120^\circ, -90^\circ, -60^\circ, -30^\circ, 0^\circ, 30^\circ, 60^\circ, 90^\circ, 120^\circ, 150^\circ, 180^\circ\}$, and the asymmetric set $\phi_j = \{85^\circ, 95^\circ, 105^\circ, 115^\circ, 125^\circ, 135^\circ, 145^\circ, 155^\circ, 165^\circ\}$.

For the third goal, I took the best variant for the symmetric set of seismograms to eliminate the errors as due to the non-symmetry, as due to a finite-difference simulation when applying the artificial noise. The FD simulation by Sabinin (2012) uses PML boundary conditions which give non-visible (see Figure 4) but non-zero waves reflected from the boundaries of area. This slightly distorts the form of some synthetic impulses.

For the synthetic seismic data being quasi-real, I added a random Gauss normal noise to the seismograms generated, different for each seismogram. Maximum amplitude of the noise was chosen as 10% of the maximum amplitude of the wave reflected from the top boundary of the anisotropic layer in the first trace of seismogram.

Finally, I added the noise to the seismograms of the asymmetric set.

All seismograms were smoothed by filters (5) in the techniques. High-frequency components of the noise are eliminated well after smoothing, as shown in Figure 3. It is principally impossible to eliminate low frequencies compared with the frequency of signal. Therefore, the signal after smoothing remains slightly deformed. I suppose that just these deformations affect the estimated value of ϕ_0 in the case of noise.

The same sets of the time windows were used for all the techniques, and for all intervals of offsets.

As illustration, in Figure 4, the seismogram without noise for azimuth 5º is presented for the variant of V_{P3} = 4800 *m/s*; and in Figure 5, the seismogram with noise for azimuth 30º is presented for the variant of V_{P3} = 3200 *m/s*.

As one can see from Figure 5, the amplitudes of noise reach really up to 50% of the maximum wave amplitudes in the middle traces, and up to 100% in the far traces.

The techniques were applied as to upper (1050 ms), as to down boundary (1250 ms) of the anisotropic layer.

In Figures 6, 7, the error of estimated ϕ_0 in degrees (difference with the correct value 60º) is presented for the symmetric set of azimuths and the upper boundary, variant V_{P3} = 3200. Figure 6 is for fixed $\theta_{\min} = 0^{\circ}$, and Figure 7 is for fixed $\theta_{\max} = 56.853^{\circ}$. The sectored methods show some instability for small values of $\theta_{\max} - \theta_{\min}$ in comparison with the others. All methods increase the error in the case of small $\theta_{\max}$ (Figure 6).

For the lower boundary and in the variant V_{P3} = 4800, the general and linear methods also show increasing errors for small $\theta_{\max}$, and small $\theta_{\max} - \theta_{\min}$, see Figure 8, and Figure 9. However, the errors of these methods are sufficiently less than of the sectored methods.

In Figures 10, 11, the variant of Figs. 6, 7 with the added noise is presented. The sectored methods demonstrate so great errors and instability that can not be recommended for applying. The other methods show large errors only for small $\theta_{\max}$ (less than 30º).

The asymmetric set of azimuths is presented by results in Figures 12-15. The variant of upper boundary and V_{P3} = 3200 without noise is presented in Figures 12, 13, and the same with the noise – in Figures 14, 15.

Typical peculiarities of the asymmetric set are: great errors of the sectored methods with instability in noised data, and stable large errors of the linear methods (up to 7º). The general method remains of small errors. The noise causes instability of all methods in the interval of $\theta_{\max} < 36^{\circ}$, provided even the general method (G) gives large errors in this interval.

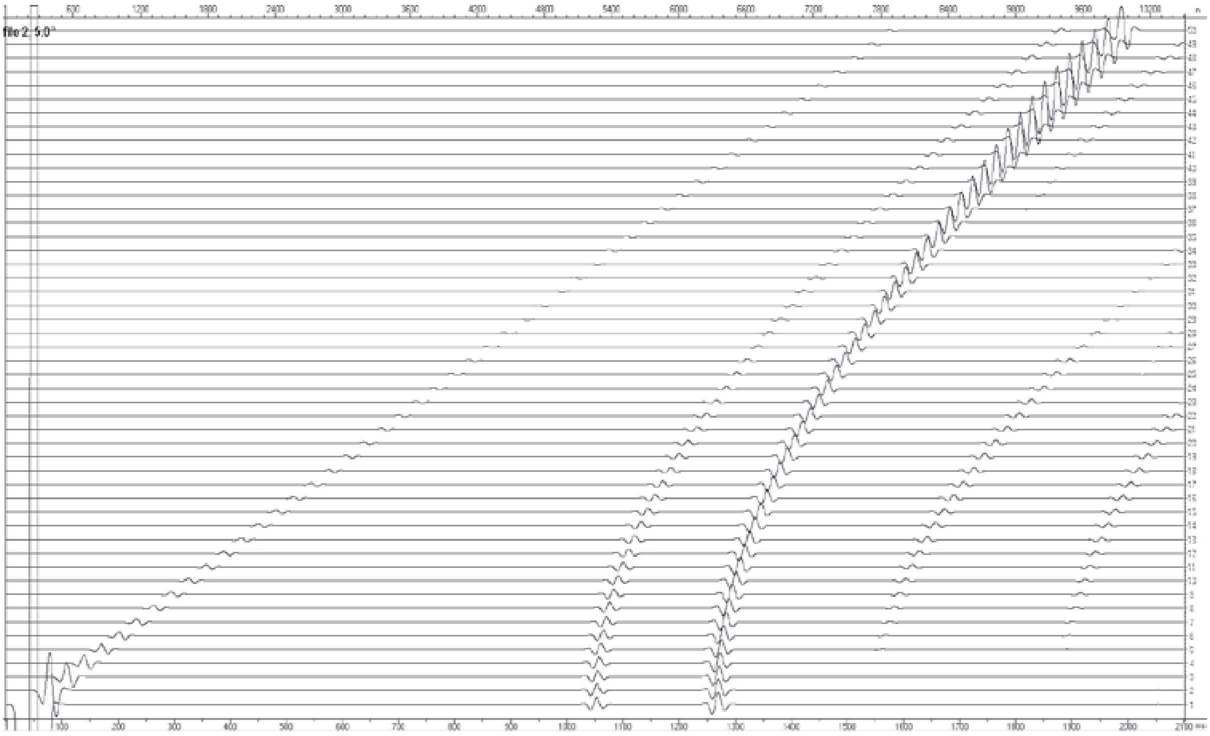

Figure 4. Synthetic seismogram without noise. Azimuth 5º, V_{P3} = 4800. Axis x – time in ms, axis y – numbers of traces. Zero time is origin of the source impulse.

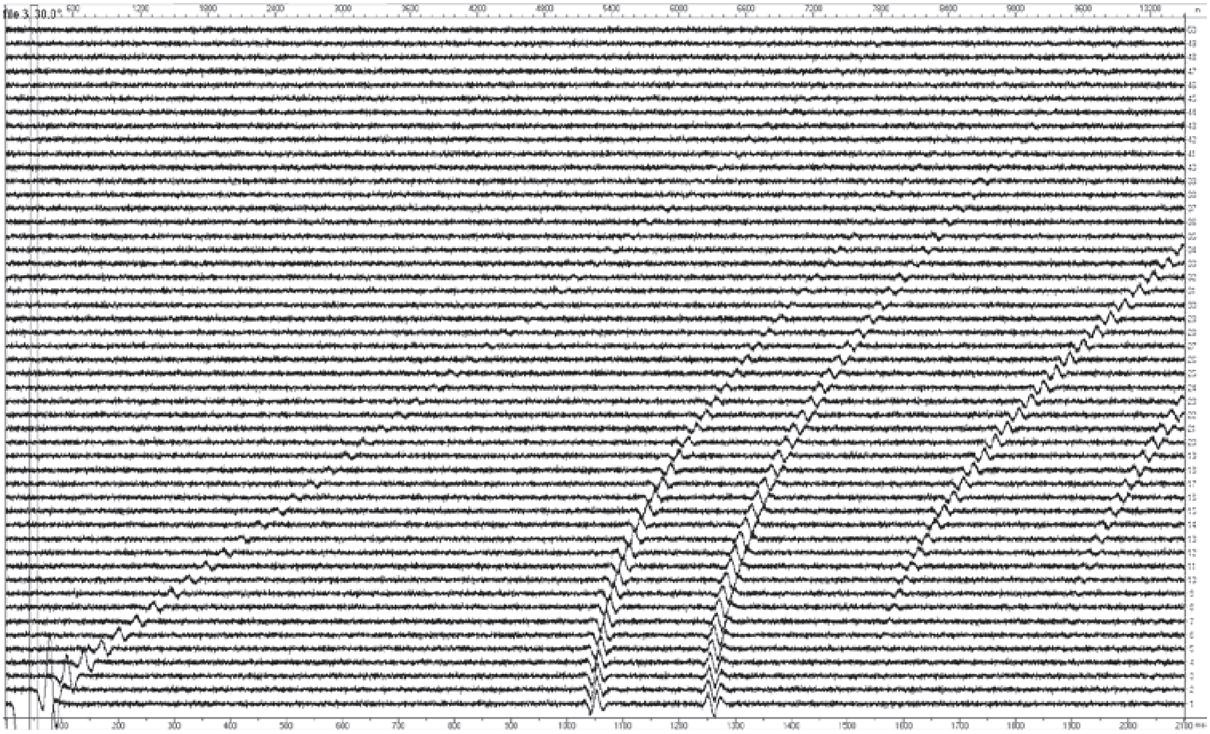

Figure 5. Synthetic seismogram with added 10% noise. Azimuth 30º, V_{P3} = 3200. Axis x – time in ms, axis y – numbers of traces.

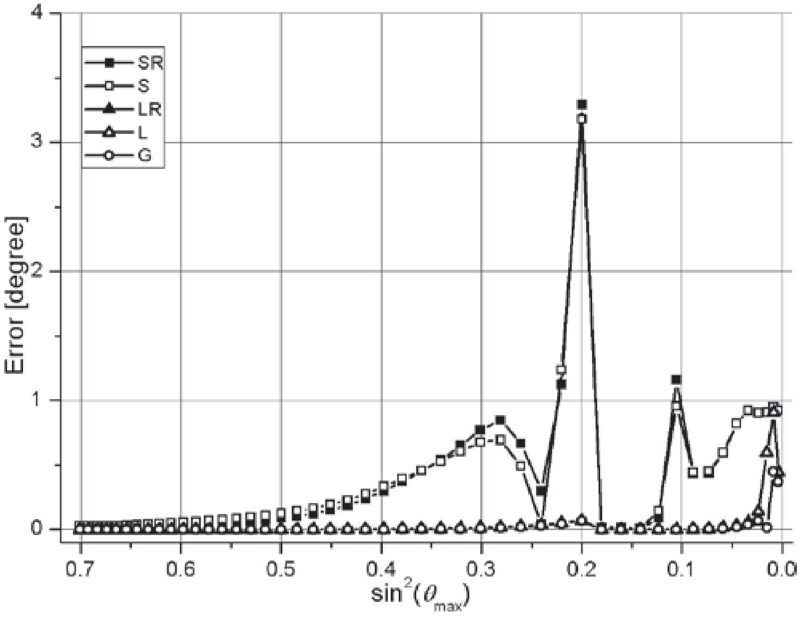

Figure 6. Errors for the symmetric set of azimuths; the upper boundary, and fixed θ_{min}=0.

Figure 7. Errors for the symmetric set of azimuths; the upper boundary, and fixed θ_{max}=56.853°.

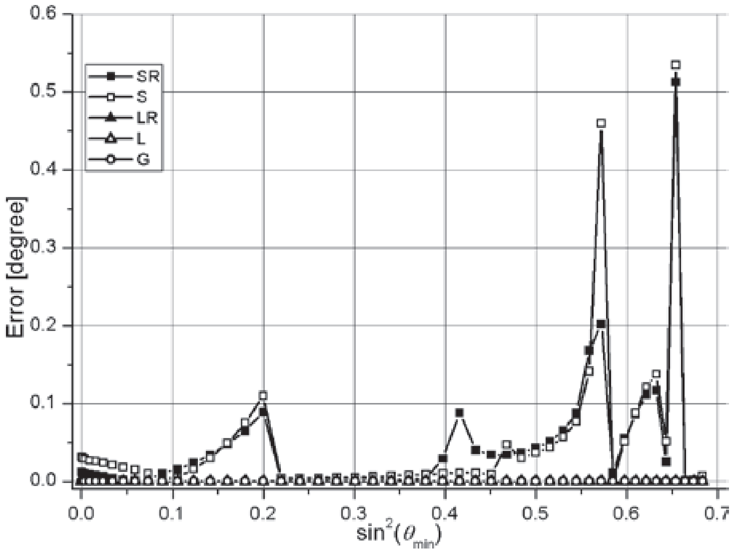

Figure 8. Errors for the symmetric set of azimuths; the lower boundary, variant V_{P3} = 4800, and fixed θ_{min}=0.

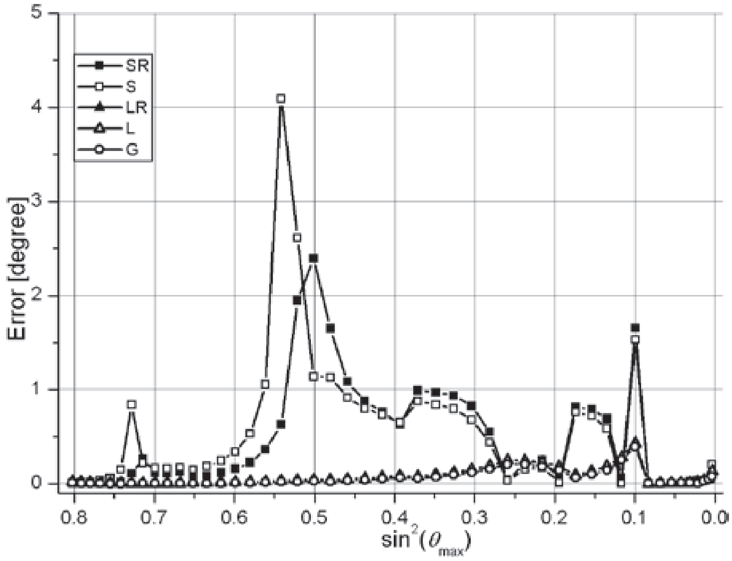

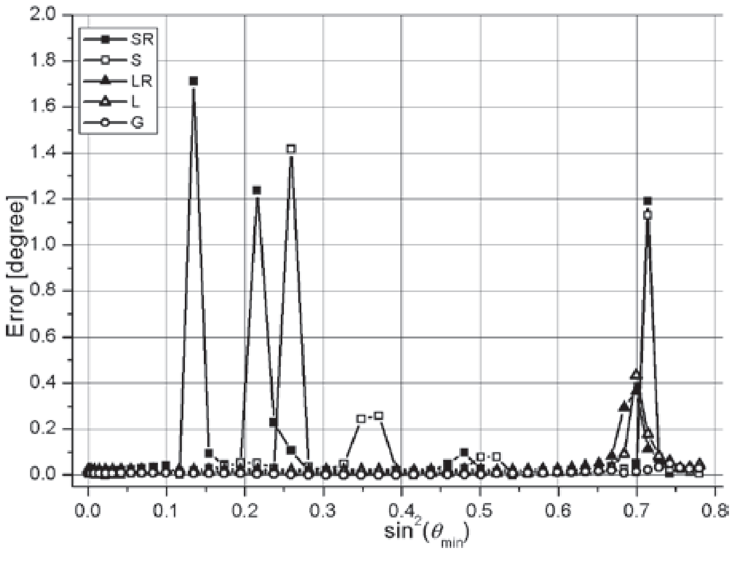

Figure 9. Errors for the symmetric set of azimuths; the lower boundary, variant V_{P3} = 4800, and fixed θ_{max}=63.6°.

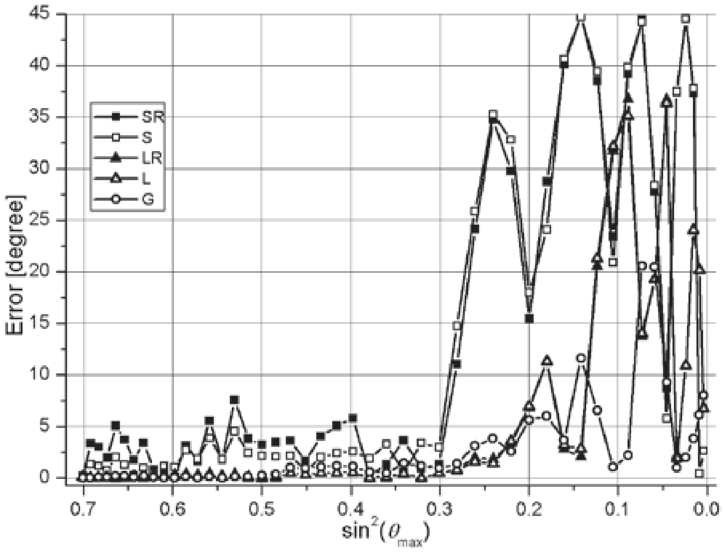

Figure 10. Errors for the symmetric set of azimuths; the noise, the upper boundary, V_{P3} = 3200, and fixed $\theta_{min}=0$.

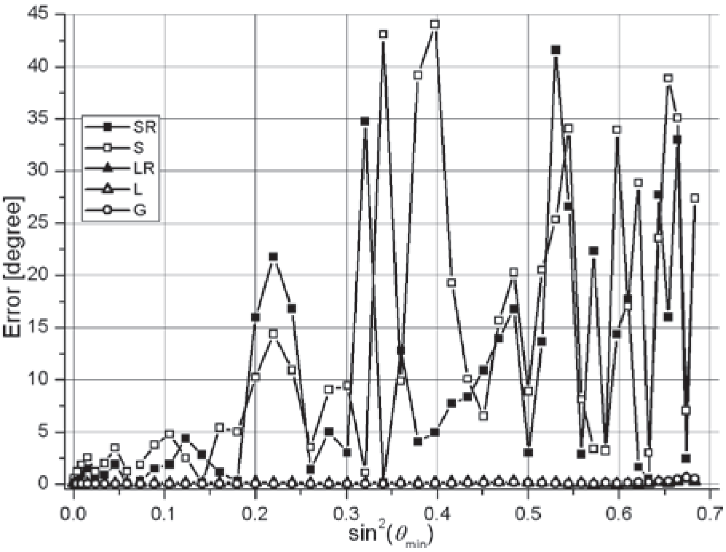

Figure 11. Errors for the symmetric set of azimuths; the noise, the upper boundary, V_{P3} = 3200, and fixed $\theta_{max}=56.853°$.

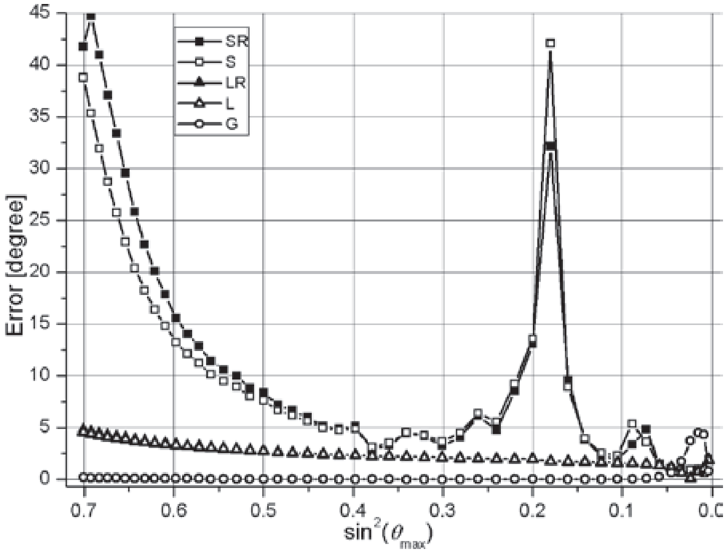

Figure 12. Errors for the asymmetric set of azimuths; the upper boundary, variant V_{P3} = 3200, and fixed $\theta_{min}=0$.

Figure 13. Errors for the asymmetric set of azimuths; the upper boundary, variant V_{P3} = 3200, and fixed $\theta_{\max}$=56.853°.

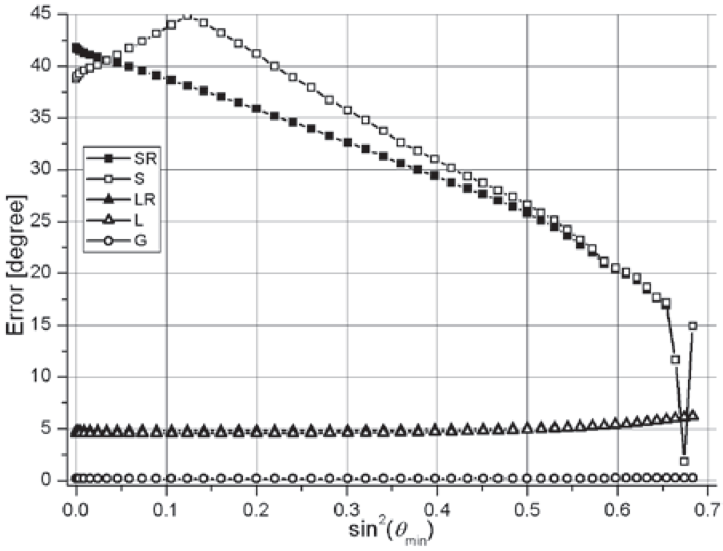

Figure 14. Errors for the asymmetric set of azimuths; the noise, the upper boundary, V_{P3} = 3200, and fixed $\theta_{\min}$=0.

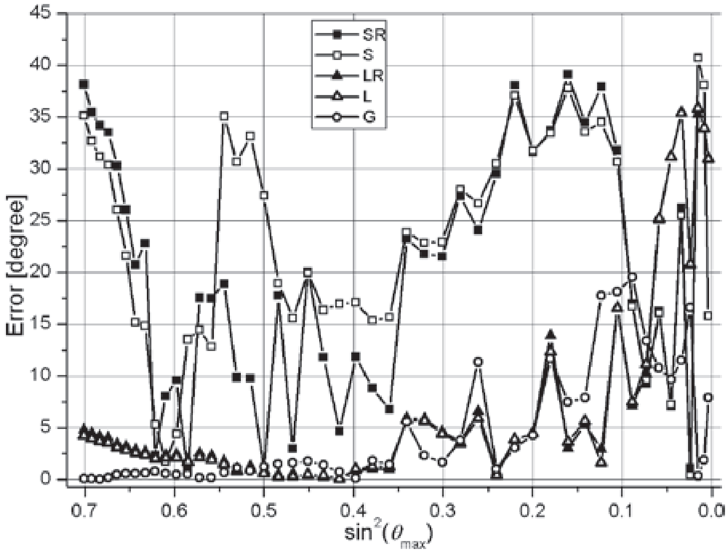

Figure 15. Errors for the asymmetric set of azimuths; the noise, the upper boundary, variant V_{P3} = 3200, and fixed $\theta_{\max}$=56.853°.

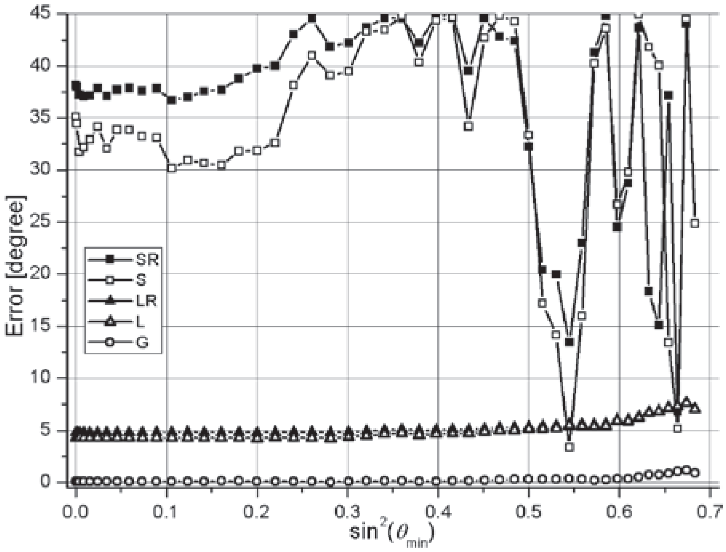

Discussion and conclusion

Some unexpected results were obtained. The first is that the sectored S and SR methods are failed. They can be used only in seismic data without noise, and for mainly symmetric distributions of azimuths ϕ in the 3D data (Figures 6 - 9). This is too ideal conditions.

The second is that the linear L and LR methods have an additional nearly constant error in mainly asymmetric distributions of azimuths ϕ in the data (Figures 12 - 15). This error is probably connected with the truncation of high terms in equation (1) of Rüger, because the general method G has not such error. Therefore, the linear methods should be applied to azimuthally symmetric data.

The third is that the smoothing data with noise by simple filters (5) gives relatively stable estimated values of ϕ_0 in a wide interval of incidence angles θ for the methods L, LR, and G (Figures 10, 11, 14, 15). The interval of instability is near the normal incidence, and has a width of $\theta_{\max}<40^{\circ}$, different in different variants (Figures 10, 14). For data without noise, this interval is $\theta_{\max}<10^{\circ}$ (Figures 6, 8). Presence of the interval of instability is an intrinsic property of the formula (1) in connection with the least-squares method. Errors in amplitudes become relatively more with decreasing θ in definition of ϕ_0 by equation (1).

The results show a superior of the general method (G). On the whole, its errors are less than of the others. Unfortunately, it has an intrinsic problem of choosing the right solution from the local solutions of non-linear system (20). All criterions described above do not guarantee the correct choosing. It is especially difficult in the interval of instability. All the methods have such problem of distinguishing solutions. The best in this sense is the method L. Its criterions are failed very rarely. Therefore, I recommend applying the method G in a coupling with the method L: after estimation of ϕ_0 by L, the value ϕ_0 is defined more precisely by G with expertly taking into consideration the local solutions of (20). The other recommendation is to avoid the interval of instability.

In applying to field data, the techniques can give worse results. The real data have much more interferences of waves than the synthetic data. It is practically impossible to clear each interfered wave of the other by filters. Distorted by this way impulses can lead to unpredictable results.

Appendix. Solution of system (20)

Let's define:

$$A=\sum_{i=1}^{n} s_i, B=\sum_{i=1}^{n} s_i t_i, C=\sum_{i=1}^{n} s_i^2, D=\sum_{i=1}^{n} s_i^2 t_i,$$

$$E=\sum_{i=1}^{n} s_i^2 t_i^2,\ F=\sum_{i=1}^{n} s_i^3,\ G=\sum_{i=1}^{n} s_i^3 t_i,$$

$$H=\sum_{i=1}^{n} s_i^3 t_i^2,\ K=\sum_{i=1}^{n} s_i^3 t_i^3,\ L=\sum_{i=1}^{n} s_i^4,$$

$$M=\sum_{i=1}^{n} s_i^4 t_i,\ N=\sum_{i=1}^{n} s_i^4 t_i^2,\ O=\sum_{i=1}^{n} s_i^4 t_i^3,$$

$$P=\sum_{i=1}^{n} s_i^4 t_i^4,\ U_0=\sum_{i=1}^{n} T_i,\ U_1=\sum_{i=1}^{n} T_i s_i,$$

$$U_2=\sum_{i=1}^{n} T_i s_i t_i,\ U_3=\sum_{i=1}^{n} T_i s_i^2,\ U_4=\sum_{i=1}^{n} T_i s_i^2 t_i,$$

and $U_5=\sum_{i=1}^{n} T_i s_i^2 t_i^2$.

Then, from the first six equations of system (20), one can derive the formulas for unknown parameters:

$$f=\frac{a_2 f_1 - a_1 f_2}{a_2^2 - a_1 b_1},\ e=\frac{f_1 - f a_2}{a_1},$$

$$d=\frac{g_1 - f a_{13} - e a_{12}}{a_{11}},$$

$$c=\frac{h_1 - f a_{24} - e a_{23} - d a_{22}}{a_{21}},$$

$$b=\frac{k_1 - f a_{05} - e a_{04} - d a_{03} - c a_{02}}{a_{01}},$$

$$a=(U_0 - fE - eD - dC - cB - bA)/n,$$

where $a_{01}=A^2-Cn$, $a_{02}=AB-Dn$, $a_{03}=AC-Fn$, $a_{04}=AD-Gn$, $a_{05}=AE-Hn$, $b_{01}=B^2-En$, $a_{02}=BC-Gn$, $b_{03}=BD-Hn$, $b_{04}=BE-Kn$, $c_{01}=C^2-Ln$, $c_{02}=CD-Mn$, $c_{03}=CE-Nn$, $d_{01}=D^2-Nn$, $d_{02}=DE-On$, $e_{01}=E^2-Pn$, $k_1=AU_0-U_1n$, $k_2=BU_0-U_2n$, $k_3=CU_0-U_3n$, $k_4=DU_0-U_4n$, $k_5=EU_0-U_5n$,
$a_{21}=a_{02}^2-a_{01}b_{01}$, $a_{22}=a_{02}a_{03}-a_{01}b_{02}$,
$a_{23}=a_{02}a_{04}-a_{01}b_{03}$, $a_{24}=a_{02}a_{05}-a_{01}b_{04}$,
$b_{21}=a_{03}^2-a_{01}c_{01}$, $b_{22}=a_{03}a_{04}-a_{01}c_{02}$,
$b_{23}=a_{03}a_{05}-a_{01}c_{03}$, $c_{21}=a_{04}^2-a_{01}d_{01}$,
$c_{22}=a_{04}a_{05}-a_{01}d_{02}$, $d_{21}=a_{05}^2-a_{01}e_{01}$, $h_1=a_{02}k_1-a_{01}k_2$,

$h_2=a_{03}k_1-a_{01}k_3$, $h_3=a_{04}k_1-a_{01}k_4$, $h_4=a_{05}k_1-a_{01}k_5$, $a_{11}=a_{22}^2-a_{21}b_{21}$, $a_{12}=a_{22}a_{23}-a_{21}b_{22}$, $a_{13}=a_{22}a_{24}-a_{21}b_{23}$, $b_{11}=a_{23}^2-a_{21}c_{21}$, $b_{12}=a_{23}a_{24}-a_{21}c_{22}$, $c_{11}=a_{24}^2-a_{21}d_{21}$, $g_1=a_{22}h_1-a_{21}h_2$, $g_2=a_{23}h_1-a_{21}h_3$, $g_3=a_{24}h_1-a_{21}h_4$, $a_1=a_{12}^2-a_{11}b_{11}$, $a_2=a_{12}a_{13}-a_{11}b_{12}$, $b_1=a_{13}^2-a_{11}c_{11}$, $f_1=a_{12}g_1-a_{11}g_2$, and $f_2=a_{13}g_1-a_{11}g_3$.

The seventh equation of system (20) takes a form:

$$c(aA_1 + bB_1 + cC_1 + dD_1 + eE_1 + fF_1 - U_6) + e\,(aB_1 + bD_1 + cE_1 + dG_1 + eH_1 + fK_1 - U_7) + 2f(aC_1 + bE_1 + cF_1 + dH_1 + eK_1 + fL_1 - U_8) = 0$$

where $A_1 = \sum_{i=1}^{n} y_i s_i$, $B_1 = \sum_{i=1}^{n} y_i s_i^2$, $C_1 = \sum_{i=1}^{n} y_i t_i s_i^2$

$D_1 = \sum_{i=1}^{n} y_i s_i^3$, $E_1 = \sum_{i=1}^{n} y_i t_i s_i^3$, $F_1 = \sum_{i=1}^{n} y_i s_i^3 t_i^2$,

$G_1 = \sum_{i=1}^{n} y_i s_i^4$, $H_1 = \sum_{i=1}^{n} y_i t_i s_i^4$, $K_1 = \sum_{i=1}^{n} y_i t_i^2 s_i^4$,

$L_1 = \sum_{i=1}^{n} y_i t_i^3 s_i^4$, $U_6 = \sum_{i=1}^{n} y_i T_i s_i$, $U_7 = \sum_{i=1}^{n} y_i T_i s_i^2$

$U_8 = \sum_{i=1}^{n} y_i T_i t_i s_i^2$, and $y_i = \sin[2(\phi_i - \phi_0)]$.

References

Abdelnour A.F., Selesnick I.W., 2004, Symmetric nearly orthogonal and orthogonal nearly symmetric wavelets. *Arabian J. for Science and Engineering*, 29, 2C, pp.3-16.

Abdelnour A.F., Selesnick I.W., 2005, Symmetric nearly shift-invariant tight frame wavelets. *IEEE Trans. Signal Process.*, 53, 1, pp.231-239.

Chichinina T., Sabinin V., Ronquillo Jarrillo G., 2003, Numerical modeling of P-wave AVOA in media containing vertical fractures / Expanded abstract. The Sixth International Conference on Mathematical and Numerical Aspects of Wave Propagation “Waves’ 2003”, Finland, Springer, p. 897 - 902.

Dasgupta R., Clark R.A., 1998, Estimation of Q from surface seismic reflection data. *Geophysics,* 63, 2120-2128.

Jenner E., 2002, Azimuthal AVO: Methodology and data examples, *The Leading Edge*, 21, iss.8, pp.782-786.

MacBeth C., 1999, Azimuthal variation in P-wave signatures due to flow. *Geophysics*, 64, 1181-1192.

Mallik, S., Craft, K.L, Meister L.J., Chambers R.E., 1998, Determination of the principal directions of azimuthal anisotropy from P-wave seismic data. *Geophysics*, 63, 692-706.

Newman P., 1973, Divergence effects in a layered earth. *Geophysics*, 38, 481-488.

Rüger A., 1998, Variation of P-wave reflectivity with offset and azimuth in anisotropic media. *Geophysics*, 63, 935-947.

Sabinin V., 2012, Viscoelastic modeling and factor Q for reflection data. *Geofisica Internacional,* 51, 4, p.377-391.

Sabinin V., 2013, QVOA techniques for fracture characterization. *Geofisica Internacional,* 52, 4, p. 311-320.

Sabinin V., Chichinina T., 2008, AVOA technique for fracture characterization: resolving ambiguity, *Geofisica Internacional*, 47, 1, p. 3-11.

Sheriff R.E., Geldart L.P., 1983, Exploration Seismology, Volume 2, Data-processing and interpretation. Cambridge University Press, Cambridge, 400 p.

Xu X., Tsvankin, 2004, Geometrical-spreading correction for P-waves in layered azimuthally anisotropic media. 74th Ann. Internat. Mtg.: Soc. of Expl. Geophys., 111-114.

WSBP, 2012, (Wavelet Software at Brooklyn Poly), Matlab Implementation of Wavelet Transforms. http://eeweb.poly.edu/iselesni/WaveletSoftware.

Geofísica Internacional (2014) 53-4: 473-490

Original paper

Thermomagnetic monitoring of lithic clasts burned under controlled temperature and field conditions. Implications for archaeomagnetism

Ángel Carrancho*, Juan Morales, Avto Goguitchaichvili, Rodrigo Alonso and Marcos Terradillos

Received: October 10, 2013; accepted: March o4, 2014; published on line: October 01, 2014

Resumen

Se presenta un estudio combinado térmico y magnético sobre un conjunto de clastos líticos de diferentes litologías tallados experimentalmente (sílex, cuarcita, caliza, arenisca y obsidiana), calentados bajos condiciones de campo y temperatura controladas. El objetivo principal de este estudio es evaluar la viabilidad de uso de estas materias primas, comúnmente encontradas en yacimientos arqueológicos prehistóricos, para fines arqueomagnéticos. Los análisis del magnetismo de las rocas comprendieron la medida de la susceptibilidad magnética a bajo campo, curvas de adquisición progresiva de la magnetización remanente isoterma (IRM), ciclos de histéresis y curvas termomagnéticas de los clastos líticos tanto antes como después del calentamiento experimental. Todas las litologías salvo la obsidiana, registraron un incremento de hasta dos órdenes de magnitud en sus parámetros dependientes de la concentración magnética, indicando la formación de nuevos minerales ferrimagnéticos. Las muestras de obsidiana y arenisca son los portadores de la remanencia más fiables, seguidos de caliza, sílex y cuarcita. Los valores de susceptibilidad magnética muestran diferencias significativas entre litologías. La magnetización remanente isoterma demostró ser también altamente discriminatoria así como los parámetros de histéresis a temperatura ambiente. Las principales alteraciones macroscópicas fueron cambios de coloración, rubefacciones, depresiones circulares (potlids) en los sílex y la formación masiva de fisuras internas en los especímenes de obsidiana. La técnica de paleointensidad multiespecimen fue aplicada en muestras representativas proporcionando resultados satisfactorios para las muestras de obsidiana y arenisca. Se discute la aplicabilidad arqueológica de los resultados así como también su relevancia geomagnética.

Palabras clave: Arqueología, arqueomagnetismo, magnetismo de las rocas, paleointensidad, tecnología lítica

---

Ángel Carrancho
Marcos Terradillos
Área de Prehistoria
Departamento de Ciencias Históricas y Geografía
Universidad de Burgos, Edificio I+D+I
Plaza Misael Bañuelos s/n. 09001
Burgos, España
Corresponding author: acarrancho@ubu.es

Ángel Carrancho
Avto Goguichaichvili
Departamento de Física
Universidad de Burgos, Escuela Politécnica Superior
Avda. Cantabria S/N 09006
Burgos, España

Juan Morales
Avto Goguichaichvili
Laboratorio Interinstitucional de Magnetismo Natural
Instituto de Geofísica
Unidad Michoacán, Campus Morelia
Universidad Nacional Autónoma de México
México.

Rodrigo Alonso
Museo de la Evolución Humana
Paseo Sierra de Atapuerca s/n. 09002
Burgos, España

Abstract

We carried out a combined thermal and magnetic evaluation on experimentally knapped clasts of different lithologies (chert, quartzite, limestone, sandstone and obsidian) heated under controlled field and temperature conditions. The main aim of this study is to estimate the feasibility of use of these raw materials, which are commonly found in prehistoric archaeological sites for archaeomagnetic purposes. Rock magnetic analysis included measurements of low-field magnetic susceptibility, isothermal remanent magnetisation (IRM) acquisition curves, hysteresis loops and thermomagnetic curves of lithic clasts both before and after experimental heating. All lithologies, except the obsidian, recorded an increase of up two orders of magnitude in their magnetic concentration-dependent parameters revealing the formation of new ferrimagnetic minerals. Obsidian and sandstone are the most reliable magnetic carriers, followed by limestone, chert and quartzite. Magnetic susceptibility values show significant differences among lithologies. Isothermal remanent magnetisation proved also to be highly discriminatory as well as the room temperature hysteresis parameters. The main macroscopic alterations resulted in colour changes, rubefactions, potlids in cherts and the massive formation of internal fissures in obsidian specimens. The multispecimen palaeointensity technique was applied on selected samples yielding satisfactory results for heated obsidian and sandstone samples. The archaeological applicability of the results is discussed as well as their geomagnetic significance.

Keywords: Archaeology, archaeomagnetism, rock-magnetism, palaeointensity, lithic technology.

Introduction

Combustion structures and burned archaeological materials constitute a valuable source of data to investigate the directional and intensity variations of the Earth's magnetic field in the past. Materials heated to high temperatures (> 600 ºC) are capable, under certain conditions, to acquire a thermo-remanent magnetisation (TRM) recording the direction and intensity of the Earth's magnetic field during the last combustion. Archaeological structures such as kilns, ovens, baths or hearths are particularly suitable for this kind of studies. For that reason, there is a growing interest in the archaeomagnetic community to explore new materials as potential geomagnetic field recorders in order to study the field evolution through time (e.g. Morales *et al*., 2011).

On the other hand, ferromagnetic minerals (*s.l.*) are particularly sensitive to modify their magnetic properties by heating. This makes rock-magnetic methods a very efficient tool with applications ranging from the reconstruction of ecosystem dynamics (e.g. Hallett and Anderson 2010) to identify fire in archaeological sites (e.g. Herries 2009). In forest fires, for example, natural burning produces a magnetic enhancement on topsoils even at moderate temperatures which can be detected with mineral magnetic methods (e.g.: Gedye *et al.* 2000). Regarding archaeological sites, the potential of mineral magnetic methods is of particular interest in palaeolithic contexts where fire identification is not straightforward and thermal alteration evidences (e.g.: ashes, charcoals, etc.) are usually few, ambiguous and generally poorly preserved. Thus, the rock-magnetic information may be useful to evaluate the technological characteristics of prehistoric societies and the cultural interpretation of prehistoric sites. As far as the study of archaeological lithic assemblages is concerned, mineral magnetic analyses have been mostly used to identify source or provenance areas in different parts of the world (e.g.: McDougall *et al.* 1983, Vasquez *et al*. 2001, Thacker and Ellwood 2002, Stewart *et al*. 2003, Zanella *et al*. 2012). However, studies concerning how heating alter the magnetic properties of prehistoric lithic assemblages are relatively scarce and basically restricted to obsidians and cherts (Borradaile *et al.* 1993, 1998; Thacker and Ellwood 2002). It is well known that heat treatment of fine grained siliceous rocks improves their flaking properties in stone tool manufacture (e.g.: Hester 1972; Purdy 1974; Domański and Webb 1992, 2007). Therefore, it would be interesting to extend our knowledge investigating other lithologies commonly found in prehistoric archaeological sites and evaluate their potential as reliable recorders of the geomagnetic field strength.

This work is an experimental study about the variations of magnetic and macroscopic properties induced by heating on an experimental set of lithic clasts from different lithologies commonly found in prehistoric archaeological sites. A collection of experimentally knapped lithic artefacts from five diverse lithologies (chert, limestone, quartzite, sandstone and obsidian) was heated under controlled field and temperature conditions monitored by standard thermocouples. The main objectives of this study are: *i)* characterise the main magnetic and macroscopic properties of these materials induced by heating, *ii)* establish magnetic criteria in order to identify heating processes in analogous prehistoric lithic materials and *iii)* evaluate the magnetic stability and determine the suitability of these lithologies to obtain absolute palaeointensity determinations as well as discuss its methodological implications. Therefore, the interest of this contribution is posed both from a geophysical and archaeological perspective.

Field experiment and sample description

Experimental heating was carried out on a clayish substrate at the locality of Humienta (Burgos, Spain; Figure 1a). A clayish substrate was selected because of the availability to perform the field experiment and because this type of substrates are quite common in archaeological contexts. To avoid possible contaminations the upper 15-20 cm of the superficial soil were removed. Temperature variations during the burning were recorded at 5 minutes intervals with a K-type thermocouple system distributed linearly at 0-1 cm of depth and another one at 3 cm of depth in the centre of the experimental hearth (T3 at quadrant 5; Figure 1b). Burning surface was subdivided in five different quadrants as illustrated in Figure 1b placing two lithic fragments of each lithology per quadrant. Experimental lithic artefacts correspond to the following lithologies: *i)* Neogene chert from Sierra de Atapuerca (Upper Miocene, Villalbal, Burgos); *ii)* Upper Cretaceous limestone from Sierra de Atapuerca (Ibeas de Juarros, Burgos), *iii)* Palaeozoic sandstone from the fluvial terraces of Arlanzón river (Sierra de la Demanda, Burgos), *iv)* Quartzite from Utrilla facies (Olmos de Atapuerca, Burgos) and *v)* Neogene obsidian from New Mexico (USA). Each lithology exhibited predominantly homogeneous texture and colours ranging from black in obsidians to white in cherts. While limestone specimens were mostly grey with reddish mottles, dark light brownish grey and light greyish colours could be distinguished in sandstone and quartzite specimens, respectively. Burning was carried out employing wood fuel (cf. *Quercus sp*.) during 80 minutes. In order to ensure that the pieces undergo the highest thermal impact during the burning, they were dispersed directly on the ground surface. This may guarantee to reproduce the conditions of similar experimental ethnoarchaeological recreations (e.g.: Hester 1972; Domański and Webb 2007).

With the exception of obsidian, this material selection is related to the type of raw materials most frequently identified in the Pleistocene archaeological sites of Atapuerca (Burgos, Spain). For some unknown reason, no evidences of archaeological fire have been yet identified so far in the Pleistocene sites, despite having a record of human occupation virtually spanning the last million years (Rodríguez *et al.* 2011). Obsidian was also included in this study because is a common raw material to manufacture stone tools in volcanic areas and it would be interesting to study the variation of its magnetic properties induced by heating. Besides intending to broadly characterize the magnetic behaviour of these lithologies, this material selection aims to explore the range of variability of their magnetic properties. This can be useful to define a magnetic pattern to detect heat treatment in archaeological lithic assemblages.

Substrate temperatures were completed with temperature readings of the air (T6; Figure 2) and of the embers of the substrate where the lithic pieces were located (T7; Figure 2). It is

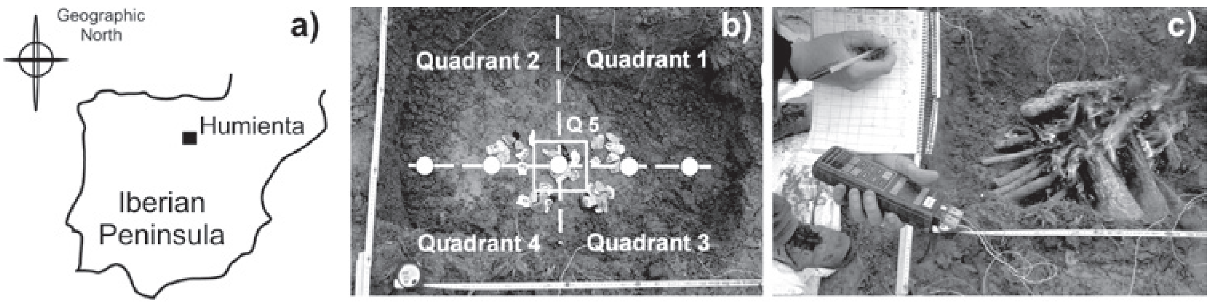

Figure 1. (a) Location of the site where the experiment was carried out. (b) Distribution of pieces by quadrants on the ground surface (Q5 refers to quadrant 5). White circles represent the location of thermocouples (T1-T5) at 0-1 cm of depth. Temperatures of the embers where the lithic pieces were located were recorded with T7 in Q5. (c) Temperature reading during the experiment.

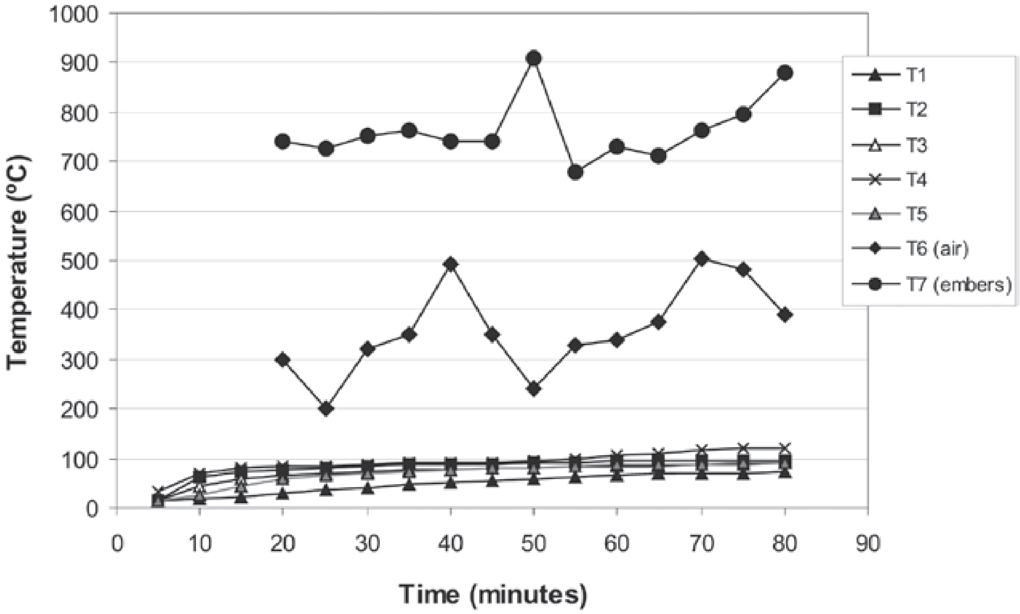

Figure 2. Temperatures recorded by each thermocouple during the experiment. T6 (temperature of the air) and T7 (temperature of the embers where the clasts were located). See text (field experiment section). Note that some temperature variations (e.g.: between min 45 and 60; T7) might correspond to wind variations or alternatively to some fuel addition during burning. More fuel help to increase the temperatures.

worth to point out that the experiment was performed after a rainy day, so the substrate kept a considerable humidity. This fact, together with the low thermal conductivity of the clay, clearly limited heat penetration with depth. This explains why despite heating continuously for 80 minutes, the temperatures of buried thermocouples did not exceed 120 °C (Figure 2). However, the thermocouple of the embers where the artifacts were located (T7; Figure 2), recorded mean heating temperatures of 700 ºC. Therefore, it is reasonable to assume that these samples definitively acquire a full thermoremanent magnetisation (TRM). Following our previous experiments we showed that burning under similar conditions samples acquire a full TRM (Carrancho and Villalaín 2011; Calvo-Rathert *et al*., 2012) and we demonstrate it here studying the magnetic properties (section 4.3). All lithic pieces were measured, photographed and their main macroscopic features described before and after the experimental burning.

Laboratory procedures

As an initial step before performing the field experiment, the low-field magnetic susceptibility (MS) was measured on each sample with a KLY-4 (AGICO, noise level ~ 3 x 10^{-8} S.I.) kappabridge.

In order to further constrain the magnetic properties, we selected one pilot sample from each lithology ("pre-burned material") and one piece of each lithology from each quadrant after burning ("post-burned material"), to carry out a series of rock-magnetic experiments with a Magnetic Field Translation Balance (MM_MFTB). These included the measurement on powered sample (~ 450 mg) of progressive isothermal remanent magnetisation (IRM) acquisition curves, hysteresis loops (± 1 T), backfield coercivity curves and thermomagnetic curves up to 700 ºC in air. Heating and cooling rates of thermomagnetic experiments were 10 - 15 ºC min^{-1} applying a field of 38 mT. Curie temperatures of Js-T curves were calculated using the two-tangent method of Grommé *et al.* (1969). Saturation magnetization (M_s), remanence saturation magnetisation (M_{rs}) and coercive field (B_c) were calculated from hysteresis loops after subtracting the dia/paramagnetic contribution. These parameters combined with the coercivity of remanence (B_{cr}) determined from the backfield curves, were used to estimate the domain state distribution of the studied collection in the Day plot (Day *et al.* 1977; Dunlop 2002). All these experiments were carried out at the Laboratory of Palaeomagnetism of Burgos University (Spain).

Results

Macroscopic alterations

Figure 3 illustrates some representative examples of the main macroscopic features observed in the different lithologies after burning. Chert is the raw material from the studied collection which undergoes more changes when heated (Figure 3e). Rubefaction is the most documented alteration (Figure 3b), being observed in all lithologies except in the obsidian. However, 90 % of obsidian pieces have produced internal fissures as the main macroscopic alteration (Figure 3f). The second most documented alteration is colour change which has affected to all lithologies although not in a very evident manner in limestone samples. It is remarkable the appearance of microretouches -which at first glance might be mistakenly confused with wear traces- (Figure 3a) and to a lesser extent, fractures (Figure 3c) and potlids (Figure 3d). The latter are subcircular depressions on the tools surfaces and have been reported in other thermally altered siliceous-rich lithic assemblages (e.g.: Borradaile *et al.* 1998).

Magnetic properties of unburned clasts

The ferromagnetic content of the pre-burned material is very poor, dominating diamagnetic (e.g.: Figure 4a) or paramagnetic behaviour and characterized by noisy curves (Figure 4b). Only obsidian (Figure 4c) and to lesser extent the sandstone samples (Figure 4d) show a higher ferromagnetic content revealing the dominant presence of magnetite as main carrier. Haematite is also present in the sandstone as can be easily distinguished by the wasp-waisted shape of its hysteresis loop (Figure 4d). Moreover, the variation in the intensity of magnetisation among lithologies becomes of up two orders of magnitude according to the progressive IRM acquisition curves of obsidian and sandstone samples (Figure 4e).

Low-field magnetic susceptibility (MS) variations between pre- and post-burned samples of different lithologies are evident as can be observed in Figure 5 and Table 1. Most chert, quartzite and limestone samples (Figure 5a,b and d) exhibit very low pre-burning MS values, even negative, indicating that the matrix is dominated by diamagnetic minerals. Paramagnetic minerals are likely to be also present especially in quartzite since some samples show low positive pre-burning MS values (Figure 5b), and also for limestone (Figure 5d). In contrast, sandstone and mainly obsidian samples exhibit the highest values (mean post-burning MS = 2.03×10^{-6} and $2,30 \times 10^{-7}$ m^3kg^{-1} respectively; Table I and Figure 5e and c), indicating that they contain ferromagnetic (*s.l.*) minerals. On average, pre-burning MS values of obsidian samples are around one order of magnitude higher than sandstone ones. Within their variability, all lithologies underwent in general a considerable MS enhancement after burning clearly indicative of mineralogical transformations. This effect is particularly evident in the sandstone. Most likely, heating induced mineralogical changes of the paramagnetic components (i.e.: phyllosilicates) rather common in these lithologies favouring the creation of ferrimagnetic minerals (i.e.: magnetite). Most obsidian samples, however, do not increase the MS values after burning. This is due to the volcanic origin of this material carrying original thermoremanent magnetization

Magnetic properties of post-burning clasts

Progressive IRM acquisition curves of the different lithologies before and after burning are illustrated in Figure 6a and b, respectively.

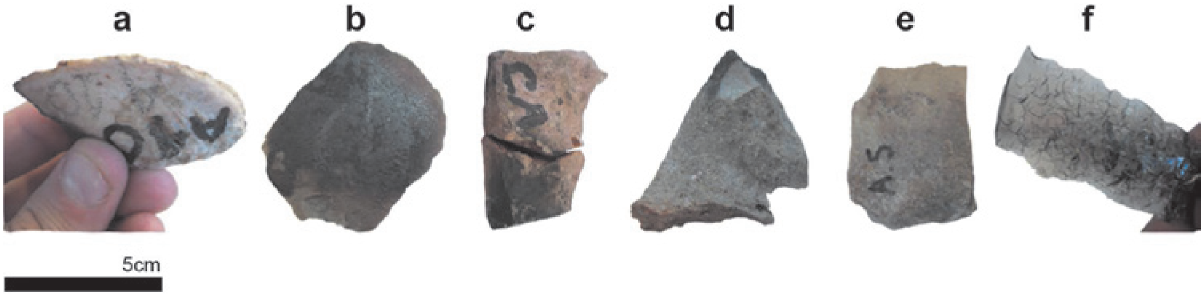

Figure 3. Representative examples of the main macroscopic alterations documented after the burning in the studied lithologies. (a) Microretouches; (b) Rubefaction; (c) Fractures; (d) Potlids; (e) increased lustre; (f) formation of internal fissures.

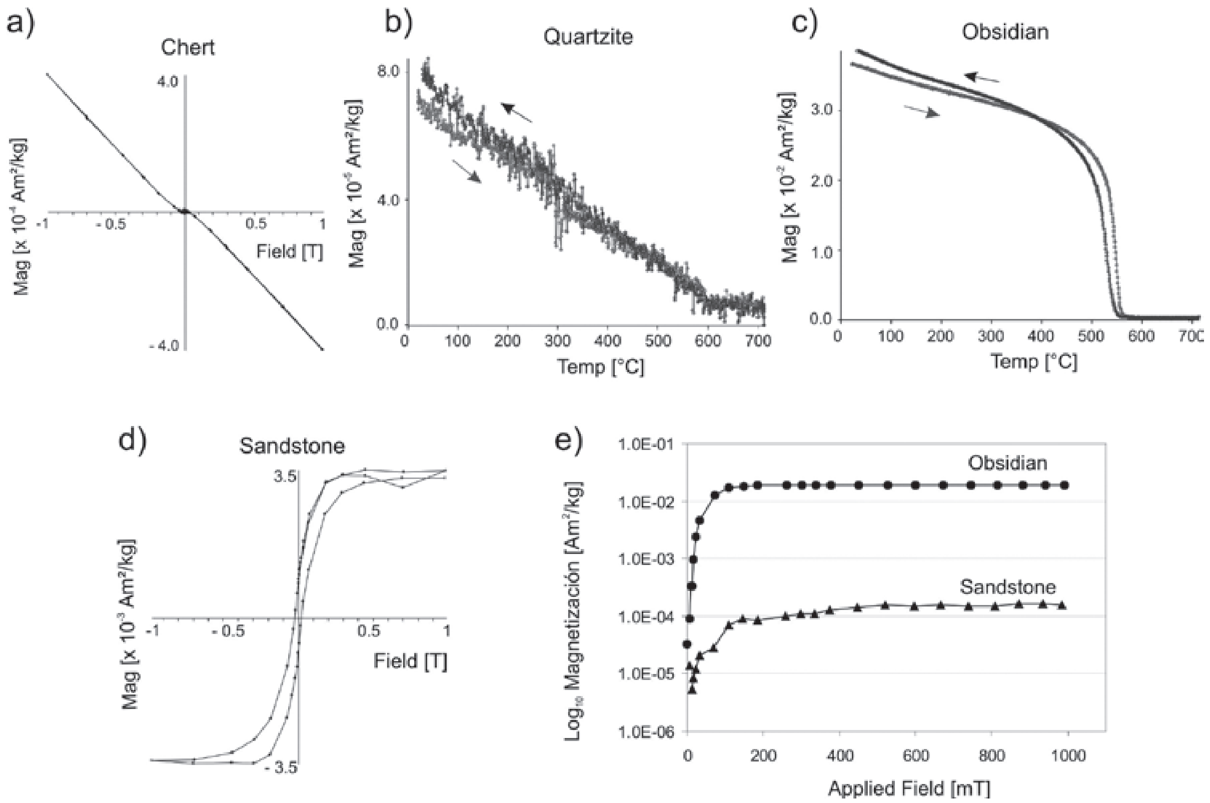

Figure 4. Representative examples of different rock-magnetic experiments carried out on the pre-burning material. (a and d) Hysteresis cycles. (b and c) Thermomagnetic curves and (e) Progressive IRM acquisition curves. Intensity values for each lithology are indicated.

Table 1. Mean magnetic susceptibility values expressed by mass for the pre- and post-burning samples of the different lithologies studied. Standard Deviation is also indicated.

Lithology	Specimens	Pre-burning mean MS (m^3kg^{-1})	St. Deviation (pre-burning)	Post-burning mean MS (m^3kg^{-1})	St. Deviation (post-burning)
Chert	10	-4.09×10^{-9}	3.08×10^{-9}	1.69×10^{-9}	1.08×10^{-8}
Quartzite	9	2.34×10^{-10}	9.71×10^{-10}	1.37×10^{-9}	1.31×10^{-9}
Obsidian	10	2.17×10^{-7}	2.22×10^{-7}	2.30×10^{-7}	2.51×10^{-7}
Limestone	10	-2.83×10^{-9}	6.29×10^{-10}	6.02×10^{-8}	1.14×10^{-7}
Sandstone	10	2.01×10^{-8}	3.88×10^{-9}	2.03×10^{-6}	2.30×10^{-6}

As expected, the studied pre-burning samples show a rather variable ferromagnetic content and thus distinct behaviour (Figure 6a). All IRM curves except the obsidian exhibit in general unstable and noisy behaviours. Most lithologies saturate around 200 mT indicating that a low-coercivity ferromagnetic mineral (magnetite and/or maghaemite) is the main magnetic carrier. Limestone and sandstone specimens do not reach saturation suggesting that some remanence is also carried by a higher coercive phase, most probably haematite (Figure 6a).

Progressive IRM acquisition curves of post-burned lithologies reach saturation around 150 – 200 mT indicating that magnetisation is dominated by a low-coercivity mineral (Figure 6b). The variation in the intensity of magnetisation among lithologies is remarkable, between one and two orders of magnitude.

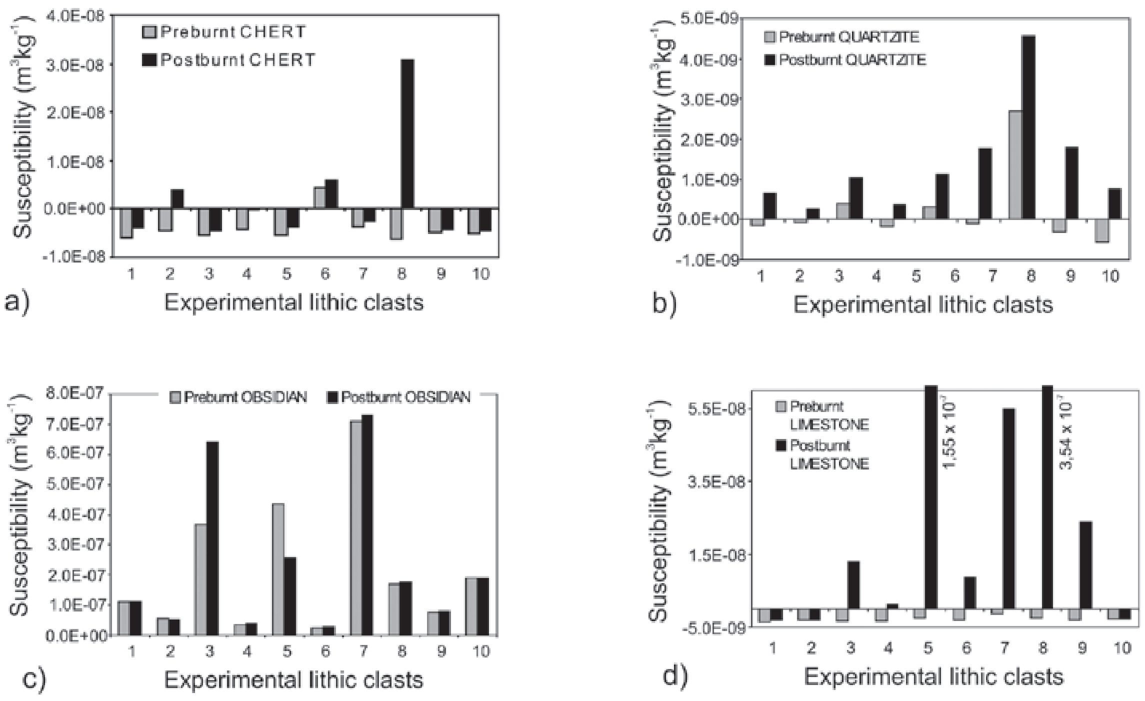

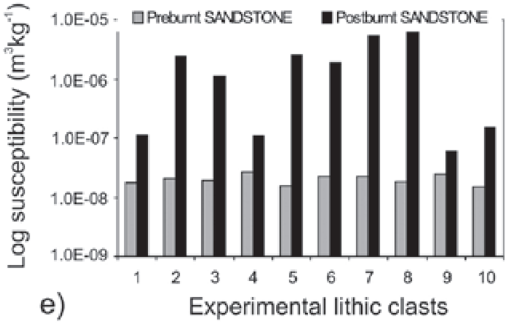

Figure 5. (a-e) Histograms showing the low-field magnetic susceptibility values of all pre- and post-burning samples for each lithology. (a) cherts; (b) quartzite; (c) obsidians; (d) limestone; (e) sandstone. Note that panel "e" is expressed in log-scale.

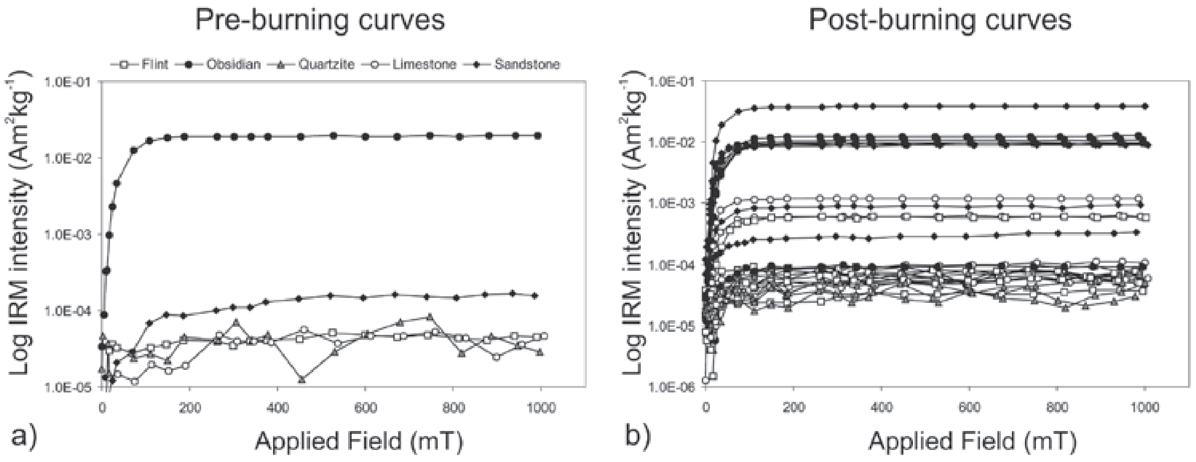

Figure 6. (a-b) Progressive isothermal remanent acquisition (IRM) curves before and after burning, respectively. Lithologies are represented in both graphs according to the legend shown in Figure 6a.

Regardless of the quadrant analysed, obsidian and sandstone are the most stable magnetic lithologies followed in decreasing order by limestone (~ 10 times weaker) and finally by chert and quartzite, which is the weakest one.

The magnetic behaviour after burning can be clearly distinguished by lithologies in Figure 7 which shows examples of progressive IRM acquisition curves, hysteresis loops and their corresponding thermomagnetic curves of representative samples of each lithology studied. The chert, limestone and quartzite exhibit diagrams with the lowest intensity of magnetisation and occasionally very noisy, dominating in all cases the diamagnetic behaviour as denoted by the original (uncorrected) shape of their hysteresis loops (Figure 7b-e-h). The abrupt drop around 580 ºC in the heating cycles of the thermomagnetic curves indicates that the main magnetic carrier of these samples is magnetite (Figure 7c-f-i). This observation is compatible with the progressive IRM acquisition curves which are saturated around 150 – 200 mT (Figure 7a and d). In contrast, the obsidian and sandstone samples exhibit diagrams with the highest intensities of magnetisation (up to two orders of magnitude) and are also probably dominated by magnetite (Figure 7j-ñ).

One aspect that we studied is to see whether there is a relationship between the thermomagnetic behaviour of the sample when heated again in the laboratory and the original heating temperature during experimental burning. In our case, it is noteworthy the high reversibility of thermomagnetic curves –coincidence between heating and cooling cycles-, indicative of high thermal stability of the sample. Those samples fully reversible (Figure 7i-l-ñ) suggest that they underwent heating temperatures of at least 700 ºC, because they do not alter when heated again in the laboratory. In contrast, the absence of thermomagnetic reversibility indicates that the sample did not originally exceed 700 ºC (e.g.: Figure 7f). Some variation in the temperatures reached is not incompatible because heating normally is not totally homogeneous on a hearth-surface (Carrancho and Villalaín 2011). All lithologies from quadrant 4 except the limestone sample (Figure 7f) exhibit a high thermomagnetic reversibility (not shown here), indicating that they most probably reached the temperature recorded by the embers´ thermocouple. The thermomagnetic irreversibility of the limestone sample (Figure 7f) can be due to the fact that this clast was quickly covered by ash causing an insulating effect avoiding heat penetration. This relationship between thermomagnetic reversibility and heating temperature is particularly interesting in the obsidian, which considering its volcanic origin surely exceeded that temperature when it formed. It is striking the similarity between the pre-burning obsidian (Figure 4c) and its respective post-burned sample (Figure 7l) in terms of intensity of magnetisation, mineralogical composition and thermomagnetic behaviour.

Figure 8 (a-b) illustrates the hysteresis ratios of pre- and post-burning samples plotted in the so-called Day plot (*Day et al. 1977*). The same information for the samples after burning differentiated by lithologies is represented in Figure 8b. The hysteresis ratios obtained range from $0.130 < M_{rs}/M_s < 0.234$ and $1.900 < B_{cr}/B_c < 8.210$ for pre-burning samples and $0.082 < M_{rs}/M_s < 0.315$ and $1.658 < B_{cr}/B_c < 6.623$ for the post-burning samples, although with interesting variations among lithologies. These values mostly indicate a pseudo-single domain (PSD) state for the magnetite grains. Pre-burning samples are rather scattered in the Day plot with the sandstone, limestone and quartzite slightly displaced to the right (Figure 8a). This might be due to the contribution of minor amounts of high coercive haematite or alternatively to a significant presence of finest superparamagnetic (SP) grains. Chert sample is in the PSD region while obsidian is nearer to the single domain (SD) area. The main difference between pre- and post-burning samples is that sandstone samples are well grouped in the PSD region closer to the SD (Figure 8b). This fact, together with the high reversibility observed in their thermomagnetic curves (Figure 7ñ) indicated that this lithology could be a good candidate for palaeointensity analysis. In any case the variability in the hysteresis parameters among lithologies is significant (Figure 8b). Quartzite is well grouped in the PSD region with hysteresis ratios relatively similar to chert samples. The latter, however, move to the right and slightly up so they could contain more SP grains on a relative basis (Dunlop 2002, Lanci and Kent 2003). Limestone is with obsidian the lithology which displays the higher dispersion in the grain size distribution which is probably related to relative variations of SP grains in these lithologies. Although is not possible to provide discriminatory values, hysteresis ratios of some lithologies such as sandstone *vs*. chert or quartzite are clearly separated, indicating that their granulometric distribution is distinctive.

Low-field susceptibility vs. SIRM (Saturation of IRM) plot provides interesting information about variations in magnetic mineral concentration (Figure 9). Sandstone and most obsidian samples plot to the right and up indicating that they are the most magnetic. Limestone

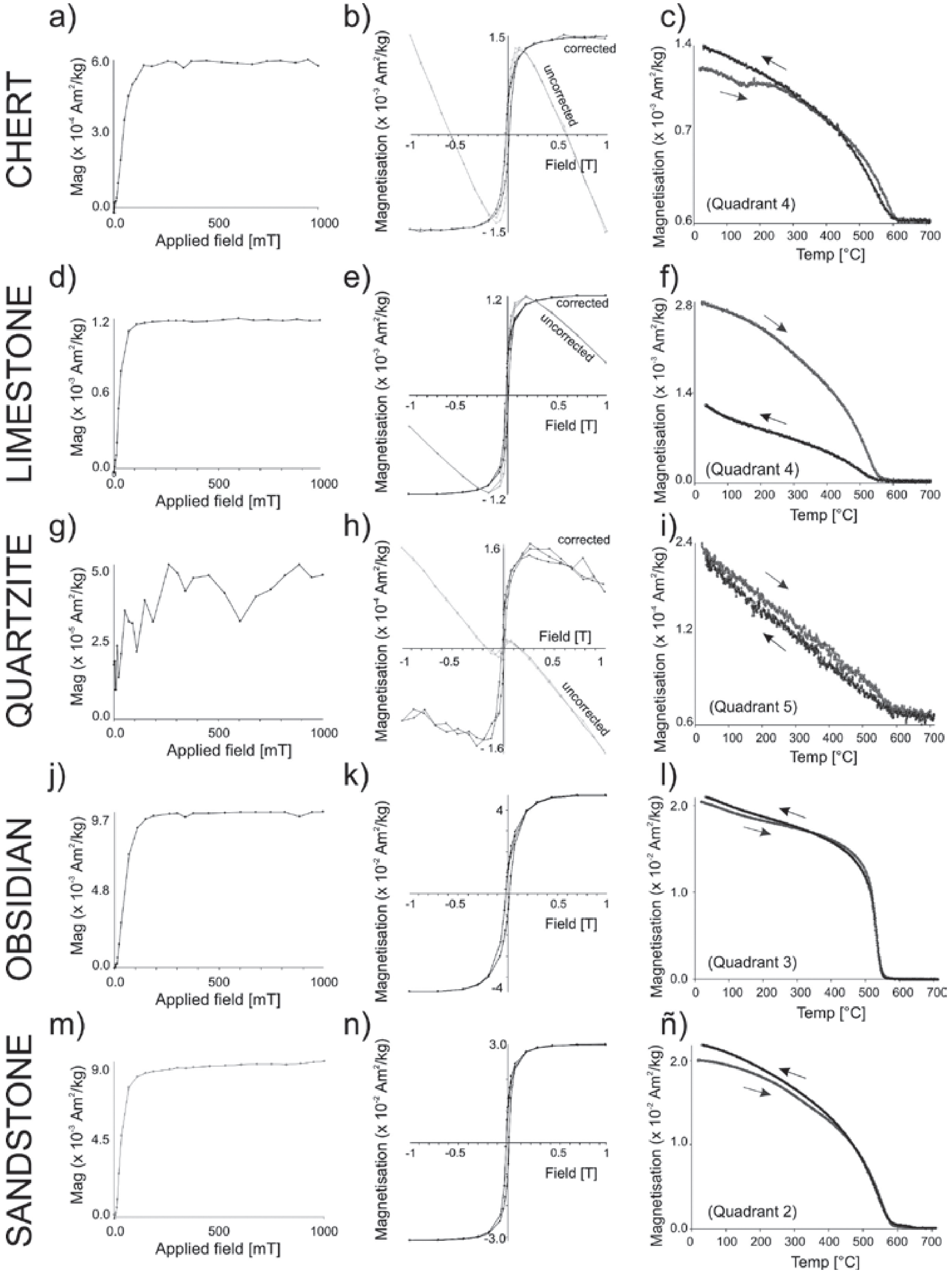

Figure 7. (a-ñ) Representative examples of IRM adquisition curves (left column), hysteresis cycles (central column) and their respective thermomagnetic curves (right column) for representative samples of each lithology after burning. Lithologies, applied field, intensity values and corresponding quadrant are indicated.

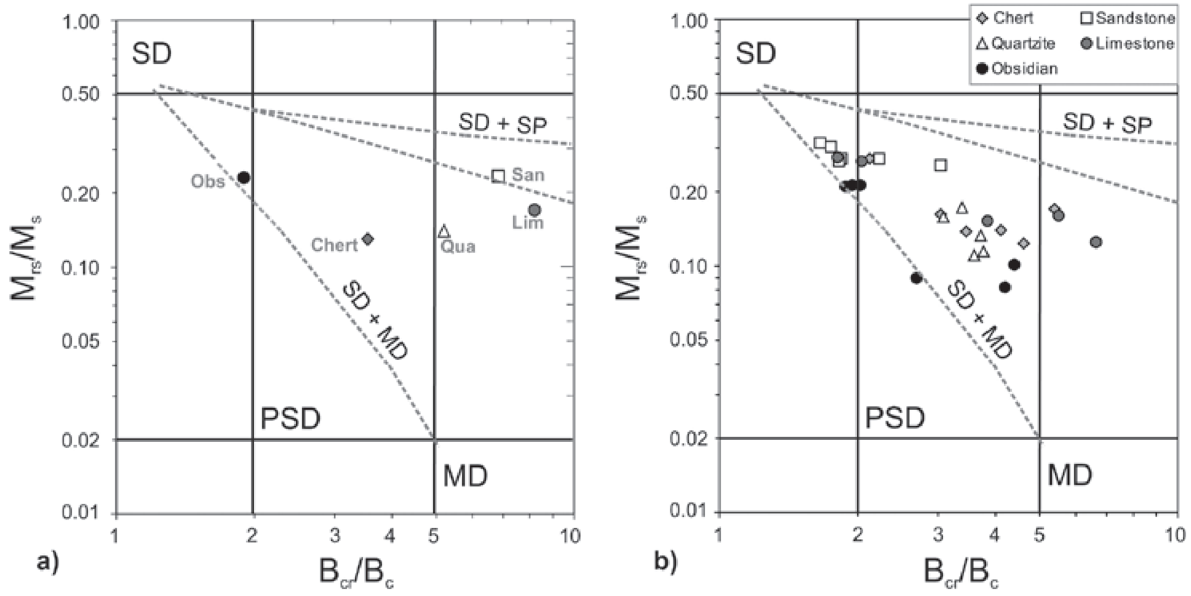

Figure 8. (a) M_{rs}/M_s vs. B_{cr}/B_c logarithmic plot (Day diagram) for pre-burning samples. Lim (limestone), San (sandstone), Qua (quartzite), Obs (obsidian). (b) Post-burning samples differentiated by lithologies according to the legend. The dashed lines represent mixing curves taken from Dunlop (2002) for mixtures of single-domain (SD) with multidomain (MD) or superparamagnetic (SP) magnetite particles.

specimens show a significant variability as it happened in their hysteresis ratios. Quartzite specimens are well grouped in the left hand corner because their ferromagnetic content is very poor. As expected, four of five chert samples do not appear in the plot because of their negative (diamagnetic) MS values. Interestingly, cherts can be characterized because their ferromagnetic content is the lowest one in comparison with the other lithologies which is also a discriminative criterion.

Absolute geomagnetic intensity determinations

Both palaeodirectional and absolute palaeointensity data are essential to define the geomagnetic vector, being the latter generally more difficult to extract from lavas and other baked material due to irreversible magnetic mineralogical changes upon conventional heating experiments (Shaw 1974). Recent studies have demonstrated the usefulness of an

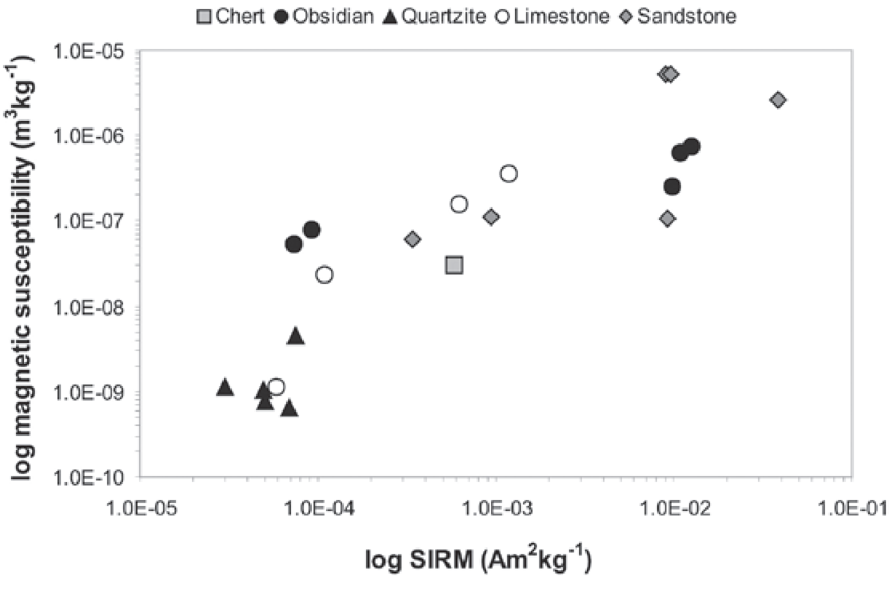

Figure 9. Scattergram of mass magnetic susceptibility vs. SIRM (Saturation isothermal remament magnetisation) for the different post-burning lithologies. Diamagnetic values (five cherts and one limestone) are excluded.

alternative methodology; the multi-specimen parallel differential pTRM method (Dekkers and Böhnel, 2006), in which minimal heating is required, thus increasing probabilities of obtaining accurate data.

Obsidians and sandstone samples showed the most suitable properties to perform absolute palaeointensty experiments. Both lithologies exhibited some features which definitively suggest that they carry a full TRM. First, they show univectorial behaviour upon stepwise thermal NRM demagnetisation with no evidences of p-TRMs (Figure 10 a-b). Note that orthogonal plots show different directions because it was not possible to orientate the small clasts during the experiment. Second, their intensity decay curves have a characteristic convex-shape behaviour where the greater part of the magnetization is removed between 520 – 560 ºC. Exactly the same behaviour is maintained for the laboratory created TRM shown on the same figure. This is typical of SD or small PSD ferromagnetic particles (Dunlop and Özdemir 1997) and is in good agreement with the hysteresis parameters obtained for both lithologies (Figure 8b). Third,

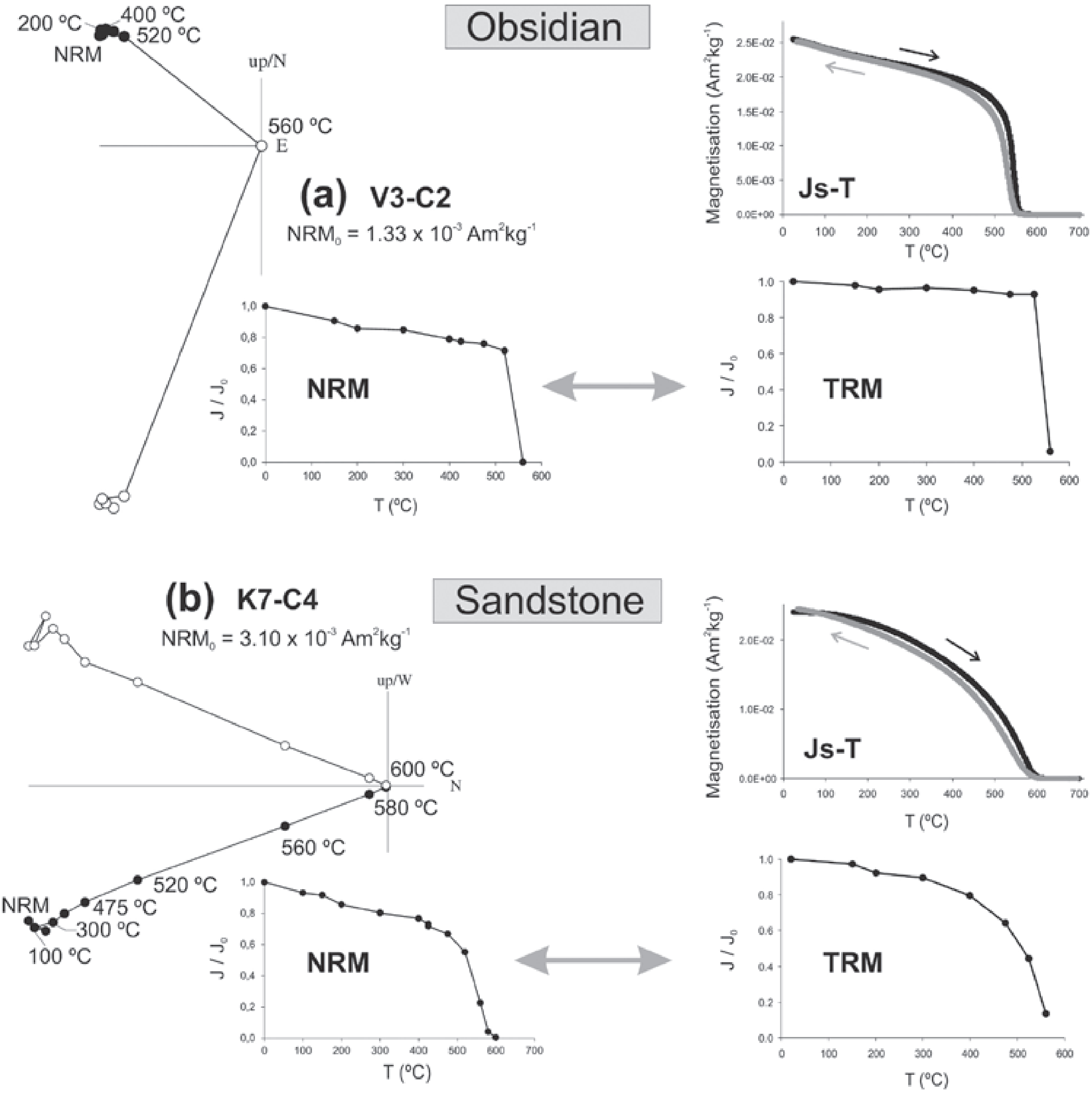

Figure 10. Thermal demagnetisation of NRM created during the artificial burning in the field and laboratory created full TRM for Obsidian (a) and Sandstone (b) samples. Also shown are corresponding continuous thermomagnetic (Js-T) curves. Please note that not exactly same samples were used for NRM and TRM demagnetisation experiements.

their respective thermomagnetic curves are totally reversible (Js-T curves shown on Figure 10) as expected by the temperatures recorded by embers´ thermocouple (T7; Figure2). All these observations agree with our previous results obtained in very similar experiments carried out in the same area showing that a total TRM can be acquired under similar experimental conditions (Carrancho and Villalaín 2011, Calvo-Rathert *et al.* 2012).

Absolute geomagnetic intensity determinations were carried out in the palaeomagnetic laboratory of LIMNA (Morelia, Mexico) using a 'compact version' of the multi-specimen parallel differential pTRM method (see below for an explanation) due to the scarcity and reduced size of available samples. Two samples of obsidians and sandstone from each quadrant were cut using a diamond-disk saw; each fragment was weighted and then pressed into salt pellets in order to obtain standard-dimensions palaeomagnetic samples. In this way, two similar ten-specimen series were formed. The TRM of all 20 specimens was measured using a JR5A spinner magnetometer. Two sets of experiments were performed. First series (even specimens E1 to E19) was heated inside an ASC TD48 thermal demagnetiser up to 475 °C under the influence of a 40 μT magnetic field, while a 50 μT laboratory field was applied for the second series (odd specimens E2 to E20). Here becomes clear the phrase 'compact version' above mentioned; two lab fields used. Since the ambient field was known (and measured) *a priori*, and in order to investigate also possible dependence of the intensity of TRM acquired by samples as a function of the position within the burning (samples heated at different quadrants), just two lab fields were selected; one lower (40 μT) and one higher (50 μT) than the known expected ambient field.

After the completion of the above described experiments the pTRM acquired by each specimen was measured and the relative difference between pTRM (gained in lab) and full TRM (produced during the experimental burning) of specimens coming from the same lithic sample (sister specimens) was calculated. Sister-specimen sets, for both obsidians and sandstones, were plotted and connected by straight lines and its intersections with the horizontal axis (zero difference) were estimated (Figure 11a-b). Mean intensities calculated separately for obsidian and sandstone samples yielded values of 46.0 and 46.7 μT, respectively. Thus, no intensity differences regarding lithologies were observed. Since samples were heated altogether under the same ambient magnetic field we adjusted a best fit line to all the specimens. After the rejection of 1 sister-specimen set showing a significantly high slope, an average ambient field of 46.4 ± 2.4 μT was determined (Figure 11c). We note, however, that in spite of the significantly high slope the rejected sister-specimen pair shows it intersects the horizontal axis at approximately 40 μT.

Discussion and perspectives

The rock-magnetic results reported here show that the experimental heating has produced remarkable alterations in the magnetic properties of the studied lithologies. It is worthy pointing out that each heating event is unique and represents very specific combustion conditions in terms of duration, temperature, etc., which are rarely fully reproducible. However, here we show that high temperature (700 ºC) heating significantly increases the concentration and varies the grain size distribution of magnetic minerals from the studied lithologies in comparison with their unburned counterparts. The intensity of magnetisation and MS values increased between one and two orders of magnitude comparing pre- and post-burning lithologies and similar variations were also observed among different post-burning lithologies. The variability in the mineral magnetic content of these lithologies before burning is certainly an important factor. Obsidian is the only lithology which does not undergo significant magnetic variations, because, as volcanic glass, it is formed at high temperature and generally contain iron oxides (e.g.: titanium-rich magnetites) carrying a stable TRM.

The main magnetic carrier in all lithologies is 'almost pure' magnetite and concentration-dependent parameters (magnetic susceptibility, IRM, saturation magnetisation, etc.) clearly indicate the increase of ferrimagnetic minerals after burning. As far as the weakest lithologies are concerned (chert, limestone and quartzite) the magnetite created after burning most likely come from the alteration of (undetermined) paramagnetic minerals unidentifiable with rock-magnetic methods. At this stage it is not possible determine which specific minerals are involved but a good summary of this type of mineralogical changes can be found in Henry (2007) and references therein. For the purpose of this article, the interesting point is that the rock-magnetic characterization of the pre-burning materials allowed identifying the obsidian and sandstone as the most suitable lithologies for archaeomagnetic analysis. The variations in the domain state of ferromagnetic particles are also notable, particularly in sandstone, which after heating acquired a grain size closer to SD state. For this reason and

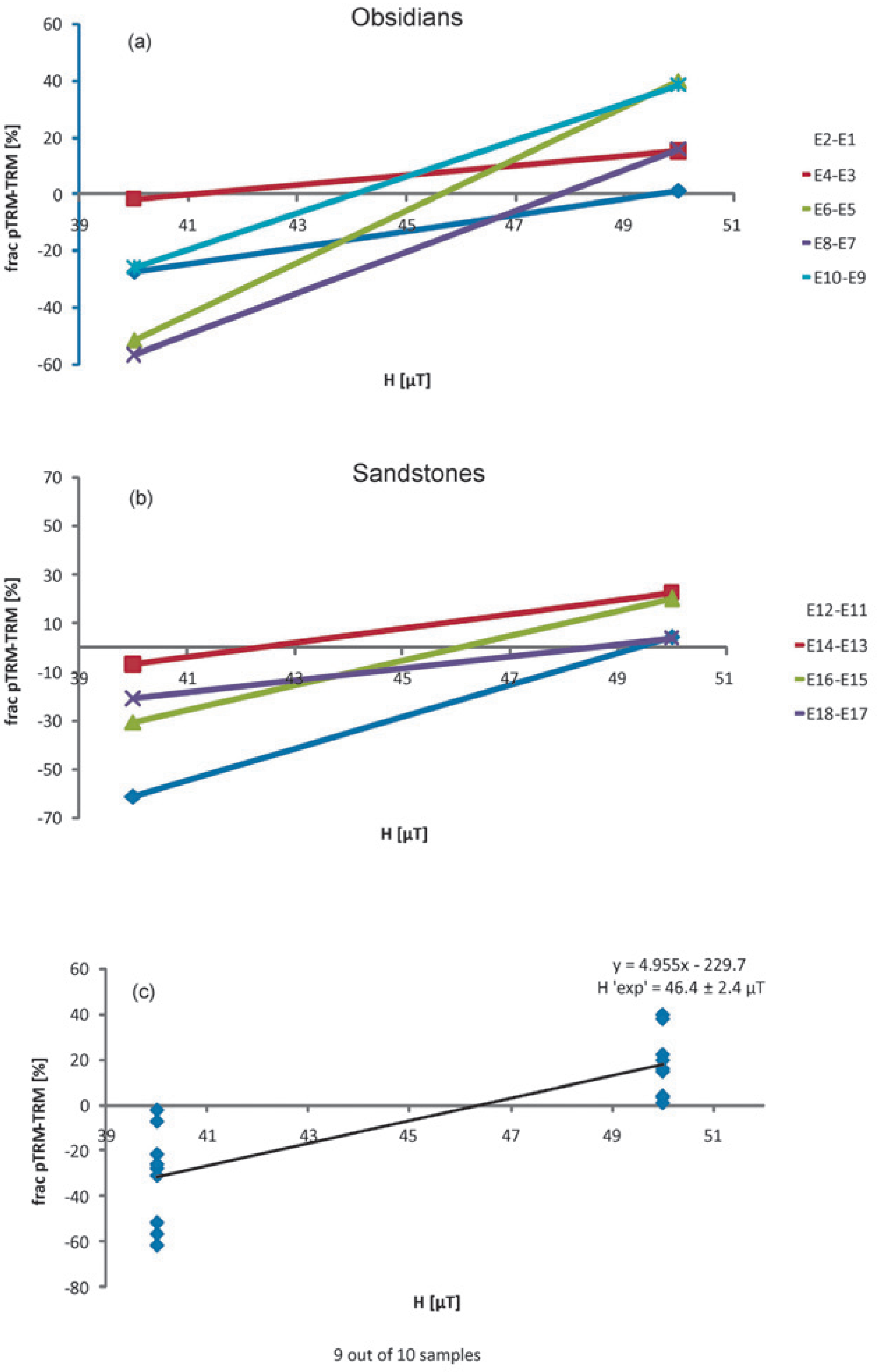

Figure 11. Palaeointensity results obtained in obsidian and sandstone specimens, (a) and (b) respectively, with the multispecimen method. Lines connect sister-specimen of the different lithologies samples. Plots represent the relative percentage differences between the pTRMs acquired at different lab fields (40 and 50 μT) and the total TRM (acquired during burning). Intersection of each line with the horizontal axis (zero difference) determines the intensity of the Earth's magnetic field during the burning. (c) Mean ambient field estimation calculated from both lithologies.

judging from high thermomagnetic stability, sandstone and obsidian were selected to carry out palaeointensity analysis. On the contrary, the chert and quartzite samples studied are not fully ferromagnetic (diamagnetism dominates their behaviour in some specimens even after burning) and their domain state distribution is PSD with a significant contribution of superparamagnetic (SP) particles. Limestone is about ten times more magnetic than chert and quartzite but it does not hold the domain state requirements for palaeointensity analysis and some thermomagnetic curves did not exhibit full reversibility (Figure 7f).

Macroscopic observations are also a valid and complementary argument to detect heat treatment, but not completely diagnostic by themselves. Heating produces a variety of macroscopic alterations in lithic assemblages such as colour changes, increased lustre, or microfractures among others that have been traditionally used as criterion to identify fire in the archaeological record. However, fire is not the only process responsible for colour variations in lithic materials (e.g.: Brown *et al*. 2009) so it is important to combine rock-magnetic and macroscopic observations as Borradaile *et al*. (1993, 1998) already shown. For example, the studied obsidians hardly change their magnetic properties when heated experimentally but in contrast produce very characteristic internal fissures which can be indicative of heat treatment. Obsidian is a volcanic glass with exceptional flaking properties and is unlikely that it was systematically heated in prehistory, so the study of its magnetic properties to identify human-induced heating processes would be probably unsuccessful. It is well-known that variability in the magnetic properties of obsidians may be significant among neighbouring areas (e.g. Zanella *et al.* 2012) and even also from flow to flow (Frahm and Feinberg 2013), which is important in provenance studies. However, the ultimate mechanism responsible of the observed magnetic properties in this study is heating. Any heating of the sample during its history could considerably disturb and reset the NRM and other magnetic properties in general (e.g.: Borradaile *et al.* 1993, 1998). Therefore, for the purpose of identifying heat treatment in archaeological lithic assemblages the provenance is not so a critical factor because it involves a different process. That is not incompatible, and indeed advisable, with the fact that the magnetic properties of a particular set of archaeological obsidians (or any other lithology) are compared with those obtained from the same lithology if the source area is known. Magnetic properties variation not only depends on some specific combustion conditions but also on the previous magnetic mineralogy before the burning. As far as obsidians artifacts are concerned, if the goal is to determine whether they have been heated in the antiquity, macroscopic features (i.e., the internal fissures reported here) seem to be more useful than mineral magnetic analyses themselves. The occurrence of potlids is another macroscopic alteration documented specially in cherts, but some caution needs to be taken here because it is known that in contexts with drastic temperatures changes they can occur without heating (e.g.: Griffiths *et al.* 1985, Borradaile *et al.* 1998).

According to the results reported here for the studied lithologies, in case of heat treatment the contrast between pre- and post-burning magnetic properties is supposed to be distinctive enough in terms of magnetic concentration and grain size distribution. These observations ideally should be accompanied as far as possible by archaeological evidences provided by the context such as charcoals, rubefied substrates or in the best case, by the presence of ashes.

It has been suggested that thermal treatment of siliceous lithologies as cherts causes a consistent marked reduction in fracture toughness as a consequence of recristalization (Domanski and Webb 1992, 2007, Domanski *et al.* 2009). An interesting aspect to consider in similar studies of archaeological lithic materials is the effect of diagenetic processes. Once the artefact -supposedly heated in its manufacture- is abandoned and subsequently becomes buried, weathering processes or recristalization events may produce the removal of para- and/or ferromagnetic minerals (Thacker and Ellwood 2002). Consequently, magnetic-concentration dependent parameters such as magnetic susceptibility or IRM would significantly be reduced hampering the unequivocal identification of heat treatment in that lithic assemblage.

Detailed studies relating the palaeofield strength and the manufacturing processes of archeological artifacts are scarce. Genevey and Gallet (2002) checked their experimental procedure to retrieve the intensity of the geomagnetic field from ancient French pottery by implementing a preliminary test on new ceramic material, obtaining results 3% lower than the expected local field value. Gómez-Paccard *et al.* (2006) carried out an archaeomagnetic study of seven contemporaneous Spanish kilns, which allowed discussing the different factors causing the observed dispersion. Catanzariti *et al.* (2008) conducted a quality control test of the archaeomagnetic method in a modern partially heated structure, obtaining results consistent with the known field value in both direction and intensity. Aidona *et al.* (2006) investigated the spatial distribution of magnetic parameters in the floor-bricks of a test furnace, constructed using similar materials and techniques than during the Roman period, concluding that archaeological kilns may need to be sampled very carefully and at close spacing in order to find the best areas for archaeomagnetic investigations because of the spatial limitation of the fire effect. More recently, Tema *et al*. (2013) performed experiments to monitor the behaviour exhibited during experimentally controlled heating of small brick fragments. Most samples exhibited stable behaviour up to 500-600 C while at higher temperatures important changes on their magnetisation occurred. They also show that they experienced different temperatures depending on their position in the kiln. The suitability of lithic clasts from pyroclastic flows to obtain absolute palaeointensity determinations has been successfully tested by other authors (Roperch *et al.* 2014; Paterson *et al.* 2010; Bardot and McClelland 2000). Yet, no similar experiments were carried out on lithic clasts of archaeological interest. Under similar heating conditions to those obtained in this experiment, we have shown that it is possible to obtain reliable palaeointensity determinations in sandstone and obsidian lithic implements. While it is true that prehistoric fires hardly achieve heating temperatures high enough to acquire a total TRM, the high thermomagnetic stability of obsidian due to its volcanic origin makes it an outstanding candidate for this type of analysis. In volcanic regions obsidian is one of the most frequent raw materials found in prehistoric archaeological sites and it should be kept in mind that these are usually well-dated contexts. Therefore, archaeological obsidians have a considerable potential as recorders of the geomagnetic field strength.

Given the wide variability in the magnetic properties among samples of the same lithology is difficult to extrapolate a characteristic magnetic pattern to unequivocally identify heat treatment in archaeological lithic assemblages. Despite the range overlap in the values of some magnetic parameters among lithologies, sandstone and obsidian consistently recorded higher mean MS values compared to limestone, chert and quartzite samples. These variations in magnetic concentration combined with the granulometric information provided by the hysteresis ratios as well as the macroscopic alterations have diagnostic potential to detect if this type of lithologies were heated in the antiquity or not. Some studies have explored the potential of mineral magnetic methods to detect heat treatment in prehistoric sites (e.g. Brown *et al.* 2009, Herries and Fisher 2010) but much effort remains to be done. This study represents a first step with clear implications for experimental archaeology. Although the geographical provenance of the studied materials is very regional and its archaeological application to detect fire perhaps only makes sense on such a scale, allowed us to magnetically characterize these lithologies when heated.

Conclusions

High-temperature (~ 700 ºC) heating generates remarkable magnetic and macroscopic variations in the five lithologies studied. All lithologies except the obsidian recorded an increase of up two orders of magnitude in their magnetic concentration-dependent parameters revealing the formation of new ferrimagnetic minerals (magnetite). Chert, quartzite and limestone are magnetically weak whereas obsidian and sandstone specimens are the most intense because their ferromagnetic content is higher. Therefore they are the most suitable raw materials for archaeomagnetic purposes. Magnetite formation after burning in the weakest lithologies most probably takes place from the transformation of paramagnetic (undetermined) minerals. Magnetic concentration-dependent parameters (e.g. low-field magnetic susceptibility, IRM, saturation magnetisation) are particularly discriminatory showing significant differences among lithologies compared with their unburnt counterparts. Room temperature hysteresis parameters also revealed a more SD state in sandstone specimens after burning so, under similar combustion conditions, it is a suitable lithology for palaeointensity analysis. The main macroscopic alterations observed (colour changes, rubefaction, potlids and microretouches) are particularly evident in cherts which barely modify their magnetic properties after burning. Alternatively, obsidians hardly change their magnetic properties by heating but the massive formation of internal fissures can be used as macroscopic criterion to detect heat treatment. The multispecimen palaeointensity technique was successfully applied to obsidian and sandstone specimens yielding a field estimation of 46.2 ± 2.4 μT (original field 45,302 μT). Finally, this study has shown how mineral magnetic methods combined with macroscopic observations can readily provide information about the burn history of lithic assemblages as well as obtain geomagnetic field information.

Acknowledgments

This study has been carried out with the financial support of the Spanish Ministry of E&C (projects CGL2012-32149, CGL2012-38481 and CGL2012-38434-C03-03). Á.C. research is funded by the *International Excellence Campus Programme, Reinforcement subprogramme*, of the Spanish Ministry of Education. J.M. acknowledges the financial support from project L012 (Proyecto de Laboratorio del IGF). A.G. is grateful for the financial support provided by CONACYT project 129653 UNAM PAPIIT IN-105215 and CONACYT sabbatical programs. M.T.B. research has been funded by Cátedra Atapuerca (Atapuerca and Duques de Soria Foundations). Further, we wish to express our thanks to R. Arauzo for providing us the place to carry out the field experiment.

References

Aidona E., Scholger R., Mauritsch H.J., Schnepp E., Klemm S., 2006, Spatial distribution of archaeomagnetic vectors within archaeological samples from Eisenerz (Austria). *Geophys. J. Int.*, 166, 46-58.

Bardot L., McClelland E., 2000, The reliability of emplacement temperature estimates using palaeomagnetic methods: A case study from Santorini Greece. *Geophys. J. Int*., 143, 1, 39–51.

Borradaile G.J., Kissin S.A., Stewart J.D., Ross W.A., Werner T., 1993, Magnetic and Optical Methods for Detecting the Heat Treatment of Chert. *J. Archaeol. Sci*., 20, 57–66.

Borradaile G.J., Stewart J.D., Ross W.A., 1998, Characterizing stone tools by rock-magnetic methods. *Geoarchaeology* 13, 73–91.

Brown K.S., Marean C.W., Herries A.I.R., Jacobs Z., Tribolo C., Braun D., Roberts D.L., Meyer M.C., Bernatchez J., 2009, Fire as an Engineering Tool of Early Modern Humans. *Science*, 325, 859-862

Calvo-Rathert M., Carrancho Á., Stark F., Villalaín J.J., Hill M., 2012, Are burnt sediments reliable recorders of geomagnetic field strength? *Quat. Res.,* 77, 326–330.

Catanzariti G., McIntosh G., Gómez-Paccard M., Ruiz-Martínez V.C., Osete M.L., Chauvin A., 2008, The AARCH Scientific Team,.Quality control of archaeomagnetic determination using a modern kiln with a complex NRM. *Physics and Chemistry of the Earth*, 33, 427–437.

Carrancho Á., Villalaín J.J., 2011, Different mechanisms of magnetisation recorded in experimental fires: Archaeomagnetic implications. *Earth and Planetary Science Letters,* 312, 176–187.

Day R., Fuller M.D., Schmidt V.A., 1977, Hysteresis properties of titanomagnetites: grain size and composition dependence. *Phys. Earth. Planet. Inter.,* 13, 260–266.

Dekkers M.J., Böhnel H.N., 2006, Reliable absolute palaeointensities independent of magnetic domain state. *Earth and Planetary Science Letters,* 248, 1-2, 507-516.

Domański M., Webb J.A., 1992, Effect of heat treatment on siliceous rocks used in prehistoric lithic technology. *J. Archaeol. Sci*., 19, 601–614.

Domański M., Webb J.A., 2007, A review of heat treatment research. *Lithic Technology* 32, 153–194.

Domański M., Webb J., Glaisher R., Gurba J., Libera J., Zakościelna A., 2009, Heat treatment of Polish flints. *J. Archaeol. Sci*. 36, 7, 1400-1408.

Dunlop D.J., 2002, Theory and application of the Day plot (Mrs/Ms versus Hcr/Hc) 2. Application to data for rocks, sediments, and soils, *J. Geophys. Res.,* 107, doi:10.1029/2001JB000487.

Dunlop D.J., Özdemir Ö., 1997, *Rock Magnetism. Fundamentals and Frontiers*. Cambridge Univ. Press, New York. 573 pp.

Genevey A., Gallet Y., 2002, Intensity of the geomagnetic field in Western Europe over the past 2000 years: New data from ancient French pottery. *J. Geophys. Res*., 107, B11, 2285, doi:10.1029/2001JB000701.

Gedye S.J., Jones R.T., Tinner W., Ammann B., Oldfield F., 2000, The use of mineral magnetism in the reconstruction of fire history: a case study from Lago di Origlio, Swiss Alps. *Palaeogeography, Palaeoclimatology, Palaeoecology,* 164, 101–110.

Gómez-Paccard M., Chauvin A., Lanos Ph., Thiriot J., Jiménez- Castillo P., 2006, Archeomagnetic study of seven contemporaneous kilns from Murcia, Spain. *Phys. Earth Planet. Int*., 57 1–2.

Griffiths D.R., Bergman C.A., Clayton C.J., Ohnuma K., Robins G.R., Seeley N.J., 1985, Experimental investigation of the heat treatment of flint. *In*: G. de G. Sieveking & M.H. Newcorner (eds.). *The human use of flint and chert*. Cambridge University Press.

Grommé C.S., Wright T.L, Peck D.L, 1969, Magnetic properties and oxidation of iron-titanium oxide minerals in Alae and Makaopuhi lava lakes, Hawaii. *J. Geophys. Res*., 74, 5277-5294.

Hallett D.J, Anderson R.S., 2010, Paleofire reconstruction for high-elevation forests in the Sierra Nevada, California, with implications for wildfire synchrony and climate variability in the late Holocene. *Quaternary Research,* 73, 2, 180-190.

Henry B., 2007, Magnetic mineralogy, changes due to heating. *In:* D. Gubbins & E. Herrero-Bervera (eds.), *Encyclopedia of Geomagnetism and Palaeomagnetism*. Springer, 512-515.

Hester T.R., 1972, Ethnographic evidence for the thermal alteration of siliceous stone. *Tebiwa* 15, 63–65.

Herries A.I.R., 2009, New approaches for integrating palaeomagnetic and mineral magnetic methods to answer archaeological and geological questions on Stone Age sites. In: Fairbrain, A., O'Conner, S., Marwick, B. (Eds.), Terra Australis 28 – New Directions in Archaeological Science. The Australian National University Press, Canberra, Australia, pp. 235–253 (Chapter 16).

Herries A.I.R., Fisher E.C., 2010, Multidimensional GIS modeling of magnetic mineralogy as a proxy for fire use and spatial patterning: Evidence from the Middle Stone Age bearing sea cave of Pinnacle Point 13B (Western Cape, South Africa). *J. Human Evol*., 59, 306-320.

Lanci L., Kent D.V., 2003, Introduction of thermal activation in forward modeling of hysteresis loops for single-domain magnetic particles and implications for the interpretation of the Day diagram. *J. Geophys. Res*., 108, B3, 2142, doi:10.1029/2001JB000944.

McDougall J.M., Tarling D.H., Warren S.E., 1983, The Magnetic Sourcing of Obsidian Samples from Mediterranean and Near Eastern Sources. *J. Archaeol. Sci*., 10, 441–452.

Morales J., Goguitchaichvili A., Aguilar-Reyes B., Pineda-Duran M., Camps P., Carvallo C., Calvo-Rathert M., 2011, Are ceramics and bricks reliable absolute geomagnetic intensity carriers? *Phys. Earth Planet. Int*., 187, 310-321.

Paterson G.A., Muxworthy A.R., Roberts A.P., Mac Niocaill C., 2010, Assessment of the usefulness of lithic clasts from pyroclastic deposits for paleointensity determination, *J. Geophys. Res*., 115, B03104, doi:10.1029/2009JB006475.

Purdy B.A., 1974, Investigations concerning the thermal alteration of silica minerals: an archaeological approach. *Tebiwa* 17, 37–66.

Rodríguez J., Burjachs F., Cuenca-Bescós G., García N., Van der Made J., Pérez González A., Blain H.-A., Expósito I., López-García J.M., García Antón M., Allué E., Cáceres I., Huguet R., Mosquera M., Ollé A., Rosell J., Parés J.M., Rodríguez X.P., Díez C., Rofes J., Sala R., Saladié P., Vallverdú J., Bennasar M.L., Blasco R., Bermúdez de Castro J.M., Carbonell E., 2011, One million years of cultural evolution in a stable environment at Atapuerca (Burgos, Spain). *Quaternary Science Reviews,* 30, 11-12, 1396-1412.

Roperch P., Chauvin A., Le Pennec J.-L., Lara L.E., 2014, Paleomagnetic study of juvenile basaltic-andesite clasts from Andean pyroclastic density current deposits. *Physics of the Earth and Planetary Interiors,* 227, 20-29.

Shaw J., 1974, A New Method of Determining the Magnitude of the Palaeomagnetic Field: Application to five historic lavas and five archaeological samples, *Geophys. J. Int.*, 39, 133-141.

Stewart S.J., Cernicchiaro G., Scorzelli R.B., Poupeau G., Acquafredda P., De Francesco A., 2003, Magnetic properties and ^{57}Fe Mössbauer spectroscopy of Mediterranean prehistoric obsidians for provenance studies. *J. Non-Cryst. Solids,* 323, 188-192.

Tema E., Fantino F., Ferrara E., Lo Giudice A., Morales J., Goguitchaichvili A., Camps P., Barello F., Gulmini M., 2013, Combined archaeomagnetic and thermoluminescence study of a brick kiln excavated at Fontanetto Po (Vercelli, Northern Italy). *J. Archaeol. Science,* 40, 2025-2035.

Thacker P.T., Ellwood B.B., 2002, The Magnetic Susceptibility of Cherts: Archaeological and Geochemical Implications of Source Variation. *Geoarchaeology,* 17, 5, 465–482.

Vásquez C.A., Nami H.G., Rapalini A.E., 2001, Magnetic sourcing of obsidians in Southern South America: some successes and doubts. *J. Archaeol. Sci*., 28, 613-618.

Zanella E., Ferrara E., Bagnasco L., Ollà A., Lanza R., Beatrice C., 2012, Magnetite grain-size analysis and sourcing of Mediterranean obsidians. *J. Archaeol. Sci*., 39, 1493-1498.